Fakultät für
Mathematik, Informatik
und Naturwissenschaften

RWTHAACHEN
UNIVERSITY

# Stoichiometric control and magnetoelectric coupling in artificial multiferroic heterostructures

Von der Fakultät für Mathematik, Informatik und Naturwissenschaften der RWTH Aachen
University zur Erlangung des akademischen Grades eines
Doktors der Naturwissenschaften genehmigte Dissertation

vorgelegt von

*Patrick Schöffmann, M.Sc.*

aus

*Ingolstadt, Germany*

Berichter*:* *Professor Dr. Thomas Brückel*
*Professor Dr. Joachim Mayer*

Tag der mündlichen Prüfung*:* *05.07.2021*

Diese Dissertation ist auf den Internetseiten der Universitätsbibliothek verfügbar.

# Zusammenfassung

Der Bedarf für schnellere und kleinere Datenträger, neue Sensortechnik und multifunktionelle Komponenten hat die Forschung an Übergangsmetalloxiden stark vorangetrieben. Da die Elektronen in diesen Materialien oft stark korelliert sind, zeigen Übergangsmetalloxide eine Vielzahl von neuartigen Effekten. Speziell der Einsatz von künstlichen multiferroischen Heterostrukturen hat großes Interesse geweckt. Die physikalischen Eigenschaften der einzelnen Schichten können auf den individuellen Einsatz zugeschnitten werden, und durch geeignete Kombination der Materialien werden neue Funktionalitäten realisiert.

Gegenstand dieser Dissertation ist die Beeinflussung der Magnetisierung von dünnen Übergangsmetalloxidschichten mittels des ferroelektrischen Substrates $[Pb(Mg_{1/3}Nb_{2/3})O_3]_{0.7}$–$[PbTiO_3]_{0.3}$ (PMN-PT).

Der erste Teil dieser Dissertation berichtet über das Wachstum und die Untersuchung von $SrCoO_{3-\delta}$. Durch Manipulation des Sauerstoffgehalts kann das antiferromagnetische und isolierende $SrCoO_{2.5}$ in das ferromagnetische und leitende $SrCoO_3$ umgewandelt werden. Für das Wachstum epitaktischer und stöchiometrischer $Sr_1Co_1O_{2.5}$ Schichten mittels Molekularstrahlepitaxie (MBE) müssen die Wachstumparameter präzise gewählt werden. Um die Co-zu-Sr Stöchiometrie *in-situ* zu bestimmen und zu optimieren kann „Reflection High Energy Electron Diffraction" (RHEED) eingesetzt werden. Das RHEED Beugungsmuster ermöglicht die Unterscheidung zwischen Co Defizit oder Überschuss und stöchiometrischer $Sr_1Co_1O_{2.5}$ Schicht. Durch Heizen in Sauerstofffluss können die hochqualitativen $SrCoO_{2.5}$ Schichten zu $SrCoO_3$ umgewandelt werden. Die $SrCoO_3$ Schichten sind stabil in Vakuum. $SrCoO_{3-\delta}$ Proben mit $\delta<0.25$ bilden drei verschiedene ferromagnetische Phasen und weisen einen Exchange bias Effekt auf. Messungen einer $SrCoO_{2.75}$ Schicht mit polarisierter Neutronenreflektometrie zeigen ein homogene Verteilung der magnetischen Phasen. $SrCoO_{2.5}$ Schichten können durch den Unterschied der Gitterkonstanten nicht direkt auf PMN-PT gewachsen werden. Durch den Einsatz einer $La_{0.67}Sr_{0.33}MnO_3$ (LSMO) Zwischenschicht kann der Unterschied der Gitterkonstanten verringert werden, was das Wachstum einer kristallinen $SrCoO_{2.5}$/LSMO/PMN-PT Heterostruktur ermöglicht.

Der zweite Teil der Dissertation behandelt die magnetoelektrische Kopplung in $Fe_3O_4$/PMN-PT(001) und $Fe_3O_4$/PMN-PT(011) Heterostrukturen, welche mit gepulster Laserabscheidung gewachsen sind. Die Proben zeigen eine starke Kopplung zwischen der Magnetisierung der ferrimagnetischen Schicht und der Verspannung und Polarisierung des Substrates wenn ein elektrisches Feld angelegt wird. Durch ein qualitatives Model können die Anteile der einzelnen Beiträge zur magnetoelektrischen Kopplung abgeschätzt werden. Sowohl die Schnittrichtung des Substrates als auch die Orientierung der Probe im Magnetfeld hat einen starken Einfluss auf das magnetoelektrische Verhalten der Schicht.

# Abstract

The demand for smaller and faster information storage media, new types of sensors and multifunctional devices has lead to a rush in research on transition metal oxides (TMO's). Strong electronic correlations in TMO's lead to a wealth of new and interesting effects. Particularly the use of artificial multiferroic heterostructures using advanced thin film growth techniques, has attracted a lot of interest, as they enable the tailoring of the physical properties of individual materials and hold the promise of new combined functionality.

The subject of this thesis is control of the magnetisation in thin TMO films using the ferroelectric substrate $[Pb(Mg_{1/3}Nb_{2/3})O_3]_{0.7}$–$[PbTiO_3]_{0.3}$ (PMN-PT).

The first part of this thesis is about the fabrication and investigation of $SrCoO_{3-\delta}$, which has different magnetic and conductive properties depending on the oxygen content. Importantly, the antiferromagnetic, insulating $SrCoO_{2.5}$ can be transformed reversibly in the ferromagnetic, metallic $SrCoO_3$. To grow epitaxial and stoichiometric $Sr_1Co_1O_{2.5}$ films by molecular beam epitaxy (MBE), the deposition parameter have to be precisely controlled. To determine the Co-to-Sr ratio *in-situ* and optimise it, Reflection High Energy Electron Diffraction (RHEED) can be used. The RHEED scattering pattern changes depending on the Co/Sr ratio and can be used to determine Co excess or deficiency and to grow stoichiometric $Sr_1Co_1O_{2.5}$ samples. High quality $SrCoO_{2.5}$ can be transformed to $SrCoO_3$ by heating in oxygen flow and the resulting films remain stable in vacuum. $SrCoO_{3-\delta}$ films (with $\delta<0.25$) form three distinct magnetic phases and show an exchange bias effect. The magnetic phases are distributed uniformly throughout the film, as can be determined by Polarised Neutron Reflectometry (PNR). Due to a mismatch of lattice constants, $SrCoO_{2.5}$ films can't be grown directly on PMN-PT. However, using an $La_{0.67}Sr_{0.33}MnO_3$ buffer layer, crystalline $SrCoO_{2.5}/La_{0.67}Sr_{0.33}MnO_3$/PMN-PT heterostructures can be grown.

The second part of the dissertation is about the magnetoelectric coupling in $Fe_3O_4$/PMN-PT(001) and $Fe_3O_4$/PMN-PT(011) heterostructures grown by pulsed laser deposition. The strain and polarisation of the substrate with applied electric field mediate the coupling to the magnetisation in the ferrimagnetic layer. Using a qualitative model, the strength of the different contributions can be estimated. The substrate cut and orientation of the sample in the magnetic field has a strong influence on the magnetoelectric behaviour of the layer.

# Table of contents

# 1 Introduction

Ever since the theory of modern computers by Alan Turing [1] and implementation by Konrad Zuse [2], the development of smaller and denser information storage systems has been a driving force in science. Starting with machines filling a whole building to save a few kilobytes of data it developed into solid state drives fitting in the palm of a hand capable of holding a library worth of information. But data volumes and demands for faster and smaller devices are ever increasing, which not only requires optimisation of existing technologies, but also research into new ones. Traditional hard disk drives use a ferro-/ ferrimagnetic medium to store the information and a read/write head with giant magnetoresistance to save and retrieve information. The giant magnetoresistance effect was so important that Albert Fert and Peter Grünberg were awarded the Nobel prize in 2007 for its discovery [3–5]. As science progresses, new avenues for developing storage media or even multifunctional devices became apparent.

A very promising class of materials for this area of research are the transition metal oxides (TMO), which are model systems for highly correlated electron physics. High electronic correlations are found in materials where the electrons are neither fully free from nor fully bound to atomic position, which results in coupling between magnetic, electronic and structural degrees of freedom. Because of these close connections, TMO's exhibit a multitude of emergent properties, such as high temperature superconductivity [6], multiferroicity [7], and metal-insulator transitions [8].

Multiferroics are materials which possess more than one ferroic order, e.g. ferromagnetism and ferroelectricity. In such a magnetoelectric multiferroic, magnetism and polarisation are intrinsically linked and, such that an external electric field is able to influence the magnetisation in the sample, or vice versa. Multiferroic materials are very rare however, as they have to break time-reversal and inversion symmetry at the same time. A way of expanding the pool of usable materials is to take two separate compounds, each with a different ferroic order, and combine them into a thin film heterostructure. This enables tailoring of physical properties as the two components can be chosen nearly independently to achieve the best possible functionality. The heterostructure can be comprised of a single or multiple layers on a substrate. The challenge in creating artificial multiferroics this way is to achieve the coupling between ferroic orders in the two materials. To facilitate this the shared interface between substrate and film and the crystallinity of the thin film have to be excellent.

In this thesis, heterostructures of an (anti-)ferromagnetic or ferrimagnetic layer and a ferroelectric substrate are investigated. $SrCoO_{3-\delta}$ (SCO) and $Fe_3O_4$ (magnetite) layers are studied in detail. The properties of the first layer, $SrCoO_{3-\delta}$, depend strongly on the oxygen content. Intriguingly, SCO can transform topotactically from the perovskite structure for $SrCoO_3$, to the brownmillerite structure for $SrCoO_{2.5}$, which is accompanied by the change from a ferromagnetic metal to an antiferromagnetic insulator. The oxygen content can be tuned by annealing in oxidising or reducing conditions [9], ionic liquid gating [10] or strain [11]. Because of the $Co^{3+}$ valence, $SrCoO_{2.5}$ is more stable compared to $SrCoO_3$, which has $Co^{4+}$ valency. The films for this investigation are grown by molecular beam epitaxy (MBE) using effusion cells for the deposition of Sr and Co and an oxygen plasma source. Because the maximum possible pressure in the MBE setup is around $10^{-5}$ mbar, SCO films always grow in $SrCoO_{2.5}$ stoichiometry. Before any coupling effects between the film and substrate can be investigated, first the growth conditions for high quality $SrCoO_{2.5}$ layers have to be ascertained. In MBE growth, the deposition rates of Co and Sr are independent, as opposed to growth methods using a target with pre-defined stoichiometry such as pulsed laser deposition or sputtering. A detailed growth study was undertaken to optimise the growth conditions, particularly the Co/Sr ratio, for $SrCoO_{2.5}$ films on $SrTiO_3$ (STO) and $(La_{0.26}Sr_{0.76})(Al_{0.61}Ta_{0.37})O_3$ (LSAT) substrates. After the successful growth of high quality, epitaxial $SrCoO_{2.5}$ films, the annealing conditions necessary to transform the films into $SrCoO_3$ were determined and the $SrCoO_3$ stability determined. The samples were then investigated for their magnetic properties by magnetometry and neutron reflectometry. Finally, SCO films were grown on ferroelectric $[Pb(Mg_{1/3}Nb_{2/3})O_3]_{0.7}$–$[PbTiO_3]_{0.3}$ (PMN-PT) substrates, with and without $La_{2/3}Sr_{1/3}MnO_3$ (LSMO) buffer layer.

As a second project, $Fe_3O_4$ films grown by pulsed laser deposition on PMN-PT(001) and PMN-PT(011) substrates are studied to understand the different mechanisms participating in magnetoelectric coupling. Magnetite is a ferrimagnetic half-metal and undergoes a Verwey metal-to-insulator transition at 120 K, which drastically increases resistivity and reduces magnetisation [8, 12]. Recent studies have shown that $Fe_3O_4$/PMN-PT(011) heterostructures show a large magnetoelectric effect [13–16], however the underlying mechanisms have not yet been studied much. After the evaluation of crystalline quality of the $Fe_3O_4$ films, influence of an electric field on the magnetisation is studied in different magnetic field and temperatures.

## Thesis structure

In the beginning of the thesis, the theory behind magnetism and magnetoelectric coupling in transition metal oxides is introduced, with a focus on magnetic interactions in SCO and magnetite. Next, the principle of relaxor ferroelectrics is explained. As scattering techniques are an integral part of the investigations presented in this thesis, the basics of scattering theory with different probes is reviewed, with a focus on scattering from thin films.

In the methods chapter, all used instruments, from thin films growth, over laboratory characterisation methods, to polarised neutron reflectometers are explained.

Chapter 4 presents the results of the growth investigation of $SrCoO_{2.5}$ and reports on the stoichiometric and structural optimisation of the thin films on STO and LSAT substrates. After the growth the annealing conditions for the transformation to $SrCoO_3$ are determined and the resulting films characterised regarding their phase stability and magnetic properties by laboratory methods and polarised neutron reflectometry (PNR).

In chapter 5, the characterisation of the ferroelectric PMN-PT substrates is shown, for both substrates orientations used in the next two chapters.

Completing the investigation of SCO, chapter 6 reports on the growth of SCO on PMN-PT and the investigation by PNR.

The study of magnetoelectric coupling in $Fe_3O_4$/PMN-PT is described in chapter 7. The chapter starts with the structural and magnetic characterisation of PLD grown samples, followed by the magnetisation dependence on the electric field. The different influences of strain, polarisation and charge contributions are discussed.

An outlook of possible future studies is given in chapter 9.

To ensure reproducibility of all results obtained here, information about the sample growth for all samples in this thesis are summarised in the supplementary information.

# 2 Theory

In the following, the magnetic interactions present in the investigated systems are sketched, based on the textbooks [17–19]. Then, properties and crystal structure of thin films and substrates are discussed. These are perovskite, brownmillerite and inverse spinel for $SrCoO_3$, $SrCoO_{2.5}$, and $Fe_3O_4$, respectively. After that, ferroelectricity in the substrate PMN-PT[a] will be introduced, followed by growth modes of thin films. Then, an overview of scattering theory and scattering by different types or radiation is given, specifically for the case of thin films.

## 2.1 Crystal structures

Table 2.1 lists the lattice constants and crystal structure of all films and substrates used in this thesis.

**Table 2.1:** Bulk crystal structures and lattice constants of materials used in this thesis

| Formula unit | Crystal structure | a [Å] | b [Å] | c [Å] | References |
|---|---|---|---|---|---|
| $SrCoO_{2.5}$ | orthorhombic brownmillerite | 5.574 | 5.470 | 15.745 | [20] |
| | pseudo-tetragonal notation | 3.905 | 3.905 | 3.936·4 | [20] |
| $SrCoO_3$ | cubic perovskite | 3.830 | 3.830 | 3.830 | [21] |
| CoO | cubic rocksalt | 4.260 | 4.260 | 4.260 | [22] |
| $Fe_3O_4$ | inverse spinel | 8.396 | 8.396 | 8.396 | [23] |
| $La_{0.67}Sr_{0.33}MnO_3$ | rhombohedral perovskite<br>$\alpha = \beta = \gamma = 90.26°$ | 5.506 | 5.506 | 13.356 | [24] |
| | pseudo-cubic notation | 3.87 | 3.87 | 3.87 | [24] |
| LSAT$^x$ | pseudo-cubic perovskite | 3.868 | 3.868 | 3.868 | [25] |
| $SrTiO_3$ | cubic perovskite | 3.905 | 3.905 | 3.905 | [25] |
| PMN-PT (30%)$^y$ | rhombohedral perovskite<br>$\alpha = \beta = \gamma = 89.89°$ | 4.017 | 4.017 | 4.017 | [26] |

$^x(La_{0.26}Sr_{0.76})(Al_{0.61}Ta_{0.37})O_3$
$^y[Pb(Mg_{1/3}Nb_{2/3})O_3]_{0.7}$–$[PbTiO_3]_{0.3}$

---

[a] $[Pb(Mg_{1/3}Nb_{2/3})O_3]_{1-x}$–$[PbTiO_3]_x$

### 2.1.1 Perovskite and brownmillerite structure

One of the most commonly investigated material systems for correlated electron systems are perovskites. Perovskites posses an $ABO_{3-\delta}$ stoichiometry, with an $A$-site cation, a $B$-site transition metal, and oxygen ions forming corner sharing octahedra around the $B$-site ion (fig. 2.1, top left).

The stability of the perovskite structure, for given choice of $A$ and $B$ site cations, can be estimated by the Goldschmidt tolerance factor [28], $t$, with the radii of the ions, $r_{A,B}$, and the oxygen radius, $r_O$,

$$t = \frac{r_A + r_O}{\sqrt{2}(r_B + r_O)}. \tag{2.1}$$

If the tolerance factor is between 0.9 and 1, the structure is stable as a cubic perovskite. For values lower than 0.9, the oxygen octahedra will tilt, resulting in an orthorhombic or rhombohedral structure.

For $\mathrm{SrCoO_3}$, the tolerance factor is $t_{\mathrm{SrCoO_3}} = 0.94$, meaning it will be perfectly cubic perovskite.

If the perovskite structure (in the following with index $P$) becomes oxygen deficient ($\delta > 0$), the oxygen vacancies will reduce the symmetry of the system and for $\delta = 0.5$, the brownmillerite structure (index $BM$) will form (fig. 2.1, top right). For $\mathrm{SrCoO_{2.5}}$, the oxygen vacancies cause the oxygen octahedra in every second layer to be replaced by tetrahedra, with the vacancies forming channels along a crystalline axis and the remaining octahedra tilt away from the $c$-axis. The unit cell will then be orthorhombic, with the a and b lattice vectors (see table 2.1) roughly $\sqrt{2}$ larger and c 4-times larger. This means the brownmillerite unit cell will be rotated by 45° in the $ab$ plane relative to the perovskite lattice. For growth considerations, it may be useful to define a pseudo-tetragonal lattice (index $BM, t$) for the brownmillerite structure, such that $a_{BM,t} = b_{BM,t} = \frac{1}{\sqrt{2}} \frac{a_{BM}+b_{BM}}{2}$ and $c_{BM,t} = c_{BM}/4$ and $\sphericalangle \vec{a}_{BM,t}\vec{a}_{BM} = 45°$ (similar for b).

#### Perovskite substrates

Two perovskite substrates were primarily used for the growth study of $\mathrm{SrCoO_{2.5}}$: strontium titanate ($\mathrm{SrTiO_3}$, STO) and lanthanum aluminate – strontium aluminium tantalate ($(\mathrm{La_{0.26}Sr_{0.76}})(\mathrm{Al_{0.61}Ta_{0.37}})\mathrm{O_3}$, LSAT).

STO is diamagnetic and undergoes an antiferrodistortive phase transition at 105 K [29]. Below the transition temperature the oxygen octahedra rotate away from the $c$ axis, changing the structure from cubic to tetragonal. This is accompanied by a compressive strain in the $ab$-plane caused by the reduction of the lattice constant of about 0.1%.

LSAT is a disordered system with a mixture of 26% La and 76% Sr in the $A$-site

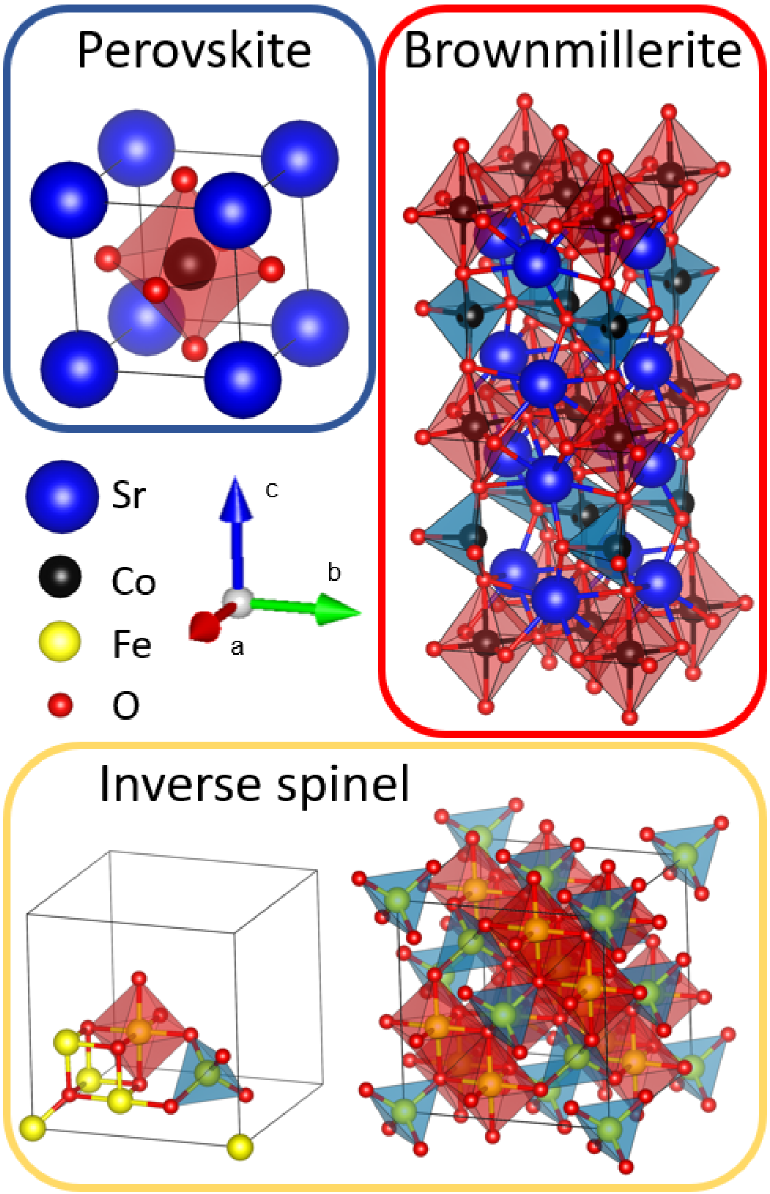

**Figure 2.1:** Overview of crystal structures. $SrCoO_{3-\delta}$ crystallises in perovskite (**top left**) or brownmillerite (**top right**) structure. Cobalt ions are indicated in black, oxygen in red, and strontium in blue. The oxygen octahedra are indicated in red, and tetrahedra in cyan. The inverse spinel structure of $Fe_3O_4$ is shown on the **bottom**. Iron ions are indicated in yellow and oxygen in red. The oxygen octahedra occupied by both $Fe^{2+}$ and $Fe^{3+}$ ions are indicated in red, and tetrahedra occupied by $Fe^{3+}$ ions in cyan. A view of a partial unit cell for better visualisation of the octahedral and tetrahedral sites is shown on the **bottom left**. Figures were created with VESTA [27].

and 61% Al and 37% Ta in the *B*-site. It is mostly diamagnetic, with a small paramagnetic moment at low temperatures, attributed to impurities [30].

### 2.1.2 Inverse spinel structure

The inverse spinel structure has the general stoichiometry $B_{tet}(AB)_{oct}O_4$, with the cations $A, B$ and oxygen forming octahedra and tetrahedra around them (fig. 2.1, bottom). $Fe_3O_4$ grows in the inverse spinel structure, with the tetrahedral sites occupied by $Fe^{3+}$ ions ($d^5$) and the octahedra by $Fe^{2+}$ ($d^6$) and $Fe^{3+}$ ions ($Fe^{3+}_{tet}(Fe^{2+}Fe^{3+})_{oct}O_4$).

## 2.2 Magnetism in transition metal oxides

### 2.2.1 Exchange interactions

The magnetism in transition metal oxides depends on many factors, though it is based on the exchange interactions between the electrons of the transition metal and their neighbours [17]. In general, the exchange between direct neighbours can be described by the Heisenberg Hamiltonian,

$$\hat{H}_{\text{Heisenberg}} = J\hat{\vec{S}}_1 \cdot \hat{\vec{S}}_2 \tag{2.2}$$

$$\text{with } \hbar^2 J \sim \hbar^2(J_{dir} + J_{kin}) = \hbar^2 J_{dir} + \frac{4t^2}{U}, \tag{2.3}$$

with the exchange constant, $J$, the direct and kinetic exchange constants, $J_{dir}$ and $J_{kin}$, the hopping matrix element, $t$, and the on-site Coulomb repulsion, $U$. For systems with strong electronic correlation, the electrons are relatively localized, such that $U >> t$, and thus direct exchange is negligible. Since in transition metal oxides the magnetic ions are not nearest neighbours, the exchange is mediated by the oxygen atoms between them. For $3d$ metals with an intermediate oxygen atom, two forms of exchange interactions are dominant, superexchange and double exchange. Because oxygen is highly electroegative, its oxidation state is $O^{2-}$, with the spins in the $2p$ orbitals aligned antiparallel due to Pauli repulsion, rendering it magnetically inert. The oxygen orbitals can, however, have a direct and kinetic exchange with the $3d$ metal orbitals and effectively mediate the exchange between the metal ions.

#### Superexchange

The superexchange interaction depends strongly on the valency and bond angle between the $3d$ metal and intermediate oxygen atom, which is described by the Goodenough-Kanamori-Anderson rules [31–33]. For a 180° angle and half filled (or empty) 3d orbitals, the superexchange is antiferromagnetic due to the kinetic exchange of neighbouring spins. The electrons can delocalize by aligning antiferromagnetically, thus lowering the energy (fig. 2.2). Superexchange can be ferromagnetic in two cases, if one $3d$ orbital is half filled and the other one is either empty or full; or for a 90° angle between two half filled 3d orbitals.

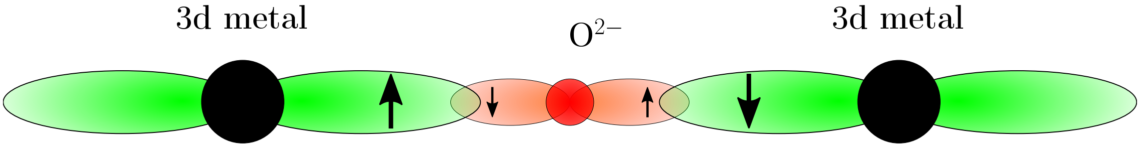

**Figure 2.2:** Schematic of the superexchange between two 3d metal ions of same valency. The spins of the $3d$ metal are aligned antiparallel due to a lowering in energy by delocalization.

### Double exchange

For $3d$ metals of different valency, double exchange interaction can occur. The additional electron on one of the ions can hop onto the oxygen-$2p$ orbital, while a $2p$ electron hops onto the second $3d$ ion. This is shown in fig. 2.3 for Fe$^{2+}$ and Fe$^{3+}$. Because the $2p$ electron can only hop onto the Fe$^{3+}$ ion if it is aligned parallel to the electron hopping from the Fe$^{2+}$ ion, double exchange leads to ferromagnetic alignment of the remaining electrons on both Fe atoms.

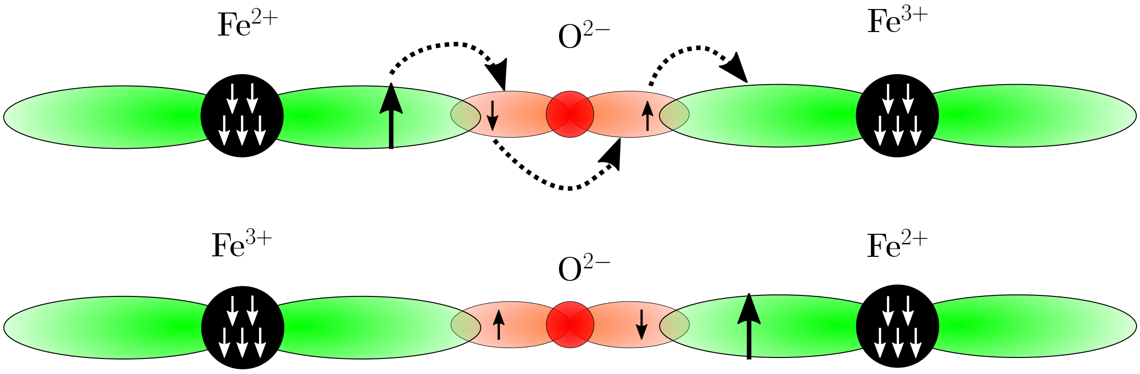

**Figure 2.3:** Double exchange interaction for Fe$^{2+}$ and Fe$^{3+}$. The double exchange of the additional electron on the Fe$^{2+}$ ion (black) couples the remaining electrons (white) ferromagnetically.

## 2.2.2 Lifting of orbital degeneracy

### Hubbard band splitting

In section 2.2.1 the Heisenberg Hamiltonian was briefly discussed. Considering the limit for large $U$, it can be energetically favourable for the $3d$ electrons to align ferromagnetically within one site, as described by the Hubbard Hamiltonian.

$$\hat{H}_{\text{Hubbard}} = \frac{1}{\hbar^2}\frac{4t^2}{U}\hat{\vec{S}}_1 \cdot \hat{\vec{S}}_2. \tag{2.4}$$

For an extended system, this causes a splitting of the $3d$ band into an upper and

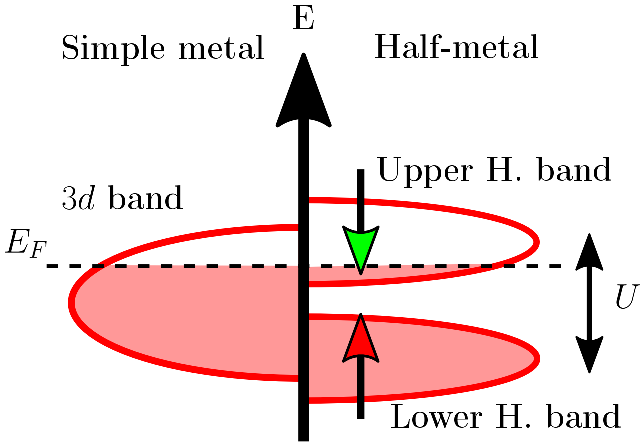

**Figure 2.4:** Example of unsplit $3d$ band for a simple metal (**left**) and Hubbard band splitting for a half-metal with a majority-spin up (**right**).

lower band with energy difference $U$ (fig. 2.4). For a half filled orbital, the electrons will fill the lower band first. Any additional electron will then occupy the higher band. This results in a majority spin lower Hubbard band and a minority spin upper Hubbard band. If the electron in the higher band is still quite localized and not very mobile, the result is a charge ordering effect. If the Fermi level is in the upper Hubbard band, the material will be a half-metal, meaning that it is a conductor for minority spin electrons and an insulator for the majority spin electrons.

### Crystal field splitting

As the ferromagnetic ions in the transition metal oxides are surrounded by oxygen octahedra or tetrahedra, the local environment has an effect on the energy levels of the $3d$ orbitals. The two $e_g$ orbitals, $z^2$ and $x^2 - y^2$, have orbital lobes along the Cartesian axes, whereas the three $t_{2g}$ orbitals, $zx, yz$, and $xy$ point along the diagonal directions (fig. 2.5). This means that for the octahedral environment the $e_g$ orbitals are oriented along the metal-oxygen bond and the $t_{2g}$ point between two metal-oxygen bonds. As a result of the Coulomb repulsion experienced by the $e_g$ orbitals, their energy is increased by $\frac{3}{5}E_{CF}$, whereas the $t_{2g}$ levels have their energy reduced by $\frac{2}{5}E_{CF}$, with $E_{CF}$ as the total energy difference (crystal field energy). For tetrahedral environment, the case is reversed, with the $t_{2g}$ energetically favourable. The occupancy of electrons in the orbitals depends on the relative strength of the crystal field energy, $E_{CF}$, favouring the filling of the lower lying level first, and the Hund's coupling ($1^{st}$ rule), $E_{HR}$, favouring a parallel alignment of all spins. Taking a $3d^5$ system in an octahedral environment as an example, for $E_{HR} > E_{CF}$, the electrons are in the same spin state, creating a high spin state, with S=$\frac{5}{2}$, whereas for $E_{HR} > E_{CF}$ the electrons fill the low lying $t_{2g}$ state first, with 3 spin up and 2 spin down, creating a low spin state with S=$\frac{1}{2}$.

### Strain splitting

The remaining degeneracy of the orbitals after the crystal field splitting can be further lifted if the system experiences strain. For a uniform in-plane strain, e.g.

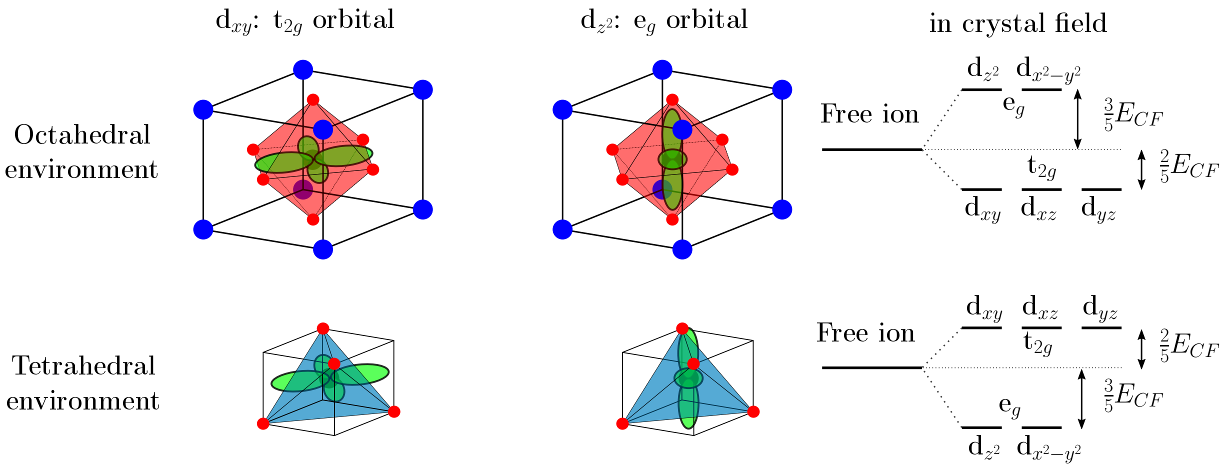

**Figure 2.5:** Crystal field splitting in octahedral (**top**) and tetrahedral (**bottom**) environment. The black spheres represent the 3d metal ions, red spheres oxygen, and the blue spheres the cation. The red shaded area represent the oxygen octahedra and cyan shaded areas the oxygen tetrahedra. The $d_{xy}$ and $d_{z^2}$ orbitals are indicated in green. On the **right**, the resulting crystal field splitting of the energy levels is indicated.

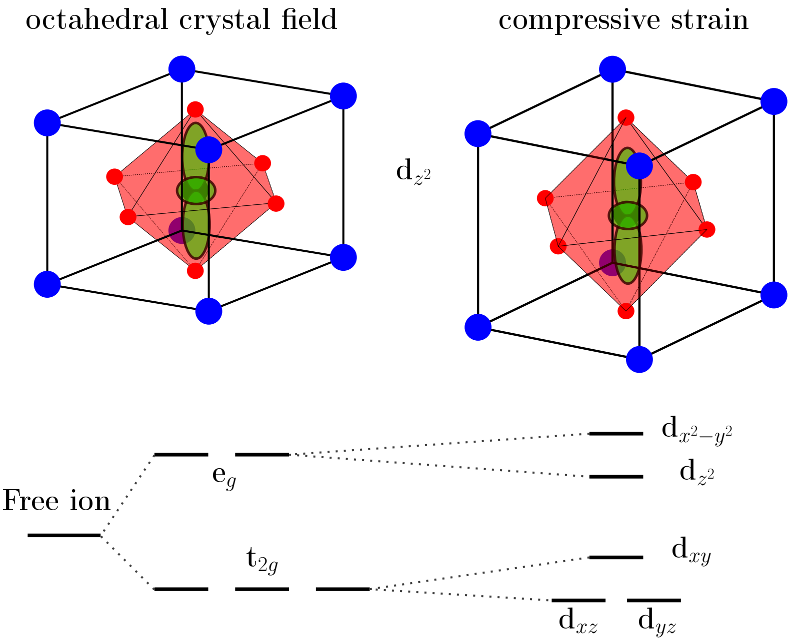

**Figure 2.6:** Crystal field splitting in octahedral environment (**left**) and further splitting by compressive strain (**right**). Below, the resulting crystal field splitting and strain splitting is shown.

for an epitaxial film on a substrate, the bonding along the out-of-plane axis will be different from that along the in-plane axes, thus breaking the degeneracy for orbitals with different $z$-component. This is shown in fig. 2.6 for compressive in-plane strain in an octahedral crystal field. The splitting due to strain is similar to the Jahn-Teller effect, but reversed, since here the elastic strain influences the electronic states, whereas for the Jahn-Teller effect, the electronic states lead to distortion and strain.

### 2.2.3 Magnetic anisotropies

Thus far, the mechanisms governing the interactions of spins inside or between neighbouring unit cells have been discussed. On larger length scales, the influence of additional effects increases. To describe the collective behaviour of a macroscopic magnetisation, anisotropies are considered. The orientation of the magnetisation within a sample is governed by the interplay between different forces, trying to align the magnetisation to minimize the energy. For uniaxial anisotropy, the energy density required to change the angle, $\theta$, of magnetisation from the initial direction, can be expressed as

$$E_{\mathrm{an}} = \mathrm{K}_1 \sin^2\theta, \tag{2.5}$$

with the anisotropy constant, $\mathrm{K}_1$. In any given sample, the shape, crystalline structure, strain state and other contributions, dictate the magnetic anisotropy in the system. In general, the anisotropy is strongly dependent on the temperature.

#### Magnetocrystalline anisotropy

The crystal structure contributes to the magnetic anisotropy due to the crystal field (see chapter 2.2.2) combined with spin orbit coupling. For the 3d metals investigated in this thesis, however, the spin-orbit part plays only a very small role compared to the crystal field. Depending on the specific crystal system and anisotropy constant, the crystal field leads to easy and hard axes of magnetisation. In a cubic system, the anisotropy energy density is given by,

$$E_{\mathrm{mc,an}} = \mathrm{K}_1 \left(\sin^2\theta \sin^2 2\phi + \cos^2\theta\right) \sin^2\theta, \tag{2.6}$$

with $\theta$ as the angle between the magnetisation and the $z$-axis and $\phi$ as the angle between magnetisation and the $x$-direction. This leads to an (un)favourable alignment along the crystalline axes, depending on the sign of $\mathrm{K}_1$.

#### Shape anisotropy

In thin films, the sample shape has a large influence on the magnetic anisotropy due to dipolar interaction. Trying to align the magnetisation in the out-of-plane direction of the film, creates a large stray field, which raises the energy density according to,

$$E_{\mathrm{s,an}} = \frac{1}{2}\mu_0 \mathrm{M}^2 \cos^2\theta, \tag{2.7}$$

for the angle $\theta$ between magnetisation and surface normal. This creates easy and hard directions of magnetisation. Along the easy axis the magnetisation saturates already in smaller fields.

The hysteresis loops in fig. 2.7 show the interplay between shape and magnetocrystalline anisotropy in a thin film sample with cubic crystal structure with the out-of-plane direction [011]. In bulk, the magnetocrystalline anisotropy would dominate and the magnetic easy axis would lie along $\langle 111 \rangle$, but for a thin film the shape anisotropy forces the easy axis in-plane. The two in-plane direction, [100] and $[01\bar{1}]$, then have an energy difference according to the magnetocrystalline anisotropy, which creates an easy axis along $[01\bar{1}]$ and a hard axis along [100].

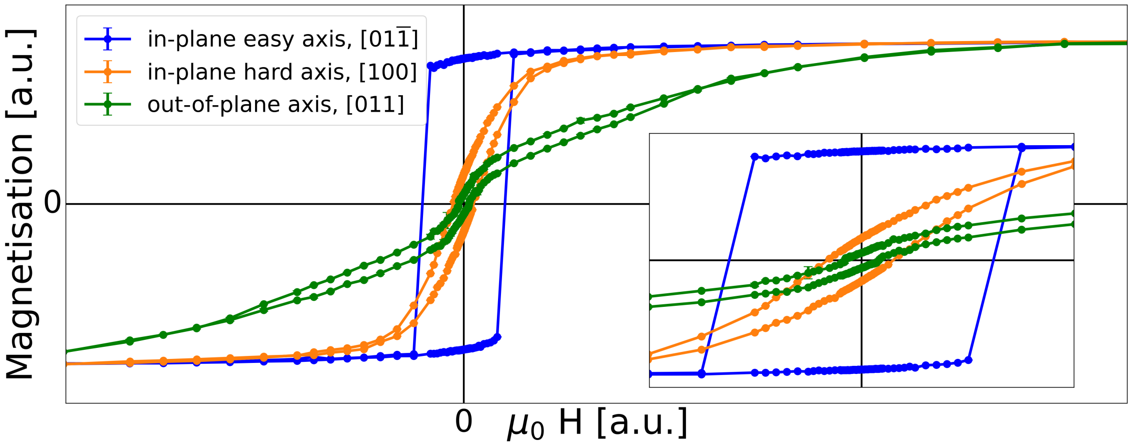

**Figure 2.7:** Magnetisation in thin film sample F2 $Fe_3O_4$/PMN-PT(011) with shape and magnetocrystalline anisotropy. The inset shows a zoom-in on the low field region.

### Magnetoelastic anisotropy and magnetostriction

A piezo or epitaxial strain can also influence the anisotropy, similarly to the already discussed effects on the orbital degeneracy (chapter 2.2.2). The deformation of the unit cell leads to a change in the atomic distances, making certain directions favourable. In fig. 2.6 for instance, the elongation along z-direction would lead to an energy minimum in the xy-plane. The magnetostriction energy, $E_{ms,an}$, for a thin film sample can be calculated by [34],

$$E_{\mathrm{ms,an}} = -\frac{3}{2}\lambda\sigma\sin^2\theta \qquad \text{for isotropic strain} \tag{2.8}$$

$$= -\frac{3}{2}\lambda_x\sigma_x\sin^2\theta\cos^2\phi - \frac{3}{2}\lambda_y\sigma_y\sin^2\theta\sin^2\phi \quad \text{for unisotropic strain,} \tag{2.9}$$

with the saturation magnetostriction constants $\lambda_{x,y}$, and the strain, $\sigma_{x,y}$, along a crystallographic axis; and the angles, $\theta$, between the surface normal, $z$, and the magnetisation, and $\phi$, between the magnetisation and the $x$-direction.

### 2.2.4 Magnetoelectric coupling

All effects discussed so far have been due to interactions between spins on a micro- and macroscopic level without external fields. Now, the effects on the magnetisation of a sample subjected to an electric and magnetic field will be discussed. The free energy (now written as F, to avoid confusion with the electric field) can be expressed as [35, 36],

$$\mathrm{F} = \mathrm{F}_0 + \underbrace{\mathrm{E}(\mathrm{P} - \frac{1}{2}\epsilon_0\chi_e\mathrm{E})}_{\text{electric displacement}} + \underbrace{\mu_0\mathrm{H}(\mathrm{M} - \frac{1}{2}\chi_m\mathrm{H})}_{\text{magnetic induction}} - \underbrace{\alpha\mathrm{EH} - \beta\mathrm{EH}^2 - \gamma\mathrm{E}^2\mathrm{H} - \delta\mathrm{E}^2\mathrm{H}^2 + ...}_{\text{magnetoelectric coupling}} \tag{2.10}$$

The terms of the equation are the field independent free energy, $\mathrm{F}_0$; electric, E, and magnetic, H, fields; polarisation, P, and magnetisation, M; electric permittivity of free space, $\epsilon_0$, and vacuum permeability, $\mu_0$ ; electric, $\chi_e$ and magnetic, $\chi_m$, susceptibility; and magnetoelectric coupling coefficients, $\alpha$, $\beta$, $\gamma$, and $\delta$.

The first two terms describe the direct interaction between the electrical and magnetic field with the associated properties of the sample, electrical displacement and magnetisation. The terms containing both, an electrical and magnetic field dependence govern the cross-coupling between electrical field with magnetisation and magnetic field with polarisation.

The first magnetoelectric coupling term, $\alpha$EH, describes direct magnetoelectric coupling and the fourth, $\delta\mathrm{E}^2\mathrm{H}^2$ strain mediated coupling. The second and third terms are linearly dependent on one and quadratic on the other field and thus far have not been investigated much. The magnetisation originating from the coupling terms can be expressed as the differentiation of the free energy by H as,

$$\mathrm{M}_{\mathrm{ME}} = -\frac{\partial F}{\partial H} = \alpha\mathrm{E} + 2\beta\mathrm{EH} + \gamma\mathrm{E}^2 + 2\delta\mathrm{E}^2\mathrm{H} + ... \tag{2.11}$$

Direct coupling is only possible if the system breaks both time inversion (required by M) and space inversion symmetry (required by P). A possible mechanism to achieve this coupling is the Dzyaloshinskii-Moriya effect. If an antiferromagnetic system is also ferroelectric, the electric dipole can lead to a spin canting, distorting the antiferromagnetic order and giving rise to a magnetic moment. As the interaction is linear in E, the effect can change the sign of the induced magnetisation.

The most common and robust coupling mechanism is strain mediation. The effect is based on an independent electrostriction (or piezoelectricity) and (inverse) magnetostriction. As all effects involve strain, they can arise in two different materials and coupled via an interface, e.g. in a thin film heterostructure. A piezoelectric substrate, such as PMN-PT (see section 2.3.3), experiences a large amount of strain in an electric field. This strain can be transferred onto a magnetic layer on top of the substrate, leading an inverse magnetostriction in the film, which, as discussed above, affects the magnetic anisotropy. Since the energy in strain coupling is quadratic in both electric and magnetic fields, it can not switch the sign of the magnetisation, but the magnetisation can still increase or decrease depending on the sign of the magnetostriction coefficient and strain. In eq. 2.9, the magnetostriction energy density depends on the product $\lambda\sigma$, such that if both terms are of same sign the energy density decreases, leading to favourable alignment along the strain the strain direction and vice versa for different sign. Positive strain is defined as tensile in-plane strain.

## 2.3 Properties of thin films and substrates

### 2.3.1 SrCoO$_{3-\delta}$

The magnetism in SrCoO$_{3-\delta}$ (SCO) is quite complex, with the oxygen deficiency having a strong influence on the interplay between ferromagnetic and anti-ferromagnetic order.

SrCoO$_3$ is a ferromagnetic metal with bulk Curie temperature of at least 305 K [37, 38] and saturation magnetisation of 2.5$\mu_B$/Co [37]. Based on charge neutrality, the Co valency in SrCoO$_3$ is 4+, with 5 electrons in the 3$d$ shell.

Generally, Co$^{4+}$, could be in three different spin states in an octahedral environment: the low spin state (LS), with 3 up and 2 down spins in the $t_{2g}$ orbitals (S=$\frac{1}{2}$), the intermediate spin state (IS), with 3 up and 1 down spins in the $t_{2g}$ orbitals and 1 up spin in the $e_g$ orbitals (S=$\frac{3}{2}$), and the high spin state (HS), with 3 up spins in the $t_{2g}$ and 2 up spins in the $e_g$ orbitals (S=$\frac{5}{2}$). In SrCoO$_3$ (P-SCO), the Co-$3d - e_g$ orbitals hybridize with the oxygen 2$p$ orbitals, leading to a negative charge transfer stabilizing the IS state [39] (fig. 2.8). Every oxygen atom contributes $\frac{1}{6}$ of an electron-hole pair for each Co ion, resulting in an effective $d^6$-HS state for the Co ion with an antiferromagnetic hole, leading to the $d^5$-IS state. The hole has a mixed character of both $e_g$ orbitals. Since oxygen hybridizes with both neighbouring Co ions, the Co $e_g$ electron arrange parallel with each other (similarly to the double exchange mechanism) giving rise to the ferromagnetism.

When SrCoO$_3$ experiences strain, particularly compressive strain, is tends to form oxygen vacancies [11], which reduces the number of holes. The exchange between two Co$^{4+}$ ions via an oxygen atom without a hole follows the antferrimagnetic superexchange. This means that the ferromagnetism is drastically reduced, even for strain values of 1% [40].

If there are enough vacancies, i.e. $\delta$ close to 0.5, the ferromagnetism vanishes. At the same time, the oxygen vacancies order and alternating layers of octahedra and tetrahedra characteristic for the brownmillerite structure form. The resulting

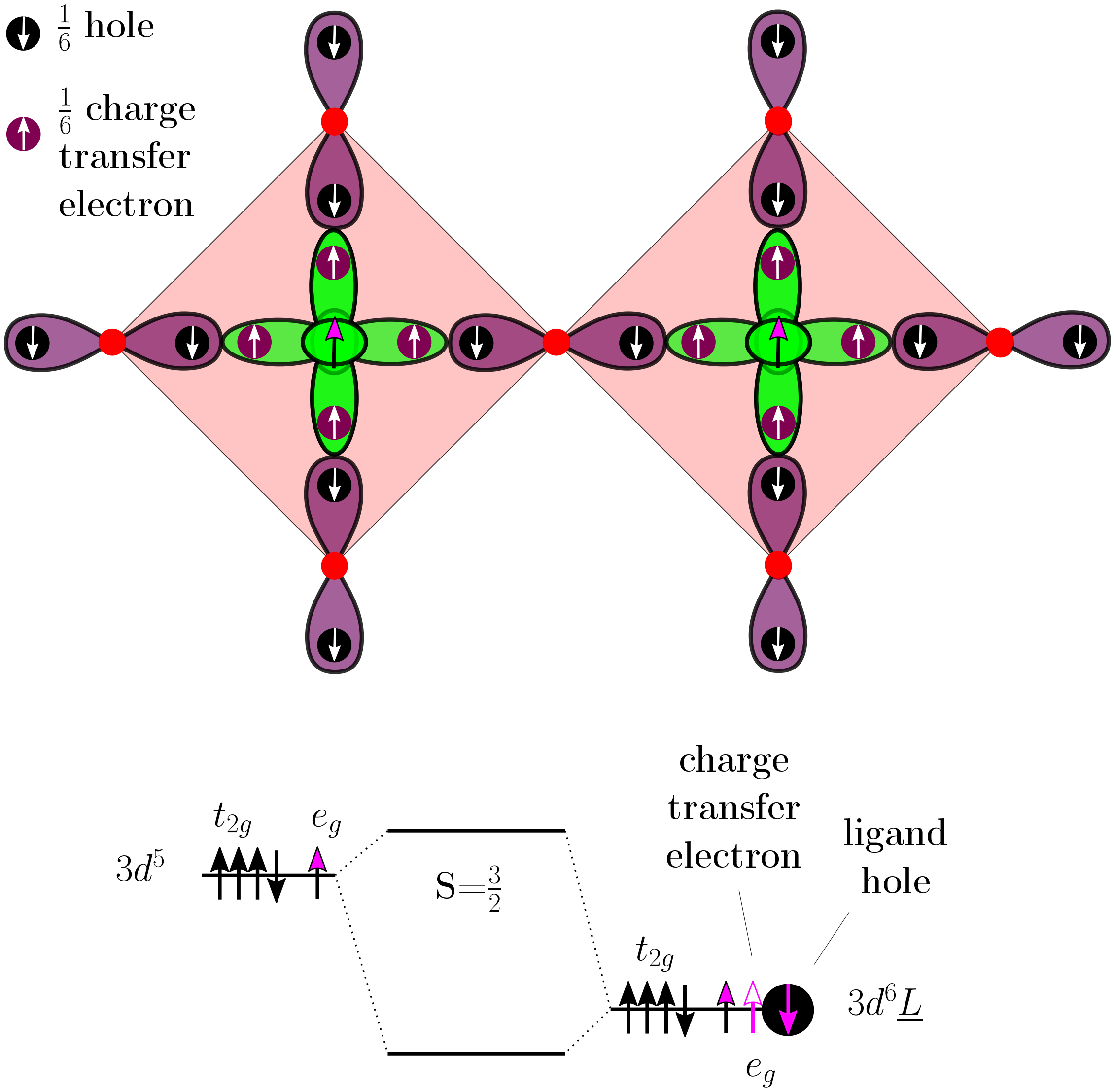

**Figure 2.8:** Schematic of the charge transfer from the hybridization of the Co $3d - e_g$ orbitals (green) with the oxygen $2p$ orbitals (purple) viewed along one of the octahedral axes on the **top**. The two oxygen atoms in out-of-plane direction are not shown. Each oxygen atom contributes $\frac{1}{6}$ electron to the central Co ion, resulting in an electron-hole-pair. The $t_{2g}$ electrons are not shown, as they don't contribute to the $\sigma$-bond. On the **bottom** the resulting $\sigma$-bonding ligand group orbital resulting from the intermediate spin state of the Co-ion after hybridization is sketched.

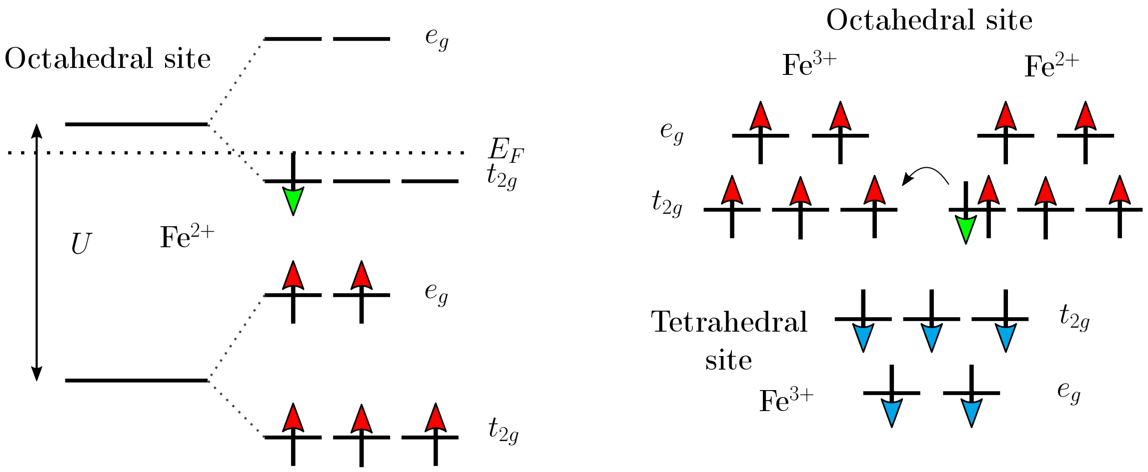

**Figure 2.9:** Spin structure of the 3d orbital of $Fe^{2+}$ (**left**). The conduction electron (green) is aligned opposite to the others, giving rise to a spin polarised current. The octahedral and tetrahedal sublattices align antiparallel to form the ferrimagnetic structure of $Fe_3O_4$ (**right**).

magnetism for $SrCoO_{2.5}$ (BM-SCO), is a G-type antiferromagntic structure with a Néel temperature of 570 K [41]. The 6 electrons of the $Co^{3+}$ ions are in the high spin state, with 3 up and 1 down spin in the $t_{2g}$ orbitals and 2 up spins in the $e_g$ orbitals (S=2). Nearest neighbour Co ions are aligned antiparallel, due to superexchange.

Since the perovskite and brownmillerite structure are chemically only different in the oxygen content and the oxygen mobility is high, they can be topotactically transformed into each other, e.g. via annealing [42].

### 2.3.2 $Fe_3O_4$

As discussed before, Magnetite ($Fe_3O_4$) grows in the inverse spinel structure. The iron atoms occupying tetrahedral sites are of valency $Fe^{3+}$ ($d^5$), whereas the octahedral sites are equally occupied by $Fe^{3+}$ and $Fe^{2+}$ ($d^6$) ions ($Fe^{3+}_{tet}(Fe^{2+}Fe^{3+})_{oct}O_4$).

Within the octahedral site, the $Fe^{3+}$ and $Fe^{2+}$ spins are arranged ferromagnetically due to a double exchange interaction. Similarly, the $Fe^{3+}$ spins of the tetrahedral sites are coupled ferromagnetically. The two sublattices are anti-parallel with each other, forming a ferrimagnetic structure. Thus, the $Fe^{3+}$ moments cancel out and the total magnetic moment of $Fe_3O_4$ arises from the ferromagnetic alignent of the $Fe^{2+}$ ions, which leads to a magnetisation of close to $4\,\mu_B/f.u.$ and a Curie temperature of 858 K.

The electric conduction is carrier based via hopping of the additional electron on $Fe^{2+}$ onto $Fe^{3+}$. Because of the Hubbard band splitting, the degeneracy of the 3d level is lifted. The Fermi level is in the minority-spin $t_{2g}$ level which leads to a half-metallic character and a strong spin polarisation (fig. 2.9).

At $T_V = 120\,K$, $Fe_3O_4$ undergoes a first-order Verwey transition, which causes a large increase in resistivity and a decrease in magnetisation [8, 12]. It is commonly assumed that above $T_V$ the valency of the octahedral Fe ions is randomly distributed and below the transition a long range order of $Fe^{2+}$ and $Fe^{3+}$ ions is established. This explains the drastic reduction in conductivity below this disorder-order transition: Above $T_V$, the conduction electron can move freely, whereas below $T_V$ it is localised on $Fe^{2+}$.

It should be noted that there is some evidence to suggest that this classic Verwey model may not be entirely accurate and that there is in fact no charge ordering on the octahedral site [43]. However, as this is not subject of this thesis, we still assume the Verwey model.

### 2.3.3 Relaxor ferroelectrics

Relaxor ferroelectrics are one of the most often used materials for strain application by voltage [44]. For classical ferroelectrics like $PbTiO_3$, a cubic, and therefore non-polar, lattice exists at high temperatures while at lower temperatures it undergoes a second order phase transition to tetragonal. Since the tetragonal phase is not centrosymmetric, a polarization by displacement of the central atom may appear, along a [100] axis.

In contrast, relaxor ferroelectrics like $Pb(Mg_{1/3}Nb_{2/3})O_3$ (PMN), maintain an overall close-to-cubic symmetry, but below a critical ("Burns") temperature, $T_B$ [45], polar nanoregions (PR) form. The dipolar moments within one PR are parallel and aligned at random along one of the possible polarisation directions [46]. The nanoregions form because of disorder in the occupation of the $B$ site by atoms of different size and valency (e.g. $Mg^{2+}$ and $Nb^{5+}$). Normally, the energy would be minimized by establishing a compositional order, but the diffusion constant in PMN is too low, such that it always exists in a disordered state. There is not yet a clear understanding if the PR form in the whole sample with domain walls separating them (model 1), or in small domains within a cubic matrix (model 2) [46]. Both theories explain the absence of a second order phase transition, either by the presence of local random fields (model 1), or by a local variation of the Curie temperature due to fluctuations in the composition that smears out the phase transition (model 2).

#### $[Pb(Mg_{1/3}Nb_{2/3})O_3]_{1-x}$–$[PbTiO_3]_x$ (PMN-PT)

$[Pb(Mg_{1/3}Nb_{2/3})O_3]_{1-x}$–$[PbTiO_3]_x$ (PMN-PT) is a solid solution of $PbTiO_3$ and $Pb(Mg_{1/3}Nb_{2/3})O_3$. The polarization direction is in the $\langle 111 \rangle$ directions (fig. 2.10). By using different crystal cuts to achieve different surface orientations of PMN-PT, different strain states can be achieved. Fig. 2.11 shows a sketch of the polarization and strain for the application of an out-of-plane electric field (dependent on the cut orientation of the crystal) of up to 4 kV/cm [47].

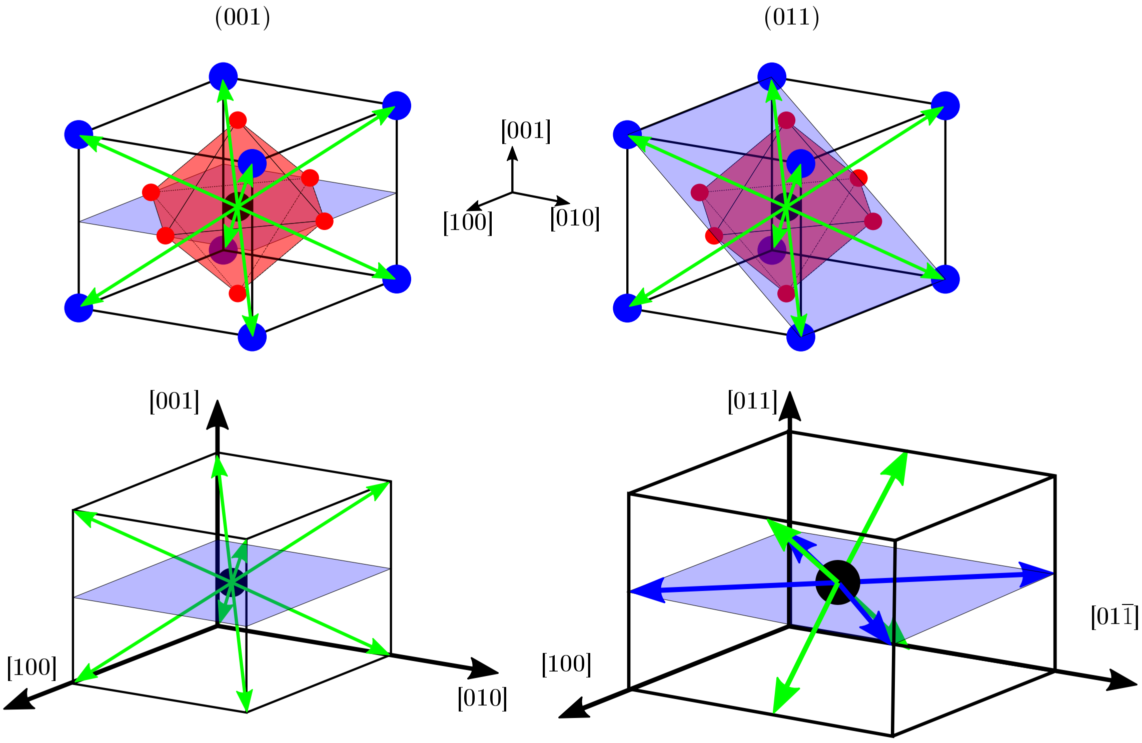

**Figure 2.10:** Structure and polarization directions (green arrow) for PMN-PT (**top**). The blue plane indicates the cut directions used in this thesis [001] and [011]. On the **bottom**, the resulting possible in-plane (blue arrows) and out-of-plane (green arrows) polarization directions are shown.

For a (001) cut, i.e. [001] direction out-of-plane, both in-plane directions, [100] and [010], are equivalent. As the polarisation is along the $\langle 111 \rangle$ directions, all polarisation axes have an equivalent in-plane and out-of-plane projection (fig. 2.10 left), leading to vanishing strain without applied electric field (fig. 2.11 b). Upon the application of voltage, the crystal experiences tensile (positive) strain as the polarisation vectors with an out-of-plane component anti-parallel to the field try to align with the field. As the electric field reaches the coercive field, the polarisation vectors switch to align with the field, which releases the tensile strain and creates a compressive (negative) strain that increases with increasing field. When the electric field is reduced, the strain relaxes. The switching process is often called a butterfly like strain loop (fig. 2.11 b).

For a (011) cut, the two in-plane directions, [100] and [01$\bar{1}$], are crystallographically distinct and therefore show drastically different behaviour in electric field. Two distinct polarisation orientations are present, 4 directions with in-plane component along [100] and out-of-plane component (green arrows in fig. 2.10 bottom right) and 4 directions with an in-plane component in both [100] and [01$\bar{1}$] (blue arrows in fig. 2.10 bottom right). As half of the polarisation directions don't have a component along [01$\bar{1}$], there is a remanent compressive strain present even without an applied electric field (fig. 2.11c,d (1)). When an electric field is applied, the behaviour along [100] is similar as for the (001) cut and resembles a butterfly shape (fig. 2.11 b). In [01$\bar{1}$] direction however, a large strain jump towards the tensile regime occurs at the coercive field ($\mathrm{E}_c \sim 1.5\,\mathrm{kV/cm}$) (fig. 2.11c,d (3)), caused by the switching of polarisation vectors with an out-of-plane component oppisite to the electric field into the (011) plane. These polarisation vectors previously had no component along $[01\bar{1}]$ and with the reorientation now contribute a large tensile strain. Once the field is increased slightly however, the strain jumps back, as the in-plane polarisation vectors realign with the field and lose their $[01\bar{1}]$ component (fig. 2.11c,d (4)).

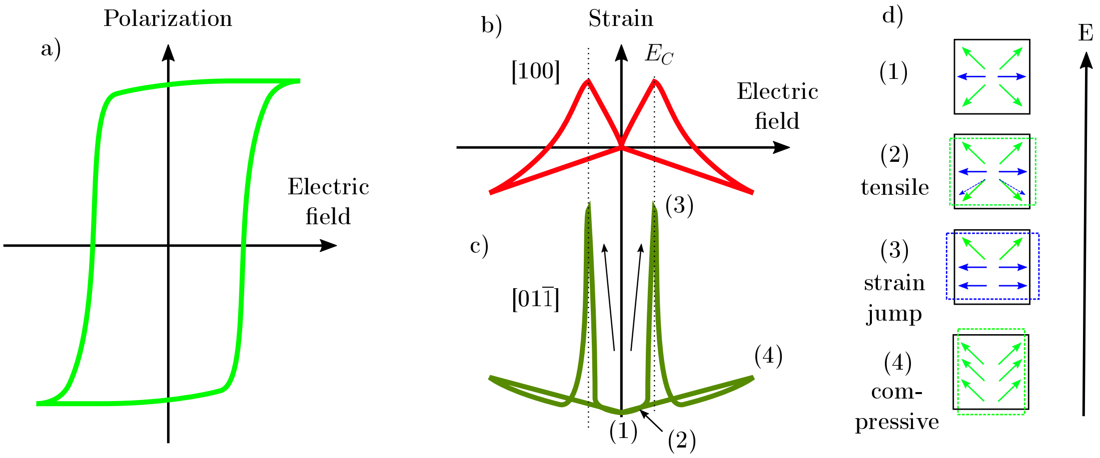

**Figure 2.11:** Schematic of polarization (a) and strain (b,c) for a PMN-PT(011) substrate poled in the [011] direction. Curve b) shows the strain in [100] direction, while curve c) shows strain in $[01\bar{1}]$ direction. The dashed line indicates the coercive field, $E_C$, at about $1.5\,\mathrm{kV/cm}$. Polarisation and strain sketches are adapted from [47]. Images d)(1)-(4) depict the evolution of polarisation vectors along $[01\bar{1}]$ with applied field. The bi-axial in-plane strain in PMN-PT(001) is similar to b).

### 2.3.4 Crystal growth modes

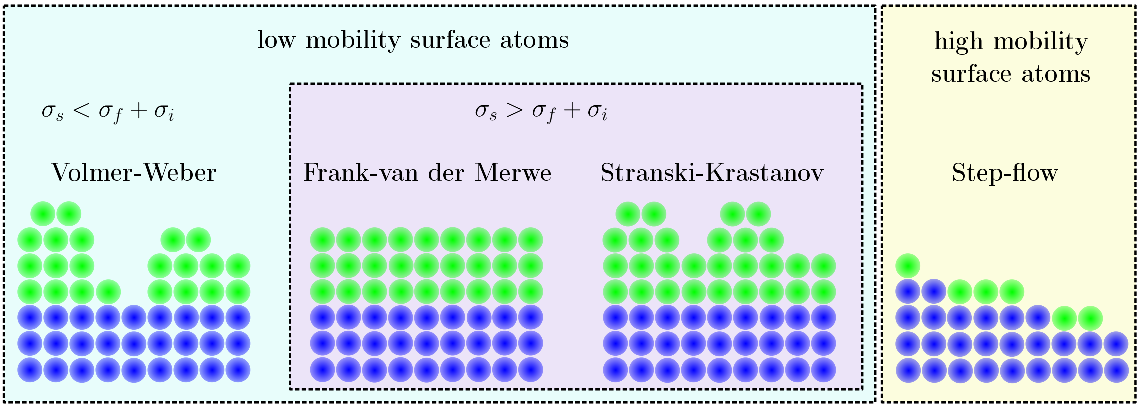

**Figure 2.12:** Possible growth modes during deposition. For low surface mobility and low interfacial energy, the film will grow in islands (Volmer-Weber). For a high interfacial energy, layer-by-layer (Frank-van der Merwe) or layer-plus-island (Stranski-Karastanov) modes are possible. For a high surface mobility, a step-flow growth can take place.

The successful growth of thin films by molecular beam epitaxy (MBE) (see chapter

3.1.1) is dependent on a large parameter space of thermodynamic and material properties, such as temperature, lattice mismatch of the materials, sticking coefficient, surface energies of the adsorbed atoms and of the substrate.

Generally, four growth modes are distinguished (fig. 2.12) [48]. The first three modes consider low mobility of the adsorbed atoms, because of low growth temperature or high atomic flux. In this case, growth is governed by the surface energies of the substrate $\sigma_s$, and film $\sigma_f$.

The Dupré equation can then be used to calculate the interfacial energy, $\sigma_i$,

$$\sigma_i = \sigma_s + \sigma_f - \beta, \tag{2.12}$$

with the specific adhesion energy $\beta$.

Using it, one can calculate the height-to-length relation of a crystal growing on a foreign substrate,

$$\frac{h}{l} = \frac{\sigma_f + \sigma_i - \sigma_s}{2\sigma_f}. \tag{2.13}$$

Following from this equation, one can separate two cases: For $\sigma_s < \sigma_f + \sigma_i$, it is not energetically favourable for the deposited material to wet the whole substrate evenly, but rather to form clusters to minimize the surface energy, resulting in island growth (Volmer-Weber). For $\sigma_s > \sigma_f + \sigma_i$, the film covers the complete substrate evenly, indicating either a layer-by-layer (Frank-van der Merwe) or layer-plus-island (Stranski-Krastanov) growth. For low lattice misfit, a layer-by-layer growth is energetically favourable. If the mismatch is too high, the upper layers, not benefiting from the reduced surface energy at the interface, begin to form islands.

For a high mobility of atoms on the surface, step-flow growth can occur. The miscut of the substrate leads to a step-like terrace structure of the surface. Adatoms nucleate at the step edge and from there additional incorporated atoms grow this step further, leading to continuation of the terrace structure.

## 2.4 Scattering

### 2.4.1 General scattering theory

To investigate the physical properties of samples, scattering of different probes from the sample can be a very useful tool. In the following, the basics of scattering theory will be explained, based on [18,49,50], though not fully derived. For a full derivation, the reader is referred to the references.

To discuss scattering, first the particle-wave duality has to be sketched. According to the de-Broglie relation, a particle beam can be described by wave properties. The wavelength, $\lambda$, of the particle-wave is inversely proportional to the momentum, $p$,

$$\lambda = \frac{h}{p}, \tag{2.14}$$

with Planck's constant, $h$. The wave vector, $\vec{k}$, is then

$$\vec{k} = \frac{\vec{p}}{\hbar} = 2\pi\frac{\vec{p}}{h}. \tag{2.15}$$

In the following the wavelength of the particles will be assumed to be constant, so the incident beam is monochromatic and there is no energy change during scattering, i.e. only elastic scattering. Further, the distances between the sample and both the source and detector is assumed to be much larger than the size of the sample (Fraunhofer approximation, see fig. 2.13).

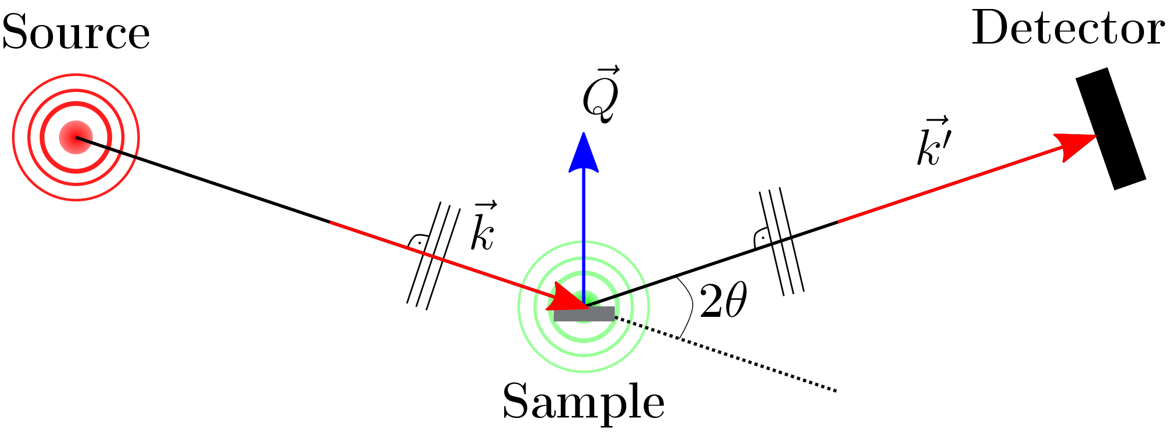

**Figure 2.13:** Fraunhofer approximation for scattering. A point source emits a wave, which appears as a plane wave front due to the large distance to the sample. The wave front interacts with the sample and is scattered under an angle of $2\theta$ relative to the initial wave vector. The emitted wave at the detector position can again be considered a plane wave. Image adapted from [49].

As such, any isotropic wave front emitted from the source will be a plain wave at the sample and equivalently, the scattered wave from the sample will be plain at the detector. The waves can be described by their wave vectors, $\vec{k}$ for the incident wave and $\vec{k'}$ for the scattered wave. The magnitude of the wave vectors is then

$$|\vec{k}| = |\vec{k'}| = \frac{2\pi}{\lambda}. \tag{2.16}$$

The difference in outgoing and incoming wave is described by the scattering vector,

$$\vec{Q} = \vec{k'} - \vec{k} \tag{2.17}$$

Following eq. 2.14, the momentum transfer, $\hbar\vec{Q}$, is then,

$$\hbar\vec{Q} = \hbar(\vec{k'} - \vec{k}) = \vec{p'} - \vec{p}, \tag{2.18}$$

with the momentum of the incidence wave, $\vec{p}$, and scattered wave $\vec{p'}$. The magnitude of the scattering vector is then dependent on the wavelength and the scattering angle with

$$Q = |\vec{Q}| \; = \frac{4\pi}{\lambda}\sin\theta. \tag{2.19}$$

When we consider scattering of the wave from all points in a sample volume, $\mathrm{V_S}$, the amplitude of the scattered wave is a superposition of the individually scattered waves,

$$A(\vec{Q}) = \frac{m}{2\pi\hbar^2}\cdot\int\limits_{\mathrm{V_S}} V(\vec{r})\,\mathrm{e}^{\mathrm{i}\vec{Q}\cdot\vec{r}}\,\mathrm{d}^3r = \int\limits_{\mathrm{V_S}} \rho_\mathrm{s}(r)\,\mathrm{e}^{\mathrm{i}\vec{Q}\cdot\vec{r}}\,\mathrm{d}^3r, \tag{2.20}$$

with the amplitude of the initial wave, $A_0$, and the interaction potential, $V(\vec{r})$, at the position $\vec{r}$. The interaction potential and the pre-factor can be written as the scattering density $\rho_\mathrm{s}(r) = \frac{m}{2\pi\hbar^2}V(\vec{r})$. The interaction potential is hereby very different for different types of scattering probes, e.g. X-rays or neutrons. The term $\vec{Q}\cdot\vec{r}$ in the exponential function is the phase difference between waves scattered at two different positions in the sample. The amplitude is thus a Fourier transformation of the scattering density. The amplitude of the scattered wave, however, is not a measurable property in most cases. Rather, the intensity distribution,

$$I(\vec{Q}) \sim |A(\vec{Q})|^2 \tag{2.21}$$

is measured. In the general case, the detector doesn't measure the whole intensity distribution, but rather the cross section visible to the detector. The number of particles, $n'$, scattered from the sample from an incident beam with the flux $j$, into the detector solid angle $\mathrm{d}\Omega$ in the energy range $\mathrm{d}E'$ is called the double differential scattering cross section

$$\frac{\mathrm{d}^2\sigma}{\mathrm{d}\Omega\mathrm{d}E'} = \frac{n}{j\mathrm{d}\Omega\mathrm{d}E'}. \tag{2.22}$$

If the detector is not energy sensitive, it effectively integrates over the whole energy range resulting in the differential cross section,

$$\frac{\mathrm{d}\sigma}{\mathrm{d}\Omega}(\theta) = \int\limits_0^\infty \frac{\mathrm{d}^2\sigma}{\mathrm{d}\Omega\mathrm{d}E'}\bigg|_\theta \mathrm{d}E' \sim |A(\vec{Q})|^2 = \left(\frac{m}{2\pi\hbar^2}\right)^2 \left|\langle\vec{k'}|V|\vec{k}\rangle\right|^2. \tag{2.23}$$

By integrating over all angles, the total scattering cross section can be determined

$$\sigma = \int\limits_0^{4\pi} \frac{\mathrm{d}\sigma}{\mathrm{d}\Omega}\mathrm{d}\Omega. \tag{2.24}$$

Using equation 2.20 and 2.21, we can rewrite the intensity as [49]

$$I(\vec{Q}) \sim \int \mathrm{d}^3R\, P(\vec{R})\, \mathrm{e}^{\mathrm{i}\vec{Q}\vec{R}}, \tag{2.25}$$

with the substitution $\vec{R} = \vec{r'} - \vec{r}$ and the static pair correlation function,

$$P(\vec{R}) = \int \mathrm{d}^3r\, \rho_{\mathrm{s}}^*(\vec{r})\rho_{\mathrm{s}}(\vec{r} + \vec{R}). \tag{2.26}$$

Depending on the experiment and probe, $P(\vec{R})$ describes a number of different correlations in the sample, such as the spatially periodic arrangement of atoms for diffraction (Patterson function) or spins for polarised neutron scattering.

### 2.4.2 Scattering with different probes

As explained in eq. 2.20, the scattering amplitude varies with the interaction between scattering probe and sample. A short overview of scattering with all probes used in this thesis will be given in this section. In general, the wavelength of the probe has to be similar to the length scale that is to be investigated. Since the de-Broglie wavelength is dependent on the mass of the probe, the energy varies strongly for a wavelength in the Å range, as shown in fig. 2.14.

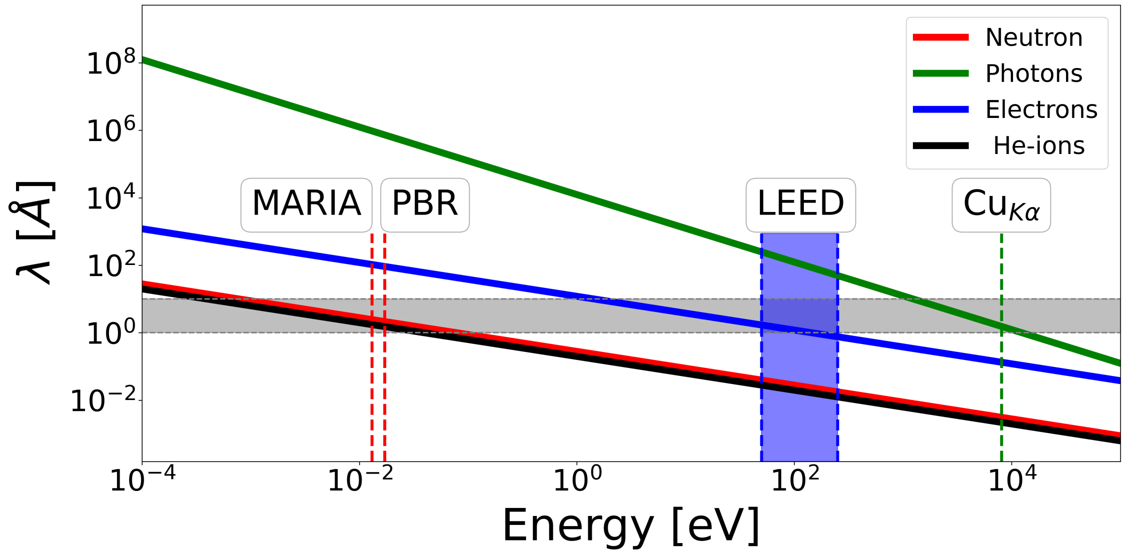

**Figure 2.14:** Wavelength-energy diagram for the probes used in this thesis. The gray shaded area indicates the typical length scale for diffraction and reflectometry between 1 and 10 Å. Energies for neutrons at the reflectometers MARIA and PBR (chapter 3.4), electrons in LEED (chapter 3.2.2), and X-rays from a $Cu_{K\alpha}$ source used for reflectometry and diffraction (chapter 3.3.2) are indicated.

### Neutron scattering

According to equation 2.20, the amplitude of the scattered wave is dependent on the interaction potential for the respective probe. In case of neutrons scattering from nuclei by the strong interaction, the Fermi-pseudo-potential can be used

$$V_{\mathrm{nuclear}}(\vec{r}) = \frac{2\pi\hbar^2}{m_n} b\,\delta(\vec{r} - \vec{R}), \tag{2.27}$$

which describes the nuclei as point like, with a corresponding scattering length, $b$, essentially half of the "radius" of the nuclear cross section $\sigma = 4\pi\,|b|^2$, with the neutron mass, $m_n$. The scattering length is dependent on the nuclear structure and varies significantly between isotopes.

For scattering from a number of atoms, $N$, that are arranged at the positions $\vec{a}$, the potential can be summed up to

$$V_n(\vec{r}) = \frac{2\pi\hbar^2}{m_n} \sum_i^N b_i\,\delta(\vec{r} - \vec{a}), \tag{2.28}$$

with the scattering amplitude

$$A_n(\vec{Q}) = \sum_i^N b_i\,\mathrm{e}^{\mathrm{i}\vec{Q}\vec{a}}. \tag{2.29}$$

The differential scattering cross section can then be calculated as

$$\frac{\mathrm{d}\sigma}{\mathrm{d}\Omega}(\vec{Q}) = \langle b\rangle^2 \left|\sum_i \mathrm{e}^{\mathrm{i}\vec{Q}\vec{a}}\right|^2 + N\left\langle (b - \langle b\rangle)^2\right\rangle, \tag{2.30}$$

which contains contributions from the coherent scattering ($\langle b\rangle^2 \left|\sum_i \mathrm{e}^{\mathrm{i}\vec{Q}\vec{a}}\right|^2$) and incoherent scattering ($N\left\langle (b - \langle b\rangle)^2\right\rangle$).

Since neutrons have a spin, they are also sensitive to the magnetic dipole moment of unpaired electrons, described by the potential

$$V_{\mathrm{magnetic}} = -\gamma_n \mu_N \hat{\vec{\sigma}} \cdot \vec{B} \tag{2.31}$$

with the gyromagnetic factor of the neutron, $\gamma_n = -1.913$, and the nuclear magneton $\mu_N = \frac{e\hbar}{2m_p}$. The spin operator, $\hat{\sigma}$, is defined by the Pauli matrices defined by

$$\hat{\vec{\sigma}}_x = \begin{pmatrix} 0 & 1 \\ 1 & 0 \end{pmatrix} \quad \hat{\vec{\sigma}}_y = \begin{pmatrix} 1 & 0 \\ 0 & -1 \end{pmatrix} \quad \hat{\vec{\sigma}}_z = \begin{pmatrix} 0 & -\mathrm{i} \\ \mathrm{i} & 0 \end{pmatrix}. \tag{2.32}$$

This leads to the differential cross section for magnetic scattering [51]

$$\frac{\mathrm{d}\sigma}{\mathrm{d}\Omega}_{\text{magnetic}} = (\gamma_n r_e)^2 \left| \frac{1}{2\mu_B} \langle \sigma'_y | \hat{\vec{\sigma}} \cdot \vec{M}_\perp(\vec{Q}) | \sigma_y \rangle \right|^2 , \tag{2.33}$$

with the electron radius, $r_e = \frac{e^2}{4\pi\epsilon_0 m_e c^2} = 2.82\,\text{fm}$, the spin of the neutron before, $\sigma_y$, and after scattering, $\sigma'_y$, and, $\vec{M}_\perp$, the magnetization perpendicular to $\vec{Q}$ (see fig. 2.15). The magnetization parallel to $\vec{Q}$ does not contribute, because its contribution averages to 0. In the following, the spin direction of the neutron will be defined parallel the y-direction, parallel to the magnetic field, as

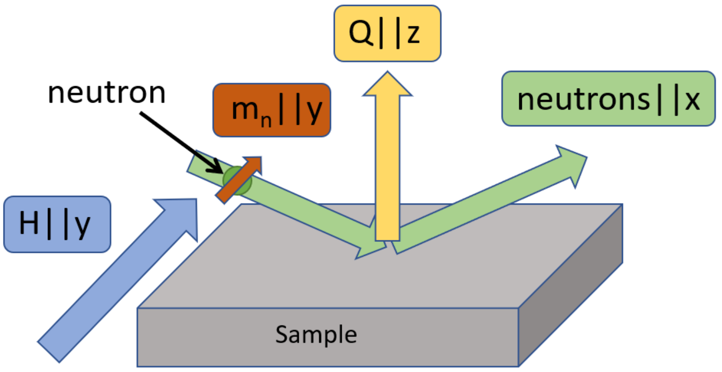

**Figure 2.15:** Definition of direction in scattering experiments.

$$\text{up} = |+\rangle = \begin{pmatrix} 1 \\ 0 \end{pmatrix}, \quad \text{down} = |-\rangle = \begin{pmatrix} 0 \\ 1 \end{pmatrix}. \tag{2.34}$$

The amplitude of the magnetic scattering is then

$$A(\vec{Q})_{\text{magnetic}} = \langle \sigma'_y | -\frac{\gamma_n r_e}{2\mu_B} \hat{\vec{\sigma}} \cdot \vec{M}_\perp(\vec{Q}) | \sigma_y \rangle = -\frac{\gamma_n r_e}{2\mu_B} \sum_{i=x,y,z} \langle \sigma'_y | \hat{\vec{\sigma}}_i | \sigma_y \rangle \, \vec{M}_\perp(\vec{Q}). \tag{2.35}$$

considering the cases for all spin states,

$$A(\vec{Q})_{\text{magnetic}} = -\frac{\gamma_n r_e}{2\mu_B} \cdot \begin{cases} \vec{M}_{\perp\vec{Q}\|y} & \\ -\vec{M}_{\perp\vec{Q}\|y} & \\ \vec{M}_{\perp\vec{Q}\|x} - i\vec{M}_{\perp\vec{Q}\|z} & \\ \vec{M}_{\perp\vec{Q}\|x} + i\vec{M}_{\perp\vec{Q}\|z} & \end{cases} \text{for the spin states} \begin{matrix} \langle +|+\rangle \\ \langle -|-\rangle \\ \langle +|-\rangle \\ \langle -|+\rangle \end{matrix} \tag{2.36}$$

the spin remains in the same direction for $\vec{M} \parallel y$ and flips for $\vec{M} \perp y$. Hence, measurements with $\vec{M} \parallel y$ are called non spin-flip scattering and measurements with $\vec{M} \perp y$ spin-flip scattering.

### X-ray scattering

X-rays (and electromagnetic radiation in general) can be scattered by the electrons in an atom by the interaction of the electric field component of the X-rays, $E\left(\frac{1}{\lambda}\right)$, with the polarizability of the atom, $\chi\left(\frac{1}{\lambda}\right)$, which are both inversely dependent on the wavelength. The incident beam polarizes the atom according to

$$P\left(\frac{1}{\lambda}\right) = \chi\left(\frac{1}{\lambda}\right) E\left(\frac{1}{\lambda}\right), \tag{2.37}$$

which subsequently re-emits the outgoing beam [52]. For small wavelengths, this can be described by the differential Thomson cross section

$$\frac{\mathrm{d}\sigma}{\mathrm{d}\Omega}_{\text{Thomson}} = \left|f_x(\vec{Q})\right|^2 \frac{r_e^2}{2}(1 - \cos^2(\theta)). \tag{2.38}$$

Here $f_x(\vec{Q})$ is the atomic form factor for X-rays, the Fourier transformation of the electron density, $\rho_e$,

$$f_x(\vec{Q}) = \int \rho_e(\vec{R})\mathrm{e}^{\mathrm{i}\vec{Q}\vec{R}_i}\mathrm{d}\vec{R}. \tag{2.39}$$

The form factor for x-rays can be compared to the magnetic form factor for neutrons, as both decay for higher Q, though the X-ray form factor drops off less quickly.

### Electron and ion scattering

Scattering of a charged particle from another by the Coulomb interaction can be described with the potential [53]

$$V_{\text{Coulomb}} = \frac{1}{4\pi\epsilon_0}\frac{C_1C_2}{r}, \tag{2.40}$$

with the permittivity of free space, $\epsilon_0$, the charge of the scattering particle, $C_1$, the charge of the particle generating the potential, $C_2$, and the distance between them, $r$.

The resulting scattering cross section, called Rutherford cross section, is given by,

$$\frac{\mathrm{d}\sigma}{\mathrm{d}\Omega}_{\text{Rutherford}} = \left(\frac{C_1C_2e^2}{16\pi\epsilon_0E_0}\right)^2 \frac{1}{\sin^4(\theta/2)}. \tag{2.41}$$

For free electrons scattering from the electrons of an atom with the nuclear charge, $Z$, this can be written as [54]

$$\frac{\mathrm{d}\sigma}{\mathrm{d}\Omega}_{\text{R,e}^-} = \left(\frac{Ze^4}{16\pi\epsilon_0E_0}\right)^2 \frac{1}{\sin^4(\theta/2)}. \tag{2.42}$$

Since the interaction potential for charged particles is much stronger compared to that for neutral ones, the cross section is much larger compared to the neutron or

X-ray cross section. For electrons, the penetration depth (inelastic mean free path), $d_{e^-}$, in nm can be estimated based on the empirical formula [55]

$$d_{e^-} = \frac{538}{E_{e^-}^2} + 0.41\sqrt{(cE_{e^-})}, \tag{2.43}$$

with the electron energy, $E_{e^-}$, in eV and the thin film thickness, $c$, in nm. For low energy electrons in the 100 eV range, this means the penetration depth is in the order of only a few monolayers.

For scattering of He-ions, the cross section can be written in the laboratory reference system to be

$$\frac{d\sigma}{d\Omega}_{\mathrm{R,He}} = \left(\frac{Z_{\mathrm{He}}Z_{\mathrm{t}}e^2}{16\pi\epsilon_0 E_0}\right)^2 \frac{1}{\sin^4(\theta/2)} \frac{\left(\sqrt{1-(m_{\mathrm{He}}/m_{\mathrm{t}})^2\sin^2\theta}+\cos\theta\right)^2}{\sqrt{1-(m_{\mathrm{He}}/m_{\mathrm{t}})^2\sin^2\theta}}, \tag{2.44}$$

with the He-ion mass and charge, $m_{\mathrm{He}}$ and $Z_{\mathrm{He}}$, and the mass and charge of the target atom, $m_{\mathrm{t}}$ and $Z_{\mathrm{t}}$ [56].

### 2.4.3 Scattering from thin films

In the following, the principle behind two different scattering regimes used in this thesis, reflectometry and diffraction, will be explained. Since all investigated samples are thin films, scattering can be divided based on the angle of incidence relative to the sample plane, as shown in fig. 2.16. In general, the sample is oriented in the $xy$ plane, with the surface normal in the $\vec{z}$ direction. For low angles, reflectometry gives insight into sample properties such as thickness, roughness of interfaces and the magnetic depth profile. For higher angles of incidence, diffraction can be used to study the crystalline structure. The crossover between the two scattering regimes is not sharp and depends on the specific sample.

#### Reflectometry

For thin film samples, reflectometry is one of the most important tools to determine the sample properties. Reflectometry is scattering under grazing incidence, due to which the atomic structure is not resolved and the film appears as a homogeneous medium. This is similar to the treatment of light scattering in classical optics and the same geometric considerations apply (fig. 2.17). A beam incident at an interface under a certain angle $\theta$ is partially reflected at the same angle and partially transmitted, under a different angle, depending on the indices of refraction. This process is repeated for all interfaces the beam encounters. The various reflected beam superimpose, creating an interference pattern. Here, reflectometry for neutrons will be explained based on [57, 58], but the results are similar for X-ray reflectometry.

Since the film is treated as a homogeneous medium, we can re-write the scattering

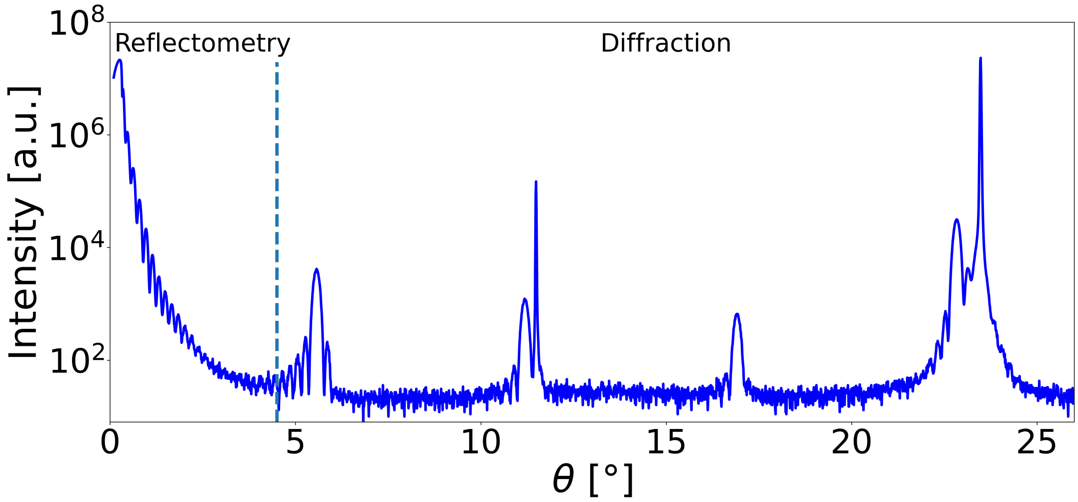

**Figure 2.16:** Scattering from thin films for small angles (reflectometry) and large angles (diffraction). The example shown here is X-ray scattering from sample L1 $SrCoO_{2.5}$/LSAT(001).

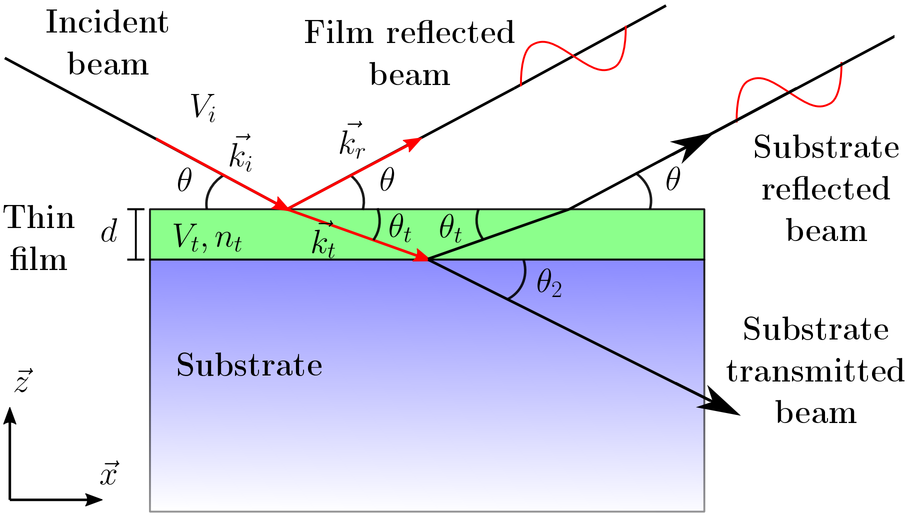

**Figure 2.17:** Scattering from a thin film sample for reflection condition. The beam reflected from the film and substrate acquire a phase difference, which results in Kiessig fringes due to constructive and destructive interference for varying incidence angle. Image adapted from [58].

potential in eq. 2.27 for the scattering potential in the medium, $V_t$ as

$$V_t = \tfrac{2\pi\hbar^2}{m_n}\rho_{SL,n} \quad \text{with} \quad \rho_{SL,n} = \tfrac{1}{volume}\sum_i b_i, \tag{2.45}$$

with the nuclear scattering length density $\rho_{SL,n}$, as the sum of the individual scattering lengths, $b_i$ times the number of atoms per unit volume.

The Schrödinger equation of neutrons in a potential $V$, is given by

$$H\Psi = \left(-\frac{\hbar^2}{2m_n}\Delta + V\right)\Psi = \mathrm{i}\hbar\frac{\partial}{\partial t}\Psi, \tag{2.46}$$

and we define the wave functions of the incidence ($i$), reflected ($r$), and transmitted ($t$) beams as

$$\Psi_x = a_x \mathrm{e}^{\mathrm{i}\vec{k_x}\vec{r}}, \text{ with } x = i, r, t \tag{2.47}$$

then the following equations must hold for the continuity of $\Psi$ and $\frac{\partial\Psi}{\partial t}$ at the interface and $a_i = 1$:

$$\begin{array}{ll c} (1) & & 1 + a_r = a_t \\ (2) & & \vec{k_i} = a_r\vec{k_r} + a_t\vec{k_t} \\ (3) & \text{components} \parallel \text{surface} & k\cos\theta + a_r k\cos\theta = a_t k\cos\theta_t \\ (4) & \text{components} \perp \text{surface} & (1-a_r)k\sin\theta = a_t n_t k\sin\theta_t. \end{array} \tag{2.48}$$

with $\left|\vec{k}\right| = k$.

This means, Snell's law holds also for neutrons

$$\frac{\cos\theta}{\cos\theta_t} = \frac{k_t}{k_i} = n_t. \tag{2.49}$$

As the nuclear scattering length density for most materials is positive, the index of refraction is slightly smaller than 1, with

$$n_t \simeq 1 - \frac{\lambda^2}{2\pi}\rho_{SL,n}, \tag{2.50}$$

and the beam in the medium is refracted towards the surface. For angles smaller than a critical angle $\theta_c$, the refractive index will become purely imaginary and the beam will be reflected completely. The critical angle is then

$$\theta_c = \cos^{-1} n_t \simeq \lambda\sqrt{\frac{\rho_{SL,n}}{\pi}}. \tag{2.51}$$

With the components perpendicular to the surface, $k_{i\perp}$ and $k_{r\perp}$, the reflectivity, $R$, and transmittance, $T$, can be calculated as

$$\begin{aligned} R = & \ |a_r|^2 = \left|\tfrac{k_{i\perp}-k_{t\perp}}{k_{i\perp}+k_{t\perp}}\right|^2 \\ T = & \ |a_t|^2 = \left|\tfrac{2k_{i\perp}}{k_{i\perp}+k_{t\perp}}\right|^2 \end{aligned} . \tag{2.52}$$

The reflectivity can then be written as a function of $Q = \left|\vec{Q}\right| = \left|\frac{4\pi}{\lambda}\sin\theta\right| = 2k_{i\perp}$, as

$$\begin{aligned} R = & \left|\tfrac{Q-\sqrt{Q^2-Q_c^2}}{Q+\sqrt{Q^2-Q_c^2}}\right|^2 \\ R \approx & \ \tfrac{1}{16}\tfrac{Q_c^4}{Q^4} \qquad \text{for } Q >> Q_c. \end{aligned} \tag{2.53}$$

After scattering, the waves reflected from the film and the substrate will interfere, based on the phase shift due to their path length difference. For angles larger than twice the critical angle, we can approximate $\theta_t = \theta$ since the refraction can be neglected. The path length difference, $p$, is then

$$p = 2d\sin\theta, \tag{2.54}$$

for the film thickness, $d$. To get constructive interference, $p$ has to be an integer multiple of the wavelength, such that

$$n\lambda = 2d\sin\theta, \text{ or } Q = n\frac{2\pi}{d} \tag{2.55}$$

This is the so called Bragg equation for constructive interference. This effect leads to an oscillatory behaviour of the intensity, called Kiessig fringes (fig. 2.18). From the distance between two maxima, $\Delta Q$, the thickness can be measured as

$$d = \frac{2\pi}{\Delta Q_{\text{Kiessig}}}. \tag{2.56}$$

If the interfaces (both vacuum-film and film-substrate) are not perfectly flat, the roughness, $\sigma_x$, for the layer $x$, can be treated as a height distribution and results in a decay of the reflectivity,

$$R_{\text{rough}} = R_{\text{flat}} \mathrm{e}^{-4\sigma_x^2 k_{x\perp} k_{x+1\perp}}. \tag{2.57}$$

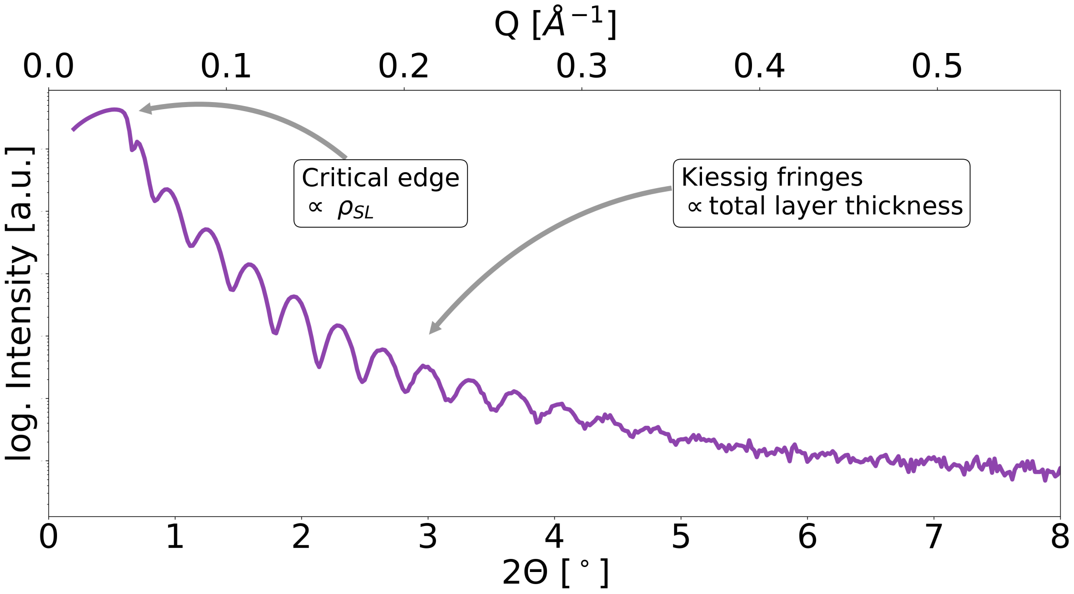

**Figure 2.18:** X-ray reflectometry from a $SrCoO_{2.5}$/LSAT(001) sample. The critical edge (critical angle), intensity drop-off for angles higher than the critical angle and the Kiessig fringes can be seen.

### Polarized neutron reflectometry

For polarised neutron reflectometry, the nuclear (eq. 2.45) and magnetic (eq. 2.31) potentials have to be considered. The combined potential can then be written as

$$V_{n,\mathrm{pol}} = V_{\mathrm{nuclear}} + V_{\mathrm{magnetic}} = \frac{2\pi\hbar^2}{m_n}\rho_{SL,n} - \gamma_n\mu_n\hat{\vec{\sigma}}\cdot\vec{B} = \frac{2\pi\hbar^2}{m_n}(\rho_{SL,n} \pm \rho_{SL,m}), \quad (2.58)$$

where $\rho_{SL,m} = \frac{m_n}{2\pi\hbar}\gamma_n\mu_n\hat{\vec{\sigma}}\cdot\vec{B}$ is the magnetic scattering length density. With the discussion of polarized neutrons in chapter 2.4.2, we can separate four cases, based on the spin direction of the neutron before and after scattering. Continuing with the same definition, the neutron beam direction $\vec{n}$ is along $\vec{x}$, the scattering vector $\vec{Q}$ is along $\vec{z}$, and the neutron spin direction described by the polarization along the magnetic field direction parallel to $\vec{z}$ (see fig. 2.15), with

$$\vec{P} = \langle 2\hat{\sigma}_y \rangle \qquad \text{and} \qquad P = \frac{n_\uparrow - n_\downarrow}{n_\uparrow + n_\downarrow}\ , \quad (2.59)$$

with the number of neutrons in the up state, $n_\uparrow$, and down state, $n_\downarrow$. The orientations are then

$$\begin{aligned} \vec{n} &\parallel \vec{x} \\ \vec{P} \parallel \vec{H} &\parallel \vec{y} \\ \vec{Q} &\parallel \vec{z} \end{aligned} \quad (2.60)$$

Since $\vec{Q} \parallel \vec{z}$, any magnetization along $\vec{z}$ does not contribute, only the magnetization along $\vec{x}$ and $\vec{y}$ has to be considered. The individual contributions were discussed in eq. 2.36: For $\vec{P} \parallel \vec{M}$, the spin direction remains the same, so there is no spin flip (NSF), whereas for $\vec{P} \perp \vec{M}$, the spin flips (SF). The nuclear component of the scattering only contributes for no spin flip. The scattering contribution for the four spin states is then,

$$\text{NSF} \begin{array}{ll} \langle +|+\rangle : & b + M_y \\ \langle -|-\rangle : & b - M_y \end{array} \qquad \text{SF} \begin{array}{ll} \langle +|-\rangle : & M_x \\ \langle -|+\rangle : & -M_x \end{array} \tag{2.61}$$

### Diffraction

In eqs. 2.25 and 2.26, the scattering intensity can be viewed as the Fourier transformation of a pair correlation function. In the case of X-ray diffraction from a crystal, the correlation function takes the periodic form corresponding to the crystal structure [59]. Fundamentally, to construct a crystal, a basis is repeated on each point of a point lattice. Depending on the basis and lattice, the crystal can exhibit a large number of symmetries, which are discussed in detail in the textbooks, such as [18].

The point lattice can be defined by the lattice vectors $\vec{a}$, $\vec{b}$, and $\vec{c}$, and the angles $\sphericalangle \vec{a}\vec{b} = \gamma$, $\sphericalangle \vec{b}\vec{c} = \alpha$, and $\sphericalangle \vec{c}\vec{a} = \beta$ which describe the translation symmetry of the crystal. Any linear combination of the basis vectors, $\vec{R} = u\vec{a} + v\vec{b} + w\vec{c}$ (with $u, v, w \in \mathbb{Z}$), from the origin, coincides again with a lattice point. The direction of the vector is then $[uvw]$. The length of the lattice vectors, e.g. $a = |\vec{a}|$, is the lattice constant. A set of parallel (translationally equivalent) lattice planes passing through three lattice points is defined by the Miller indices $(hkl)$: if the plane closest to the origin intercepts the lattice directions at $a/h$, $b/k$, and $c/l$, the lattice plane satisfies the equation

$$\frac{hx}{a} + \frac{ky}{b} + \frac{lz}{c} = n, \tag{2.62}$$

with the integer n. The distance between the lattice planes, $d(hkl)$, for an orthorhombic lattice ($a \neq b \neq c$, $\alpha = \beta = \gamma$) is given by,

$$d(hkl) = \sqrt{\left(\frac{h^2}{a^2} + \frac{k^2}{b^2} + \frac{l^2}{c^2}\right)}. \tag{2.63}$$

Along with the lattice, the basis defines the crystal structure. It is the set of atoms that repeats at every lattice point and build up, together with the lattice, the crystal lattice, as shown in fig. 2.19.

Since a diffraction experiment is basically the measurement of the Fourier transform of a crystal lattice, it is useful to define a reciprocal lattice by the lattice vector,

$$\vec{G} = h\vec{g_1} + k\vec{g_2} + l\vec{g_3} \quad \text{for the real space vector} \quad \vec{R} = u\vec{a} + v\vec{b} + w\vec{c}\ , \tag{2.64}$$

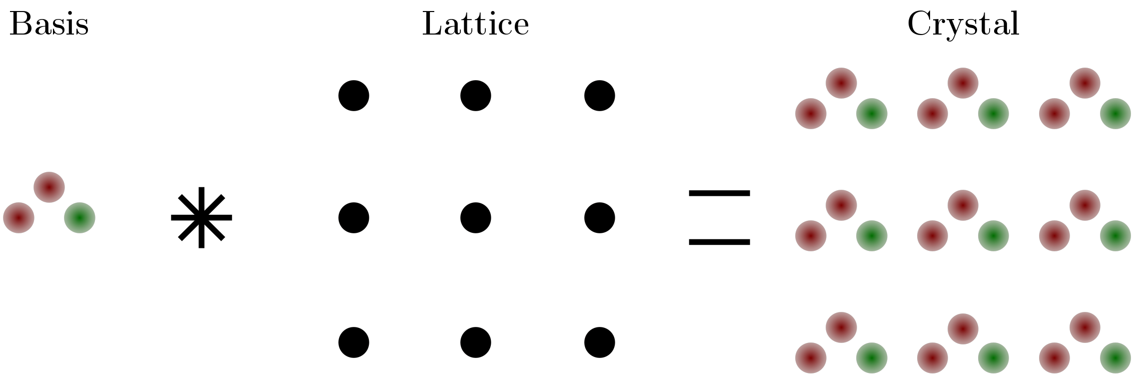

**Figure 2.19:** Construction of a crystal by the repetition of a basis at every point of the lattice.

with the definitions,

$$\begin{array}{lll} \vec{g_1} = \frac{\vec{b}\times\vec{c}}{\vec{a}\cdot(\vec{b}\times\vec{c})} & \vec{g_1}\cdot\vec{a} = 2\pi & \vec{g_1}\cdot\vec{b} = \vec{g_1}\cdot\vec{c} = 0 \\ \vec{g_2} = \frac{\vec{a}\times\vec{c}}{\vec{a}\cdot(\vec{b}\times\vec{c})} & \vec{g_2}\cdot\vec{b} = 2\pi & \vec{g_2}\cdot\vec{a} = \vec{g_2}\cdot\vec{c} = 0 \\ \vec{g_3} = \frac{\vec{a}\times\vec{b}}{\vec{a}\cdot(\vec{b}\times\vec{c})} & \vec{g_3}\cdot\vec{c} = 2\pi & \vec{g_3}\cdot\vec{a} = \vec{g_3}\cdot\vec{b} = 0 \end{array} \tag{2.65}$$

If we now consider a basis of one atom, the scattering from the crystal can be described by the scattering amplitude according to eq. 2.20. Because of discrete scattering centres in the lattice, the integral can be transformed into a sum. For the one dimensional case of a number of $N$ unit cells in $\vec{c}$ direction, the amplitude can then be written as

$$A(\vec{Q}) \sim b \sum_{atoms} \mathrm{e}^{iN\vec{Q}\vec{c}}, \tag{2.66}$$

with the scattering length, $b$. The intensity is then given by the square of the amplitude as,

$$I(\vec{Q}) \sim \left|A(\vec{Q})\right|^2 = |b|^2 \frac{\sin^2(\frac{1}{2}NQc)}{\sin^2(\frac{1}{2}Qc)}. \tag{2.67}$$

The maximum intensity is then at $\frac{1}{2}Qc = j\pi$, for an integer $j$. This results in the Bragg equation, already shown for reflectometry (2.55):

$$Q_{\text{Bragg}} = j\frac{2\pi}{c}. \tag{2.68}$$

The intensity as a function of $Q$ is shown in fig. 2.20 for different values of $N$. If we generalize the condition for constructive interference to three dimensions, we can write it in vector form as

$$\vec{Q}\cdot\vec{R} = 2\pi j. \tag{2.69}$$

From the definition of the reciprocal lattice in eq. 2.65, it is then immediately clear, that this is only fulfilled for the Laue condition,

$$\vec{Q} = \vec{G}. \tag{2.70}$$

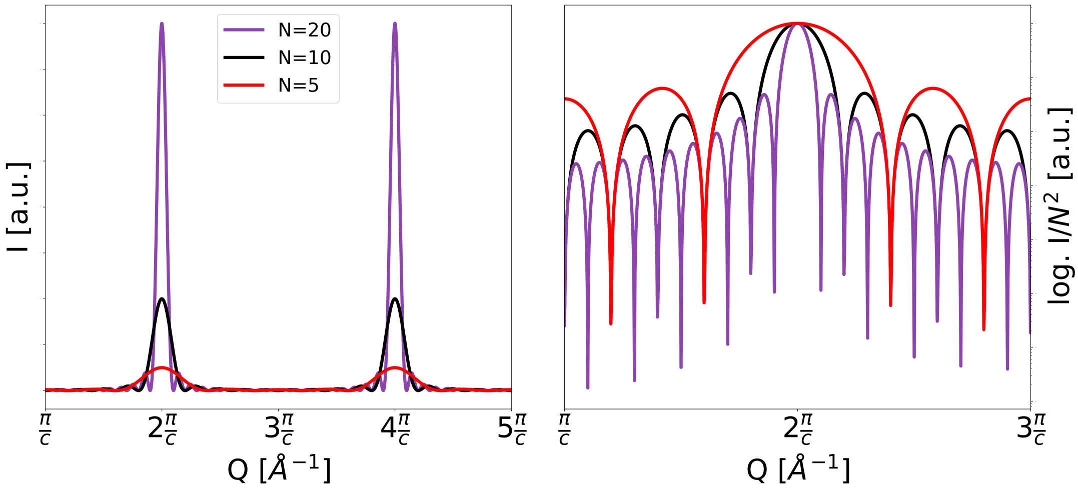

**Figure 2.20:** Laue oscillations for diffraction from $N$ layers in linear scale **(left)** and logarithmic scale divided by $N^2$ **(right)**.

This condition can be visualized by the Ewald construction, shown in fig.2.21. Following the crystallographic convention, the starting point of $\vec{k}$ is the sample, with its end being the origin of the reciprocal lattice. The Ewald sphere spans a sphere of radius $|\vec{k}| = 2\pi/\lambda$ around the starting point of $\vec{k}$. The Laue condition is fulfilled if $\vec{k'}$ also lies on a reciprocal lattice point, so that $\vec{Q} = \vec{G} = \vec{k'} - \vec{k}$.

Returning to the intensity shown in fig. 2.20, around the Bragg peaks, the intensity oscillates depending on the number of unit cells, $N$, with the distance between maxima given by,

$$\Delta Q_{\text{Laue}} = \frac{2\pi}{Nc}. \tag{2.71}$$

This equation can be used to determine the thickness of the crystalline medium and, together with the film thickness determined by reflectometry (eq. 2.56), can be used to determine the fraction of the sample that is crystalline or amorphous,

$$d_{\text{film}}^{\text{Reflectometry}} = \frac{2\pi}{\Delta Q_{\text{Kiessig}}} \tag{2.72}$$

$$d_{\text{crystal}}^{\text{Diffraction}} = \frac{2\pi}{\Delta Q_{\text{Laue}}} = Nc. \tag{2.73}$$

An example of an XRD measurement of a thin film on a substrate is given in fig. 2.22, which shows the sharp Bragg peaks for the substrate and broader Bragg peaks with Laue oscillations for the film.

In summary, diffraction gives information about the crystalline structure, by determining the inter-planar spacing (parallel to $\vec{Q}$) and the number of crystalline layers. For thin films on a substrate, the Bragg peak position is also a measure of strain, since the lattice constant of a bulk crystal is different from that of a strained film.

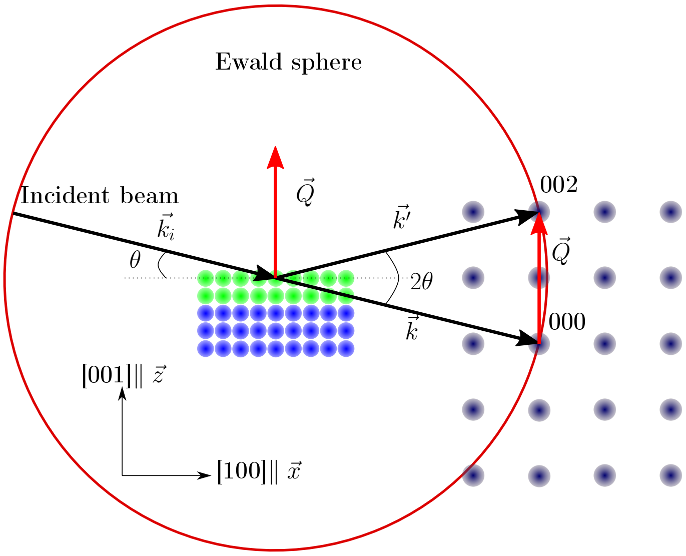

**Figure 2.21:** Ewald construction for diffraction from a thin film sample, in the case of the (002) reflex.

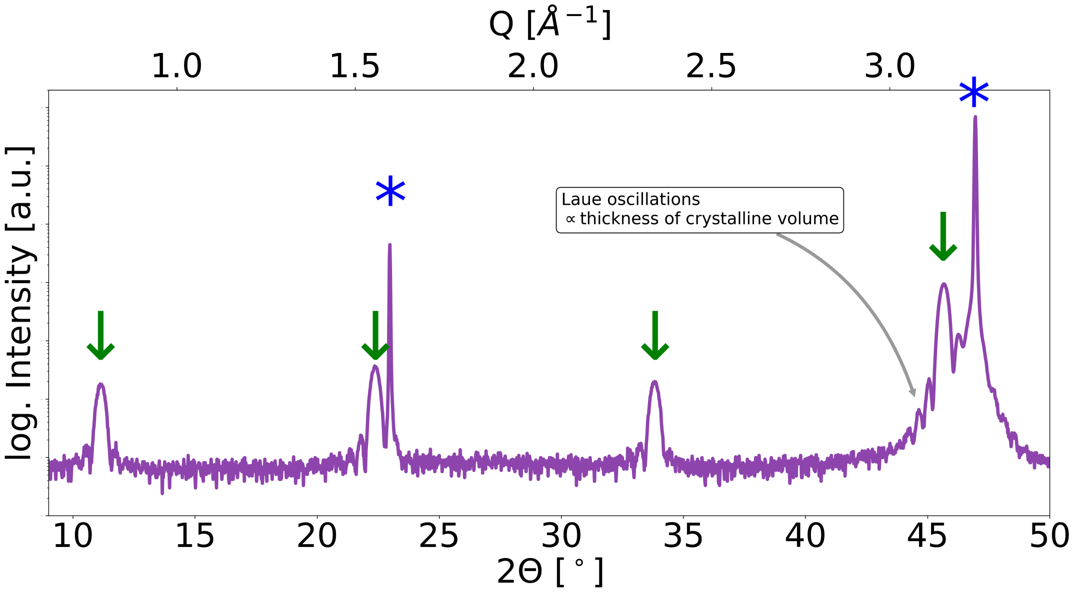

**Figure 2.22:** X-ray diffraction of sample L2 $SrCoO_{2.5}$/LSAT(001). The substrate peaks are marked with stars and the film peaks with arrows.

### Diffraction from a 2-dimensional structure

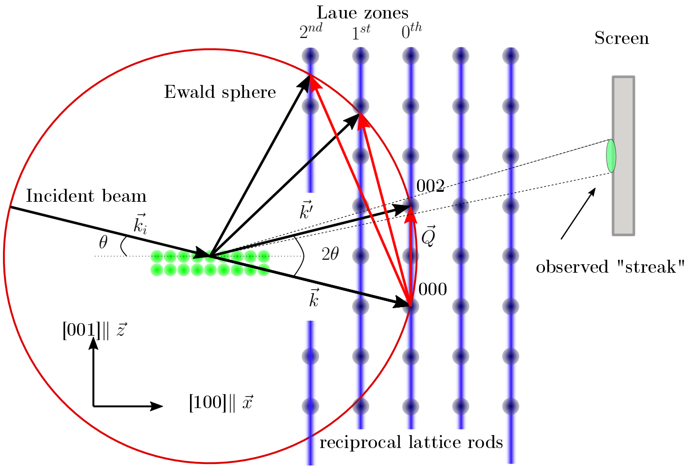

**Figure 2.23:** Ewald construction for diffraction from a quasi 2-dimensional sample, such as for low energy electrons, or electrons in reflection.

The observations made above assume that the scattering probe can interact with the complete film, i.e. that the penetration depth of the probe is larger than the film thickness. For low energy electrons (or electrons in grazing incidence (e.g. RHEED, see chapter 3.2.1)) that condition is not met. Since the electrons only interact with the first one or two monolayers, the film appears 2-dimensional. In reciprocal space, this leads to an elongation of the lattice points in the direction perpendicular to the surface into lattice rods (fig. 2.23). The scattering condition is then fulfilled for all intersections of these reciprocal lattice rods with the Ewald sphere.

In the case of high energy electrons scattering in reflection, the Ewald sphere is small (as it scales inversely with the wavelength) and the angle of reflection is shallow. The reciprocal lattice rods are not 1-dimensional due to imperfections in the film surface and the Ewald sphere is not infinitesimally thin due to an unavoidable wavelength uncertainty. As a result, the intersection of both is not spot-like, but rather extended along the out-of-plane direction [60]. This is especially true for the $0^{th}$ order Laue zone as here the angle is the smallest and thus the intersection the biggest.

# 3 Methods and instrumentation

## 3.1 Sample preparation

### 3.1.1 Molecular beam epitaxy (MBE)

The main deposition method used for this thesis is Molecular Beam Epitaxy (MBE). Two different systems were used, the MBE setup at MLZ (MBE-MLZ) in Garching and the OMBE at Forschungszentrum Jülich. Both systems are DCA M600 setups and therefore very similar (fig. 3.1) [61].

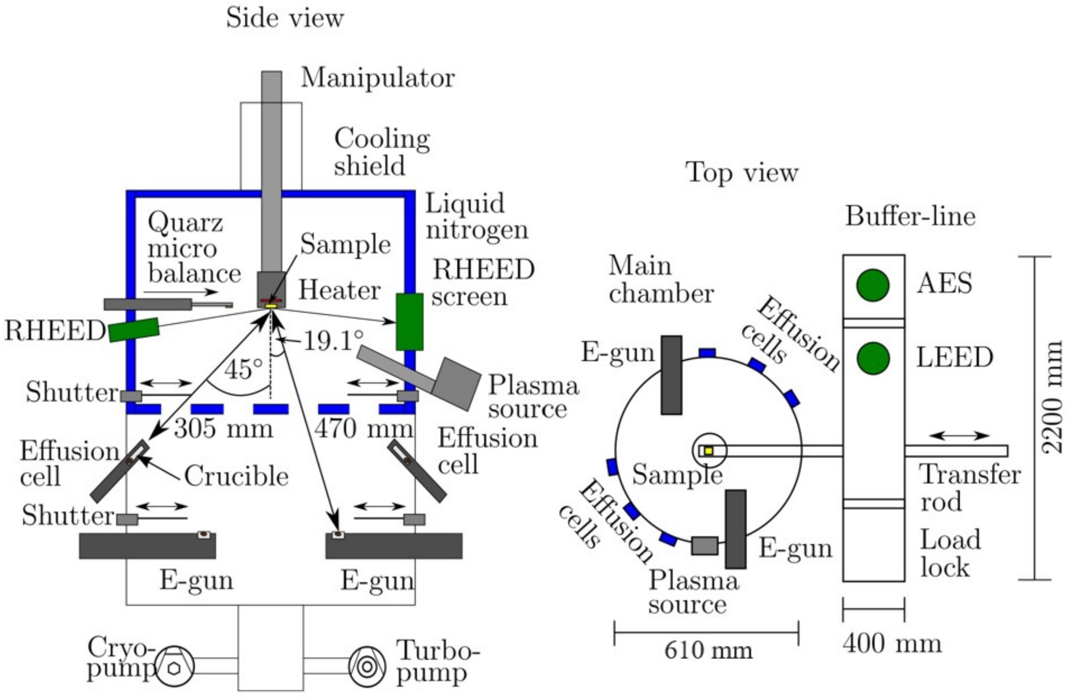

**Figure 3.1:** Schematic of the DCA M600 molecular beam epitaxy setup.
**Left**: Overview of the main chamber, with effusion cells, e-guns and plasma source for thin film growth, and RHEED for analysis of the crystallinity and growth mode during deposition. **Right**: Top view of the complete system of main chamber, buffer line and load lock. In the buffer line, a LEED and an AES setup is mounted. Taken from [62].

The MBE setup consists of 3 vacuum chambers: load-lock, buffer line, and main chamber. The chambers are connected via gate valves to transfer samples in vacuum.

The load-lock is a small vacuum chamber used to transfer samples into and out-of the system without needing to vent the buffer line and growth chamber. It can be heated to 200°C to minimize the amount of adsorbed water introduced into the system. A pressure of $5{\cdot}10^{-8}$ mbar is maintained with a Pfeiffer HiPace 80 turbo pump. Two sample trolleys, with space for twelve sample holders each, can be moved between the load lock and buffer line with a rail system and magnetically coupled rotators.

The buffer line is used for storage of samples in ultra high vacuum (UHV) and houses a low-energy electron diffraction (LEED) system and an Auger electron spectroscopy (AES) instrument. It is pumped with a 240 l/s Gamma Vacuum 300 L ion pump to a pressure of $5{\cdot}10^{-10}$ mbar. Samples can be transferred to the main chamber with a transfer arm.

In the main chamber, a Pfeiffer HiPace 700 turbo pump and a CTI Cryogenics cryo-pump sustain a base pressure of $1{\cdot}10^{-10}$ mbar. Additionally, a liquid nitrogen cryo-shield further acts simultaneously as a getter pump and cooling system. Around the main chamber, six water-cooled effusion cells and two electron guns (e-guns), each housing four crucibles, are used to evaporate material. Each source is equipped with a shutter, allowing for either simultaneous or sequential deposition. A plasma source is used to supply atomic oxygen for the growth of complex oxides.

Nearly all elements used for this thesis were deposited using the effusion cells. The cells are heated until the material inside the crucible starts to evaporate. Using a quartz crystal micro balance (QCM) at the sample position, the amount of evaporated material can be determined, by measuring the change in resonance frequency of the quartz crystal,

$$\frac{\Delta f}{f} = \frac{\Delta m}{\rho \cdot F \cdot d}, \tag{3.1}$$

which depends on the deposited mass, $\Delta m$, the density of the quartz, $\rho$, the area, F, and the thickness of the deposited layer, d [63].

For co-deposition, the frequency change for individual elements are calibrated, such that the frequency change ratio corresponds to the desired stoichiometry. Then, once the evaporation rate is stable for the duration of the deposition (≈ 1-2 hours), the QCM is retracted and the substrate lowered from its waiting position above the main shutter to the deposition position.

An *in-situ* reflection high-energy electron diffraction (RHEED) system is used to monitor the crystalline structure of the thin film during growth. Additionally, a residual gas analyser can be used to measure the composition inside the chamber.

### 3.1.2 Pulsed laser deposition (PLD)

For the deposition of $Fe_3O_4$ films, the Pulsed Laser Deposition (PLD) system of the neighbouring institute PGI-7 was used. The samples were deposited by M. Hussein

Hamed (PGI-6).

A 50W KrF laser is used to ablate an $Fe_2O_3$ target. It operates with a wavelength of 248 nm and a pulse length of 25 ns. The used laser fluence is about $1.5\,\mathrm{J/cm^2}$, with a frequency of 5 Hz. For the deposition of $Fe_3O_4$, the chamber is flooded with oxygen, which raises the base pressure of $1 \cdot 10^{-7}$ mbar to the deposition pressure of $2 \cdot 10^{-6}$ mbar. The material plume ejected from the target condenses on the substrate that is heated to 500°C. Due to the non-equilibrium conditions during PLD growth, the oxygen content in the film is not necessarily the same as in the target. In fact, to grow $Fe_2O_3$ films from the target used here, the oxygen pressure in the chamber need to be much higher than for the growth of $Fe_3O_4$.

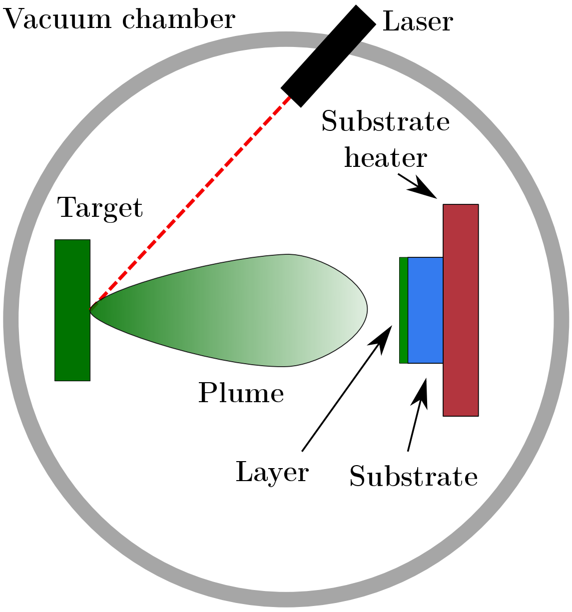

**Figure 3.2:** Sketch of a pulsed laser deposition setup. A laser locally heats the target, causing a material plume to be ejected towards the substrate. The material adsorbs onto the substrate and forms a layer.

# 3.2 In-situ methods of the MBE system

## 3.2.1 Reflection high-energy electron diffraction (RHEED)

To achieve high quality thin film samples, control of growth mode and stoichiometry is highly important. To observe the crystallinity of the layer during growth, Reflection High-Energy Electron Diffraction (RHEED) is used. An electron beam with an energy of 15 keV is directed towards the sample, where it scatters under shallow angle. The elastically scattered electrons are then observed on a fluorescent screen (fig. 3.3).

As explained in chapter 2.4.3, the scattering condition is fulfilled if the Ewald sphere intersects a reciprocal lattice point. Because of the shallow incidence angle, the

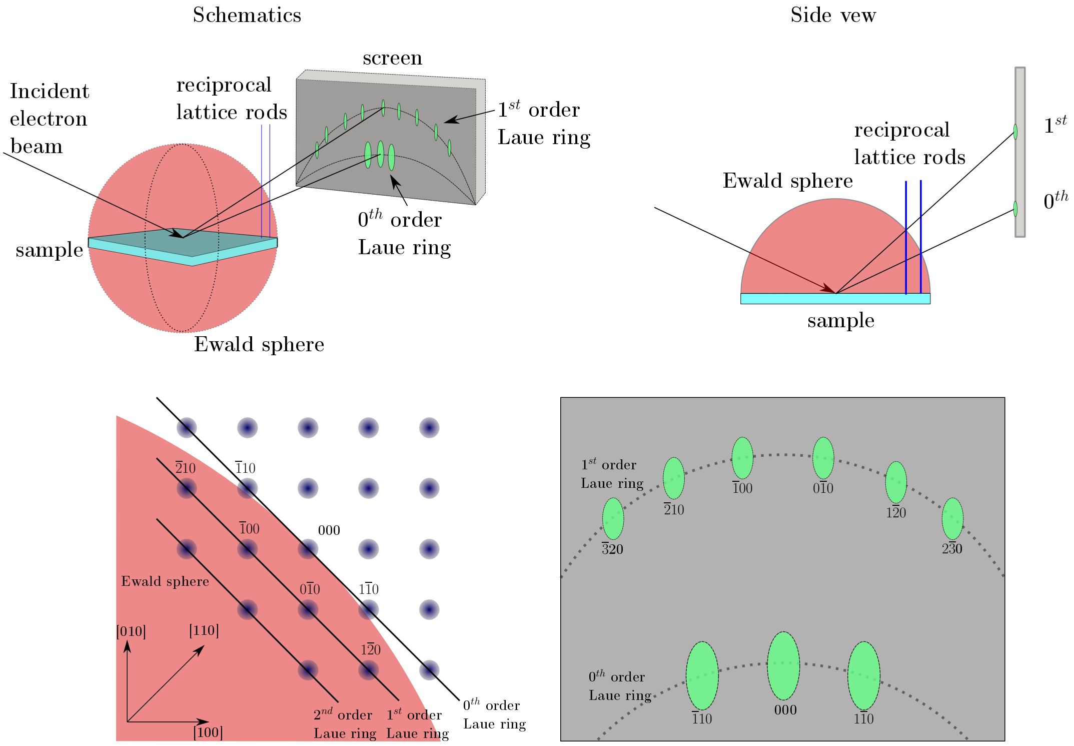

**Figure 3.3: Top:** Schematic and Ewald construction for RHEED. Since the penetration depth of the electrons is very low, the diffraction condition gets smeared out in the out-of-plane direction. Instead of reciprocal lattice spots, lattice rods are intersecting the Ewald sphere, giving rise to Laue rings on the fluorescent screen. **Bottom:** Origin of the individual diffraction spots for a cubic substrate with scattering along the [110] direction.

penetration depth of the electrons is low and the depth information is lost making RHEED very surface sensitive. The scattering can be treated as from a 2 D structure and the reciprocal lattice points elongate into rods perpendicular the surface. The scattering condition is then met for intersections of the lattice rods with the Ewald sphere. The diffraction pattern for a single crystal thin film is then a set of rings originating from the lattice plane perpendicular to the beam direction.

The diffraction pattern can be used to gather information on the present crystallographic phases or amorphous growth.

### Growth observation by RHEED

RHEED can be used during thin film growth and hence the growth mode can be determined.

Layer-by-layer growth can be confirmed by observing an oscillatory behaviour in the intensity of the specular reflected spot (fig. 3.4) [64]. For a complete layer, the intensity is at a maximum. As the next layer starts to form, the intensity drops due to the increasing surface roughness, reaching a minimum when the layer is half formed. As the layer gets completed, and thus flat, the intensity once again reaches a maximum. For step flow growth, the amplitude stays constant, as there is no nucleation within one terrace, but only at the step edge and the roughness of the film doesn't change. If there is island growth, the electrons may transmit through the island with a resulting spot like pattern (fig. 3.4) [60].

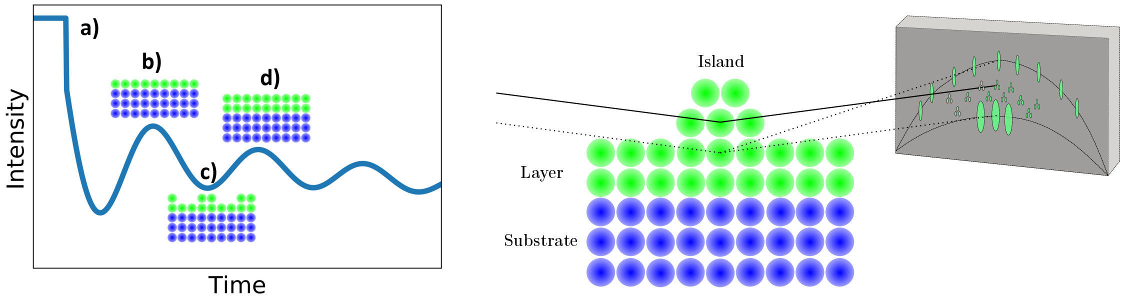

**Figure 3.4: Left:** Illustration of the RHEED intensity oscillations. After the start of the deposition (a), the intensity decreases drastically, since the roughness increases. With the completion of the first monolayer (b), a local maximum is reached. As the next layer is deposited, the intensity decreases to a minimum until the layer is half deposited (c). The intensity increases again until the second monolayer is complete (d). **Right:** RHEED in transmission through an island creating a spot pattern.

## 3.2.2 Low-energy electron diffraction (LEED)

Using Low-Energy Electron Diffraction (LEED), the cristallinity and in-plane lattice parameter of the sample can be determined *in-situ*. Electrons with energies, $E$, between 50 eV and 500 eV are hitting the sample perpendicular to the surface and get backscattered (fig. 3.5) [65]. The de-Broglie wavelength of the electrons, $\lambda$, can be calculated with

$$\lambda[\text{Å}] = \sqrt{\frac{150.4}{E[eV]}}, \tag{3.2}$$

to be in the Å range. Following the Bragg condition, the electrons scattering from crystalline structure of the sample produce a diffraction pattern. Because the penetration depth of electrons for the used energies is only a few monolayers, LEED is very surface sensitive.

The distance between the Bragg spots can be used to calculate the lattice constant of the film, by relating the geometric scattering condition to the real space measurement setup,

$$a = \frac{hR}{\sqrt{2m_e e}} \frac{\sqrt{U}}{d}, \tag{3.3}$$

with Planck's constant, $h$, the radius of the screen, $R$, mass of the electron, $m_e$, elemental charge, $e$, the voltage, $U$, and distance between neighbouring spots, $d$.

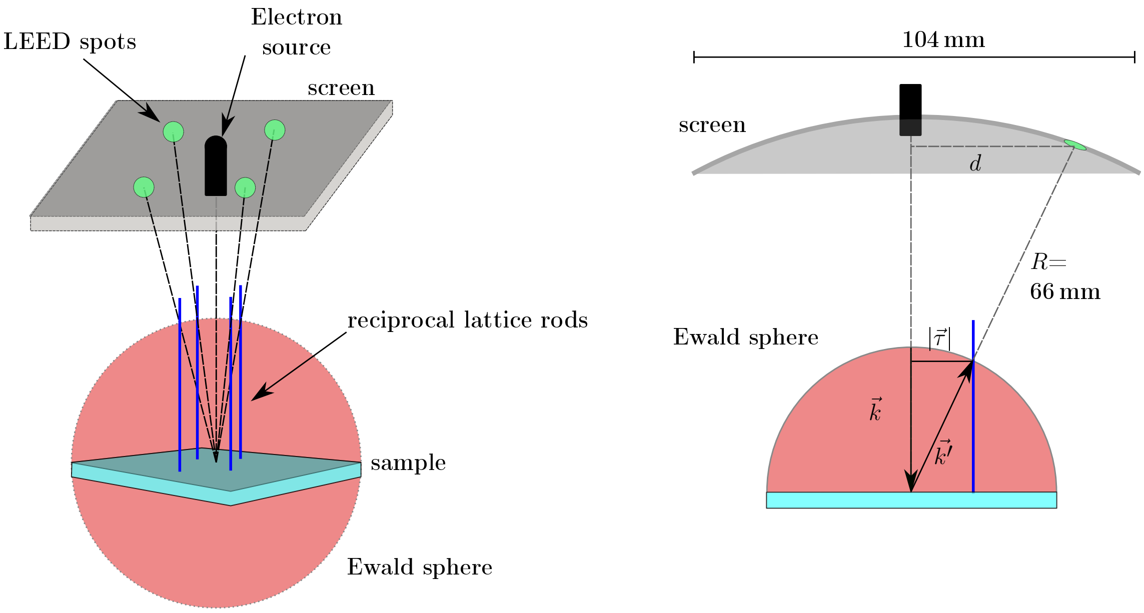

**Figure 3.5:** Schematic of the LEED setup. **Left:** Electrons impinge on the sample surface and are scattered back onto the screen. **Right:** By considering the scattering condition and the experimental setup, the in-plane lattice constant of the film can be determined using eq. 3.3. The screen radius for the used Specs Er-LEED system is 66 mm.

### 3.2.3 Auger electron spectroscopy (AES)

To measure the surface chemical composition of a sample or substrate *in-situ*, Auger Electron Spectroscopy (AES) is used. Electrons are accelerated towards the sample, where they scatter inelastically, transferring enough energy to expel a core shell electron. To fill the vacancy, another electron transitions to the lower energy. The associated energy loss is transferred to a third (Auger) electron, which leaves the atom. By measuring the energy spectrum of the backscattered electrons, the characteristic Auger line for each element can be recorded, allowing for the determination of the composition.

## 3.3 In-house methods

### 3.3.1 Atomic force microscopy (AFM)

To image the surface of the sample, and get local information about the topography, Atomic Force Microscopy (AFM) is used. A sharp tip attached to a cantilever is moved across the sample surface (fig. 3.6). It interacts with the sample via a variety of forces, though mainly by the attractive van-der-Waals force and Pauli repulsion described by the Lennard-Jones potential (inset in fig. 3.6) [66]:

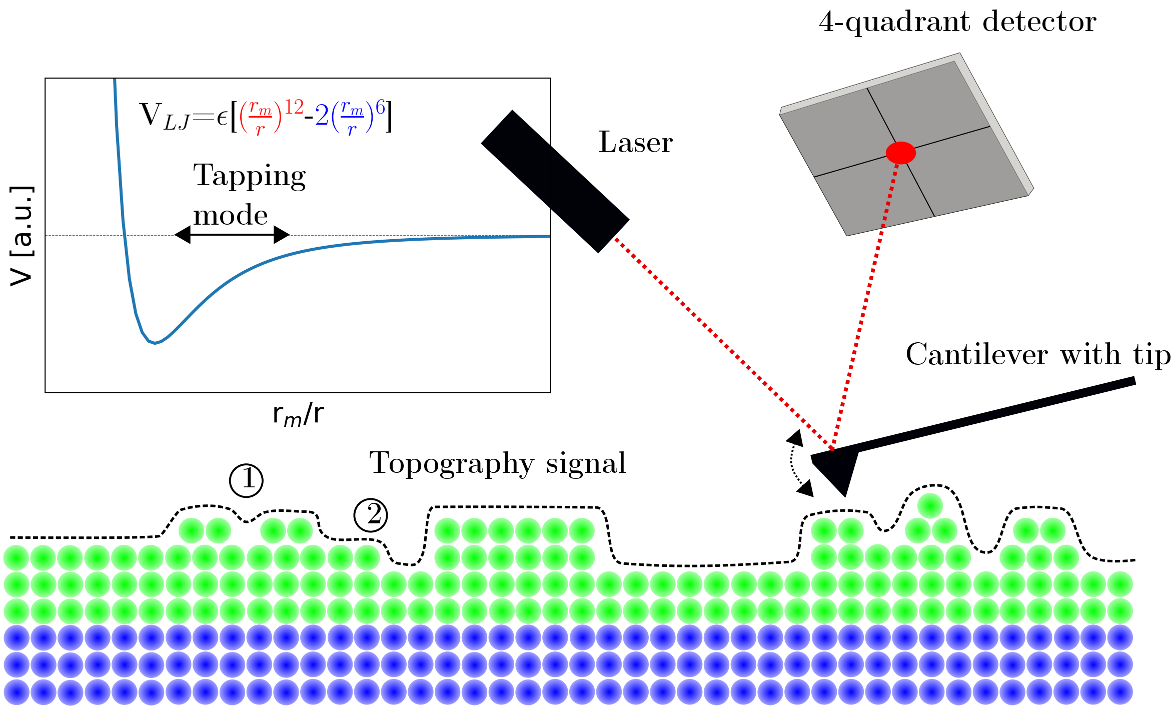

**Figure 3.6:** Sketch of the AFM setup. The tip of the cantilever scans over the surface of the sample, oscillating up-and-down. The deflection of the cantilever is measured by a laser that is reflected from the back of the cantilever onto a four quadrant detector. The dashed line shows the measured topography signal. Because the tip has a certain width, small holes (1) and sharp steps (2) are smeared out. The height of steps is still accurately measured, but for holes thinner than the tip width, the height is underestimated. The **inset** shows the Lennard-Jones potential describing the interaction of the tip with the sample. For short distances, the interaction is repulsive, for larger distances attractive.

$$V_{LJ} = \epsilon[(\frac{r_m}{r})^{12} - 2(\frac{r_m}{r})^{6}], \tag{3.4}$$

with the distance, $r$, binding energy, $\epsilon$, and the equilibrium distance, $r_m$.

Other forces and associated properties can be probed by specialized AFM modes, such as MFM for imaging the magnetic stray field, and PFM for imaging piezoelectric domains. As the tip interacts with the sample, the cantilever gets deflected towards or away from the sample. That deflection can be measured by a laser, reflected from the back of the cantilever onto a four quadrant detector. The sample is then measured by scanning the tip line by line over the surface.

Based on the distance between the tip and sample, three measurement regimes can be distinguished: For large distances, the tip is only weakly attracted by the sample and not in direct contact (non contact mode). For very small distances, the tip is in the repulsive regime (or at the attractive-repulsive crossover) in contact with the sample (contact mode). For in-between distances, the AFM can operate in tapping mode, where the cantilever oscillates close to its resonance frequency, sweeping between the repulsive and attractive regime. This minimizes the close contact with the sample, reducing the damage to tip and sample, while still obtaining a high resolution image. In tapping mode, the phase change of the oscillation can also be measured and contains information about the stiffness of the sample. A change in phase in a certain region of the sample can indicate a different chemical makeup. From the topography signal, the root-mean-square roughness, $\sigma_{\mathrm{RMS}}$, can be calculated as

$$\sigma_{\mathrm{RMS}} = \sqrt{\frac{1}{N}\sum_{n=0}^{N}(z_i - z_o)^2}, \tag{3.5}$$

with the mean height, $z_0$, and the local height, $z_i$ at the position $i$. The error of the roughness is estimated by calculating the standard deviation of four subsections of a measurement.

The instrument used in this thesis is an Keysight 5500 SPM. Typically the HQ:NSC15/Al BS cantilevers from MikroMasch were used, which have a spring constant of 40 N/m, resonance frequency around 325 kHz and a conical tip that is 15 µm high and has a tip radius of $< 8$ nm. The images were evaluated with the program Gwyddion [67].

### Piezoresponse force microscopy (PFM)

Another operating mode of AFM specific for ferro- or piezoelectric samples is Piezoresponse Force Microscopy (PFM). The sample is scanned in contact mode with an applied bias voltage to the sample or tip. This bias causes a piezoresponse in the sample which causing a deformation that can be measured by the deflection of the cantilever. In vertical PFM, the out-of-plane deformation caused by out-of-plane bias ($d_{33}$ coefficient of the piezoelectric tensor) is recorded. The amplitude signal is related to the strength of the deformation, while the phase is dependent on the polarisation direction.

The instrument used for PFM was an Asylum Research Cypher SPM operated by PGI-6 with HQ:NSC18/Pt cantilevers from MicroMash.

## 3.3.2 X-ray reflectometry (XRR) and diffraction (XRD)

Two X-ray reflectometers were used, the Bruker D8 Discover of the neutron optics group of the Heinz Maier-Leibnitz Zentrum, for X-Ray Reflectometry (XRR) and the Bruker D8 Advance of JCNS-2 for reflectometry and X-Ray Diffraction (XRD). In the D8 Advance (sketch in fig. 3.7), the sample is stationary in a horizontal position, with both the source and detector arm moving by an angle $\theta$, for a $\theta/2\theta$ measurement. In the D8 Discover, the sample is mounted vertically, held by a suction stage. During the measurement, the source moves at an angle $2\theta$ for a sample angle of $\theta$. Both setups use a Cu-K$_{\alpha 1}$ source but the D8 Advance is equipped with a channel cut monochromator. The monochromator is responsible for filtering out unwanted wavelengths, most importantly the Cu-K$_{\alpha 2}$ and Cu-K$_{\beta}$ lines, as well as the Bremsstrahlung. The monochromator is is required for diffraction. Both instruments use two Göbel mirrors, one after the source and one before the final slit. These mirrors, together with the slits, are necessary to collimate the beam to the high degree necessary for high resolution reflectometry. The available angular range of the D8 Advance is 0°-110°.

To fit the measurements, the GenX software is used [68].

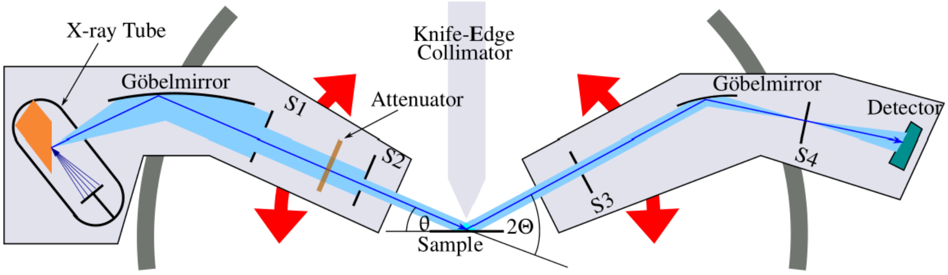

**Figure 3.7:** Sketch of the Bruker D8 Advance. Taken from [69].

### 3.3.3 Hard X-ray photoemission spectroscopy (HAXPES)

A determination of the oxidation state of transition metals can be achieves using HArd X-ray PhotoEmission Spectroscopy (HAXPES). A synchrotron source emits high energy (hard) X-rays, which excite a core shell electron, ejecting it from the atom. The kinetic energy of the photoelectron is measured, and because it is characteristic to the atoms oxidation state, it is possible to determine the valency of the atom. This is particularly useful if multiple oxidation states for a compound exist, such as iron oxides. Satellite peaks are present in the spectra if the outgoing electron excites a valence electron, thus losing some energy. The use of hard X-rays makes it possible to obtain information of large parts of the thin film ($\sim$25 nm), which is not possible for softer laboratory X-rays, as the mean free path of the electrons would be too low to leave the sample.

The measurement in this thesis was taken and analysed by M. Hussein Hamed at the beamline P22, DESY, using an X-ray energy of 6 keV.

### 3.3.4 Rutherford backscattering spectroscopy (RBS)

To measure the stoichiometry of the deposited thin films, Rutherford Backscattering Spectroscopy (RBS) was performed by Jürgen Schubert and Willi Zander (PGI-9).

A beam of He-ions with an energy of 1.4 MeV is accelerated towards the sample [70]. By measuring the energy of the scattered ions, $E_{He,f}$, the mass of the target atom it was scattered by, $M_t$, can be calculated by

$$\frac{E_{\mathrm{He,f}}}{E_{\mathrm{He,i}}} = \left( \frac{\sqrt{1-(M_{\mathrm{He}}/M_{\mathrm{t}})^2 \sin^2\theta} + (M_{\mathrm{He}}/M_{\mathrm{t}})\cos\theta}{1+M_{\mathrm{He}}/M_{\mathrm{t}}} \right)^2 , \tag{3.6}$$

with the initial He ion energy $E_{He,i}$, the He ion mass, $M_{He}$, and the scattering angle $\theta$. For thin samples, the signal for each element is peak like. For thicker samples, such as substrates, the ions lose energy inside the sample, leading to an elongation of the signal towards zero energy, resulting in a step-like shape (fig. 3.8).

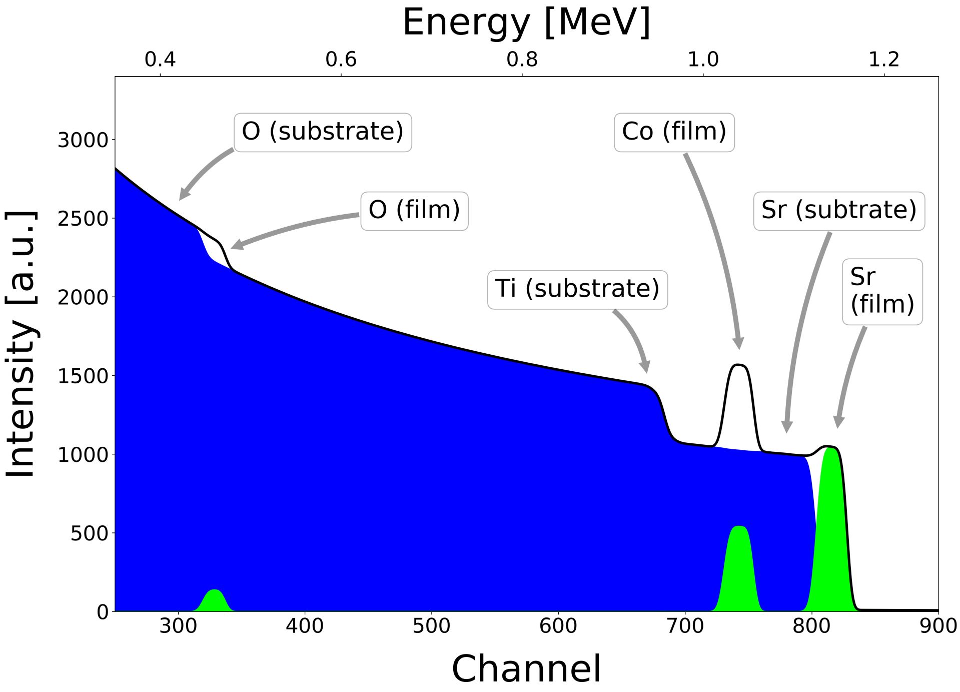

**Figure 3.8:** Simulation of a $Sr_1Co_1O_{2.5}$ film on a $Sr_1Ti_1O_3$ substrate. The black line shows the simulated total intensity, with the film contribution in green and substrate contribution in blue. Because the substrate thickness is effectively infinite for RBS, the signal is elongated towards 0 energy.

The differential scattering cross section is dependent on the square of the atomic number of the target atom, $Z_t$:

$$\frac{d\sigma}{d\Omega}(E,\sigma) = \left(\frac{Z_{He}Z_t e^2}{4E}\right)^2 \frac{4\left(\sqrt{1-(M_{He}/M_t)^2 sin^2\theta} + cos\theta\right)^2}{sin\theta\sqrt{1-(M_{He}/M_t)^2 sin^2\theta}}, \tag{3.7}$$

so RBS is more sensitive to heavier atoms.

To simulate the spectra, the RUMP software was used [71].

### 3.3.5 Magnetic properties measurement system (MPMS)

A Quantum Design Magnetic Properties Measurement System (MPMS) is used for magnetic characterisation [72]. It uses a Superconducting QUantum Interference Device (SQUID) and a superconducting magnet inside a liquid helium Dewar vessel to be able to measure in a temperature range from 1.9 K to 400 K with field of to 7 T.

The sample is held inside a plastic straw and inserted into the MPMS chamber, which is filled with a helium exchange gas. The superconducting magnet generates a longitudinal field along the straw direction, i.e. in the sample plane parallel to the direction of travel. To measure the sample, it is moved through a set of pickup coils made of a superconducting wire, with the outer coils wound opposite to the inner coils, forming a second-order gradiometer (fig. 3.9) [73]. The magnetic moment of the sample induces a current in the coils, which is inductively coupled into the rf SQUID circuit. Because of the design of the coils, the uniform magnetic field is not detected. The SQUID circuit itself is a superconducting loop with a set of Josephson junctions [74]. Because the Cooper pairs in the superconductor are following a single particle wavefunction, the phase difference along the loop is quantized to integer multiples of $2\pi$ and the flux to integer multiples of the magnetic flux quantum $\Phi_0 = 2.07 \cdot 10^{-15}\,\mathrm{Vs}$. Any external flux, such as the one caused by the sample magnetization, leads to an induced phase change that needs to be compensated by a Josephson current [75]. This current can be measured to calculate the external magnetic flux. Because of this, the SQUID is extremely sensitive to small magnetic fields, with a sensitivity of about $5{\cdot}10^{-12}\,\mathrm{Am}^2$ [76].

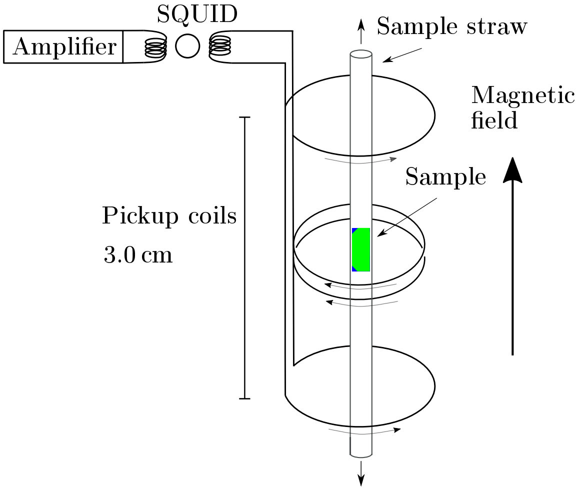

**Figure 3.9:** Schematic of the MPMS setup. The sample inside the straw is moved through the SQUID pickup coils. The magnetic moment of the sample generates a current in the pickup coils, which is coupled through the SQUID to an amplifier. Drawing adapted from [76].

A magneto-electric setup is available to apply a voltage to the sample, based on the design of Borisov *et* al. [77], which was implemented by O. Petracic and L.-M. Wang (JCNS-2). The sample is contacted via two copper wires, which are glued to the sample via silver paste. The wires are connected to a feedthrough at the end of the sample rod, leading to a voltage source outside the system. In previous PhD theses [78, 79] a Vespel rod was used to mount the sample, which lead to a significant background signal. In this thesis, the sample was mounted, similarly to regular measurements, inside a straw (fig. 3.10). This procedure was developed by T. Bhatnagar-Schöffmann.

For the movement of the sample, two different sample stages are used, a standard transport (DC) and a reciprocating sample option (RSO) [76]. The DC option uses a stepper motor to move the sample gradually through the pickup coils, whereas the RSO uses a servo to rapidly oscillate it. Because of the higher sensitivity of the RSO option ($5{\cdot}10^{-12}\,\mathrm{Am}^2$), it is used for most measurements. However for measurements with an applied voltage, the DC option has to be used, as the electrical connection is not possible for the RSO option.

**Figure 3.10:** Picture of a sample mounted in the MPMS magneto-electric option.

### 3.3.6 Physical properties measurement system (PPMS)

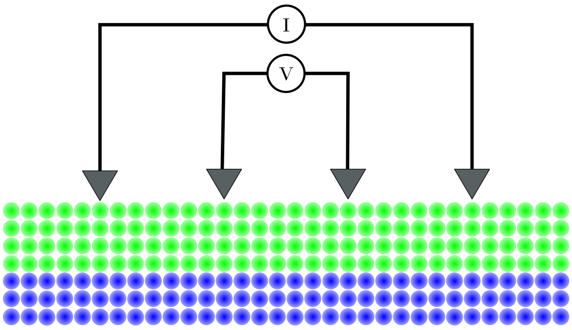

**Figure 3.11:** Measurement of the sheet resistance. A current is driven between the outer 2 contacts and the voltage is measured between the inner contacts.

To measure the film resistivity, a Quantum Design Physical Properties Measurement System (PPMS) was used. It is composed of a cryostat, which enables measurements in a temperature range from 1.9 K to 400 K. A superconducting magnet can be used to apply fields of up to 9 T. The sheet resistance is measured in a 4 point probe mode, shown in fig. 3.11, with

$$R_S = \frac{\pi}{\ln(2)}\frac{V}{I}. \tag{3.8}$$

### 3.3.7 Transmission electron microscopy (TEM)

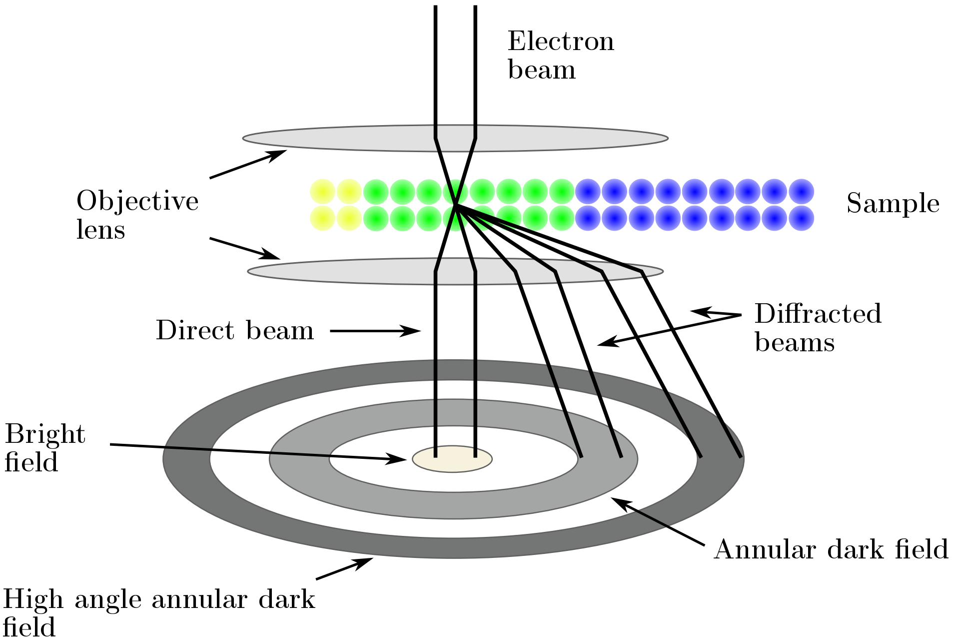

**Figure 3.12:** Sketch of the basic principle of STEM imaging. A parallel electron beam is transmitted through the sample, either directly, or diffracted. The objective lens focusses both beams onto the detector plane, where the direct beam is imaged in the bright field detector and the diffracted beam in the annular dark field detector.

Transmission Electron Microscopy (TEM) is used to investigate the crystallinity and structure of the sample cross section and, in combination with Energy-Dispersive X-ray spectroscopy (EDX), to study the composition. It is performed in scanning mode (STEM) by Juri Barthel (ER-C-2) with a FEI Tecnai G2 F20 [80], operated at 200 keV. It uses a Fischione Model 3000 high angle annular dark field detector for scanning mode, which offers a resolution of 1.9 Å.

To prepare a sample for TEM measurements, a thin lamella (∼50 nm) is cut out of the sample using a Focussed Ion Beam (FIB) in a FEI Helios NanoLab 460F1 [81] and thinned down further by ion milling (∼20 nm) in a Fischione Nanomill Model 1040. The resulting cross section of the sample is thin enough for the transmission of electrons for the used energy range.

In the STEM, a narrowly collimated, parallel electron beam is transmitted through the lamella while scanning over the selected area. Part of the beam is transmitted directly through the sample, while a smaller part is diffracted (fig. 3.12). An objective lens focusses the beams onto the plane of the detectors. The direct beam is observed in the bright field, while the diffracted beam is integrated over the whole angular range in the Annular Dark Field (ADF) and for higher angles in the High Angle Annular Dark Field (HAADF). The dark fields are more sensitive to heavier elements, while the bright field is more sensitive to lighter elements.

Besides obtaining the structural information, elemental analysis can be performed by EDX. Inelastically scattered electrons eject a core shell electron. That vacancy gets filled by a higher shell electron, emitting a photon (x-ray) with a characteristic energy. The photon hits a semiconductor detector, where its energy can be determined. By mapping the energy spectrum of the generated x-rays, the elemental composition and stoichiometry can be determined.

### 3.3.8 Tube furnace

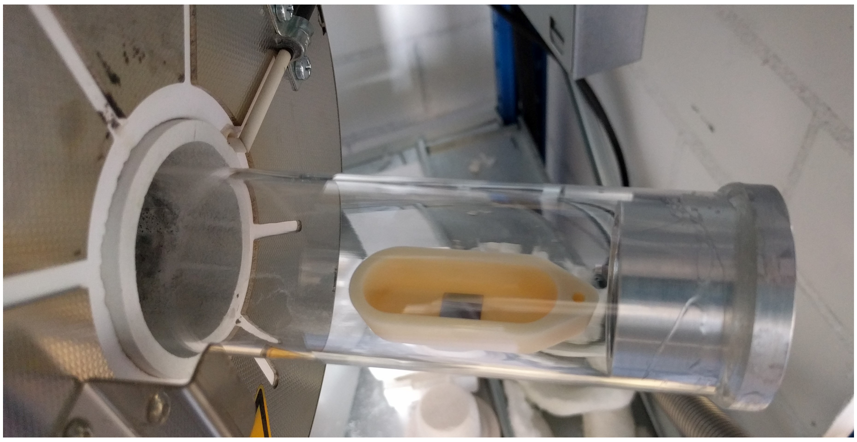

**Figure 3.13:** Photo of the alumina crucible in the quartz glass tube in the tube furnace on Garching.

To anneal samples under oxygen flow, two furnaces were used. A GSL-1500X from MTI Corporation, located in Jülich, with a high purity alumina tube that can be heated to 1400°C under an oxygen flow of up to 50 ml/min. In Garching, a Nabertherm RT 50-250/13, tube furnace with a custom build quartz glass tube for gas flow of up to 200 ml/min is used (fig. 3.13). Both furnaces are programmed similarly, with heat up and down time of 90 min without active cooling and an annealing time between 3-9 h. During annealing, the sample was kept in an alumina crucible.

## 3.4 Polarised neutron reflectometry (PNR)

To measure the magnetic depth profile of thin films, Polarised Neutron Reflectometry (PNR) is performed, with the two reflectometers, MARIA at the Heinz-Meier Leibnitz Zentrum (MLZ) in Garching, Germany and the PBR at the NIST Center for Neutron Research (NCNR) in Gaithersburg, USA. Both instruments operate at a reactor source with a power of 20 MW, and are capable of full polarisation analysis, however their design is quite different.

### 3.4.1 Magnetic reflectometer with high incident angle (MARIA)

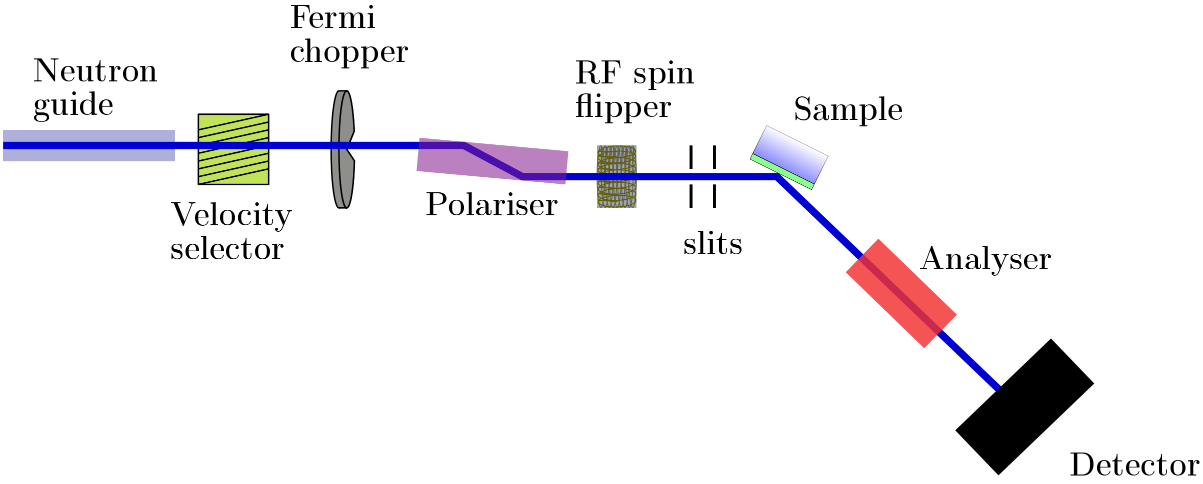

**Figure 3.14:** Sketch of the neutron reflectometer MARIA at the MLZ. It uses a velocity selector to monochromatise the neutron beam and a double reflection polariser to select one spin state. After scattering, the outgoing spin state is selected by a $^3$He analyser. Finally, the neutrons are detected with a $^3$He area detector.

The MAgnetic Reflectometer with high Incident Angle (MARIA), is a neutron reflectometer designed to measure thin, 3 - 300 Å, samples [82]. A velocity selector us used to monochromatize the beam to a wavelength between 4.5 Å and 10 Å (up to 40 Å for unpolarised neutrons) with a resolution of $\Delta\lambda/\lambda$=10 %, which can be further improved to 1%, by the use of a Fermi chopper. To polarise the neutron beam, a double reflection polariser is used, which reflects one polarisation direction and transmits the other, based on a difference in scattering length density for the two spin directions. A radio frequency (RF) flipper can invert the polarisation before the sample position. A hexapod sample stage is used to translate and rotate the sample mounted on a cold-finger cryostat, with a minimum temperature of 5 K, while keeping the sample in the centre of rotation. To apply a magnetic field, a Bruker electromagnet is used, which can reach a field of up to 1.3 T. After scattering, a $^3$He analyser selects the observed polarisation. A $^3$He area detector, with 1024x1024 pixels, is used to detect the specular and off-specular scattering.

The polarised neutron flux at the sample position is $5{\cdot}10^7\,\mathrm{n\,cm^{-2}\,s^{-1}}$ with an accessible $Q_z$ range of 0.002 Å $^{-1}$ - 3.2 Å $^{-1}$.

### 3.4.2 Polarized beam reflectometer (PBR)

In the Polarized Beam Reflectometer (PBR) a monochromatic neutron beam of $\lambda$=4.75 Å is achieved with a pyrolytic graphite monochromator and a Be filter to filter out $\lambda/2$ neutrons (fig. 3.15). The wavelength uncertainty, $\frac{\Delta\lambda}{\lambda}$ is 3%. A Fe/Si supermirror is used to polarise the beam, which along with a Mezei spin flipper enables the selection of the initial spin state (up or down). After scattering, another

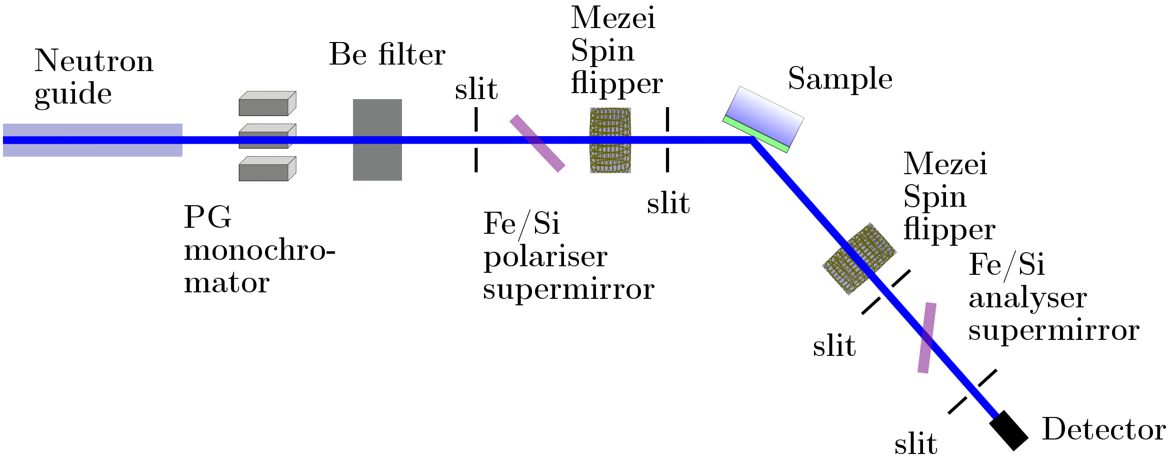

**Figure 3.15:** Sketch of the neutron reflectometer PBR at the NCNR after [83]. A pyrolythic graphite monochromator with a Be filter is used to select a wavelength of 4.75 Å. The polarisation and analysis is achieved with a set of Fe/Si supermirrors and Mezei flippers, before and after the sample. A few cm wide $^3$He pencil detector is used to detect the neutrons.

flipper and supermirror select the analysed spin state, enabling fully polarised measurements. A magnetic field of up to 3 T can be applied at the sample position with a superconducting magnet. A cold-finger cryostat is used to mount the sample. The detector is a $^3$He pencil detector which observes the reflected beam. Simultaneous observation of off-specular scattering is not possible. The sample holder used for the experiment at PBR is shown in fig. 3.16.

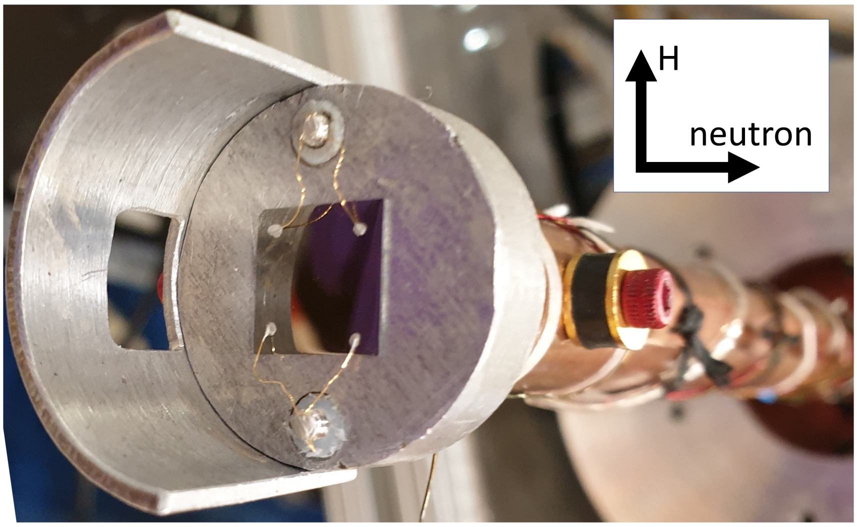

**Figure 3.16:** Photo of the sample holder used for PBR experiments with 4 contacts on the film to apply an electric field.

# 4 Strontium cobaltite

The aim of this project was to study the influence of controllable strain on the topotactic transition in $SrCoO_{3-\delta}$ (SCO) between $SrCoO_{2.5}$ (BM-SCO) and $SrCoO_3$ (P-SCO). The starting point is the successful growth of $SrCoO_{2.5}$ using molecular beam epitaxy (MBE). While $SrCoO_3$ films can be natively grown using PLD, the oxygen pressure during the growth in the MBE chamber is not high enough to grow $SrCoO_3$ directly. Thus it is necessary to grow $SrCoO_{2.5}$ films and fill the oxygen vacancies afterwards. Both STO and LSAT substrates were used for the growth and annealing study. While initial experiments with STO already provided good film quality, later growth on LSAT resulted in an even better crystalline quality. In the following samples on STO are labelled with "**S**" and on LSAT with "**L**", with a letter or number suffix for the sample part or for simultaneously grown sample, where applicable (see supplementary information S.3). The second step was the successful transition of $SrCoO_{2.5}$ to $SrCoO_3$ by annealing in an oxygen rich environment and investigation of the phase stability and magnetic properties by laboratory methods and neutron reflectometry. Next, the PMN-PT substrates for the strain study were characterized and samples of $SrCoO_{2.5}$ on PMN-PT with an LSMO buffer- and electrode layer were prepared. This sample was then investigated in detail by neutron reflectometry and TEM.

## 4.1 Growth and stoichiometric control of $SrCo_xO_{2.5}$

The growth procedure for the $SrCoO_{2.5}$ films in the MBE in Garching followed the procedure outlined below. Films produced in Jülich followed a slightly different procedure, which will be discussed further in chapter 4.1.2. An overview of the specific deposition conditions for each sample is given in the appendix S.3.

The effusion cells were heated in UHV with about 3-4°C/min to the temperature required to sustain a stable molecular beam, which was between 500-620°C for Sr and 1320-1550°C for Co, depending on the filling of the crucibles. To reach the required Co cell temperature and let it stabilize about a day was needed. After the cells reached the temperatures, the deposition rate was calibrated via the frequency change of the quartz crystal micro balance (QCM) at the substrate position. The temperature was slowly adjusted so that the frequency change matched the desired value. As a starting point, the frequency changes determined in [84], listed in table 4.1, were taken. After the frequency changes matched the desired value, their stability was observed for at least 30 min to ensure that there was no deviation which would lead to incorrect stoichiometry. After the stability was verified the

QCM was retracted and the chamber flooded with oxygen at a flow of 0.12 sccm which raised the pressure to 4-7·$10^{-6}$ mbar. Once the pressure was stable, the oxygen plasma was started and stabilised at 300 W forward and 0 W reflected power. Before the deposition, the substrate was annealed at 1000°C for STO and LSAT for 2 hours to remove organic contaminants and ensure a smooth surface. For deposition, the substrate was brought to the deposition temperature (which will be discussed in the next section) with a heating rate of 50°C/min. During growth, the film was monitored by RHEED. The deposition time varied depending on the desired thickness between 1-2 hours. After the deposition was finished, the sample was cooled down to room temperature with 50°C/min while keeping the oxygen plasma and flow active.

**Table 4.1:** Growth parameter for $Sr_1Co_1O_{2.5}$ films from [84]

| Substrate temperature | Co frequency change in UHV | Sr frequency change in UHV | frequency change ratio (R) |
|---|---|---|---|
| 600°C | -0.061 Hz/s | -0.061Hz/s to -0.185 Hz/s | 0.33 to 0.37 |

### 4.1.1 Growth temperature

The stoichiometric samples in my Master's thesis [84], which only focussed on sample growth, were grown at a temperature of 600°C, but the dependence of the surface morphology on the growth temperature was not studied. Higher substrate temperatures during the growth of perovskite or brownmillerite thin films often leads to higher quality surface structure, with temperature as high as 1000°C for some films [85]. For $SrCoO_{2.5}$ the growth temperatures in literature range from 710°C to 900°C [40, 86, 87]. To determine which temperature leads to the best sample quality a sample series at three different growth temperatures, 850°C, 750°C, and 600°C was prepared (fig. 4.1).

For growth at 850°C, the sample surface is comprised of terraces of 20Å height with 550 Å deep holes in between, leading to a very high roughness of 186 Å. For 750°C, the sample is much smoother, with smaller holes of 200 Å and terraces of ∼12 Å height. The smoothest surface was achieved for a growth temperature of 600°C. The surface has a terrace structure without holes, similar to the pure substrate, characteristic for a high quality sample grown in the layer-by-layer mode. The step height is between 8-10 Å. Intensity oscillations of the specular spot in RHEED of a sample prepared at 600°C also indicate layer-by-layer growth (fig. 4.2 left). Initially, the oscillations are irregular, with a peak period of 2.6 min, 3.6 min, and 5.2 min. After that the oscillations have a constant period of 2.6 min. Comparing the oscillation period and growth time with the total thickness determined by XRR (inset in fig. 4.2 left) indicates a layer height of ∼9.5 Å per 2.6 min oscillation. This, coupled with a similar step height in AFM indicates that, after an initial period, half a unit cell ($c/2 = 7.87$ Å) of $SrCoO_{2.5}$ grows at a time. In the initial stage of growth, up to 11.7 min, the increasing time for each oscillation indicates that for very thin

**Table 4.2:** Roughness for samples grown at different temperatures for fig. 4.1

| Sample | Growth temperature [°C] | Roughness [Å] | Step height [Å] |
|---|---|---|---|
| S1 | 850 | 186 | ∼ 20 |
| S2 | 750 | 34 | ∼ 12 |
| S3 | 600 | 4 | 8 |

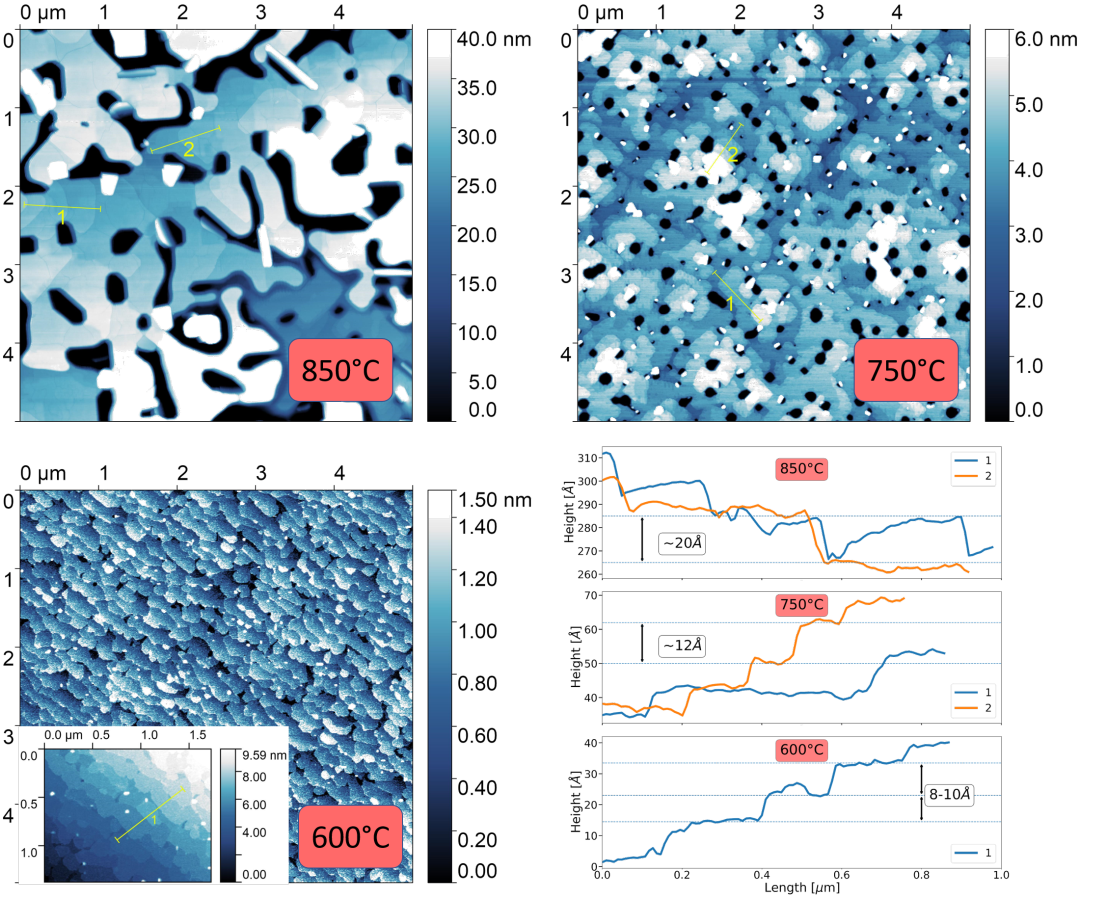

**Figure 4.1:** AFM images and height profiles for SrCoO$_{2.5}$/STO samples grown at different temperatures. All data was levelled by subtracting a plane background. The inset for 600°C shows a magnification of the measurement levelled by a single terrace.

films below 2.75 monolayer = 35.4 Å, the film forms a transition layer before settling into the constant half-monolayer growth. This could be caused by strain relaxation to an in-plane multi-domain state, as the *a* and *b* lattice constants of $SrCoO_{2.5}$ are not the same. Indeed, a TEM measurement of a different sample shows a very thin intermediate layer that continues the STO symmetry before the layer relaxes and a Moiré pattern becomes visible in the bulk of the film, indicating a multi-domain structure. A similar behaviour was found by Jo *et* al. in $SrFeO_{2.5}$ films on STO, with a thickness of the intermediate layer of a few nm [88].

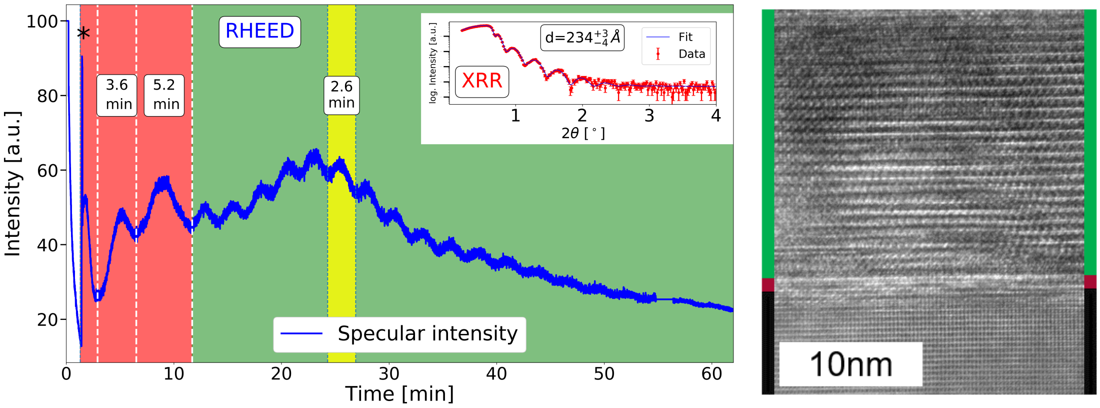

**Figure 4.2: Left:** RHEED intensity oscillations for sample S4 $SrCoO_{2.5}$/STO. The peak marked with '*' is due to an adjustment of the intensity, so as to not saturate the measurement. Initially, the oscillations are irregular (red area), with a period between 2.6 min and 5.2 min. After that the oscillations in the green region show a constant period of 2.6 min (example marked in yellow). The inset shows the corresponding XRR measurement and fit. **Right:** TEM image of sample S5 $SrCoO_{2.5}$/STO measured by J. Barthel. The first few monolayers (red) show a perovskite type structure similar to the substrate (black), with the bulk of the film (green) exhibiting a Moiré pattern indicating a multi-domain state. This matches the observations of the RHEED oscillations.

## 4.1.2 Stoichiometric issues

During the growth study it became apparent that the frequency change ratio, $R = \Delta f_{Co}/\Delta f_{Sr}$, with the individual frequency changes, $\Delta f_{Co}$ and $\Delta f_{Sr}$, for the Co and Sr cells, determined for stoichiometric samples was not stable. Initial samples prepared at $R$=0.36 or even lower $R$ (Sr richer) showed a large Co excess and rough surface with a large amount of particles (fig. 4.3).

A series of samples were grown to find the correct $R$ again, but even after achieving stoichiometric samples again for an adjusted ratio of $R$=0.26, follow-up samples again showed a different stoichiometry. Once the correct $R$ was found, the stoichiometry remained stable only until the MBE was opened to refill material or maintenance. After opening, the correct $R$ had to be found again from scratch. In fig. 4.4 the stoichiometry and $R$ is shown for the samples from my Master's thesis [84] and this thesis, indicating the large range of frequency change ratios that lead to

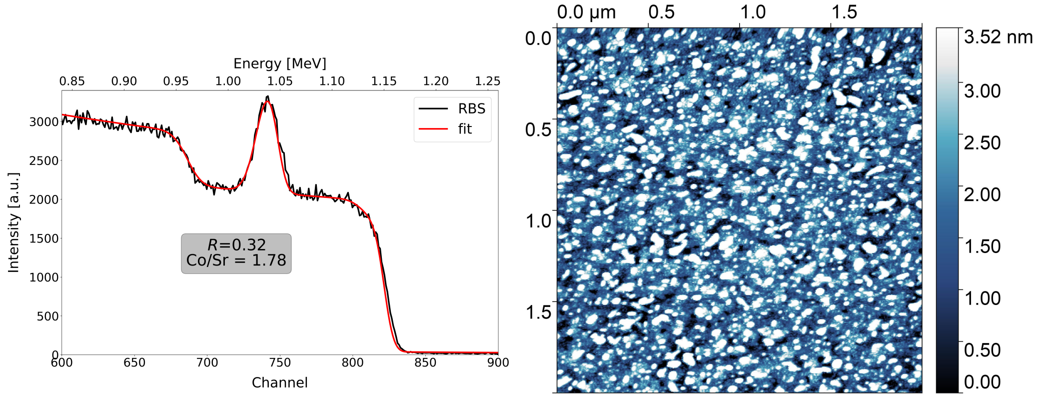

**Figure 4.3:** RBS and AFM measurements of sample S6 $SrCoO_{2.5}$/STO for $R$=0.32, showing a stoichiometry of Co/Sr=1.78 and a large amount of particles at the surface.

stoichiometric samples (green area).

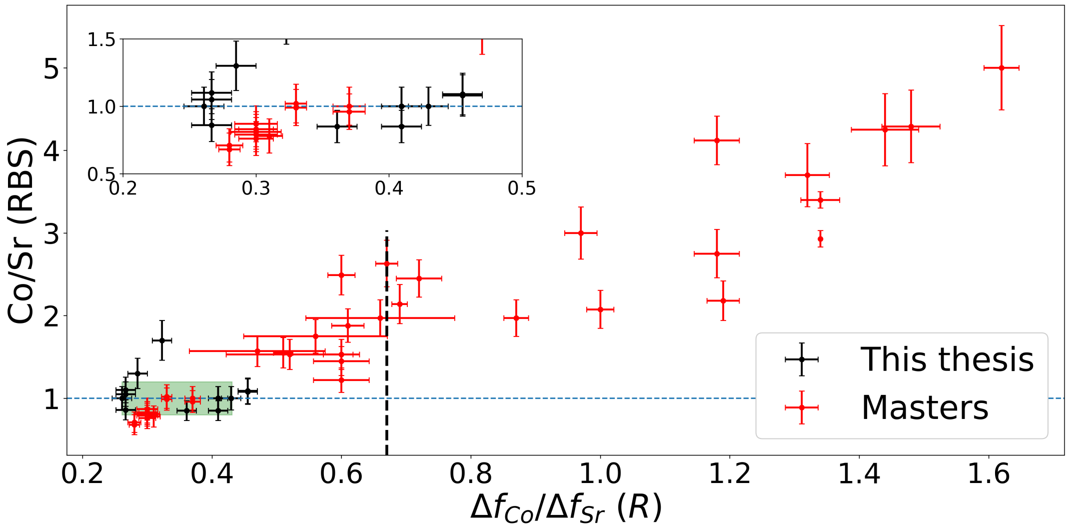

**Figure 4.4:** Co/Sr ratio measured by RBS for a given frequency change ratio from my Master's thesis [84] (red) and this thesis (black). The green region indicates the frequency change ratio for which 1:1 stoichiometric sample were grown. The theoretical frequency change, based on the mass ratio $\frac{\Delta f_{Co}}{\Delta f_{Sr}} = \frac{m_{Co}}{m_{Sr}} = 0.67$ for stoichiometric films is indicated by the black line. The inset show a magnified view of the 1:1 stoichiometry region.

The reason for the drastic change is probably oxidation of the Sr source material in the oxygen atmosphere during growth. Since the frequency changes are calibrated in UHV, the assumption is that the frequency change measured by the QCM is based on the mass of the pure elements, Sr and Co. While this assumption is valid for Co, which is hard to oxidise (hence the need for a plasma source), Sr oxidises at pressures as low as $10^{-7}$ mbar [89]. During the deposition the pressure reaches up to $\sim 8 \cdot 10^{-6}$ mbar. If the Sr source material oxidises partially or completely during deposition, subsequent samples with the same nominal growth rate would be Sr deficient as the calibrated frequency change would be based on SrO, not Sr. It

**Table 4.3:** Mean free path for SrO and Co at a pressure of $2{\cdot}10^{-6}$ mbar

| Molecule | Temperature | Molecular radius | mean free path |
|---|---|---|---|
| Co | 1400°C | 240 pm | 113 m |
| SrO | 550°C | 284(Sr) pm + 152(O) pm | 17 m |

was observed that the measured Sr frequency change is strongly dependent on the pressure, in the pressure range of deposition. Fig. 4.5 shows the Sr frequency change over a large pressure range and at deposition pressures. Initially a jump in the frequency change from -0.033 Hz/s to -0.039 Hz/s is observed, which is caused by the oxidation of Sr to SrO and related mass change on the QCM,

$$\Delta f_{SrO} = \frac{m_{SrO}}{m_{Sr}} \Delta f_{Sr} = 1.18 \cdot \Delta f_{Sr} \tag{4.1}$$

As the pressure increases above $10^{-6}$ mbar the frequency change drops below the initial value. In the bottom part of fig. 4.5, the pressure was increased step wise and a clear decrease in frequency change for each pressure step is evident. A similar effect was reported by Kim *et* al. [90] and is attributed to source oxidation.

To show that the decrease of the frequency change is not caused by a reduction on the mean free path due to the elevated pressure, this issue will be discussed further. The mean free path of atoms and molecules can be calculated by,

$$l = \frac{k_\mathrm{B} T}{\sqrt{2}\pi (2r)^2 p}, \tag{4.2}$$

with Boltzmann constant, $k_\mathrm{B}$, the molecular radius, $r$, and the pressure, $p$ [91]. Estimating the mean free path for Co and SrO, by taking the molecular radii as an approximation, reveals a value by one order of magnitude smaller value for SrO than for Co (see table 4.3). However, the mean free path for SrO is still far too large to explain the reduction in the SrO rate as seen in fig. 4.5.

Since this effect is strongly pressure dependent, calibrating the rates in UHV creates an additional uncertainty, as there can be small differences in pressure between depositions even if the same oxygen flow is used. For this reason, for the growth of later samples in Jülich, the rates were calibrated in oxygen atmosphere and with active plasma. This lead to a higher reproducibility in stoichiometry.

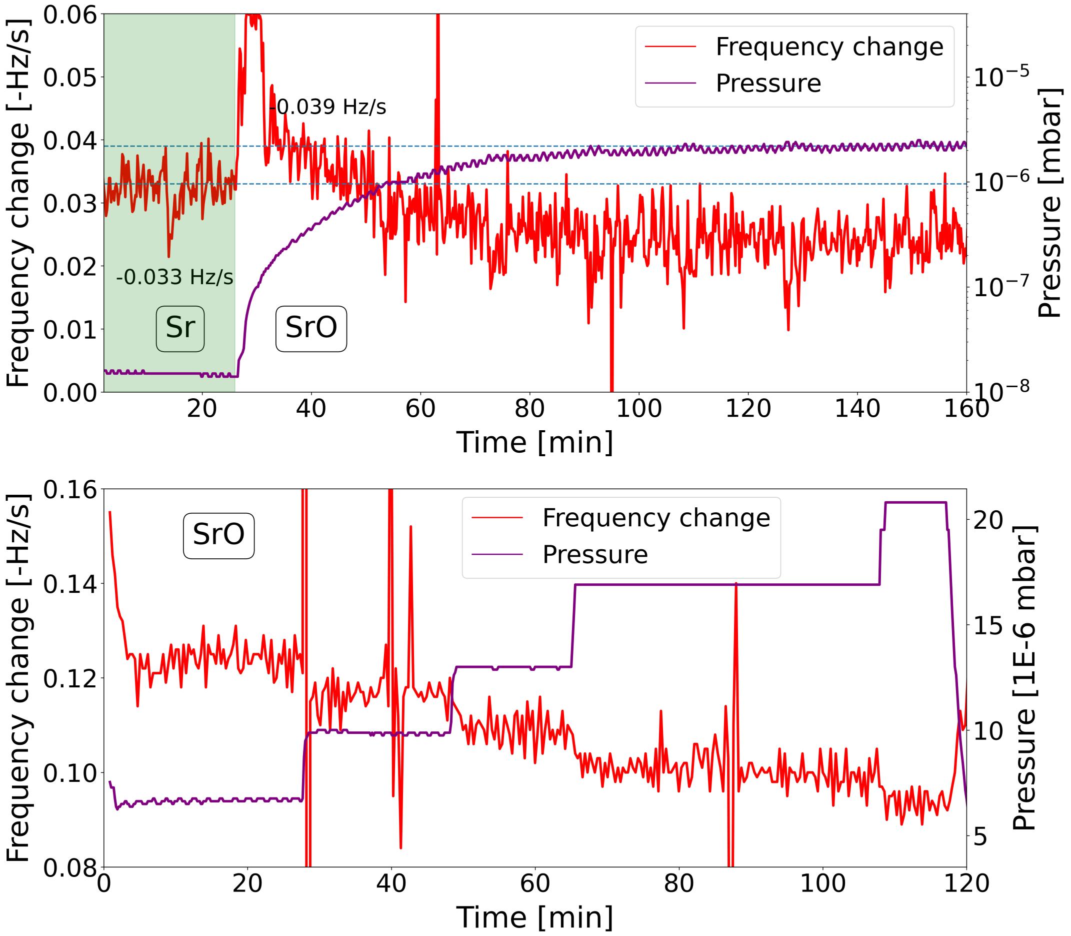

**Figure 4.5:** Sr/SrO frequency change for different pressure ranges. On the **top**, non-oxidised Sr (green area) is evaporated at initially low pressure. As soon as the pressure reaches ∼$10^{-7}$ mbar, the jump in the frequency change indicates oxidation to SrO. In the **bottom**, the pressure dependence in frequency change for SrO is clear.

### 4.1.3 Co/Sr evaluation by laboratory methods

Because of the unpredictable oxidation state of the Sr source material, the growth parameters for the films had to be constantly adjusted which is extremely time consuming, as only one sample can be grown per day, and the Co effusion cell needs one day to come up to the necessary temperature. Additionally, for RBS measurements, a sample series had to be sent to Jülich to be analysed. This meant that using RBS to determine the stoichiometry was not viable for quickly changing conditions. Therefore, a way to determine the stoichiometry with easily available methods had to be found. A series of samples was grown and characterized by a combination of RHEED, AFM, XRD, and XRR to determine the best method for evaluating the stoichiometry and quality. Large parts of the findings of this and the next section were published in [92] and are partially taken verbatim from the publication. The main contributor to publication [92] is the author of this thesis. The contributions include sample growth and all measurements shown here apart from RSM (not published), TEM, and RBS.

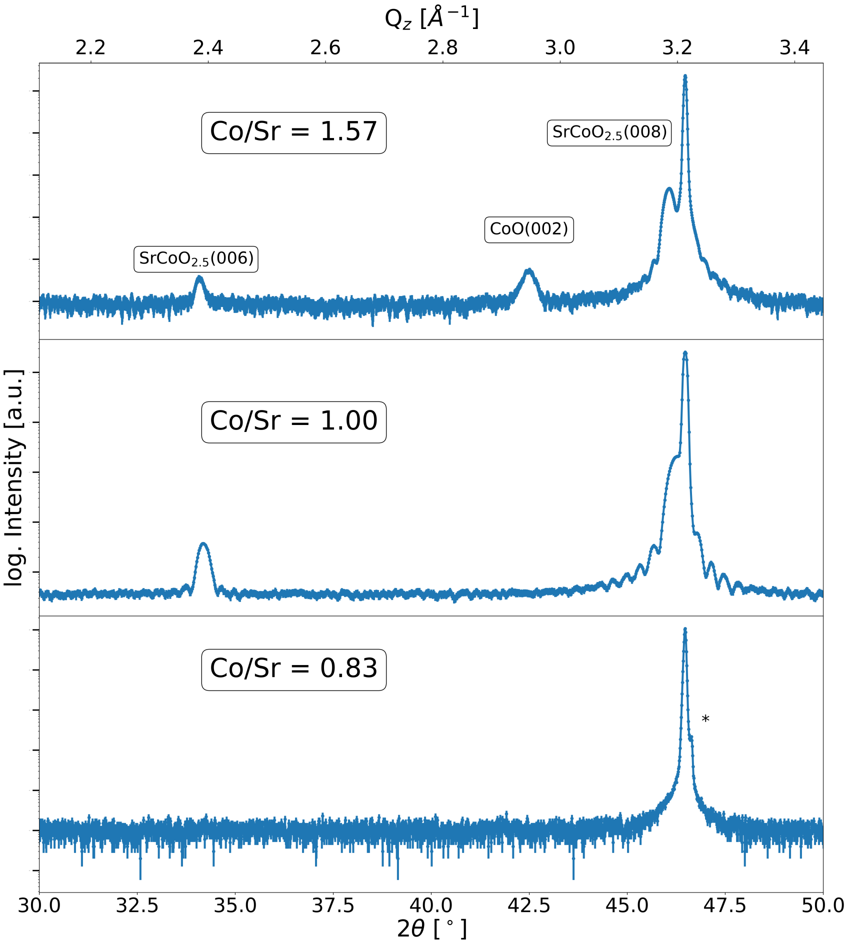

**Figure 4.6:** XRD $\theta - 2\theta$ patterns of $SrCoO_{2.5}$ films grown on $SrTiO_3(001)$ for various stoichiometries; **top** S7: Co/Sr=1.57 representative of Co excess, **middle** S3 Co/Sr=1.00 representative of ideal stoichiometry (XRR of the same sample in fig. 4.8), and **bottom** S8 Co/Sr= 0.83 representative of Co deficiency. The peak marked with $\star$ is due to a monochromator issue and not related to the sample.

A rough estimation of the stoichiometry can be made from the observed crystalline structure peaks in XRD measurements. Fig. 4.6 shows a sample with Co excess, a stoichiometric one, and a sample with Co deficiency. Stoichiometric samples reveal only peaks of the brownmillerite phase in *c*-axis orientation and are single phase. Assuming a constant unit cell volume equal to the bulk value, the calculated in-plane lattice constant of the film matches the substrate, indicating epitaxial growth. Reciprocal space maps confirm a coherently strained film (fig. 4.7). The in-plane lattice constants of the film are $a=5.53^{+0.01}_{-0.01}$ Å and $b=5.51^{+0.02}_{-0.01}$ Å, which matches the STO lattice constant multiplied by $\sqrt{2}$, as the the films grows in a $[110]_{\mathrm{film}}||[100]_{\mathrm{substrate}}$ orientation. The thickness of the crystalline layer, derived from the Laue oscillations, is 254±3 Å, which is slightly lower than the total film thickness of $292\,^{+2}_{-4}$ Å as determined by XRR from Kiessig fringes (fig. 4.8). For high Co excess of 57 % the brownmillerite structure peaks remain visible (fig. 4.6 top). A change in peak position towards lower angles indicates an in-plane compressive strain of 0.4 %. Additionally, CoO peaks exist in the diffraction pattern. The logical conclusion would be that the surplus Co is precipitated into CoO crystallites. Bulk stoichiometric $SrCoO_{3-\delta}$ is known to segregate easily into crystalline $Sr_6Co_5O_{15}$ and $Co_3O_4$ [93]. This is a strong indication that for Co excess, $CoO_x$ is easily formed. The thickness of the crystalline layer is 312±16 Å compared to 391±6 Å film thickness. In contrast, the Co deficient SCO film of 17% less Co does not reveal any crystalline structure at all (fig. 4.6 bottom).

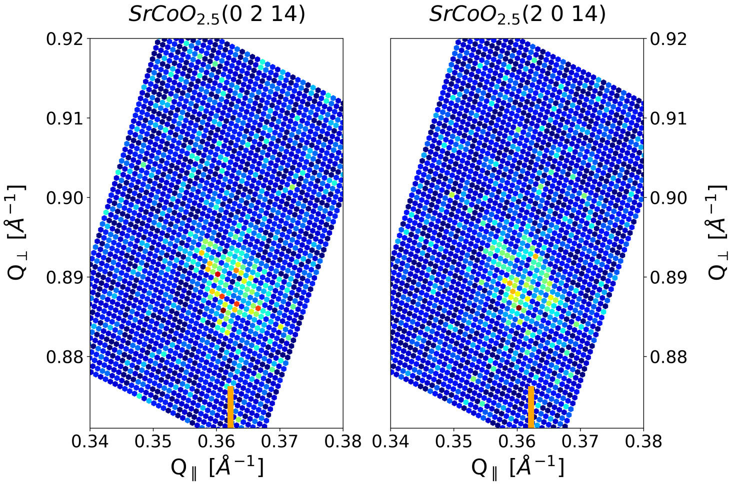

**Figure 4.7:** Reciprocal space map around the (0 2 14) and (2 0 14) Bragg reflexes of sample S9 SCO/STO. The film peaks have the same in-plane lattice constant as the substrate multiplied by $\sqrt{2}$ (indicated by the orange lines), showing a coherently strained film. Measurements taken by G. Mussler and A. Shkurmanov (PGI-9).

Thus, from the XRD measurements, samples with large Co excess or deficiency can be identified. However, small amounts of Co excess, below 10%, will not be identifiable as the CoO peak is not distinguishable from the background.

The existence of the CoO excess phase for a low level excess should still be observable by other techniques though. The MBE system is equipped with an *in-situ* RHEED

**Table 4.4:** Fit of the XRD and XRR measurements of sample S3 with Co/Sr=1.00 sample in figs. 4.8 and 4.6

| layer | thickness (XRD)[Å] | thickness (XRR) [Å] | roughness [Å] |
|---|---|---|---|
| Top layer | - | $5.5^{+4}_{-0}$ | $3.8^{+0.3}_{-0}$ |
| $SrCoO_{2.5}$ | $254^{+3}_{-3}$ | $292^{+2}_{-4}$ | $12^{+1}_{-1}$ |
| STO substrate | - | - | $2^{+3}_{-0}$ |

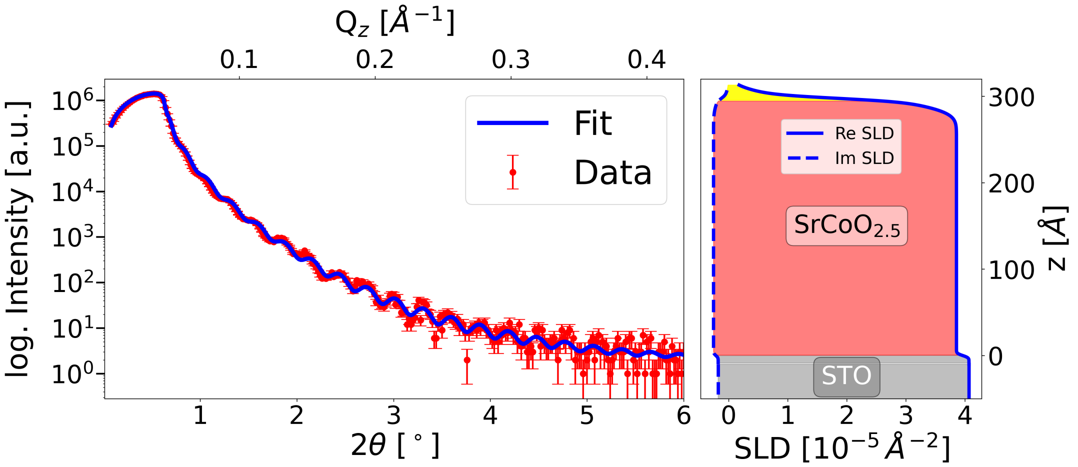

**Figure 4.8:** XRR measurement and scattering length density profile of sample S3 SCO/STO with Co/Sr =1.00. A small top layer with reduced SLD had to be assumed. (XRD of the same sample in fig. 4.6 middle).

setup, which can be used to study the film crystallinity during and after growth.

The RHEED pattern of the STO substrate is characterized by sharp Bragg reflexes, Laue rings, and Kikuchi lines, which confirm excellent crystallinity and low surface roughness (Fig. 4.9a). For stoichiometric samples, well defined Bragg spots and a Laue ring are visible, as well as faint indications of Kikuchi lines (Fig. 4.9b). The intensity of the specular spot shows oscillations during growth which is characteristic of layer-by-layer growth (Fig. 4.9b).

For large Co excess of 30%, two additional sets of spots emerge in the diffraction pattern indicating two distinct 3d structures. First, small and sharp speckles indicating a 3d structure with good crystallinity (Fig. 4.9c: A and in Fig. 4.11a) and second big, broad spots corresponding to small crystalline size (Fig. 4.9c: B). In contrast, for Co deficiency, here 22% (Fig. 4.9d), the RHEED pattern reveals only very faint Bragg spots and a washy Laue ring, indicating diminishing crystallinity.

To correlate the observed differences in RHEED patterns with the surface morphology, AFM was performed. The topography of the prepared $SrTiO_3(001)$ substrate is given in fig. 4.9a and reveals a terrace structure with step width of about 0.4 $\mu$m and 4 Å height, corresponding to the height of one unit cell of STO. The rms roughness is 4 Å. The stoichiometric sample exhibits terraces with a length of about 0.2 $\mu$m, height of 9 Å, which is close to half of a unit cell of SCO, and a rms roughness of 4.5 Å, fig. 4.9b. The topography is similar to PLD grown $SrCoO_{3-\gamma}$ thin films

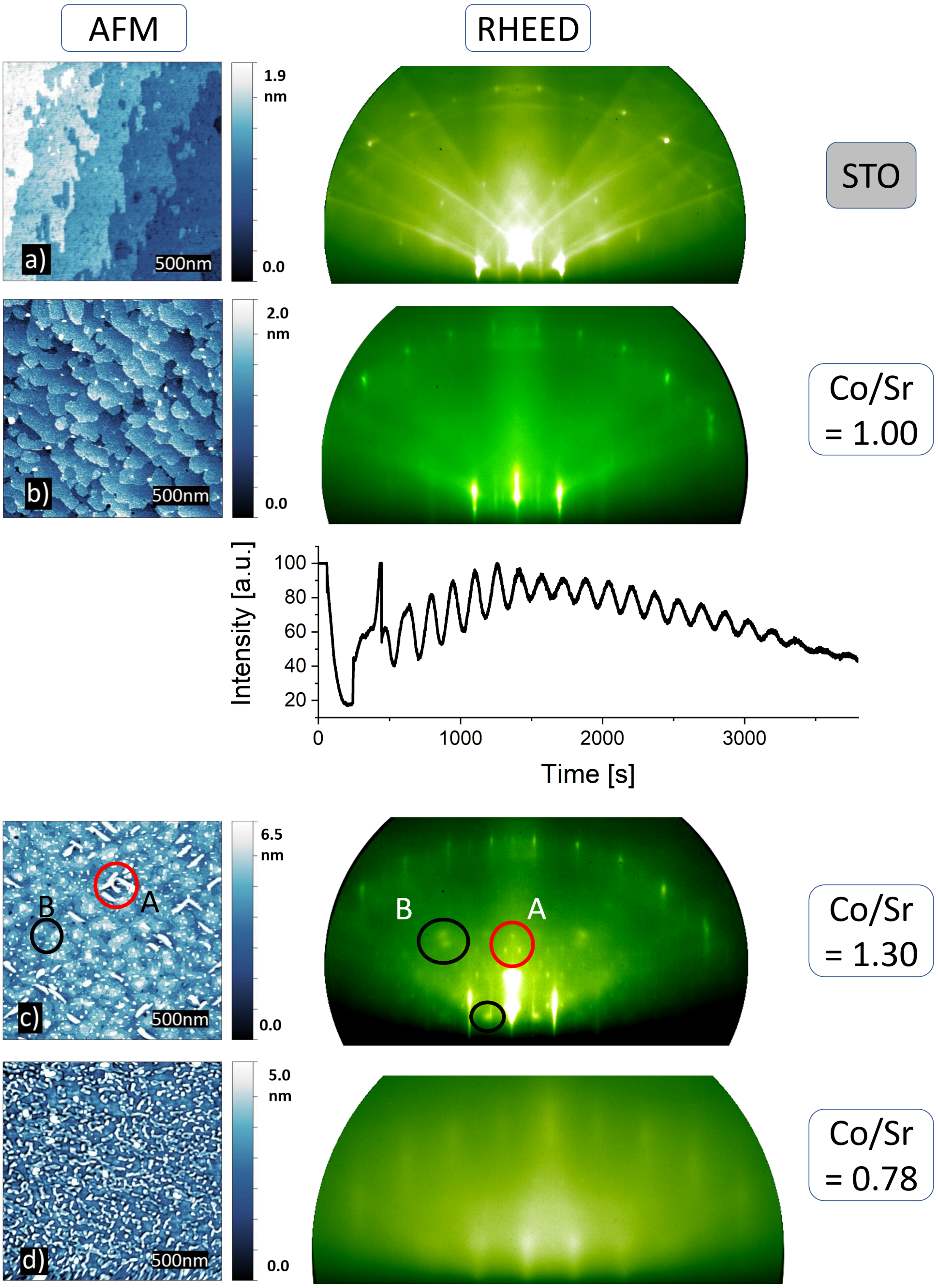

**Figure 4.9:** RHEED and AFM measurements of **a)** STO substrate, **b)** sample S3 with Co/Sr =1, showing a similar terrace structure to the substrate in AFM and well defined Laue ring ad Bragg spots in RHEED. The Co excess in sample S10 (Co/Sr = 1.3) in **c)** has two distinct precipitates in the AFM (big 'A' and small 'B') which correspond to the speckles and spots in RHEED. For Co deficiency (sample S11: Co/Sr=0.78) in **d)** the layer is amorphous.

reported by Hu et al. [94].

Increasing the Co excess destroys the terrace structure, fig. 4.9c. Instead, a combined layer and island growth is visible, with additional small horizontal and vertical structures of an average length of 500 Å, and diagonal structures of an average length of 0.163 $\mu$m and width of 600 Å. These 3d structures cover about 15% of the surface area. Evidently, the diagonal structures in the AFM image are related to the emergence of the small speckles in the RHEED image (Fig. 4.9(c): A) while the small horizontal structures detected by AFM correlate to the broad spots in RHEED. As the films are much less uniform, the rms roughness is increased to 14 Å. Neglecting these additional structures, the rms roughness of the underlying film is 8 Å which is still higher than for the stoichiometric sample. We may conclude that these diagonal structures in the AFM topograph are CoO islands, as confirmed by TEM-EDX below. Conversely, for SCO thin films with Co deficit neither terraces nor layered island structures are observed, fig. 4.9c. The surface is diffuse, with worm-like structures of 430 Å width and high rms roughness of 15 Å.

For a comprehensive picture of the island structures detected by AFM, a SCO thin film with about 15% Co excess was studied by TEM and EDX. Fig. 4.10 shows a cross-sectional lamella of the SCO film in the STO[110] direction (this is the diagonal direction in the AFM images). The lamella was taken from an area that exhibited a large number of the diagonal structures observed in AFM and was identified by EDX as CoO. Growth of CoO precipitates is observed on the substrate as well as within the film. The TEM images further confirm an epitaxial film on the substrate, with a mismatch of the in-pane lattice constants of only 0.1%. The c-axis is out-of-plane, as previously measured by XRD. As discussed in sections 4.1.1, the film has a possible in-plane multi-domain state, due to strain relaxation, as there is a visible Moiré pattern in the TEM image.

### 4.1.4 Stoichiometric control by RHEED

On approaching the 1:1 stoichiometry of Co and Sr from Co excess the CoO(002) peak of the thin film vanishes in the XRD pattern before the perfect stoichiometry is reached. Fig. 4.11c gives a comparison of XRD patterns for 12% Co excess and perfect stoichiometry. For both stoichiometries no CoO peak is visible within the detection limit of the XRD instrument. In contrast, comparing the RHEED patterns of the perfect sample (fig. 4.9b) to the ones with 12% Co excess (fig. 4.11a) and 30% Co excess (fig. 4.9c), there are clear differences: In the RHEED pattern of the sample with Co/Sr=1.3 there are two types of reflexes present that don't originate from the brownmillerite $SrCoO_{2.5}$ structure: small and sharp speckles, labelled 'A'; and broad spots 'B'. The broad spots are completely absent for Co/Sr=1.12 (Fig. 4.11a). The existence of the broad spots is correlated with large Co excess (Co/Sr$\geq$ 1.3). If these spots are missing and only the sharp, small speckles are present, the stoichiometry is closer to 1. But even for small Co excess, here Co/Sr=1.12, the speckles are clearly visible. Only for the perfectly stoichiometric samples the speckles have disappeared (fig. 4.9b). Hence, the RHEED pattern is still correlated with the stoichiometry

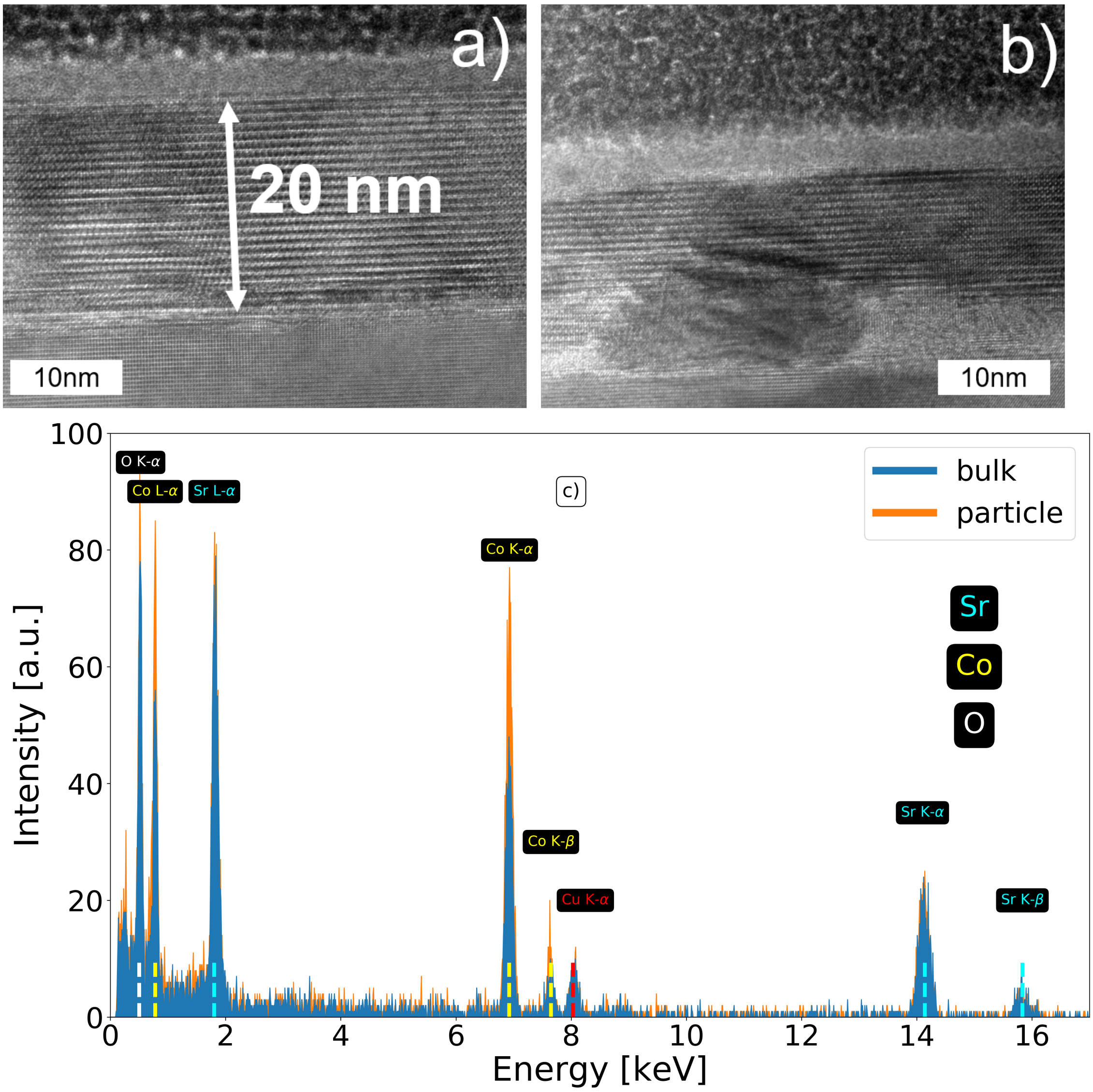

**Figure 4.10:** TEM images of sample S5 with Co excess of about 15%, showing **a)** crystalline part of the film and **b)** a CoO particle within the film, and **c)** EDX spectra showing the stoichiometry of a point in the sample and one on a particle. Images a) and b) adapted from [92]. Measurements performed by J. Barthel (ER-C-2).

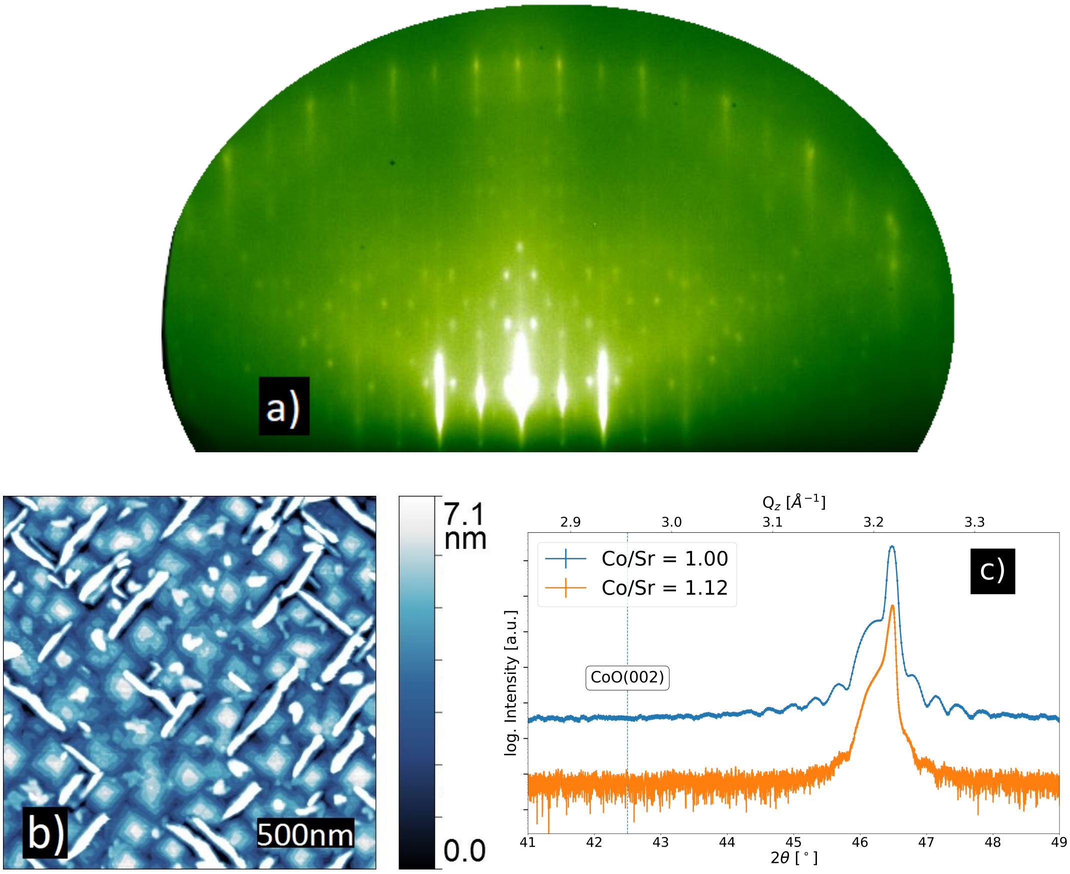

**Figure 4.11:** Measurements of sample S12 $SrCoO_{2.5}$ with Co/Sr=1.12, a) RHEED at 15 keV and with $< 110 >$ azimuth and b) AFM topography. c) comparison of XRD measurements for thin films with stoichiometries Co/Sr=1.12, and Co/Sr=1.00 revealing an absence of the CoO(002) peak for both samples. The data for Co/Sr=1.12 were multiplied with a factor of 100 for clarity. Figure adapted from [92].

while XRD becomes insensitive.

Obviously, the speckles for the film with Co/Sr=1.12 are related to the elongated CoO islands in the AFM topography and TEM images (fig. 4.11b and 4.10b). On the other hand the RHEED pattern of the Co deficient film (fig. 4.9d) exhibits worse crystallinity than for the other stoichiometries, which is also mirrored in the disappearance of the SCO film peaks in the XRD (fig. 4.6c) and no observable island or terrace structures on the AFM image (fig. 4.9c).

Analysing the evolution of the RHEED patterns with varying Co/Sr stoichiometry, it turns out that this method is superior to XRD to determine the crystallinity and the associated stoichiometry. In the following, this way of using RHEED to determine the exact frequency change ratio for stoichiometric films was used to determine that the films were grown in the correct stoichiometry and to adjust the growth rates upon deviation.

## 4.2 Changing the oxygen content by annealing

To find the correct method for the topotactic transition of the $SrCoO_{2.5}$ film to $SrCoO_3$, two different methods were investigated, *in-situ* oxygen plasma annealing and annealing in a tube furnace with oxygen flow.

### *In-situ* plasma annealing

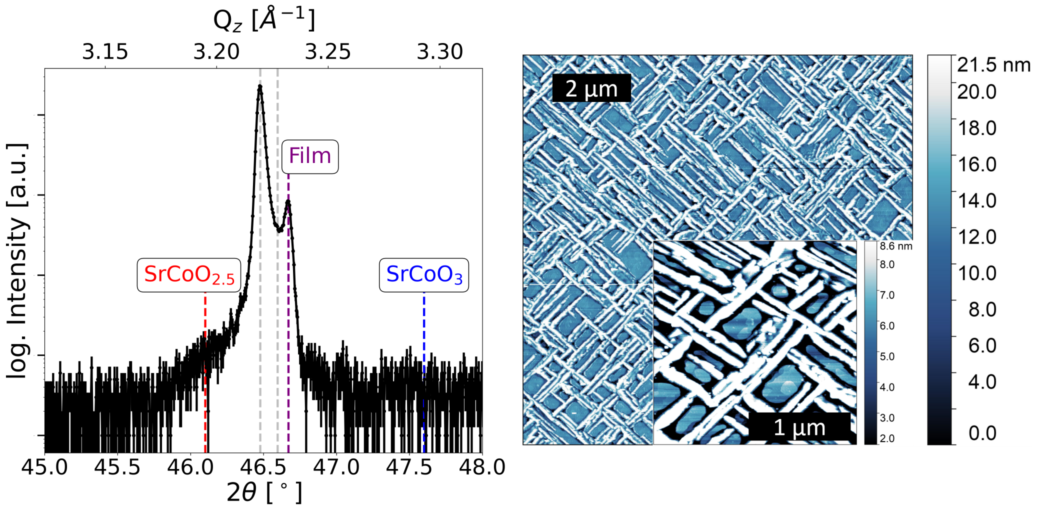

**Figure 4.12:** XRD (**left**) and AFM (**right**) of a sample S13 $SrCoO_{2.5}$/STO, annealed in oxygen plasma at 600°C for 11 h. The purple line indicates the film peak after annealing, the red line the $SrCoO_{2.5}$(008) peak of the virgin sample, and the red line, the $SrCoO_3$(002) peak position. To verify that this peak is actually caused by the film, the two grey lines in the XRD mark the STO(002) peak originating from the Cu-$K_{\alpha 1}$ radiation and the absence of a Cu-$K_{\alpha 2}$ peak. The AFM shows a large amount of diagonal structures and a high surface roughness. The inset shows a magnified view of the measurement.

As a first try to transform the sample into the perovskite structure, a sample grown on STO was kept at the deposition temperature of 600°C in oxygen plasma for 11 h directly after growth in the MBE system. Fig. 4.12 shows the XRD measurement after annealing: The brownmillerite peak is only faintly visible and a peak just to the right of the substrate indicates a partial transformation to $SrCoO_3$. The possibility of this peak being caused by a monochromator misalignment can be excluded, as it is not at the Cu-$K_{\alpha 2}$ STO(002) Bragg peak position. Since the film peak is closer to the brownmillerite than the perovskite position, the transformation was not very successful. The film peak is at lower angle than the $SrCoO_{2.75}$(002) peak, indicating that the sample would not be ferromagnetic. The transformation could possibly be progressed further by increasing the annealing time or temperature, but the AFM measurement in fig. 4.12 reveals a very rough surface with $R_{RMS}$=65.4 Å and long diagonal structures, indicating that the surface gets severely deteriorated by the long exposure to the plasma and high temperature. Since the plasma treatment could not successfully transform the film to $SrCoO_3$ and increased the surface roughness significantly, it is not considered a suitable way to oxidise the films.

### Annealing in a tube furnace

To find a way of transforming the films to $SrCoO_3$ in a non-destructive manner, samples on STO and LSAT were annealed in a tube furnace with 50 ml/min oxygen flow at different temperatures. The samples were heated to, and cooled from, the annealing temperature over 90 min. Once the samples were back at room temperature, the crystalline structure was measured by XRD (fig. 4.13).

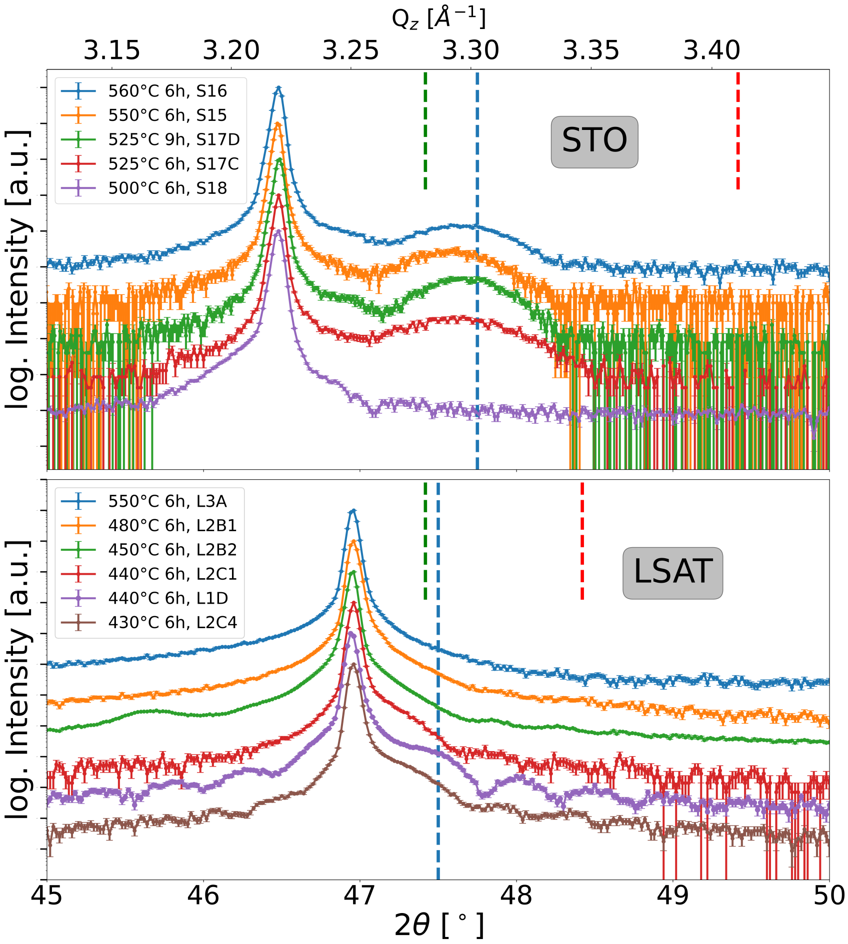

**Figure 4.13:** XRD measurements of $SrCoO_{2.5-3}$/STO (**top**) and $SrCoO_{2.5-3}$/LSAT (**bottom**) samples after annealing at different temperatures in a tube furnace with 50 ml/min $O_2$ flow. The dashed lines indicates the observed (blue), bulk (green) and fully epitaxial strained (red) $SrCoO_3(002)$ peak positions. The sample number is given in the plot label.

For films on STO, the perovskite phase was observable for annealing temperatures between 525°C and 560°C and heating time of 6-9 h. The $SrCoO_3(002)$ peak is close to the fully relaxed position and relatively broad, indicating a nearly relaxed layer. The full range XRD measurement shows no indications of brownmillerite peaks in the annealed sample (fig. 4.14)

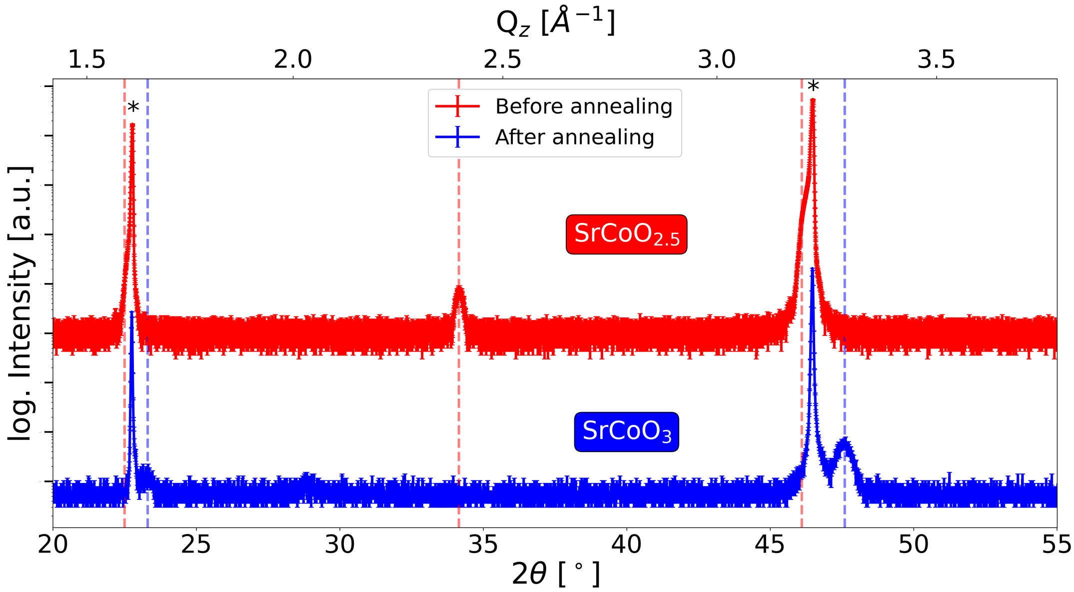

**Figure 4.14:** X-ray diffraction measurement of sample S15 $SrCoO_{2.5}$/STO before (red), directly after (blue) annealing at 550°C for 6 h, showing the transition from brownmillerite to perovskite structure. The dashed lines indicate the Bragg peak positions for $SrCoO_{2.5}$(00i) (red, i=4,6,8) and $SrCoO_3$(ooj) (blue, j=1,2). The STO(001) and STO(002) peaks are marked with a star.

Samples on LSAT, using the same temperature as for STO led to an amorphous film (fig. 4.13). Since the brownmillerite peak is also absent, a suitable annealing temperature for LSAT has to be lower than for STO. Indeed, only for films annealed at 440°C for 6 h, a clear perovskite peak with Laue oscillations is observable. For even a small temperature deviation of 10°C the perovskite structure quality is strongly reduced.

To systematically investigate the changes due to the annealing and the stability of the perovskite phase, sample L1 was studied in detail. X-ray and electron diffraction measurements were taken before the annealing. The sample was then annealed at 440°C for 6 h and broken into 3 pieces. The pieces were analysed simultaneously by XRD, SQUID and PPMS without delay, so that one may assume that the oxygen content is the same for all measurements. Before growth, the sample showed excellent crystallinity in XRD, LEED and RHEED (fig. 4.15) and is perfectly stoichiometric, according to the evaluation of the RHEED measurement outlined in section 4.1.4.

The XRR measurements before and after (tab. 4.5 and fig. 4.16) show the same thickness within the uncertainty, as well as a thin top layer with reduced SLD. The thickness of the crystalline layer, derived from Laue oscillations around the $SrCoO_{2.5}$(002) and (008) Bragg peaks, before annealing is only 8 Å lower than the total layer thickness, signifying an excellent crystallinity of 96 %. After the annealing, the brownmillerite structure is gone and the $SrCoO_3$(002) Bragg peak is

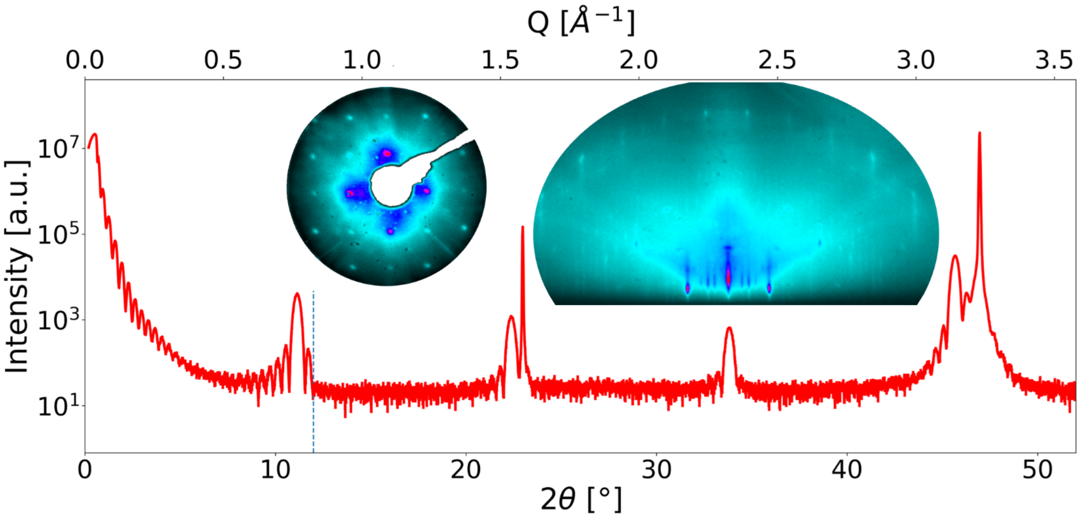

**Figure 4.15:** Full range $\theta - 2\theta$ X-ray scan, LEED at 150eV and RHEED of sample L1 $SrCoO_{2.5}$/LSAT showing an excellent bulk and surface crystallinity and a Co/Sr=1 stoichiometry. The dashed line indicates where the XRR and XRD measurements were joined.

prominent, with clear Laue oscillations. The total layer thickness stays the same within the uncertainty, with a rougher top layer. The calculated crystalline thickness even exceeds the total thickness. This is obviously not possible, so the XRD measurement might overestimate the thickness of the crystalline layer. Nevertheless, this means that the perovskite structure is completely formed with excellent crystalline quality.

To test the stability of the perovskite structure, the sample was kept in a vacuum chamber, installed at the X-ray reflectometer, pumped down to $7{\cdot}10^{-5}$ mbar. XRD $\theta - 2\theta$ scans around the $SrCoO_3(002)$ Bragg peak were then measured between 44° and 50°. To get good statistics, one measurement was taken within 100 min. Fig. 4.17-top shows that there was no change in peak position, intensity, or Laue oscillations within 43 h, indicating that the perovskite structure is stable in vacuum. After the measurement, the sample was exposed to ambient air (fig. 4.17 bottom). The same 100 min $\theta - 2\theta$ loops were taken in air, but unfortunately, after 2 loops the instrument got misalignment, corrupting the measurement. Nevertheless, the XRD after 45 h shows a complete re-transformation to the brownmillerite structure. This re-transformation will be investigated in the next sections in more detail.

**Table 4.5:** Fit of the XRD and XRR measurements of L1 $SrCoO_{2.5/3}$/LSAT (fig. 4.16). ⋆ The thickness determined by XRD after annealing is likely overestimated, as it exceeds the total layer thickness measured with XRR.

**Before annealing**

| layer | thickness (XRD) [Å] | thickness (XRR) [Å] | roughness [Å] |
|---|---|---|---|
| Top | - | $15^{+2}_{-1}$ | $3.8^{+0.2}_{-0.00002}$ |
| $SrCoO_{2.5}$ | $214^{+3}_{-3}$ | $222^{+2}_{-4}$ | $3^{+2}_{-0.0002}$ |
| LSAT | - | - | $6^{+1}_{-2}$ |

**After annealing**

| layer | thickness (XRD) [Å] | thickness (XRR) [Å] | roughness [Å] |
|---|---|---|---|
| Top | - | $14^{+2}_{-2}$ | $8^{+2}_{-1}$ |
| $SrCoO_3$ | $249^{+3}_{-3}(\star)$ | $223.5^{+0.9}_{-0.8}$ | $3.00^{+0.04}_{-0.0002}$ |
| LSAT | - | - | $2^{+1}_{-0}$ |

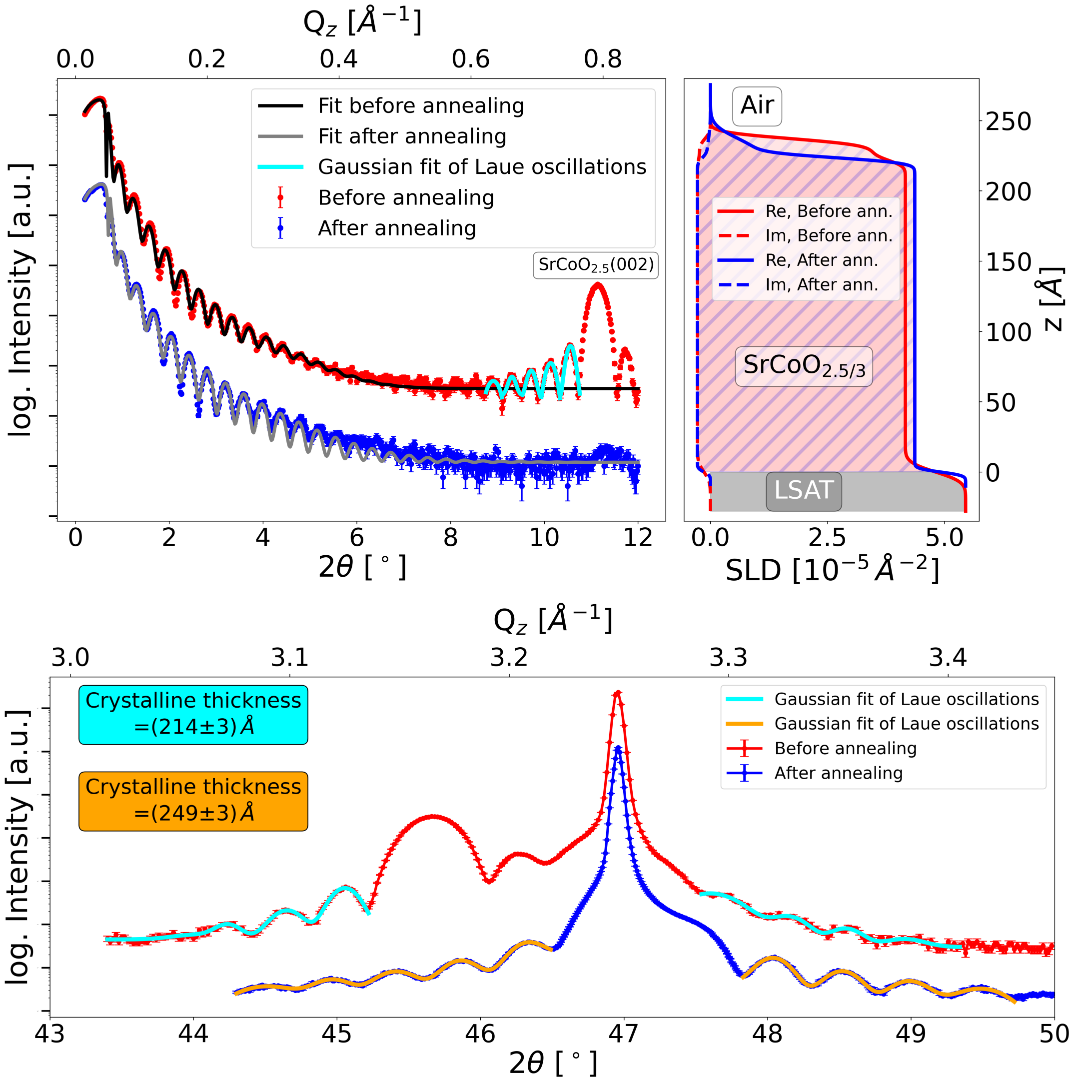

**Figure 4.16:** XRR and XRD measurements and fits of sample L1 $SrCoO_{2.5/3}$/LSAT, before and after annealing. The comparison shows a perfect transition from brownmillerite to perovskite structure. The XRD measurement after annealing is a sum of the individual measurements in fig. 4.17 top.

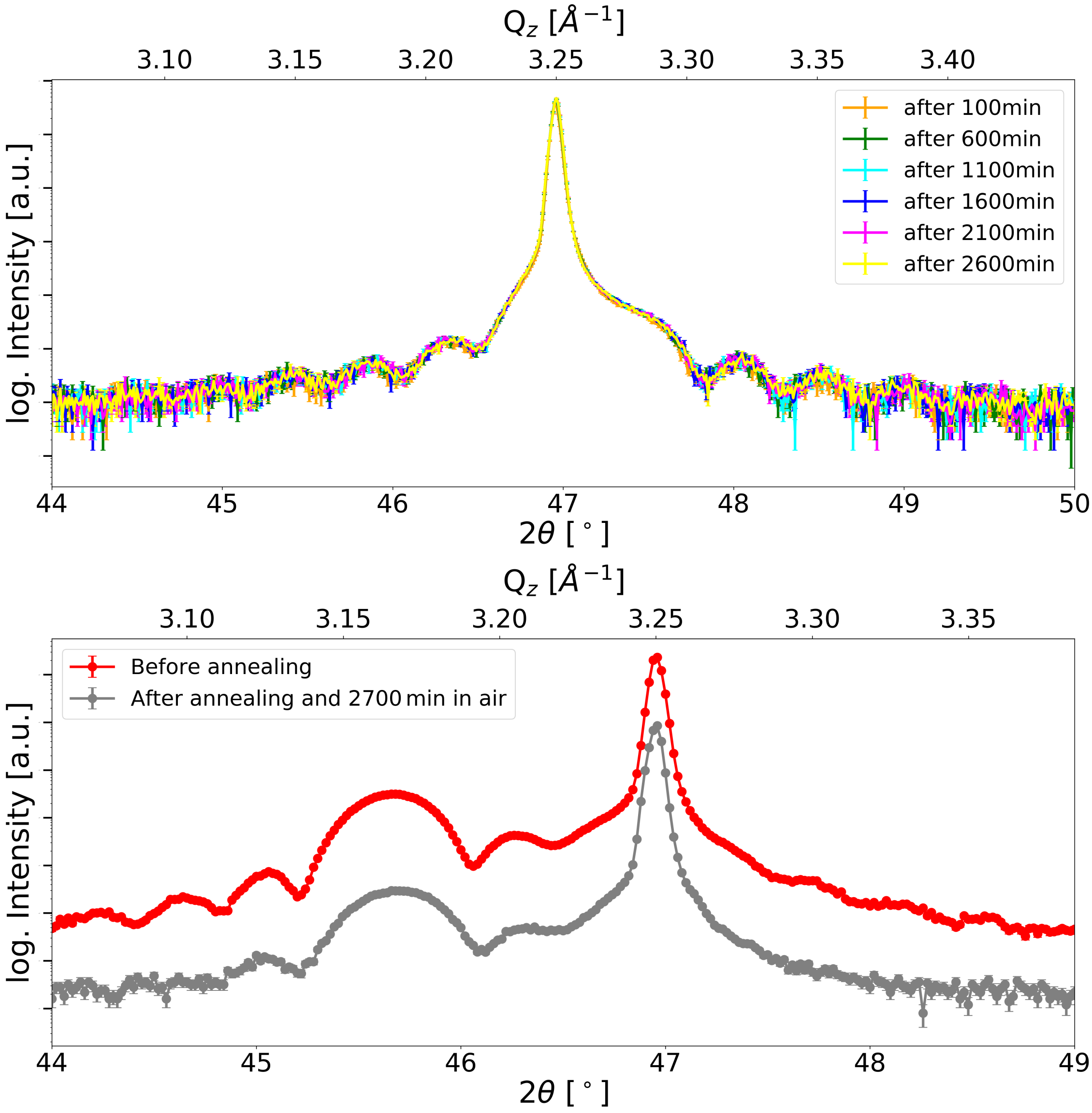

**Figure 4.17:** XRD measurements of L1 $SrCoO_3$/LSAT. **Top:** In vacuum taken in loops of 100 min showing no change in crystallinity. Every fifth loop is shown. **Bottom:** Before annealing and after 2700 min in air (after exposure to vacuum for 2600 min).

## 4.3 Magnetic and conductive properties of annealed samples

Xie *et* al. showed that in polycrystalline $\mathrm{SrCoO}_{3-\delta}$ samples a magnetic phase separation can occur for $\delta \neq 0$ [95]. They identify a transition temperature of 280 K with the $\mathrm{SrCoO}_3$ phase, 220 K with $\mathrm{SrCoO}_{2.88}$, and 160 K with $\mathrm{SrCoO}_{2.75}$ and found all three phases in samples with $\delta$>0.12.

Field-cooled SQUID measurements in the MPMS of $\mathrm{SrCoO}_{3-\delta}$/STO samples show ferromagnetic behaviour with three transition temperatures around 170 K, 219 K, and 296 K (fig. 4.18 left). The bulk Curie temperature of $\mathrm{SrCoO}_3$ without oxygen deficiencies is 280 K - 302 K [96], therefore the measurements were started at 350 K. Beforehand, the sample was annealed in oxygen. The different transition temperatures indicate a partial de-oxidization of the film creating regions of different oxygen stoichiometry, either during the cooling process in the SQUID, or between annealing and measurement. Since the transitions observed by Xie *et* al. are present here as well, it stands to reason that a similar separation occurs in our sample.

The saturation magnetisation of the sample is very low, about 0.04 $\mu_B$/Co at 75 K (fig. 4.18 right). Gu *et* al. report a variable saturation magnetisation depending on epitaxial strain, with 0.86 $\mu_B$/Co for thin films on STO and 2.1 $\mu_B$/Co for LSAT [40], which is both lower than the bulk value of 2.5 $\mu_B$/Co. They correlate a saturation magnetisation of 0.86 $\mu_B$/Co with an oxygen content of $\mathrm{SrCoO}_{2.835}$.

The SCO thin film on LSAT exhibits a similar separation of magnetic phases, with clear maxima in the zero-field-cooled (ZFC) measurement at 172 K, 220 K, and 274 K (fig. 4.19 top-left). Since the sample is oxygen deficient, there could be a part of the sample in the brownmillerite structure and thus have an antiferromagnetic contribution which could induce an exchange bias in the ferromagnetic part of the film. To test this, the sample was field-cooled at 3 T and hysteresis loops were measured (fig. 4.19 top-right). At 10 K an exchange bias field of 0.05 T was observed and 0.03 T at 100 K. This confirms that a sizeable part of the sample has an oxygen deficiency of $\delta$>0.25, turning it antiferromagnetic which also explains the reduced magnetic signal of the SCO films compared to literature values.

The resistivity, $\rho$, of the film shows an insulating behaviour, which can be fit below 200 K with a modified Arrhenius law

$$\rho = \rho_0 \mathrm{e}^{(E_a/2k_\mathrm{B}T)^b}, \tag{4.3}$$

with an activation energy, $E_a$, of 1.87±0.03 eV and $b$=0.25, but still has a relatively low resistivity. The exponential factor $b$ is used to describe variable range hopping transport for very low temperatures, which is not the case here, but a fit with the typical Arrhenius law (b=1) did not result in a good agreement. Such deviations are not uncommon in disordered systems such as in the case of oxygen vacancies here [97]. The behaviour is similar to polychrstalline $\mathrm{SrCoO}_{2.7}$ and $\mathrm{SrCoO}_{2.8}$ samples in [38].

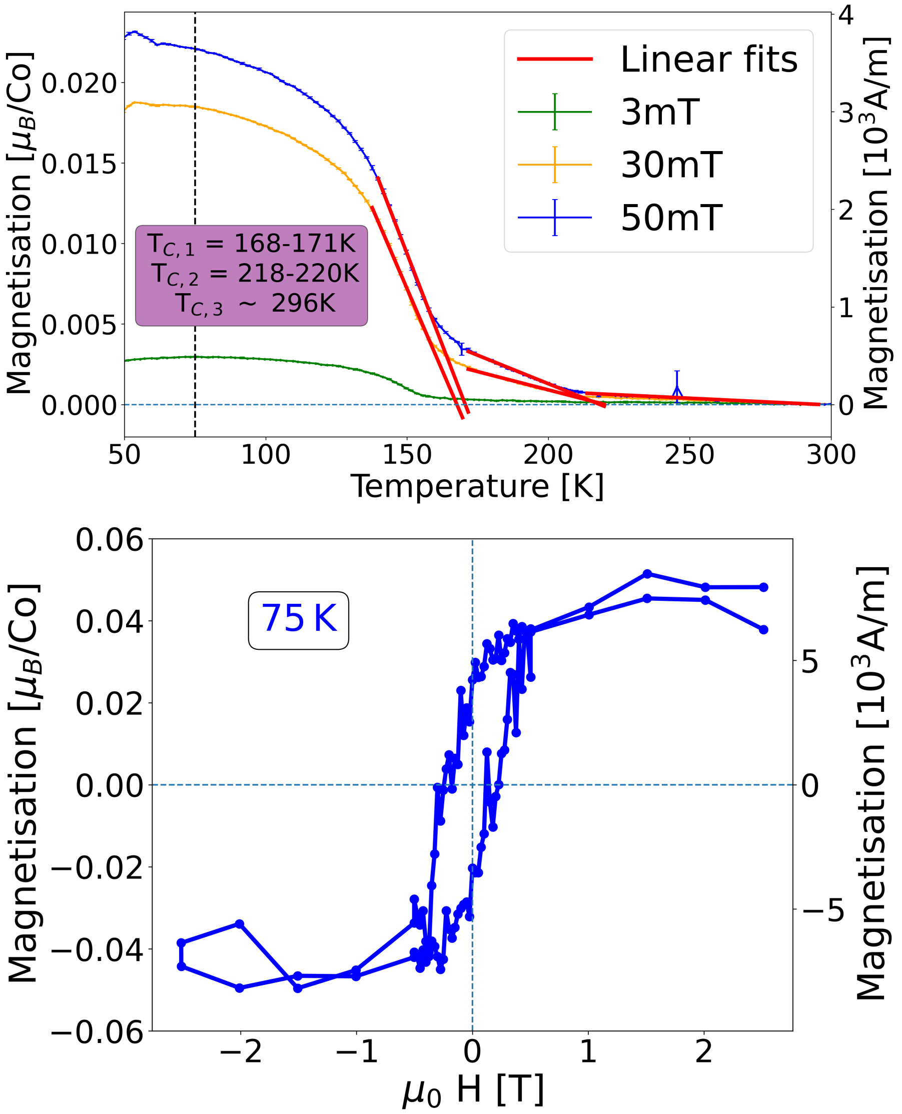

**Figure 4.18: Top:** Field-cooled magnetisation measurements of sample S14 $SrCoO_{3-\delta}$/STO, after annealing. Three regions with different slopes can be identified, probably corresponding to three magnetic phases in the sample. There was an experimental problem below 50 K, which lead to unreliable data below 50 K, hence the data are not shown. **Bottom:** Hysteresis loop of sample S14 $SrCoO_{3-\delta}$/STO, after annealing, measured at 75 K (indicated by the dashed black line in the left).

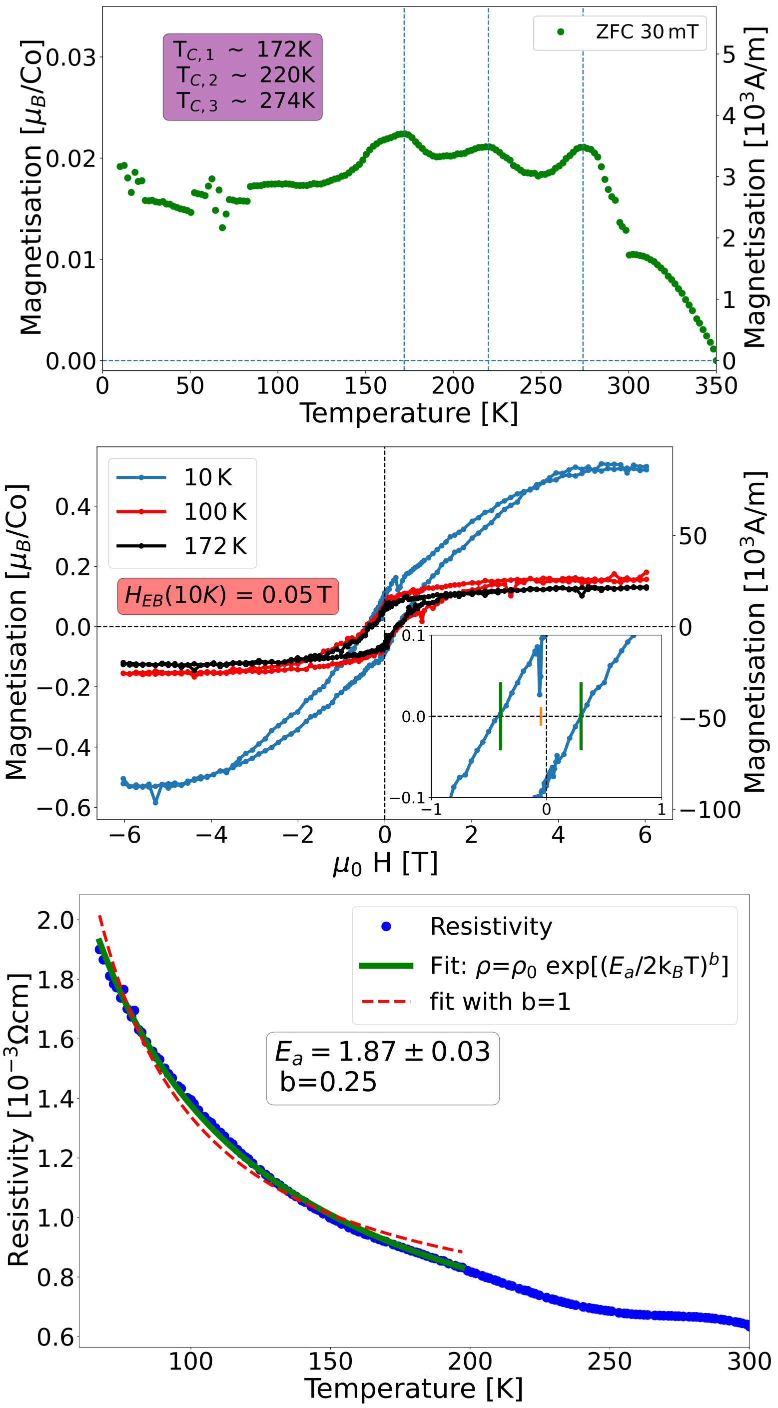

**Figure 4.19: Top:** Zero-field-cooled magnetisation measurements after annealing. There are three magnetic phases present, as indicated by the peaks in the measurement. **Middle:** Hysteresis loops after field cooling in 3 T. The inset shows the exchange bias effect. The green lines indicate the coercive fields and the orange line the exchange bias field. **Bottom:** Resistivity measurement of sample L1 $SrCoO_{2.5}$/LSAT after annealing. All measurements are of sample L1 $SrCoO_{3-\delta}$/LSAT.

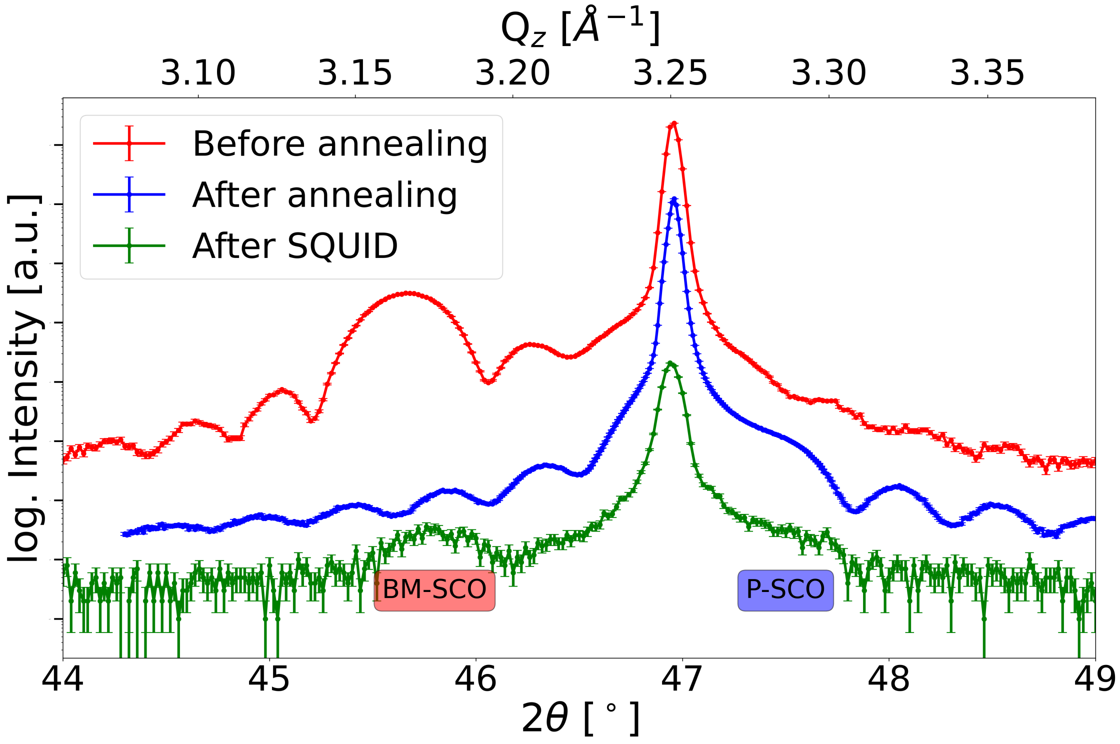

**Figure 4.20:** Comparison of XRD measurements for the part of sample L1 $SrCoO_{3-\delta}$/LSAT measured in SQUID to the pure brownmillerite and perovskite phase.

Both, magnetisation and resistivity, indicate a quick oxygen loss of the sample after annealing, as oxygen deficient phases are present in both measurements. An XRD measurement taken shortly after the SQUID measurement confirms that the sample consists of a mixture of brownmillerite and perovskite phase (fig. 4.20). This means that the sample is not stable in the He atmosphere of the SQUID. This is surprising given that the oxygen content in the SQUID is very low. If there were an oxygen contamination present in the SQUID, the antiferromagnetic to paramagnetic transition of oxygen would be visible at ∼43 K, which is not the case in the measurement [98]. Another difference between the conditions in SQUID and vacuum XRD is that in SQUID the sample was measured up to a temperature of 350 K, whereas in XRD it as kept at ∼300 K. In literature, a perovskite to brownmillerite transition was shown to occur in vacuum between 398 K and 533 K depending on the substrate [94]. If the sample lost oxygen during the short time it was heated to 350 K, this would explain the partial transition to the brownmillerite phase.

For a deeper understanding of the process of oxygen loss, another sample was annealed in $O_2$ and $\theta - 2\theta$ loops were measured in air. The intensity map was constructed from the XRD loops (fig. 4.21). In the initial ∼10 h it shows the shift of the $SrCoO_3$(002) peak from the right of the substrate peak towards lower angles. After only ∼3 h, the peak has been shifted to the bulk theoretical position for $SrCoO_{2.75}$, which is the lowest oxidation state with ferromagnetic character. Between 10 h and 30 h, the perovskite peak gradually loses intensity and vanishes. At 10 h, the $SrCoO_{2.5}$(008) peak emerges at slightly higher angle than in the as-grown sample and shifts slowly to the same position as before annealing.

Calculating the out-of-plane lattice constant of the perovskite phase from the $SrCoO_3$(002) peak at 47.4° reveals that, initially, the film is completely relaxed, with c=3.83 Å, though as the film peak is merging with the substrate peak, determining the exact peak position is difficult. The peak shifts by about -0.7° which means the c-axis elongates to c=3.89 Å. The $SrCoO_{2.5}$(008) peak appears at 45.67° and shifts only slightly to 45.65°, meaning the out-of-plane lattice constant is c/4=3.968 Å-3.970 Å.

To summarize, the perovskite phase is very unstable, with oxygen loss nearly immediately after exposing the film to air. The film is completely transformed back to the brownmillerite phase after about 30 h, with the film retaining a very good crystallinity. The oxygen vacancies seem to be disordered, since the SQUID measurement show three distinct magnetic phases with different oxygen content and the resistivity shows a modified Arrhenius behaviour.

The stability of the film in vacuum and instability on air is surprising, as the opposite behaviour would be expected. A difference between the perovskite phase obtained here (and in ref. [95]) and those commonly shown in literature (e.g. refs. [40, 99]), is the separation of magnetic phases. Reports on single phase samples don't mention any instability or transition to brownmillerite. The only sample age dependent transition in single phase perovskite SCO is reported in $SrCoO_{3-\delta}/DyScO_3$ ($\delta < 0.2$), however, it is not attributed to a transition to brownmillerite and rather a strain dependent structural phase transition without oxygen loss [96]. Furthermore, ionic liquid gating was shown to be able to switch the oxygen content (and even intercalate hydrogen [99]) in single phase $SrCoO_{3-\delta}$ films [10]. Taking these two findings, the instability in air of the perovskite phase film prepared in this thesis could be due to moisture in air acting as a catalyst for the transition to brownmillerite. The disorder of magnetic phases could indicate that parts of the sample lose oxygen more easily, which could explain the transition at lower temperatures as compared to literature. This hypothesis could be tested by building a chamber in the XRD that can be filled with a dry oxygen atmosphere and repeating the time dependent XRD measurements to determining if the perovskite phase remains as stable as in vacuum.

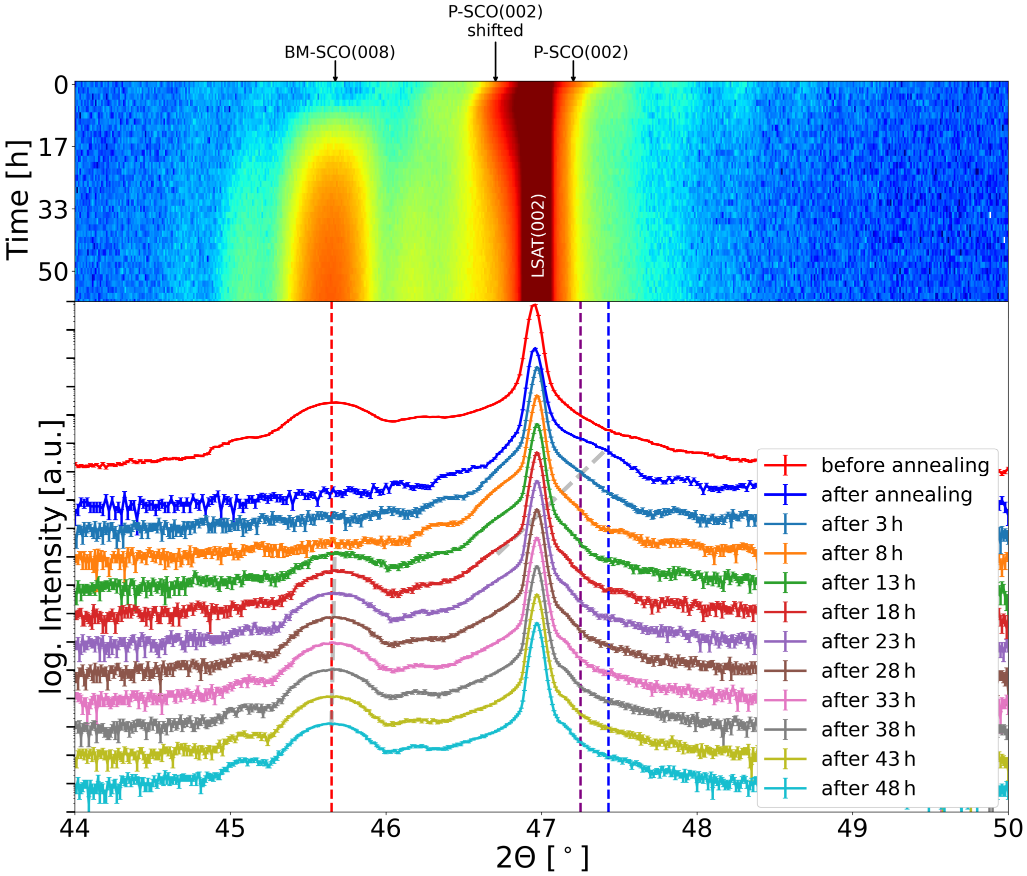

**Figure 4.21:** XRD measurements of L2 $SrCoO_3$/LSAT after annealing in air. Measurements were taken continuously, with one scan from $2\theta$=45°-50° within 100 min. On the bottom, every third measurement used to construct the intensity map are shown. The grey dashed lines are a guide to the eye for the peak shifts. The blue and purple lines indicate the angle for the $SrCoO_3(002)$ and $SrCoO_{2.75}(002)$ Bragg peaks for a relaxed film, and the red line indicate the observed strained $SrCoO_{2.5}(008)$ peak.

## 4.4 Investigation of magnetization in depth resolution

To determine if there is a depth dependence the re-transformation from the perovskite to brownmillerite structure, an annealed $SrCoO_3$/STO sample was measured with half-polarised neutron reflectometry at MARIA. The annealing conditions were 550°C for 6 h in 50 ml/min in the tube furnace in Garching. Before annealing, the sample was $287\,^{+5}_{-5}$ thick, including a top layer with slightly reduced scattering length density (SLD), and about 13 Å rough (tab. 4.6 and fig. 4.22).

The XRD measurement subsequent to the annealing shows a perovskite peak close to the expected peak position and a vanishing brownmillerite peak (fig. 4.23). A complete transformation can not be confirmed, since the only available instrument on site is a non-monochromatised D2 Phaser powder diffractometer. A potential brownmillerite peak might be hidden in the background. However, given that the observed perovskite peak is very close to the expected position, the sample is at least mostly converted to the perovskite phase.

The PNR measurement was then conducted with a cold finger cryostat and magnet set-up after field-cooling at 1 T to 10 K (fig. 4.24). The measurement was fitted by assuming the same thickness as measured in XRR (tab. 4.7). The SLD of the film was fitted by defining the oxygen content as a free parameter and allowing it to vary between 2.5 and 3. The resulting stoichiometry is $SrCoO_{2.75\,^{+0.02}_{-0.02}}$. The asymmetry between the up and down channels is only about 5% at the point of highest splitting, which corresponds to a magnetisation of $(0.05\,^{+0.03}_{-0.03})\,\mu_{B/Co}$. As the oxygen stoichiometry is at the lower limit for ferromagnetism, this very small moment is feasible and matches the saturation magnetisation of SQUID measurement discussed earlier (fig. 4.18). The sample shows uniform magnetisation throughout the layer. Trying to fit the data with a more granular layer structure to attempt to localise the oxygen deficiencies didn't result in a better fit, indicating that they are distributed randomly throughout the thickness of the film. As the time between annealing and mounting the sample in MARIA was $\sim$1 hour and the measured stoichiometry is $SrCoO_{2.75}$, the oxygen loss was a slightly quicker than for the LSAT sample investigated in fig. 4.21, but given the different substrate and possibly different atmospheric conditions, still comparable.

Because of the quick oxygen loss a measurement of the fully oxidised film was not possible. However the results obtained here are still interesting, as they point to a random distribution of the oxygen vacancies, since no difference in the oxygen content near the air-film or film-substrate interface was found. This matches to the fast oxygen dynamics reported in literature [94].

**Table 4.6:** Fit of the XRR measurement of S9 $SrCoO_{2.5}$/STO before annealing (fig. 4.22)

| layer | thickness [Å] | roughness [Å] |
|---|---|---|
| Top layer | $46^{+2}_{-3}$ | $12.8^{+0.3}_{-0.5}$ |
| $SrCoO_{2.5}$ | $241^{+3}_{-2}$ | $13^{+5}_{-2}$ |
| STO substrate | - | $6^{+2}_{-1}$ |

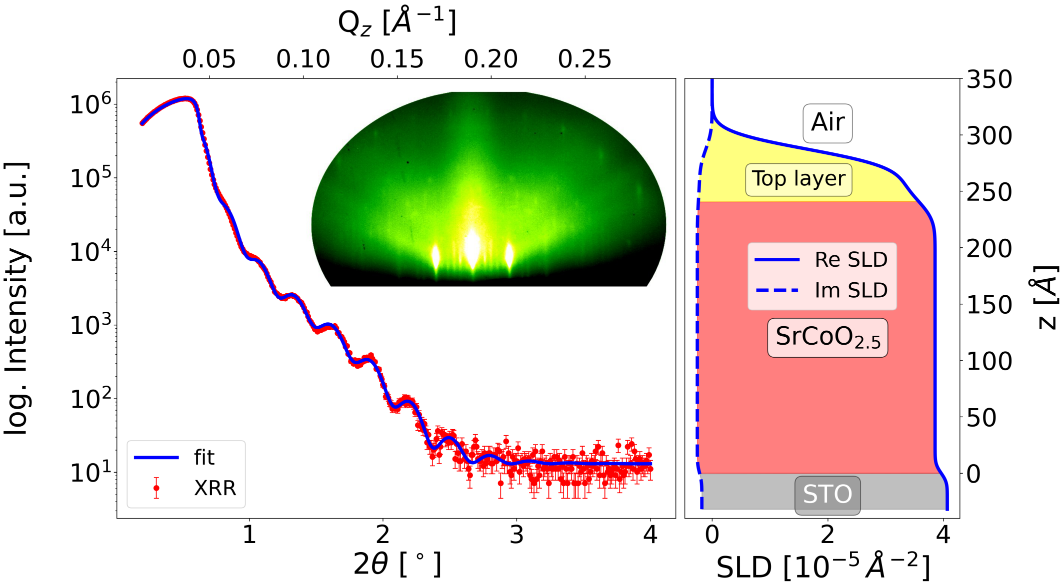

**Figure 4.22:** XRR measurement and scattering length density profile of sample S9 $SrCoO_{2.5}$/STO before annealing. The inset shows the RHEED image after growth.

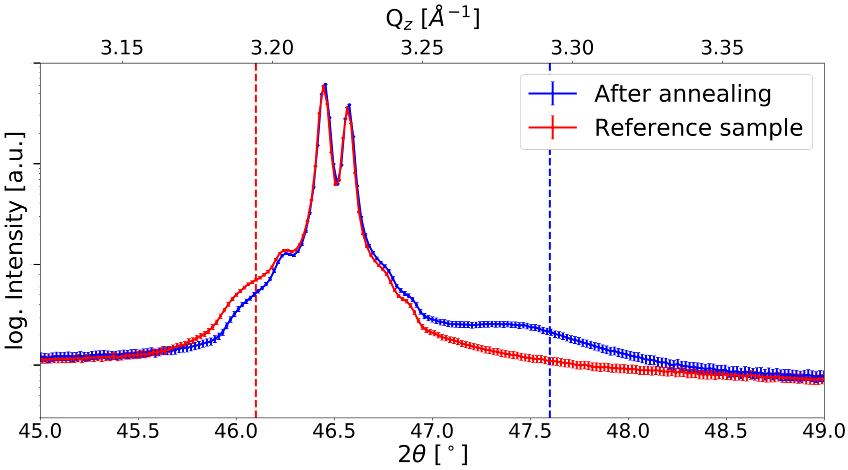

**Figure 4.23:** XRD measurement of sample S9 $SrCoO_3$/STO after annealing taken with the D2 Phaser. A measurement of a $SrCoO_{2.5}$/STO sample is shown as a baseline reference. The red and blue lines show the $SrCoO_{2.5}$ and $SrCoO_3$ peak positions from fig. 4.14.

**Table 4.7:** Fit of the PNR measurement of S9 $SrCoO_{3-\delta}$/STO after annealing in $O_2$ flow (fig. 4.24)

| layer | thickness [$\mathring{A}$] | roughness [$\mathring{A}$] | magnetic moment [$\mu_B/Co$] |
|---|---|---|---|
| $SrCoO_{2.75\,{}^{+0.02}_{-0.02}}$ | $287.0\,{}^{+1.1}_{-0.9}$ | $11.7\,{}^{+0.3}_{-0.4}$ | $0.05\,{}^{+0.03}_{-0.03}$ |
| STO substrate | - | $2\,{}^{+5}_{-0}$ | - |

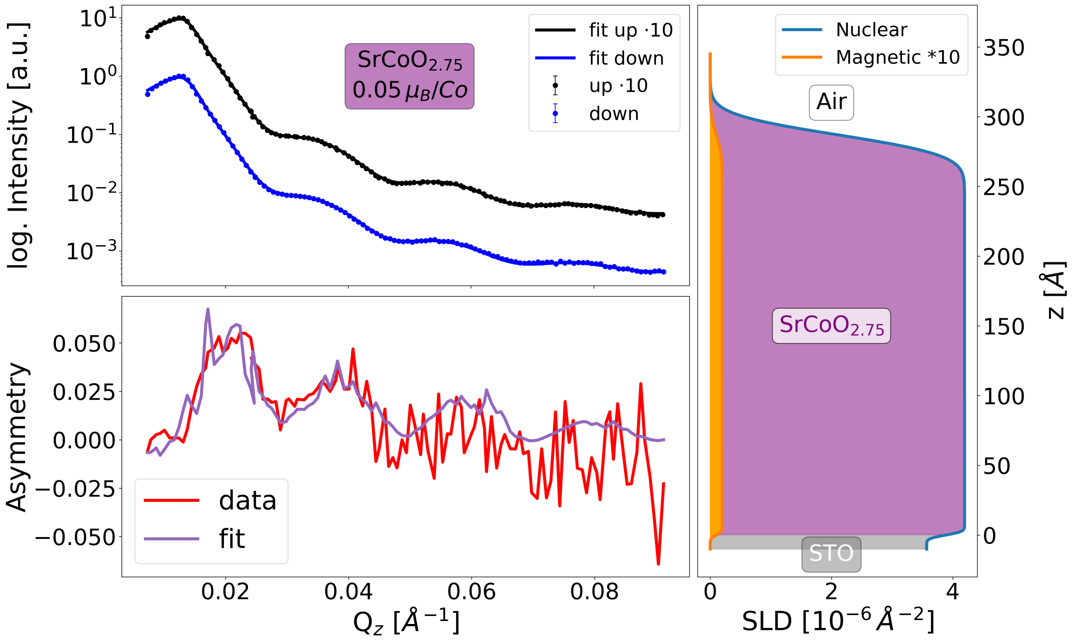

**Figure 4.24:** PNR measurement, asymmetry and scattering length density after annealing of sample S9 $SrCoO_{3-\delta}$/STO in the tube furnace in Garching. The up channel and fit have been multiplied by 10 for visual clarity.

## 4.5 Conclusion

A detailed growth study of $SrCoO_{2.5}$ on various substrates was completed and the deposition conditions for thin films of excellent quality determined. A method of evaluating the stoichiometry *in-situ* via RHEED was developed, which proved extremely useful for transferring the deposition parameters to a second MBE system with different conditions. The transition from $SrCoO_{2.5}$ to $SrCoO_3$ was successfully completed by annealing in oxygen flow and the stability and re-transformation studied. XRD results confirm a stable $SrCoO_3$ phase in vacuum for at least 24 h without deterioration. SQUID and PNR measurements indicate a random distribution of $SrCoO_{3-\delta}$ $(0<\delta<0.5)$ phases for oxygen deficient samples. The investigation of $SrCoO_{2.5}$ will be continued in chapter 6 with a focus on the coupling to a ferroelectric substrate, but first, the substrate characterisation will be discussed in the next chapter.

# 5 Properties and characterisation of PMN-PT substrates

For experiments with thin films and strain or magnetoelectric coupling $[Pb(Mg_{1/3}Nb_{2/3})O_3]_{0.7}$–$[PbTiO_3]_{0.3}$ (PMN-PT) substrates are used. An overview of the properties will be given here. $SrCoO_{2.5}$ films, were grown on PMM-PT(001), while for $Fe_3O_4$ films (chapter 7) both, PMN-PT(001) & PMN-PT(011) were used.

## 5.1 PMN-PT in (001) & (011) orientation

In chapter 2.3.3, a theoretical overview of relaxor ferroelectrics was already given, but some important aspects will be mentioned again here. In PMN-PT, below the ferroelectric Curie temperature ($T_C$ ~130°C [101]), the electric polarisation vectors within one polar nanoregion (NR) are aligned parallel and oriented along a $\langle 111 \rangle$ direction. Upon application of an electric field in out-of-plane direction ([001] or [011] depending on substrate cut), the polarisation follows a hysteretic behaviour (fig. 5.1 left). The strain evolution, however, is different, depending on the cut.

For PMN-PT(001) the in-plane strain is biaxial, i.e. the same along [100] and [011] (fig. 5.1 top right) and follows a butterfly shape. Upon the application of a small electric field below the coercive field, $E_C$ ~1.5 keV, a tensile strain develops as the polarisation starts to align with the electric field. For $E>E_C$, the field is strong enough to switch the polarisation, which releases the tensile strain. Further increase of the field then leads to a compressive regime. As the electric field is reversed, the compressive strain is reduced, until it vanishes for zero field. For a negative field, the loop is symmetric.

For PMN-PT(011), the strain behaviour along [100] is similar to the above discussed case. Along $[01\bar{1}]$ a large jump in strain occurs at the coercive field, caused by the switching of polarisation vectors with a component opposite to the electric field towards an in-plane (011) orientation (fig. 5.1 bottom right). For a slightly larger field, the strain jumps back towards the compressive regime as the polarisation finally switches out-of-plane towards the field direction. When the field is reduced, the strain relaxes linearly. For a negative field, the loop is symmetrical, again with a large jump in strain at the coercive field.

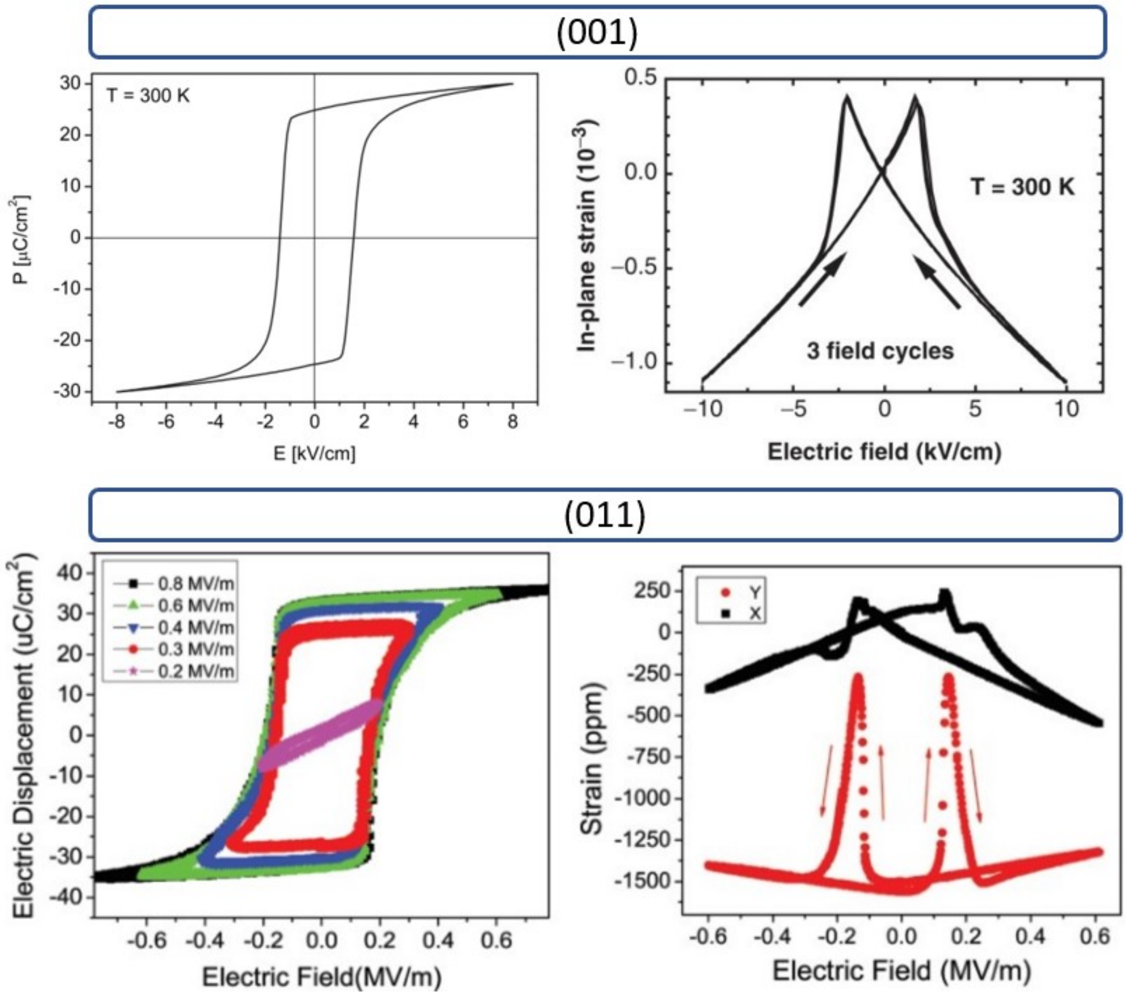

**Figure 5.1: Top-Left:** Polarisation of $PMN_{0.72}$-$PT_{0.28}$(001) [100]. Reprinted from A. Herklotz *et* al. *Journal of Applied Physics*, **108**, 094101 (2010), with the permission of AIP Publishing. **Top-Right:** Strain of $PMN_{0.72}$-$PT_{0.28}$(001), adapted from [100]. **Bottom:** Polarisation (**left**) and strain (**right**) of $PMN_{0.68}$-$PT_{0.32}$(011) [47]. The directions are: x=[100] and y=$[01\bar{1}]$. Reprinted from T. Wu *et* al. *Journal of Applied Physics*, **109**, 124101 (2011), with the permission of AIP Publishing.

## 5.2 Characterisation of PMN-PT(001) & (011)

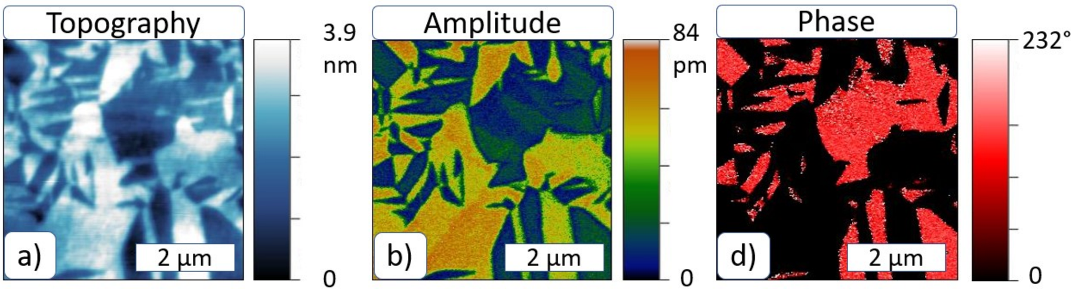

**Figure 5.2:** PFM measurement of a PMN-PT(001) substrate, showing **a)** topography, **b)** amplitude, and **c)** phase.

To obtain local information and confirm the domain state of the substrate, piezoresponse force microscopy (PFM) was performed on a PMN-PT(001) substrate (fig. 5.2). The domain pattern is similar to those found in literature [102]. There is a clear distinction between domains of opposite out-of-plane polarisation directions, in the contrast of both amplitude and phase. The substrate roughness is 8 Å.

X-ray rocking and diffraction measurements around the PMN-PT(002) reflex were performed on PMN-PT(001) at the Walther-Meissner-Institut (WMI) with S. Geprägs, to determine changes of the bulk crystallinity of the substrate with voltage. Fig. 5.3 top shows the rocking curve and diffraction measurement around the PMN-PT(002) Bragg peak. The unpoled substrate has a very broad and low intensity rocking curve. After a slow (∼0.02 kV/cm·s) voltage cycle between ±4 kV/cm the rocking curve gets much narrower. At the same time there is an observable shift in the position of the Bragg reflex of 0.03°, which corresponds to a change in out-of-plane lattice constant from 4.043 Å to 4.046 Å. This correlates to an in-plane contraction of 0.06%, which is comparable to literature [103]. For higher voltages, the rocking curve begins to show multiple peaks and the Bragg peak shows a clear tail towards higher angles, indicating faceting of the substrate. Reflectometry measurements on a substrate with a deposited $La_{0.67}Sr_{0.33}MnO_3$ layer reveal a substrate roughness of $12^{+1}_{-1}$ Å, which is higher than for standard substrates like STO and LSAT (≤6 Å) (fig. 5.3 bottom, and supplementary S.4 for a comparison of fit results). Kiessig fringes are still clearly observable however, so the increased roughness does not pose a problem.

For PMN-PT(011), the reflectivity along the two in-plane directions for an unpoled sample is quite different (fig. 5.4). For a $Fe_3O_4$/PMN-PT(011) sample, the $[01\bar{1}]$ direction has a broad, irregular rocking curve and the reflectivity measurement a very broad plateau of total reflection. This is likely caused by facets on the sample which create different scattering planes. The superposition of the scattering from the different planes then creates the long plateau. This also explains the initial low intensity for rocking and XRR measurements and subsequent increase as the electric field is ramped. After one voltage cycle, the scattering plane, and thus the plateau of total reflection, is well defined. In the [100] direction the rocking curve has a clear peak and the XRR measurement shows a sharp plateau. Upon

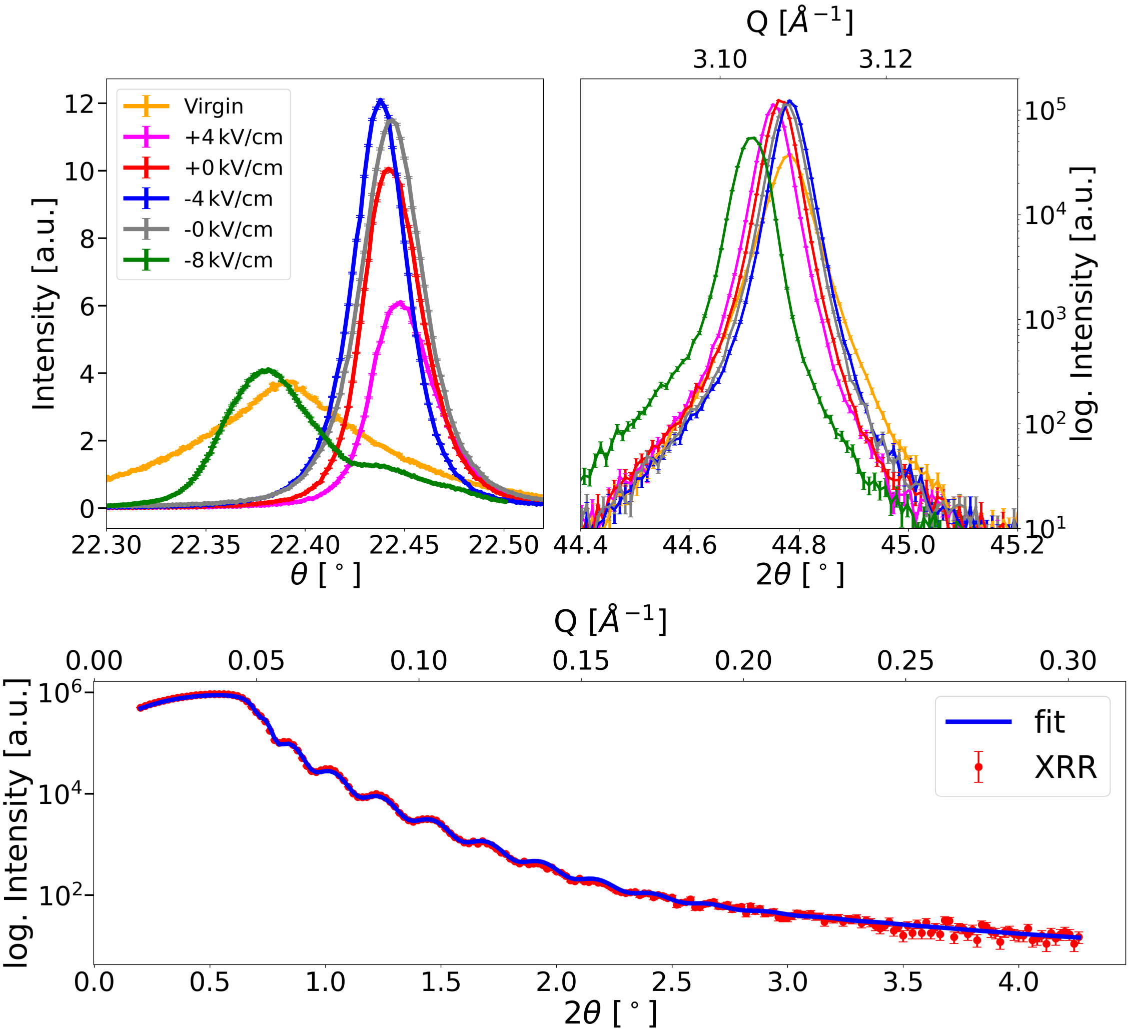

**Figure 5.3: Top:** X-ray measurements of sample LP1 SCO/LSMO/PMN-PT(001)/Au sample with amorphous SCO layer (LSMO layer deposited by A. Sarkar). Rocking curves (left) and diffraction measurements around the PMN-PT(002) peak (right). **Bottom:** XRR measurement of sample 0587 LSMO/PMN-PT(001) (fit parameter are listed in supplementary S.4). Sample prepared by A. Sarkar.

application of an electric field, the surface structure of the sample changes. To ensure all measurements are comparable, the rocking curves and XRR were measured in both directions before proceeding to the next field step, by rotating the sample stage 90°. The field was increased by ∼0.02 V/cm·s and measurements for every 0.4 kV/cm taken (fig. 5.4). Above 1.8 kV/cm, the rocking curve along [01$\bar{1}$] becomes more uniform, although still very broad and the rocking curve along [100] broadens into a similar shape. The reflectivity curve along [01$\bar{1}$] becomes clearer and matches that of the [100] direction, which, apart from a reduced intensity, doesn't change. The change in rocking curves and reflectometry does not revert once the voltage is switched off. Neither direction shows clear Kiessig fringes, which may be explained by a high substrate roughness. The reason for this is unclear, as the (001) oriented substrate was reasonable smooth.

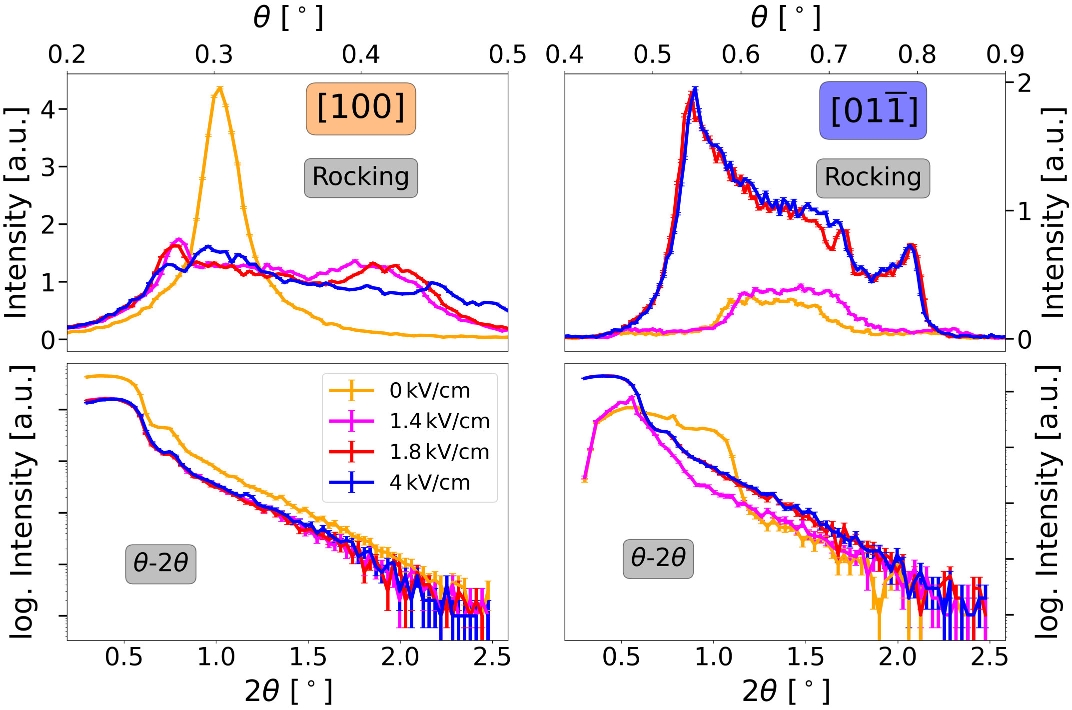

**Figure 5.4:** Rocking curves (**top row**) and XRR measurements (**bottom row**) in [100] (**left column**) and [01$\bar{1}$] direction (**right column**) with voltage on sample FM1 $Fe_3O_4$/PMN-PT(011)/Au (MBE grown).

# 6 Strontium cobaltite - Influence of strain

In chapter 4, the growth parameters for $SrCoO_{2.5}$ (BM-SCO) and conditions for the transformation to $SrCoO_3$ (P-SCO) have been established. As the change of oxidation state by annealing was successful, the possibility of changing the oxygen content by varying the strain were investigated. Petrie *et* al. reported on the oxygen content of $SrCoO_{3-\delta}$ (SCO) films grown on substrates with varying lattice constant, resulting in different strain states in the film and found that for higher tensile strain the oxygen content decreases [11]. Until now however, there has not been an investigation to find out whether variable strain can be used to tune the oxygen content in SCO and thus the physical properties. For that purpose, BM-SCO films were grown on the ferro- and piezoelectric substrate, $[Pb(Mg_{1/3}Nb_{2/3})O_3]_{0.7}$–$[PbTiO_3]_{0.3}$ (PMN-PT). PMN-PT in (001) orientation was chosen, which has uniform strain in both in-plane directions. The substrates were bought from Crystal GmbH. Samples with the $SrCoO_{2.5}$ layer directly on PMN-PT have the suffix "**P**". Later samples with an $La_{0.67}Sr_{0.33}MnO_3$ (LSMO) buffer layer "**LP**" were used.

## 6.1 $SrCoO_{2.5}$/PMN-PT

After the substrate was characterised, the $SrCoO_{2.5}$ thin films were grown on PMN-PT(001). The planned sample structure is shown in fig. 6.1 a. The SCO film is deposited directly on the PMN-PT with Au films on the top and bottom acting as electrodes to apply the electric field.

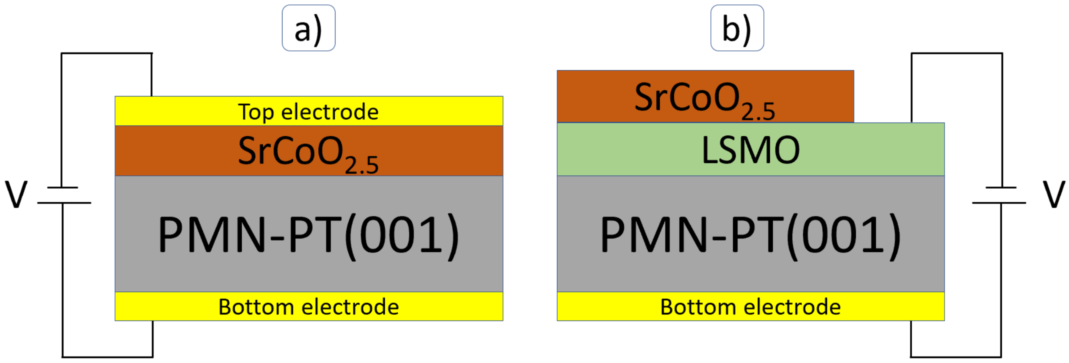

**Figure 6.1:** Sample structure for **a)** $SrCoO_{2.5}$ layer directly deposited on the PMN-PT substrate, and **b)** with LSMO buffer layer (see next section).

To clean the surface before deposition, the substrate was heated to 730°C, since at higher temperatures Pb loss might occur. Before each deposition on PMN-PT, a sample on STO or LSAT was prepared a day before to confirm the deposition conditions. Then the same conditions were used to grow on PMN-PT.

Fig. 6.2 a shows the RHEED image of the substrate along the [110] direction before deposition. During growth, the intensity of the specular RHEED spot decreases rapidly for the first ∼10 min and continues to decay slowly for the remaining 50 min (fig. 6.2 c). Images taken during the deposition show initial small island growth, indicated by broad spots, which coalesce into bigger island structure after ∼13 min. There is no indication of intensity oscillations. The AFM measurement of the completed layer confirms a surface completely covered by islands and a roughness of 25 Å (fig. 6.2 b). In the XRD, there is no indication of $SrCoO_{2.5}$ Bragg peaks (fig. 6.2 d). The thickness of the film based on the calibrated growth rate is 23 nm.

A similarly bad growth was observed for multiple samples. The substrate imparts a 3 % tensile strain onto the $SrCoO_{2.5}$ layer which might be too high to grow successfully. To circumvent this strain problem, a buffer layer was grown, which will be discussed in the next section. The aim of the buffer layer is to provide a better match of lattice constants for the $SrCoO_{2.5}$ film compared to the substrate. The buffer layer should be able to grow on the lattice mismatched PMN-PT substrate and relax the epitaxial strain via defect formation.

## 6.2 $SrCoO_{2.5}$/LSMO/PMN-PT

As a buffer layer, $La_{0.67}Sr_{0.33}MnO_3$ (LSMO) was chosen. From the PhD project of T. Bhatnagar-Schöffmann it is known that LSMO grows in good crystallinity and partially relaxed on PMN-PT(001). To facilitate the use of LSMO, samples of LSMO/PMN-PT were prepared by T. Bhatnagar-Schöffmann and A. Sarkar in Jülich and transported to Garching, were the $SrCoO_{2.5}$ layer was deposited. The deposition conditions for LSMO are taken from [85], with a reduced growth temperature. As the PMN-PT substrate tends to lose Pb at temperatures higher than 750°C-800°C [104], the substrate annealing and LSMO growth temperature was set at 730°C. Since the LSMO layer can also act as the top electrode, the top Au layer is not needed, but the SCO layer must not cover the complete LSMO layer. Thus, using a sample holder with a mask, the SCO layer was deposited in a rectangle of 7x10 $mm^2$ on the 10x10 $mm^2$ LSMO layer as shown in fig. 6.1 b. Both SCO and LSMO films were intended to be 20 nm thick. Fig. 6.3 shows the LEED and RHEED pictures of an LSMO/PMN-PT sample after growth, which reveals good crystallinity. The SCO layer was grown after annealing at 600°C for 1 h to remove surface contamination. From the RHEED image, Co excess is clearly visible, but the SCO film has good crystallinity in LEED and RHEED. AFM measurements were taken for the substrate and both layers (fig. 6.4). The unannealed substrate (fig. 6.4a) has some contaminant particles and a roughness of 10.0±0.5 Å. To image the substrate after annealing, the edge of the substrate which was hidden by

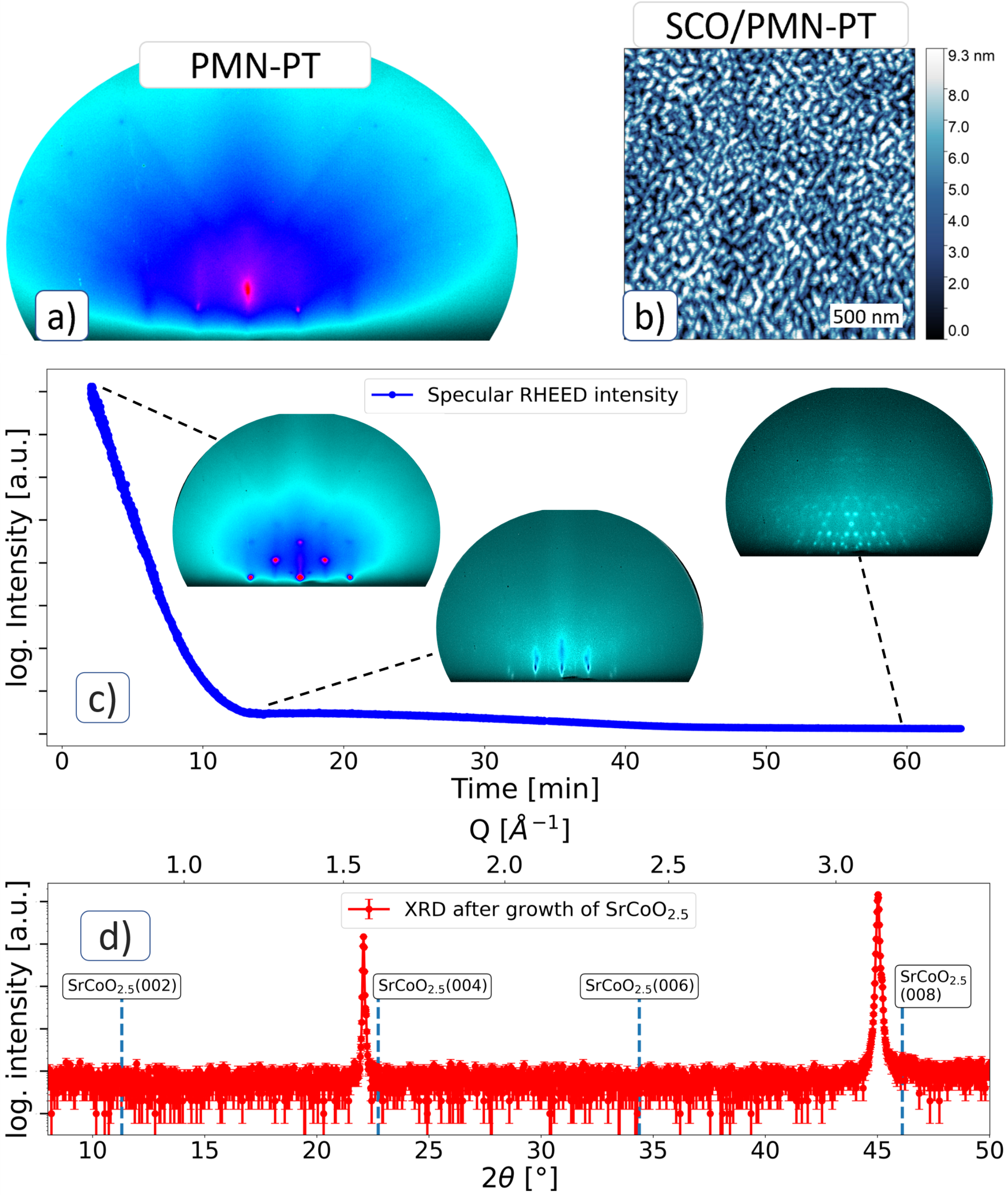

**Figure 6.2:** **a)** RHEED image along [110] of the PMN-PT(001) substrate before deposition. **c)** RHEED intensity oscillations during the growth of sample P1 $SrCoO_{2.5}$/PMN-PT with images at different stages as insets. **b)** AFM and **d)** XRD measurements after growth. The dashed lines in the XRD indicate $SrCoO_{2.5}$ Bragg peak angles.

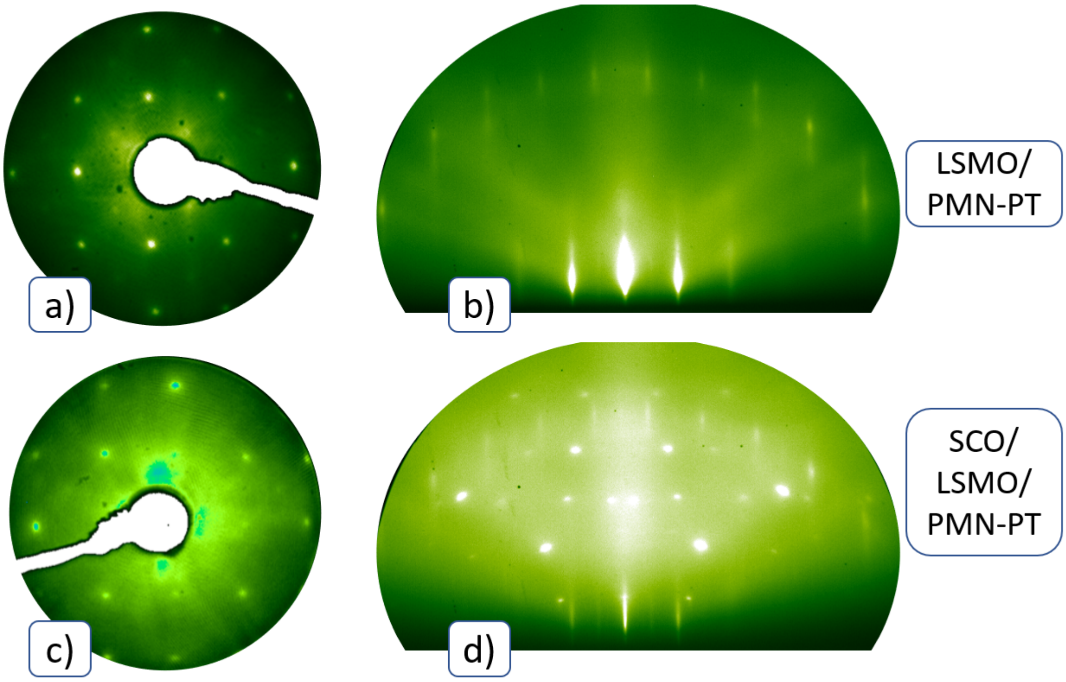

**Figure 6.3:** LEED at 100 eV and RHEED of sample LP2 LSMO/PMN-PT (a and b) and SCO/LSMO/PMN-PT (c and d). The $SrCoO_{2.5}$ layer exhibits Co excess but also good crystallinity.

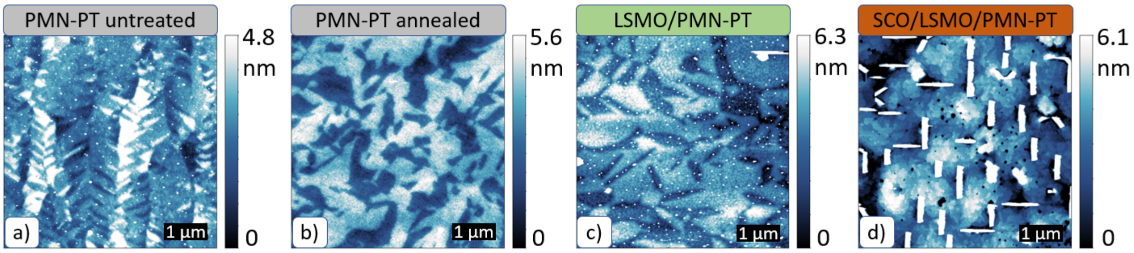

**Figure 6.4:** AFM images of sample LP2 SCO/LSMO/PMN-PT: **a)** untreated substrate, **b)** substrate edge after deposition of LSMO, **c)** LSMO film, and **d)** $SrCoO_{2.5}$ layer.

the sample holder during deposition was measured after LSMO growth (fig. 6.4b). The surface contaminant particles were removed by annealing, and the roughness increased slightly to 11.4±0.8 Å. The LSMO layer (fig. 6.4c) grows well on the substrate, keeping the domain pattern intact. The roughness again increased slightly to 12.4±0.8 Å. The SCO film grew in the same way SCO films with Co excess grew on STO and LSAT substrates, with ~8 Å steps building up plateaus. The Co excess forms vertical and horizontal CoO structures, which increase the roughness to 40±4 Å. Neglecting the islands, the roughness of the SCO film is 18.9±0.7 Å, which is higher than previous SCO films on STO and LSAT, but still smooth enough for scattering experiments.

XRD measurements of an SCO/LSMO/PMN-PT sample, show a clear LSMO peak and a split $SrCoO_{2.5}$ peak (fig. 6.5). The two side peaks of the $SrCoO_{2.5}(008)$ peak are 0.3° apart, which corresponds to a 0.1 Å difference in the c-axis parameter. The

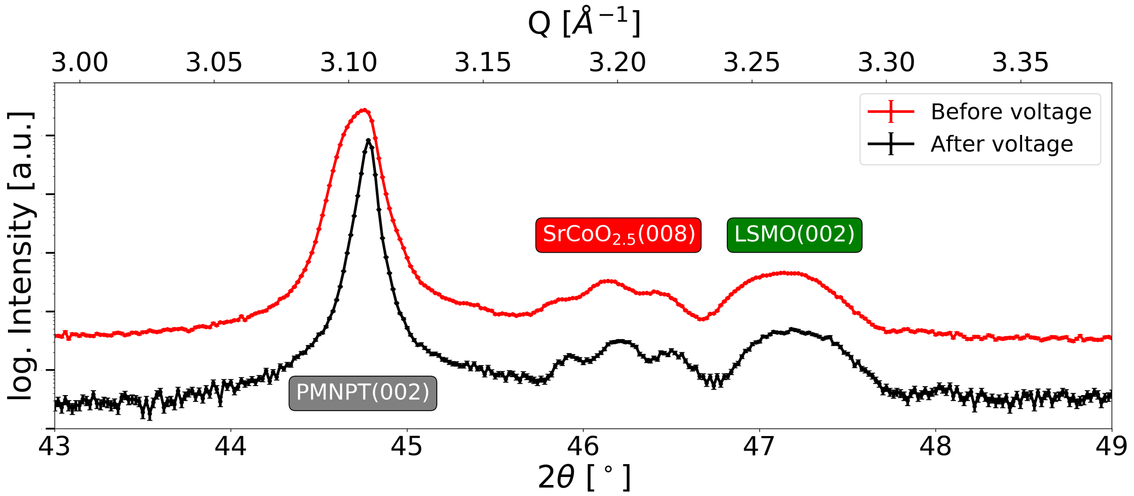

**Figure 6.5:** XRD measurements of sample LP2 $SrCoO_{2.5}$/LSMO/PMN-PT(001) before and after the MARIA beamtime, during which +8 kV/cm were applied rapidly.

origin of the side peaks is still unclear. If the peaks originate from a $SrCoO_{2.5}$ phase of different crystalline orientation the only peak close to $SrCoO_{2.5}$(008) with sufficient intensity to be detected is the $SrCoO_{2.5}$(220) peak at 46.58°, but this peak alone can't explain the origin of the twin side peaks. A difference in strain state for different parts of the sample leading to different angles for the same Bragg peak seems unlikely, given the close match of $SrCoO_{2.5}$ and LSMO lattice constants. The LSMO layer is nearly relaxed with only 0.2 % tensile strain, and the SCO layer (taking the centre peak) is only 0.1 % strained.

X-ray reflectometry was measured on the part of the sample with deposited SCO layer (fig. 6.6). The measured surface roughness agrees very well with the roughness measured by AFM for substrate and LSMO layer (table 6.1). The SCO layer roughness measured by XRR is between the AFM roughness with and without islands. A top layer of reduced density was used to account for these particles.

To gain more insight into the sample structure and to study interdiffusion between the different layers, transmission electron microscopy was performed by J. Barthel (ER-C). The measurements were taken after neutron experiments which will be discussed in the next section. In fig. 6.7a and 6.8a, two regions of the same sample are shown. The SCO layer grows epitaxial on the LSMO buffer layer which is relaxed compared to the substrate, as can be seen from the Fourier transformation of the layer structure in fig. 6.7b. CoO particles, identified by EDX in fig. 6.8b, are present in the SCO layer as expected from the RHEED images. In the STEM-EDX measurement, no inter-diffusion between the layers or the substrate is detected (fig. 6.8b). The La signal in the substrate does not indicate interdiffusion, as the La-L edge overlaps with the Ti-K edge. The fact that no Pb signal is detected in the LSMO layer proves that there was no interdiffusion during growth. During the measurement, the SCO layer started to deteriorate due to beam damage (fig. 6.9). The single crystalline structure breaks down from the top of the SCO and forms small

**Table 6.1:** Fit of the XRR measurement of LP2 $SrCoO_{2.5+\delta}$/LSMO/PMN-PT(001) in fig. 6.6 and roughness determined by AFM (fig. 6.4)

| layer | thickness [Å] | XRR roughness [Å] | AFM roughness [Å] |
|---|---|---|---|
| Top | $14^{+0}_{-2}$ | $12.1^{+0.4}_{-0.2}$ | - |
| $SrCoO_{2.5}$ | $195^{+2}_{-1}$ | $29^{+9}_{-4}$ | $40^{+4}_{-4}$ / $18.9^{+0.7}_{-0.7}$ without islands |
| LSMO | $222^{+2}_{-2}$ | $11^{+1}_{-1}$ | $12.4^{+0.8}_{-0.8}$ |
| PMNPT | - | $12^{+1}_{-1}$ | $11.4^{+0.8}_{-0.8}$ |

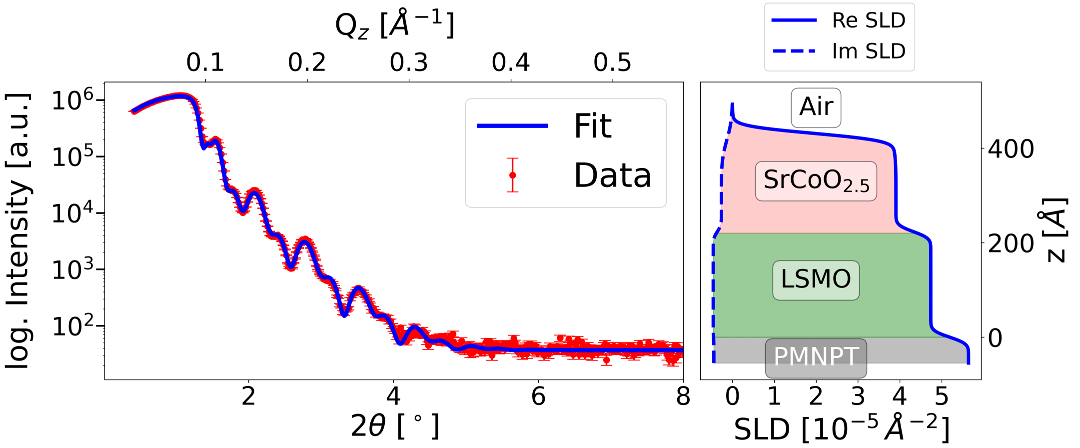

**Figure 6.6:** XRR measurements of sample LP2 $SrCoO_{2.5}$/LSMO/PMN-PT(001) before applied voltage.

clusters of a few nanometers. Only the SCO is affected, once the particles reach the LSMO, the damage doesn't propagate further. The breakdown of the SCO layer takes place within a minute. The energy and dose rate during the measurement are 200 kV and 1500 electrons/Å$^{2}$s, which is a relatively low dose rate [105]. For this reason, high magnification STEM imaging of atoms in this sample is not possible, as the layer would be destroyed too quickly.

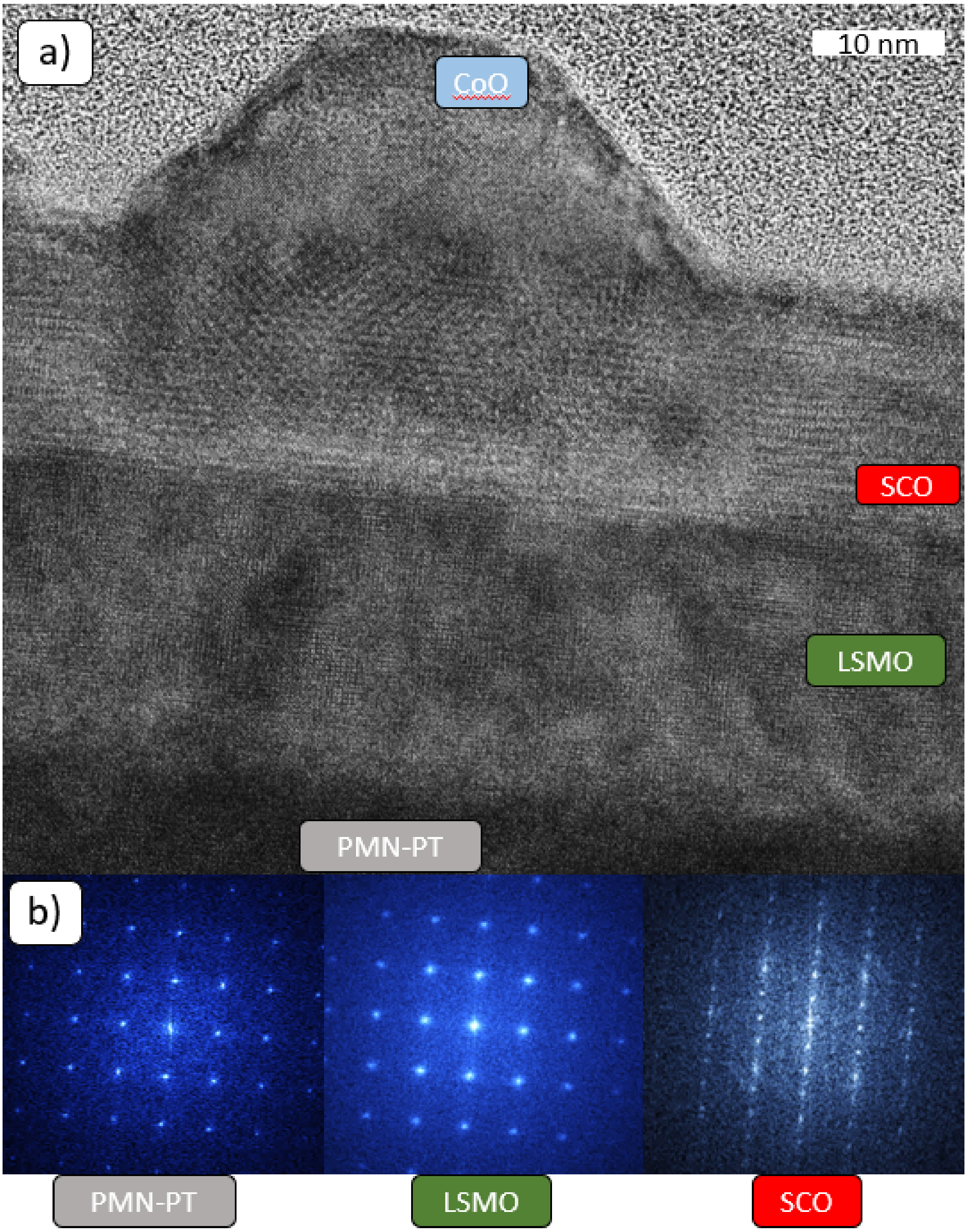

**Figure 6.7:** TEM images of sample LP2 $SrCoO_{2.5}$/LSMO/PMN-PT(001) showing a large CoO particle embedded in the SCO layer (**a**). Based on the Fourier transformations (**b**) the LSMO layer is relaxed on the substrate, while the SCO layer matches the LSMO lattice. Measurement performed by J. Barthel (ER-C).

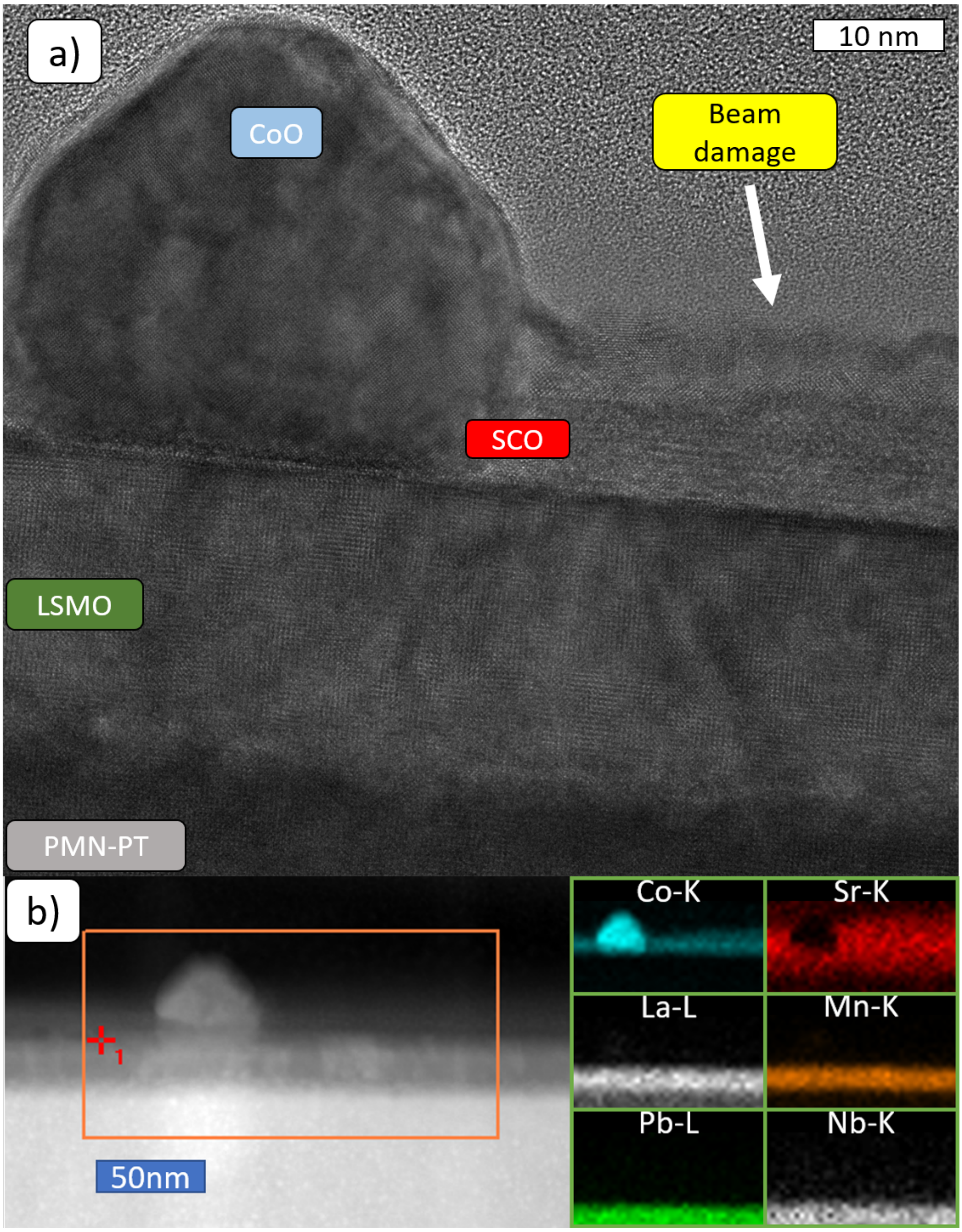

**Figure 6.8:** TEM images of sample LP2 $SrCoO_{2.5}$/LSMO/PMN-PT(001). During the measurement, the SCO layer started to deteriorate due to beam damage from the top downwards and formed small particles, the exact composition of which is currently unknown (**a**). STEM-EDX of image b shows no signs of inter-diffusion (**b**). The La signal in the substrate is due to the La-L edge overlapping with the Ti-K edge. Measurement performed by J. Barthel (ER-C).

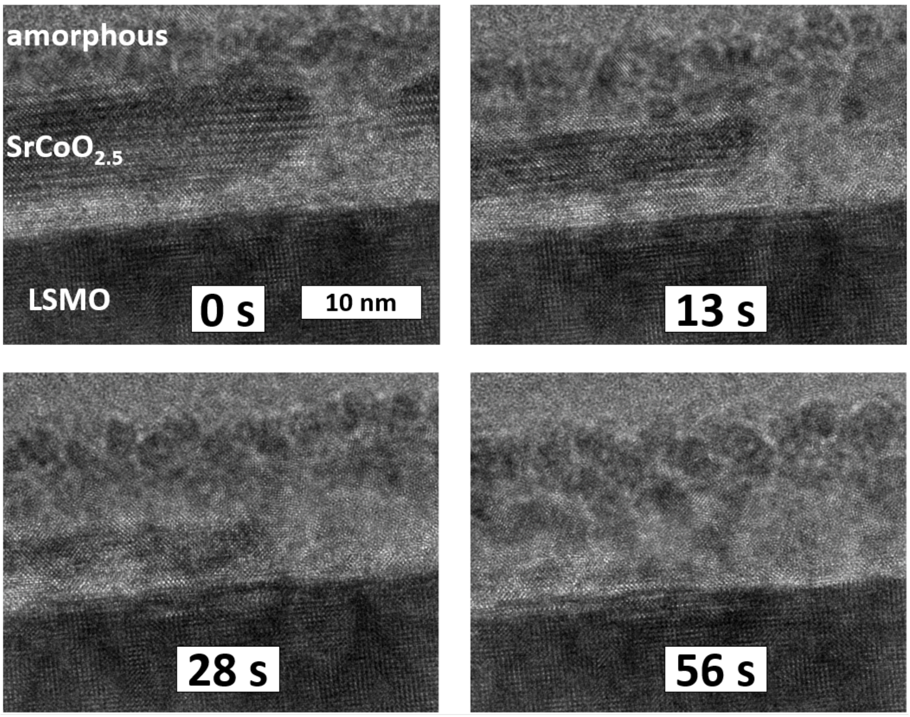

**Figure 6.9:** TEM images of sample LP2 $SrCoO_{2.5}$/LSMO/PMN-PT(001) showing the quick deterioration during the measurement. The images were taken within one minute. Measurement performed by J. Barthel (ER-C).

## 6.3 Changes in magnetic depth profile with voltage

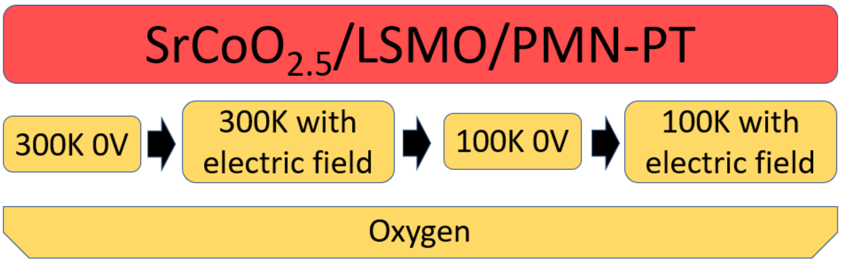

**Figure 6.10:** Experimental plan for sample LP2.

To investigate the changes in oxygen content and magnetic properties experienced by $SrCoO_{3-\delta}$ with strain, a set of polarised neutron reflectometry (PNR) experiments was planned for both initial oxidation states, i.e. $SrCoO_{2.5}$ and $SrCoO_3$ using MARIA at the MLZ (fig. 6.10). First, a $SrCoO_{2.5}$/LSMO/PMN-PT sample is investigated in oxygen atmosphere, to probe how the oxidation state changes with variable strain. The sample was measured first with and without electric field along [001] direction, at 300 and then 100 K, i.e. above and below the Curie temperature of the phases observed in the SQUID measurements in chapter 4.3. Since the sample had to be cooled below the Curie temperature of $SrCoO_3$ in oxygen, and a magnetic field had to be applied, a cryomagnet was used to satisfy all requirements. A second set of measurements with the same temperatures, voltages and magnetic field was supposed to be measured on $SrCoO_3$/LSMO/PMN-PT in vacuum, to see the decrease in oxygen content with strain.

Fig. 6.11 shows a simulation of the first measurement to be carried out on sample LP2 $SrCoO_{2.5}$/LSMO/PMN-PT for 0 kV/cm based on the thicknesses and roughnesses determined by XRR (table 6.1). The magnetisation of the LSMO layer was based on those measured in the thesis [85]. A clear splitting of the up and down channels and a resulting magnetic scattering length was expected due to the magnetisation of the LSMO layer, with only nuclear scattering in the SCO layer. Based on the TEM and XRR measurements in the previous section, the interfaces are expected to be sharp.

The measurement was then performed at 300 K and 700 mT in 1100 mbar oxygen (fig. 6.12). Trying to fit the measurement based on the parameter obtained by XRR did not result in a reasonable agreement between fit and measurement. To improve the fit, two interdiffusion layers were introduced to smoothen the transition between the scattering length densities (SLD's) of the layers. The SLD's also had to be decreased to match the data. With these assumptions, the fit matches the measurement well, but the model does not agree with the findings of TEM and XRR, which show sharp interfaces and no reduction in the SLD's.

Two factors contribute to the measurement problems. First, there were problems caused by the cryomagnet. The detector image in fig. 6.13a shows a signal between the direct and specular beam that doesn't originate from the sample. These contributions seem to originate from scattering by the sample holder or cryomagnet.

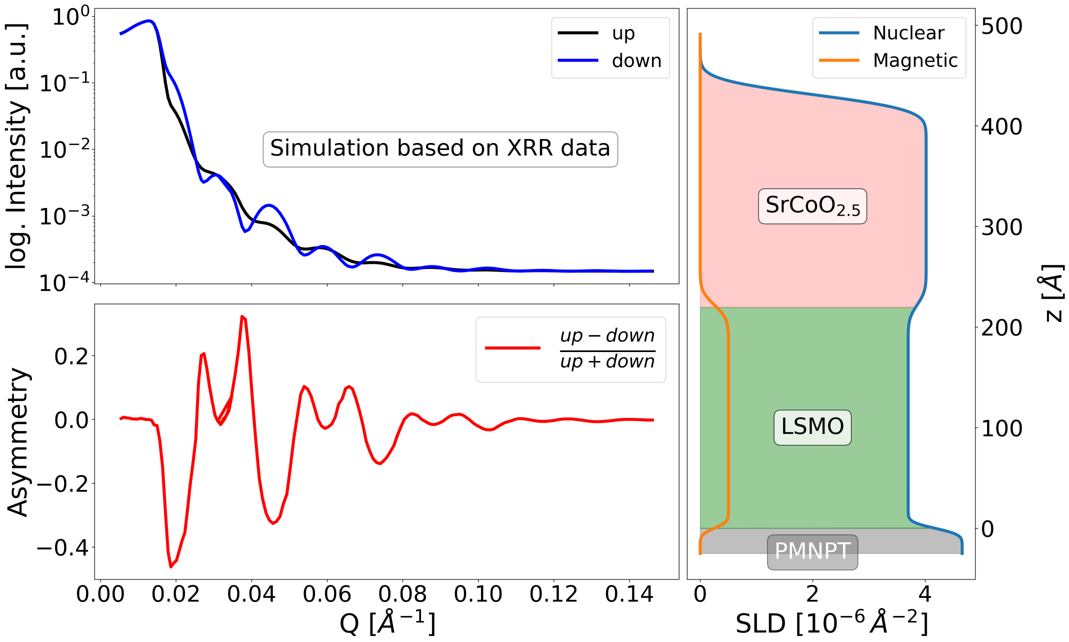

**Figure 6.11:** Simulation of the PNR measurement of sample LP2 $SrCoO_{2.5}$/LSMO/PMN-PT based on the sample parameters determined by XRR (table 6.1).

Also, the sample was not stable within the cryomagnet when the incidence angle was scanned. During the alignment of the sample in the beam, a rotation of the sample by a different angle than the cryomagnet was sometimes observed. This means that the incident angle was not always clearly defined. This effect was only mildly present for the 0 kV/cm measurement and the specular beam stayed in the integration area typically used to calculate reflected intensity. Since this experiment was the first ever in which the cryomagent was used at MARIA, this problem was unknown and unexpected.

Secondly, the discrepancy could be partly due to the sample geometry, as the SCO layer does not cover the whole sample area, but only 70%. The sample was oriented in the way shown in the insert in fig. 6.12, which should not cause any angle dependent difference in the signal due to SCO coverage. The problem could arise from a superposition of the signal from the neutrons scattering from the completely covered sample part, (SCO/LSMO/PMN-PT) and that from the non-covered part (LSMO/PMN-PT). To try and avoid this issue, the data was fit in a two-step model. First, the two parts (with and without SCO) were simulated keeping the same LSMO and PMN-PT parameters. Then, the two fits were added in the 0.7:0.3 ratio given by the sample geometry. This also didn't result in a reasonable fit, as seen in the supplementary figure S1.

After the 0 kV/cm measurement, the sample was measured with voltage. Unfortunately, the analysis of the substarte properties with applied voltage was not complete at the time of the measurement. As a result, 8 kV/cm were applied to the sample, which is high enough to create facets, as discussed in chapter 5. The heavily deteriorated sample surface can be seen in the detector images and $\alpha_i$-$\alpha_f$ maps in

**Table 6.2:** Fit of the PNR measurement of LP2 $SrCoO_{3-\delta}$/STO (fig. 6.12)

| layer | thickness [Å] | roughness [Å] | scattering length density [$10^{-6}$ Å$^2$] | magnetic moment [$\mu_B/u.c.$] |
|---|---|---|---|---|
| $SrCoO_{2.5}$ | $166^{+3}_{-10}$ | $16^{+2}_{-3}$ | $3.85^{+0.07}_{-0.05}$ | - |
| interdiffusion 2 | $47^{+4}_{-3}$ | $30.0^{+0.1}_{-12}$ | $3.42^{+0.1}_{-0.08}$ | $0^{+0.2}$ |
| LSMO | $130^{+3}_{-3}$ | $20^{+3}_{-3}$ | $3.27^{+0.07}_{-0.07}$ | $1.4^{+0.1}_{-0.1}$ |
| interdiffusion 1 | $60^{+0.3}_{-9}$ | $28^{+7}_{-5}$ | $3.24^{+0.08}_{-0.08}$ | $0.01^{+0.3}_{-0.01}$ |
| PMN-PT | - | $40.0^{+0.6}_{-5}$ | $4.35^{+0.09}_{-0.08}$ | - |

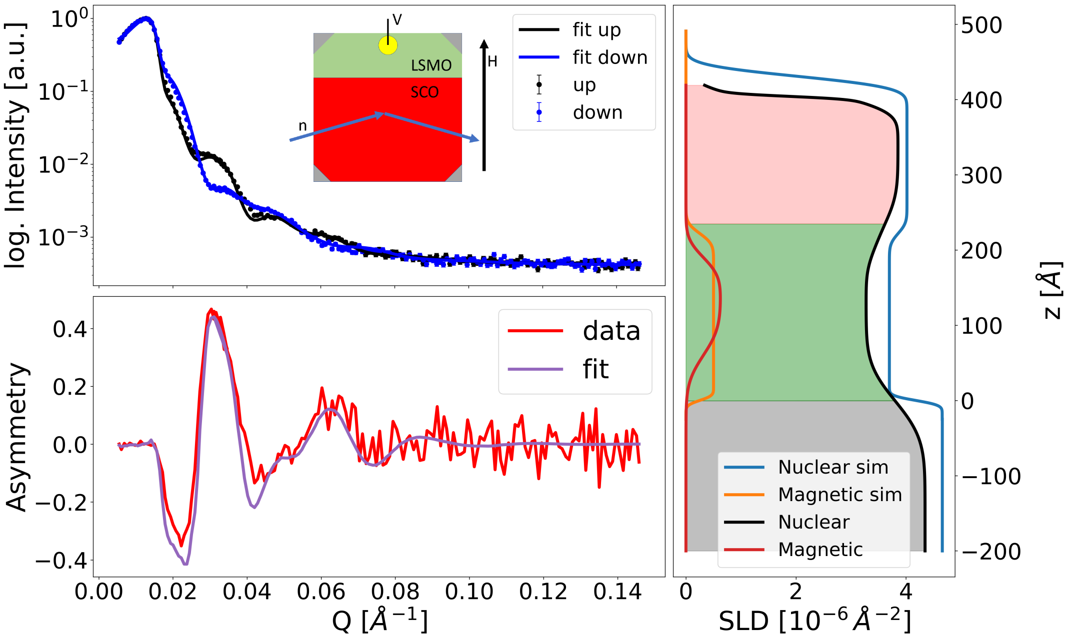

**Figure 6.12:** PNR measurement of sample LP2 $SrCoO_{2.5}$/LSMO/PMN-PT. In the scattering length density profile, the simulated profile of fig. 6.11 is shown for comparison. The measurement was performed at 300 K and 700 mT in 1100 mbar oxygen.

fig. 6.13. The specular beam fig. 6.13d is extremely broad and multiple reflexes are seen fig. 6.13b, along with a tail towards the right. This means multiple scattering planes are present on the sample, which all contribute a signal. Also, the angle at which the specular beam is observed in the detector changed significantly relative to the sample angle and deviated from the $\theta - 2\theta$ relation. This is likely the result of the problems with the cryomagnet discussed above.

As a result, the reflectometry curve is extremely smeared out, with even the plateau of total reflection no longer clearly defined (fig. 6.14). Since the measured data is intrinsically unreliable, due the superimposed signals that can not be segregated, any attempt to fit is doomed to fail.

The experiment performed here was the first ever use of the cryomagnet at MARIA and the difficulties involved with its operation were not yet known. For future

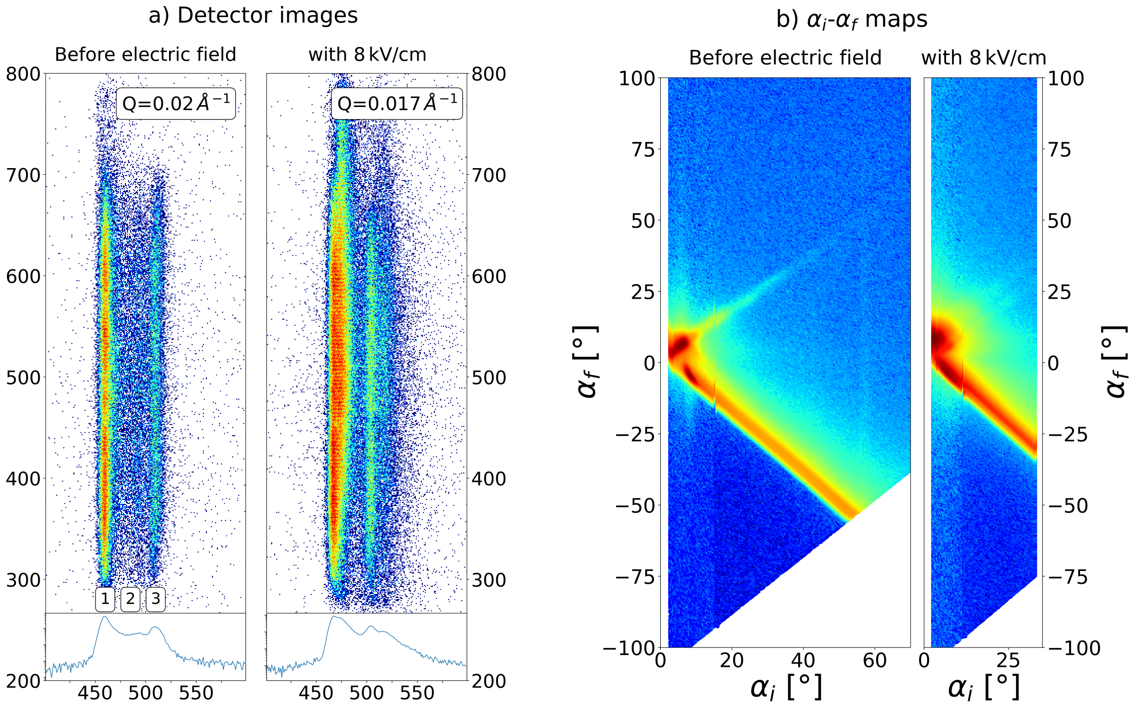

**Figure 6.13: a)** Detector images before voltage and with 8 kV/cm. The line profile on the bottom depicts the integrated intensity along the vertical. Different beams contribute to the detector image: (1) the direct beam, (2) stray beam, and (3) the specular beam. **b)** $\alpha_i$-$\alpha_f$ map before the application of voltage and with 8 kV/cm. With voltage, there are more reflexes in the detector image and the specular reflex gets extremely broadened.

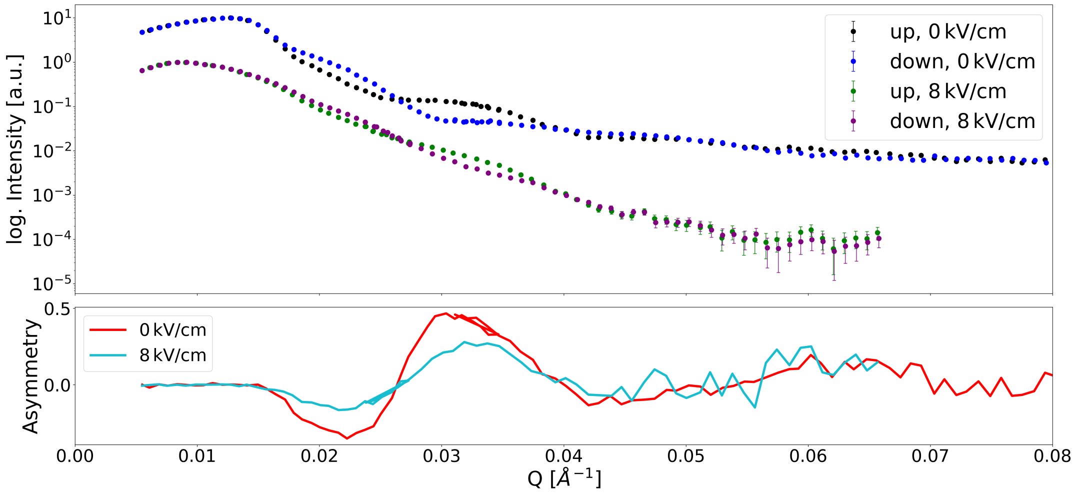

**Figure 6.14:** PNR measurement of sample LP2 $SrCoO_{2.5}$/LSMO/PMN-PT at 8 kV/cm compared to 0 kV/cm. The 0 kV/cm data has been multiplied by 10 for visibility.

experiments the stability of the sample in the cryomagnet has to be improved and the source of the unknown scattering events identified. Due to the difficulties in measuring with the cryomagnet even for 0 kV/cm, further measurements for $SrCoO_{2.5}$/LSMO/PMN-PT were not performed. For measurements of $SrCoO_3$/LSMO/PMN-PT, the correct annealing conditions to transform the $SrCoO_{2.5}$ layer to $SrCoO_3$ would have to be found. As the correct temperature for the transition is strongly substrate dependent, the temperatures known for STO and LSAT will likely not be suitable. To continue this work successfully, it would require a minimum of 5 samples with good crystallinity to determine suitable conditions for the transition to $SrCoO_3$ on PMN-PT. However, since the samples are partially grown in Jülich (LSMO layer) and Garching (SCO layer), this is very time consuming. For these reasons, the project was not pursued further.

## 6.4 Conclusion

$SrCoO_{2.5}$ films were grown on PMN-PT substrates. Due to growth problems directly on PMN-PT, an LSMO buffer layer was introduced, which facilitated a good structural quality in $SrCoO_{2.5}$/LSMO/PMN-PT samples. This sample was then investigated by PNR in oxygen atmosphere. Due to problems caused by sample geometry and instrumentation, a successful evaluation of the reflectometry experiment was not possible.

The results obtained are still encouraging though. Since $SrCoO_3$ is stable in vacuum, the cryomagnet responsible for a lot of the problems during the $SrCoO_{2.5}$/LSMO/PMN-PT PNR measurements is not needed for $SrCoO_3$. Thus, using a normal cold-finger cryostat, the influence of the strain and possible transition to $SrCoO_{2.5}$ could be observed. From the growth study shown here, it is only a question of time to grow the necessary samples, since the deposition conditions are known and can be adjusted easily. The annealing temperature would have to be found, but since the transition was successful on both LSAT and STO, the successful annealing on LSMO/PMN-PT should be possible as well.

# 7 Magnetoelectric coupling in $Fe_3O_4$/PMN-PT heterostructures

In the quest for novel data storage devices and multifunctional components, the direct control of magnetism by an electric field is a promising approach. Magnetoelectricity can be realised directly, in a material possessing both ferroelectricity and ferro- or ferrimagnetism. However, materials with these properties are rare, as they have to simultaneously break inversion and time-reversal symmetry. Another way is to couple a ferroelectric material with a ferro- or ferrimagnetic one via a shared interface. Taking for instance a ferroelectric substrate and growing a magnetic film on top may result in a magnetoelectric heterostructure. The coupling between the two systems can be mediated by either strain or polarisation. Strain can influence the magnetisation via magnetostriction and change the magnetic anisotropy, whereas the polarisation of the ferroelectric substrate can influence the magnetisation via a change in charge at the interface and thus an electron accumulation or depletion. This effect is sometimes called polarisation or charge coupling in literature. How these two effects contribute to the total coupling is still investigated, as determining the interplay is not straight forward and is also material specific.

In the following, the investigation of magnetoelectric coupling in Magnetite ($Fe_3O_4$) on two orientations of $[Pb(Mg_{1/3}Nb_{2/3})O_3]_{0.7}$–$[PbTiO_3]_{0.3}$ (PMN-PT) is reported. This project was initially started by A. Sarkar who left the institute and handed the project over. The orientations chosen for PMN-PT are (001), i.e. the same as for the SCO project, and PMN-PT(011).

Liu *et* at. [14] investigated the resistance and magnetisation of $Fe_3O_4$/PMN-PT(011) under an applied field of 10 kV/cm. They found an increase of the resistance under compressive strain and a spike in resistance at the Verwey transition. The Verwey transition temperature decreases by 8 K in both resistance and magnetisation measurements for 10 kV/cm. As the sign of the resistance change didn't depend on the electric field polarity, they concluded that strain coupling is dominant over polarisation coupling. To truly understand the effects of strain and polarisation on the magnetisation though, a deeper investigation of the intermediate states, between zero and maximum applied electric field is needed. Identifying the individual contributions is complicated for $Fe_3O_4$ films on PMN-PT(011), as the strain is non-isotropic along the two in-plane directions [100] and $[01\bar{1}]$. Comparing $Fe_3O_4$/PMN-PT(011) to $Fe_3O_4$/PMN-PT(001), which has isotropic in-plane strain (along [100] and [010]) helps to distinguish different contributions to magnetoelectric coupling.

In the beginning of the project, magnetite films were grown by MBE on (011) oriented PMN-PT by A. Sarkar. Their structural properties for applied electric field studies was already discussed in chapter 5.2. Later, PLD samples were prepared by M. Hussein Hamed (PGI-6) on PMN-PT(001) and PMN-PT(011) and used for structural and magnetic characterisation, including polarised neutron reflectometry.

Since multiple substrate orientations and resulting in-plane orientations are investigated, the following colour convention is adopted for clarity: For a scattering direction in XRR and XRD or magnetic field in SQUID along the [100] direction, the data is shown in orange and magenta, while for measurements along $[01\bar{1}]$, the data is shown in red and blue.

## 7.1 Magnetite thin films grown by MBE

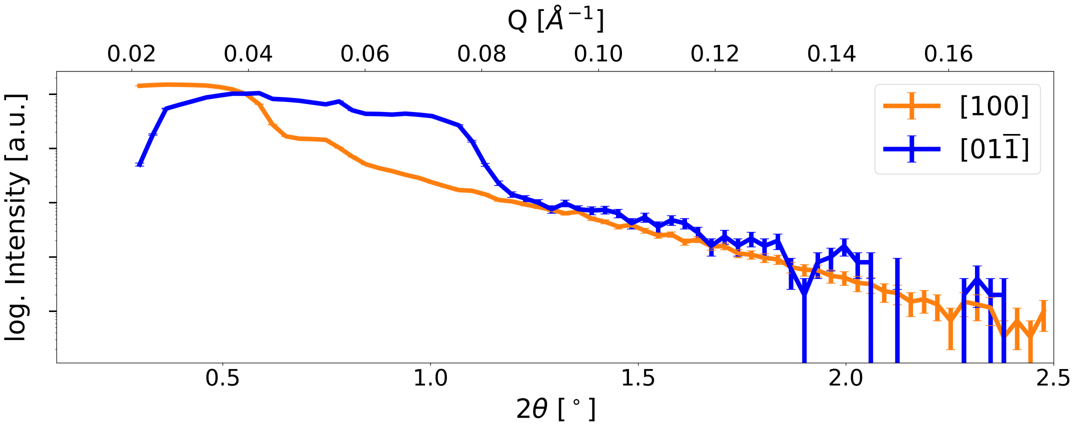

**Figure 7.1:** XRR measurements in [100] and $[01\bar{1}]$ direction of the MBE grown sample FM1 $Fe_3O_4$/PMN-PT(011) in the unpoled state.

Magnetite thin films were grown on PMN-PT(011) by A. Sarkar by MBE in Jülich. X-ray reflectometry measurements of the $Fe_3O_4$/PMN-PT(011) sample, showed almost no thickness oscillations and a smeared out plateau of total reflection for unpoled samples (fig. 7.1). The bad reflectivity signal was present in all MBE grown samples. The cause is most likely a badly defined interface between substrate and film either due to a large substrate roughness or interdiffusion between film and substrate. As the thickness is then no longer well defined over the whole sample, the thickness oscillations dampen and diminish. Using these samples for characterisation would be problematic in two ways: The physical properties of a system without clearly defined interface are expected to differ drastically from those of with a sharp interface, particularly as the magnetoelectric coupling investigated here is mediated via the strain transferred onto the film. Secondly, as the samples will be investigated by neutron reflectometry, a smearing out of the thickness oscillations to the extend observed here would make it extremely difficult to measure any change in the system. For these reasons, the MBE grown $Fe_3O_4$ samples are not further considered for investigation.

## 7.2 Samples grown by PLD

### 7.2.1 Structural and magnetic characterisation

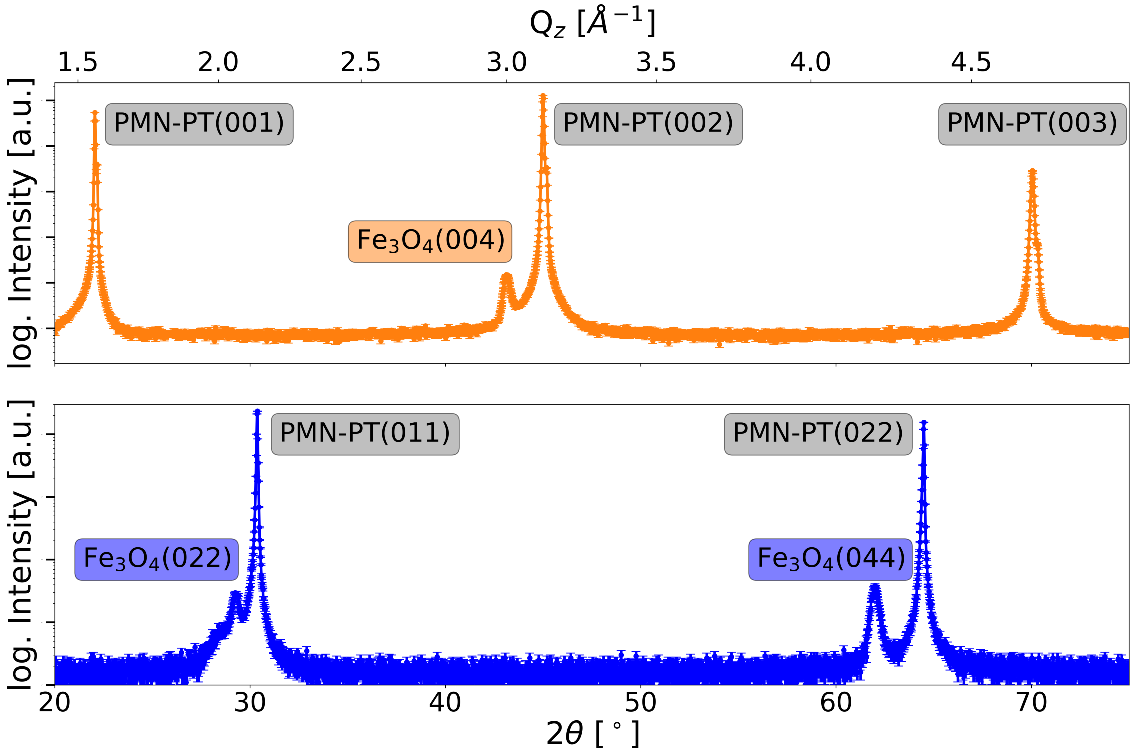

**Figure 7.2:** XRD measurements of sample F1 $Fe_3O_4$/PMN-PT(001) (**top**) and F2 $Fe_3O_4$/PMN-PT(011) (**bottom**).

Magnetite films were grown by M. Hussein Hamed (PGI-6) using pulsed laser deposition (PLD). Out of the four studied $Fe_3O_4$ samples, F1 is on PMN-PT(001) and F2-F5 on PMN-PT(011).

XRD measurements of $Fe_3O_4$/PMN-PT(001) and $Fe_3O_4$/PMN-PT(011) (fig. 7.2) show only $Fe_3O_4$ and substrate peaks without excess phases, however no Laue oscillations are visible. This indicates the samples are polycrystalline or have a lot of defects, as Laue oscillations are correlated with the thickness of the single crystalline volume.

Figures 7.3 and 7.4 show X-ray reflectometry measurements for both substrate orientations and tables 7.1 and 7.2 list the corresponding XRR fit parameters. The PLD grown samples exhibit higher interfacial quality for both crystal orientations compared to the MBE grown samples (figs. 5.4 and 7.1), although the rocking curves are still very broad, particularly for PMN-PT(001) and for PMN-PT(011) while scattering along the $[01\bar{1}]$ direction. The broadening of the rocking curve implies that the sample surface is not macroscopically flat, so the sample is either bent or faceted before any electric field is applied.

For PMN-PT(001), the full width at half maximum (FWHM) of the rocking curve

**Table 7.1:** Fit of the XRR measurement of F1 $Fe_3O_4$ PMN-PT(001) in fig. 7.3

| Layer | thickness [Å] | roughness [Å] | FWHM [°] |
|---|---|---|---|
| Top | $16.4^{+0.6}_{-0.4}$ | $5.0^{+0.2}_{-0}$ | 0.39 |
| $Fe_3O_4$ | $359^{+2}_{-2}$ | $5.0^{+0.6}_{-0}$ | |
| PMN-PT | - | $11^{+1}_{-0.8}$ | |

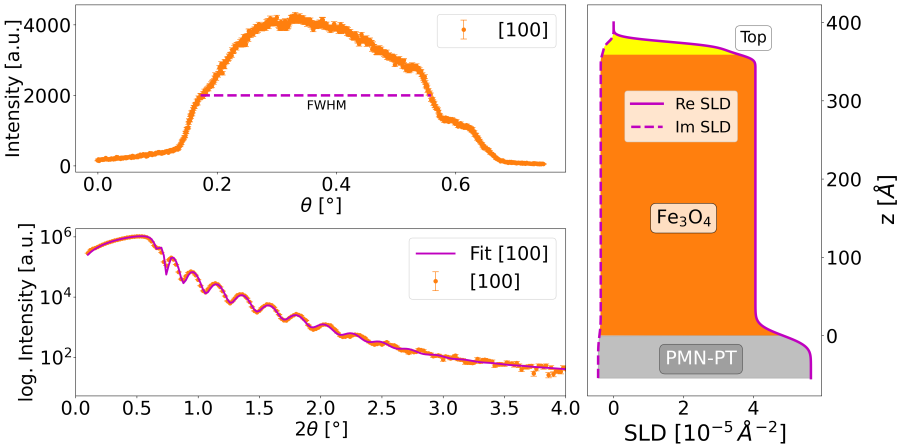

**Figure 7.3:** Rocking curves (**top left**), XRR measurements (**bottom left**) and SLD profile (**right**) of sample F1 $Fe_3O_4$/PMN-PT(001).

**Table 7.2:** Fit of the XRR measurement of F3 $Fe_3O_4$ PMN-PT(011) in fig. 7.4

| Layer | thickness [Å] | roughness [Å] | Direction | FWHM [°] |
|---|---|---|---|---|
| Top | $25^{+0}_{-0.9}$ | $10^{+0.2}_{-0.2}$ | [100] | 0.06 |
| $Fe_3O_4$ | $441^{+3}_{-4}$ | $9^{+0.2}_{-0.2}$ | [01$\bar{1}$] | 0.27 |
| PMN-PT | - | $18^{+3}_{-2}$ | | |

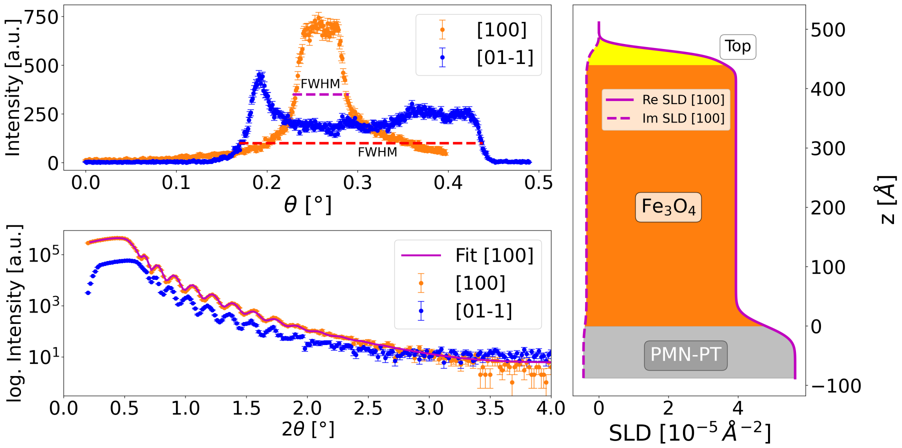

**Figure 7.4:** Rocking curves (**top left**), XRR measurements (**bottom left**) and SLD profile (**right**) of sample F3 $Fe_3O_4$/PMN-PT(011).

is 0.39°, but thickness oscillations are clearly visible in the reflectivity (see fig. 7.3). For PMN-PT(011), as a result of the broad rocking curve, with FWHM of 0.27° along $[01\bar{1}]$, the plateau of total reflection is elongated. In [100] direction, however, the rocking curve is much slimmer with a FWHM of 0.06° (see fig. 7.4). A top layer of reduced density had to be assumed for both substrate orientations to fit the reflectometry data. The (011)-oriented substrate is relatively rough, with $18^{+3}_{-2}$ Å, however this does not deteriorate the reflectivity significantly, in contrast to the MBE grown samples. For all XRR measurements only the specular reflectivity was measured without correction for diffuse scattering. In the future, it should be verified if the diffuse scattering can be neglected or if there is a significant contribution due to the faceting.

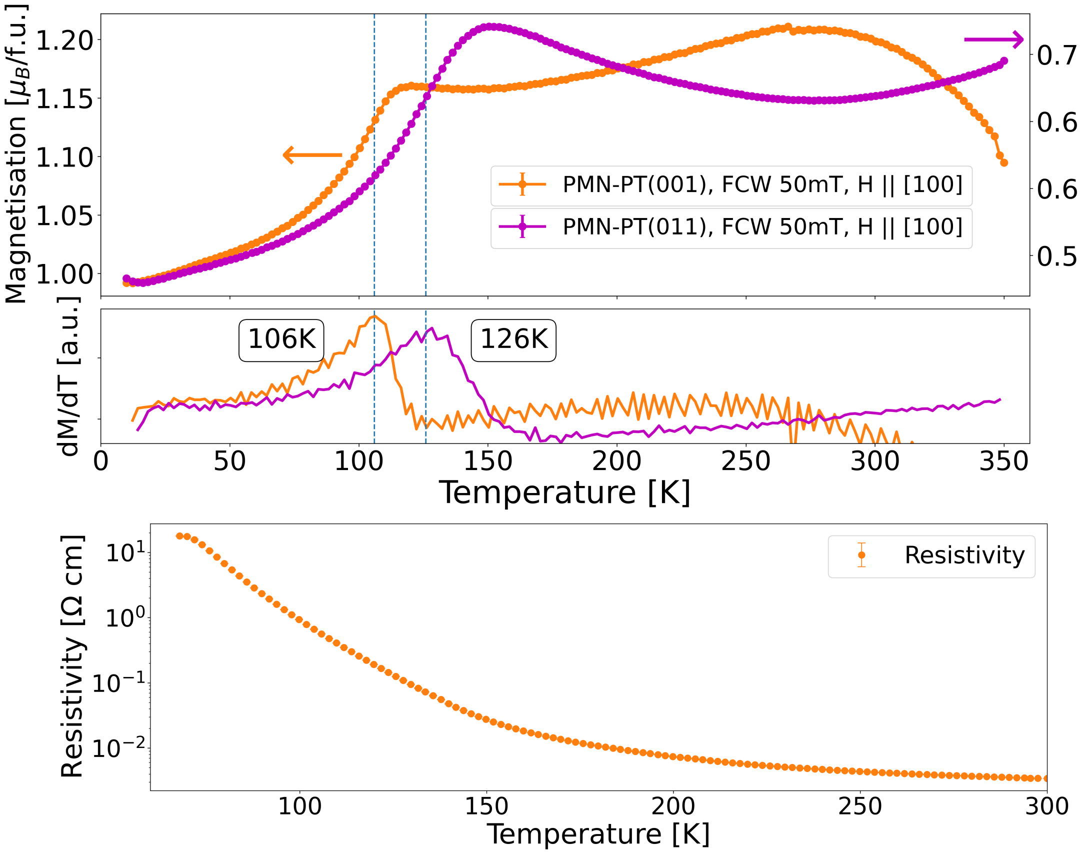

**Figure 7.5:** Field-cooled warming magnetisation measurement of sample F1 $Fe_3O_4$/PMN-PT(001) and F2 $Fe_3O_4$/PMN-PT(011) showing a clear Verwey transition at 126 K and 106 K, respectively (**top**). Resistivity measurement of sample F2 $Fe_3O_4$/PMN-PT(011) (**bottom**).

Temperature dependent magnetisation measurements, with the magnetic field along the [100] direction, reveal a clear Verwey transition at 126 K for PMN-PT(011) confirming the oxidation state of the sample to be $Fe_3O_4$ (fig. 7.5). The transition is not visible in the resistivity measurement (fig. 7.5), which is not surprising, as it is smeared out for films below 50 nm [106]. The magnitude of the resistivity matches well to literature [107]. For the sample on PMN-PT(001), the Verwey transition is lowered by 20 K in the magnetisation measurement, indicating worse crystallinity compared to $Fe_3O_4$/PMN-PT(011). However, the transition is still clearly visible.

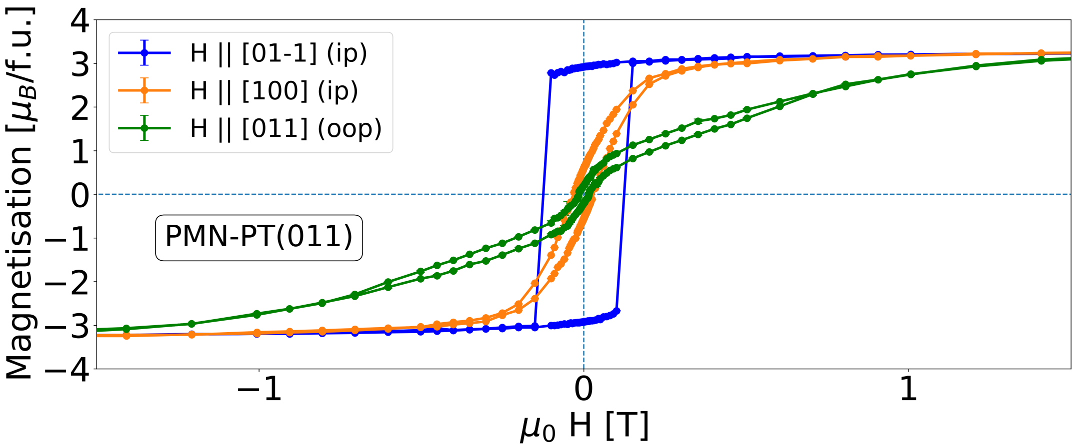

**Figure 7.6:** Magnetic hysteresis loops at 300 K of sample F2 $Fe_3O_4$/PMN-PT(011) along both in-plane (ip) and the out-of-plane direction (oop). The magnetic easy axis is along the $[01\bar{1}]$ substrate direction. The oop data has not been corrected for demagnetisation, as the demagnetisation contribution is very small.

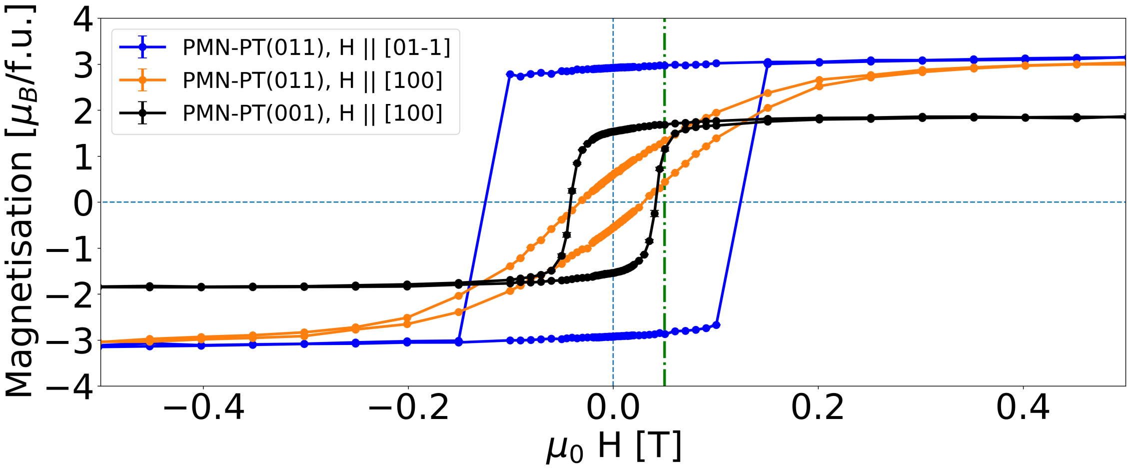

**Figure 7.7:** Magnetic hysteresis loops at 300 K of samples F1 $Fe_3O_4$/PMN-PT(001) and F2 $Fe_3O_4$/PMN-PT(011). The green line indicates 50 mT, the field at which the magnetoelectric measurements (chapter 7.2.2) were performed. The magnetic field was chosen such that the film is not fully saturated along $[01\bar{1}]$.

Hysteresis measurements reveal the magnetic easy axis of the $Fe_3O_4$ film on PMN-PT(011) to be along the $[01\bar{1}]$ substrate direction (fig. 7.6). Curiously, the saturation magnetisation of $3.2\,\mu_B$ for PMN-PT(011) and $1.9\,\mu_B$ for PMN-PT(001) (fig. 7.7) is much lower than the reported value of $4.0\,\mu_B$. This could be caused by parts of the sample not being crystalline. As no Laue oscillations were observed in the XRD measurements, a determination of the crystalline volume is not possible. Additionally, crystalline defects can cause a reduced saturation magnetisation [108].

High resolution TEM (HRTEM) images taken by J. Barthel (fig. 7.8) reveal a high defect density, as can be seen from the contrast variation throughout the film (fig. 7.8 c), which can explain the reduced saturation magnetisation. Furthermore, the discrete spots in the Fourier transformation of the film show that the sample is single crystalline. The interface between film and substrate is not flat, which was expected from the interface roughness determined by XRR (fig. 7.8 b). The images were taken after a neutron beamtime discussed later, during which the sample experienced 1.5 electrical field cycles between $\pm 4\,\mathrm{kV/cm}$, which could be responsible for some, but certainly not all of the structural defects. As the sample was only exposed to 1.5 electric field cycles and only a small deterioration of the rocking curve was measured during the neutron experiments (discussed in section 7.2.3), the sample quality observed in the TEM images is likely not much different from the the as-grown state.

An oxidation to $\gamma$-$Fe_2O_3$, which has a saturation magnetisation of $2.5\,\mu_B/\mathrm{f.u.}$, would destroy the Verwey transition, even for small stoichiometric fluctuations of $\delta$=0.012 in $Fe_{3(1-\delta)}O_4$ [111,112]. To unambiguously confirm that the oxidation state is $Fe_3O_4$, hard X-ray photoemission spectroscopy (HAXPES) was performed and analysed by M. Hamed at P22, DESY (fig. 7.9). The HAXPES data show a contribution of $Fe^{3+}$ and $Fe^{2+}$ to the Fe $2p_{3/2}$ peak and a merging of the satellite peaks, confirming that the sample is indeed $Fe_3O_4$.

Overall, since the PLD grown samples show good reflectivity and a clear Verwey transition we have proven the films to be $Fe_3O_4$, and the samples are suitable for further investigation by magnetoelectric SQUID and polarised neutron reflectometry.

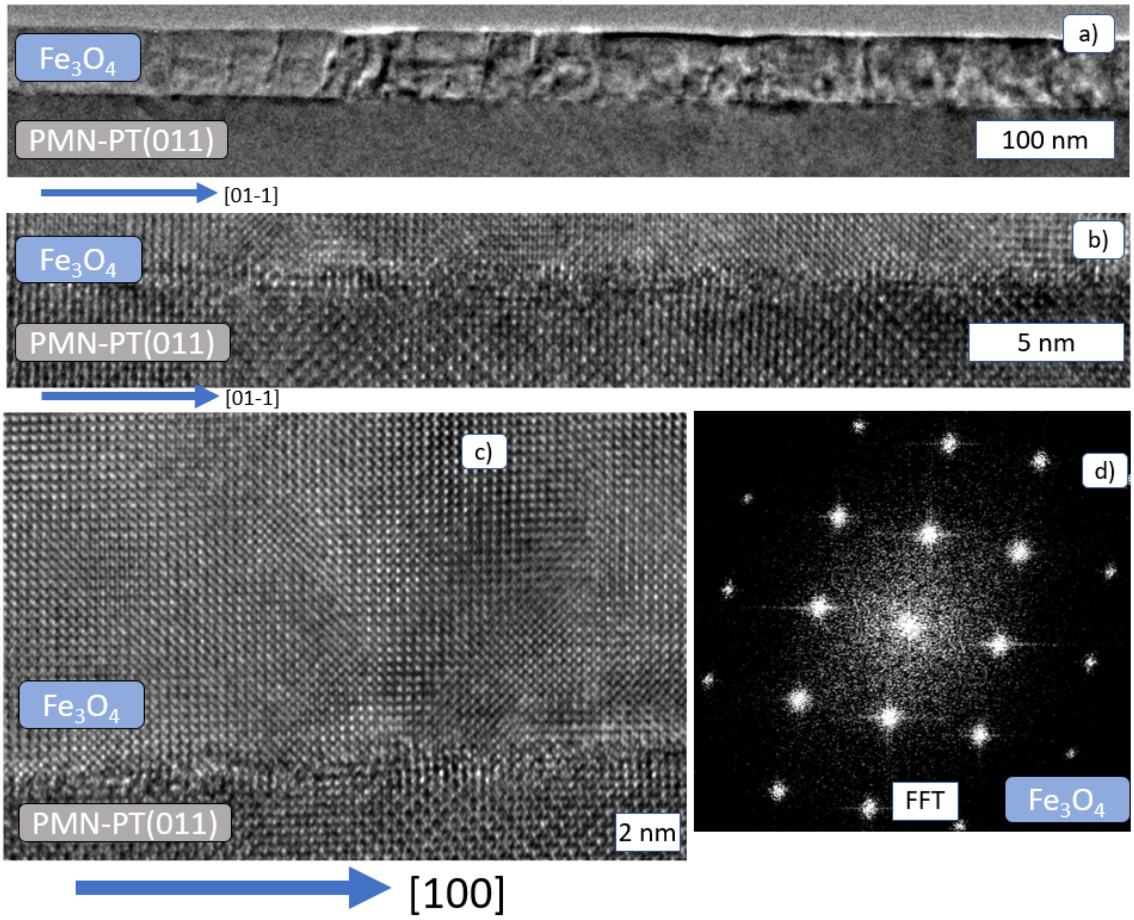

**Figure 7.8:** HRTEM images of sample F3 $Fe_3O_4$/PMN-PT(011). Image d) shows the Fourier transformation of the $Fe_3O_4$ layer. The images were taken after the PNR measurements discussed in the next section, i.e. after applied electric field.

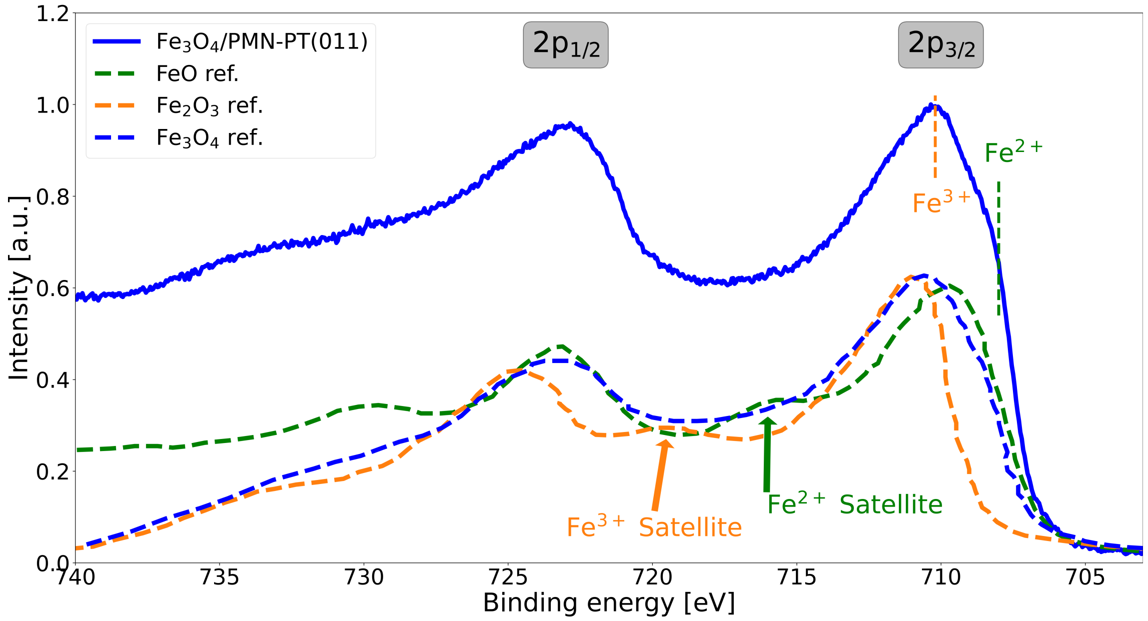

**Figure 7.9:** HAXPES measurement of sample F4 $Fe_3O_4$/PMN-PT(011). The measurement was performed and analysed by M. Hamed at P22, DESY. The image shows the Fe $2p_{1/2}$ and $2p_{3/2}$ peaks as well as reference spectra from literature ($Fe_2O_3$ and $Fe_3O_4$ from [109] and FeO from [110]). Reprinted FeO spectrum with permission from S. Gota, E. Guiot, M. Henriot, and M. Gautier-Soyer, PHYSICAL REVIEW B, **60** 20, 14387-14395 (1999) Copyright 1999 by the American Physical Society. Reprinted $Fe_2O_3$ and $Fe_3O_4$ spectra with permission from T. Fujii, F. M. F. de Groot, G. A. Sawatzky, F. C. Voogt, T. Hibma, and K. Okada, PHYSICAL REVIEW B, **59** 4, 3195-3202 (1999) Copyright 1999 by the American Physical Society. The contribution to the $2p_{3/2}$ peak from $Fe^{3+}$ and $Fe^{2+}$ are indicated by dashed lines.

### 7.2.2 Magnetoelectric coupling

To study the effect of substrate strain and electric polarisation on the magnetisation of the magnetite layer, magnetoelectric coupling measurements were performed with SQUID. Since an electric field can't be applied with the RSO option, the DC transport head was used for all measurements requiring voltage. Since the DC head has lower sensitivity, the error for those measurements is larger. To apply the electric field, the sample was contacted with Ag-paint covering the bottom of the substrate and point contacts on the top of the film. The electric field is then applied along the out-of-plane direction, i.e. [001] for films on PMN-PT(001) or [011] for PMN-PT(011). To study several samples with identical properties, the samples were broken into smaller parts which were investigated by different methods. Samples with the same number and a (letter or letter and number) suffix are pieces from the same sample. This is especially relevant for samples on PMN-PT(011), as the substrate has two different in-plane orientations that are investigated.

To regain the magnetic state after measurement, the common method is to anneal the sample at $T>T_C$. As the Curie temperature of $Fe_3O_4$ ($T_C$=858 K) is quite high, and heating the samples above the Curie temperature could change the oxidation state, the samples used for magnetoelectric coupling have not been subjected to a saturation field.

$Fe_3O_4$/PMN-PT(001)

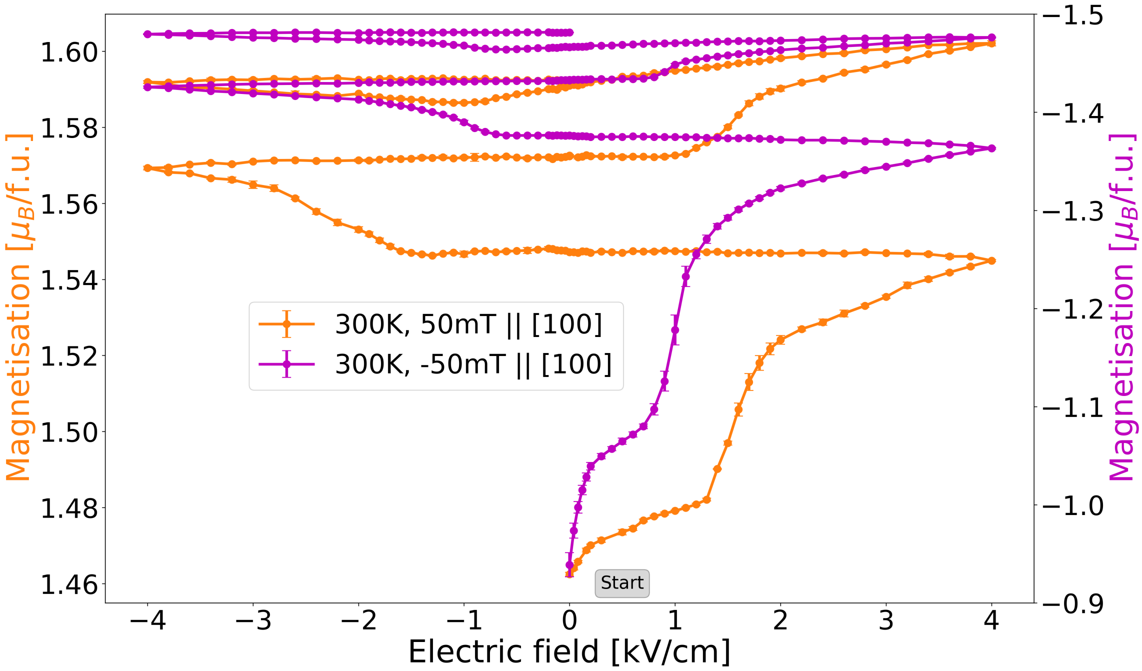

**Figure 7.10:** Magnetoelectric coupling measurement for sample F1C $Fe_3O_4$/PMN-PT(001) at 300 K with ±50 mT applied along the [100] direction and electric field between ±4 kV/cm. The -50 mT loops are taken directly after the +50 mT loops.

Fig. 7.10 shows the change in magnetisation of $Fe_3O_4$/PMN-PT(001) caused by ±4 kV/cm electric field loops in a static magnetic field of ±50 mT applied along the [100] direction at 300 K. The first two loops were measured in +50 mT (orange), after which the magnetic field was reversed to -50 mT. At an electric field value between ±1.3-1.6 kV/cm the magnetisation increases strongly. The total change for the first complete loop in +50 mT is 0.11 $\mu_B$/f.u. This increase can be repeated with quickly diminishing amplitude for subsequent loops (fig. 7.11). The electric field at which the jump occurs roughly coincides with the coercive field of electrical polarisation and maximum tensile strain of the PMN-PT substrate (see fig. 5.1 in chapter 5). For all loops after the second, the magnetisation crosses itself and shows a butterfly like curve. There is still a small remanent change, although the change per loop is less than 0.01 $\mu_B$/f.u. The butterfly shape of the later loops resembles the butterfly loop of the strain, with the tensile strain regime exhibiting lower magnetisation and the compressive strain regime exhibiting higher magnetisation. As the remanent increase decreases with each loop and the butterfly shape remains, for later loops the magnetisation should eventually only follow reproducible butterfly

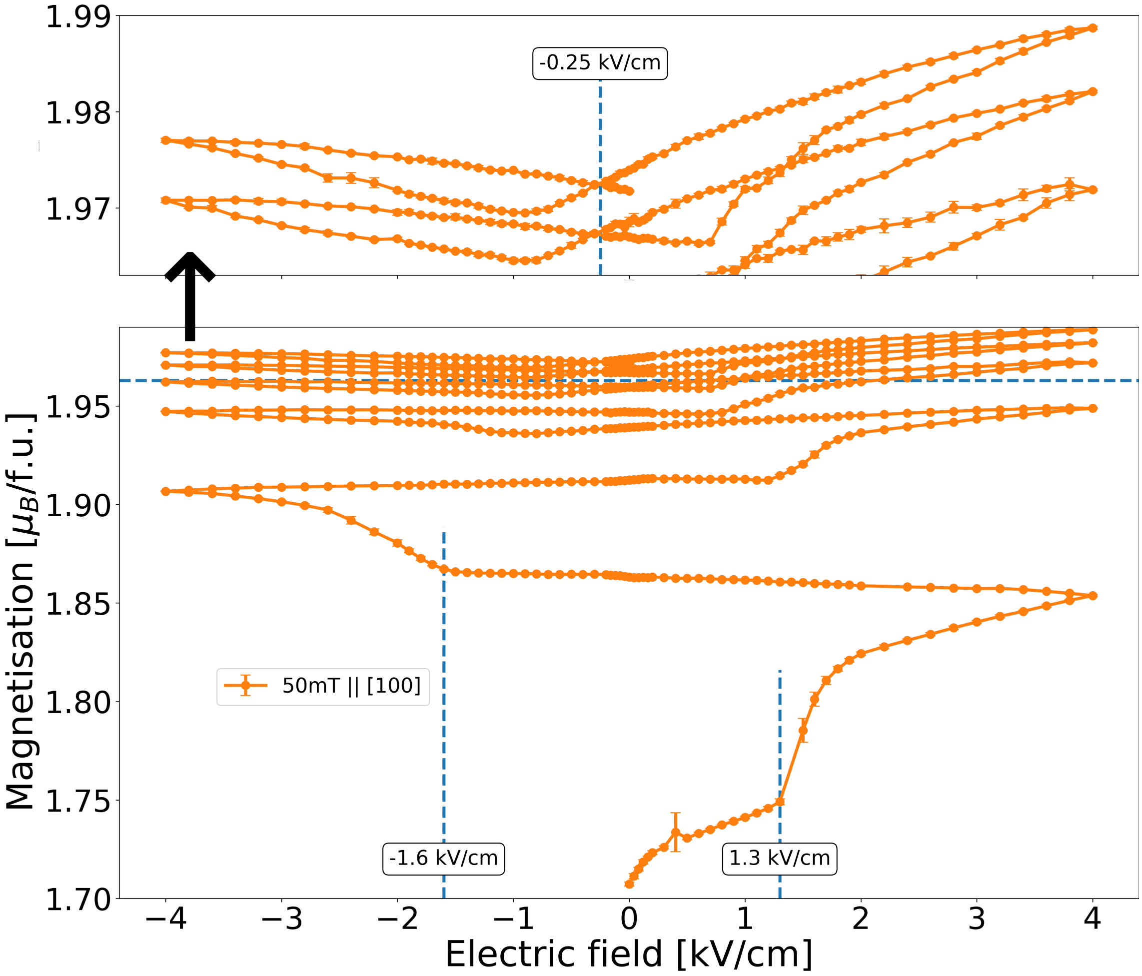

**Figure 7.11:** Magnetoelectric measurement of sample F1B $Fe_3O_4$/PMN-PT(001) showing multiple loops for +50 mT at 300 K. The top image shows a magnification of the upper part from the dashed line onwards. The electric field is applied along [001] and the magnetic field along [100].

loops. Upon switching the magnetic field direction, the behaviour is reset and the first two loops for negative field direction again show a large jump in magnetisation. The first loop for -50 mT exhibits a much larger change of -0.5 $\mu_B$/f.u. than the first loops for positive field. This is likely because the initial magnetisation state for -50 mT is much less ordered than for +50 mT and thus the magnetoelectric coupling can influence the magnetisation more.

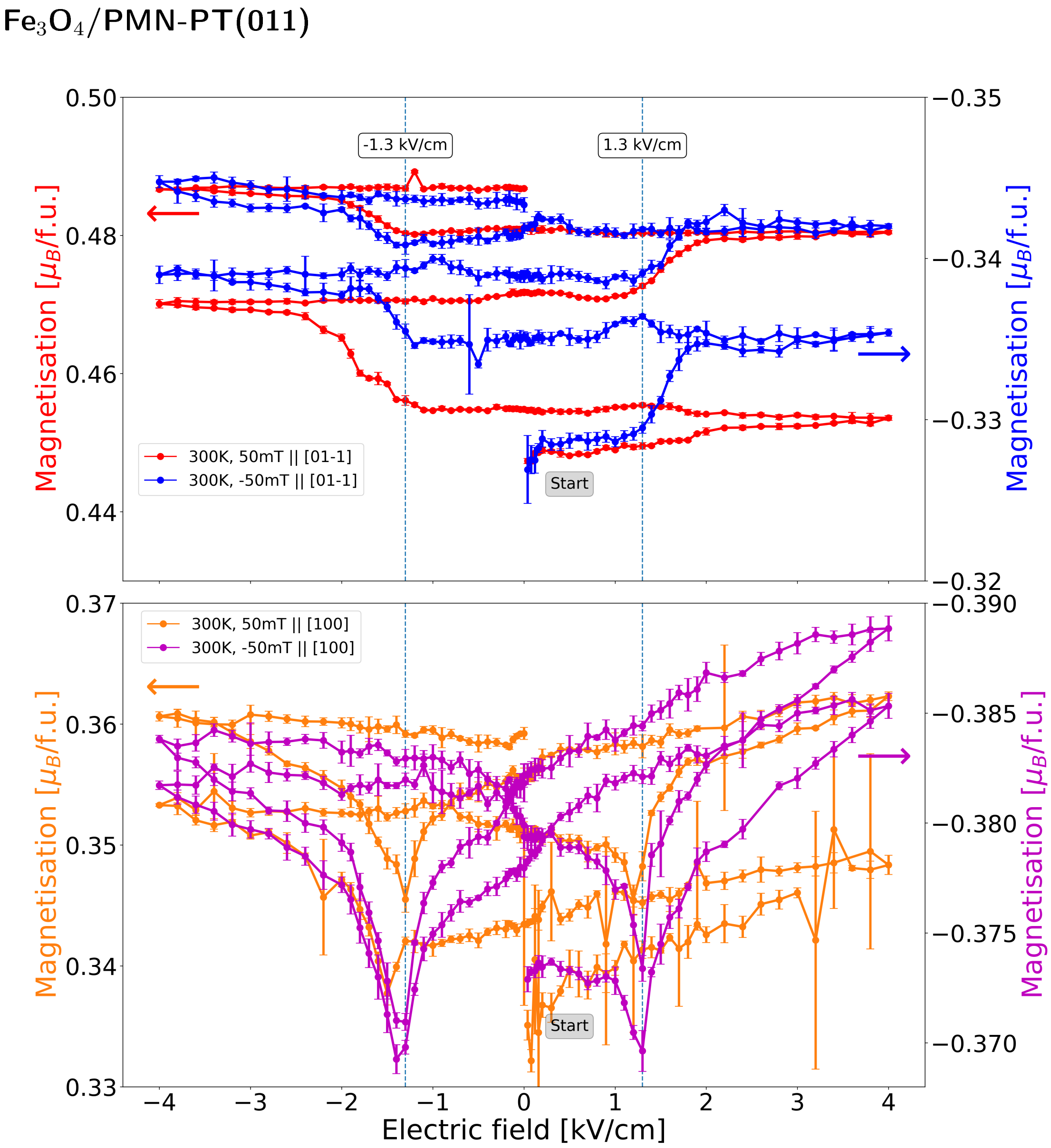

**Figure 7.12:** Magnetoelectric coupling measurement for sample F2 Fe$_3$O$_4$/PMN-PT(011) at 300 K with ±50 mT applied along the [01$\bar{1}$] (**top**, sample F2D) [100] direction (**bottom**, sample F2B) and electric field between ±4 kV/cm. The 50 mT loops for both orientations are measured using different sample pieces and the -50 mT loops are taken directly after the +50 mT loop.

Fig. 7.12 shows, analogous to the previous measurements, magnetoelectric loops for Fe$_3$O$_4$/PMN-PT(011) with the magnetic field along [01$\bar{1}$] (top) and [100] (bottom).

For the magnetic field along $[01\bar{1}]$, the behaviour is similar to the first loop for PMN-PT(001), with a jump in magnetisation at approximately ±1.3 kV/cm, but for multiple loops there is no crossing (fig. 7.13 top). The jump in magnetisation occurs at roughly the same electric field for all samples in $[01\bar{1}]$ direction, with the exact value varying slightly between samples. Between the jumps, the magnetisation increases linearly, as indicated by the blue dashed lines, with the slope decreasing with increasing number of loops. Conversely, if the magnetic field is along the [100] direction, the butterfly shape is immediately present in the magnetoelectric coupling measurement, although a slight remanent change is still visible (fig. 7.12 bottom and 7.13 middle). The crossover point varies for different samples between 0 kV/cm and -1 kV/cm. The shape of the butterfly loop is also sample dependent, varying between nearly symmetric and with pronounced minima in fig. 7.12 bottom and very asymmetric in fig. 7.13.

While there is a clear magnetoelectric coupling for 300 K, there is only negligible change in magnetisation along [100] with electric field at 50 K (fig.7.14). In the $[01\bar{1}]$ direction however, there is still an effect. The magnetisation follows the electric field linearly, with higher magnetisation for a negative electric field and a total change of 0.004 $\mu_B$/f.u. between ±4 kV/cm. This effect can't be attributed to the intrinsic ferroelectricity in $Fe_3O_4$ since this effect only exists below 38 K [13].

Field cooled measurements in ±50 mT, taken before the application of voltage and after two voltage cycles, also show an increase in magnetisation for +50 mT and reduction for -50m T, confirming that the change in magnetisation is remanent and does not revert to its original state when the electric field is removed, even for low temperatures (fig. 7.15).

In literature, a reduction in the Verwey transition temperature with electric field was observed after application of 10 kV/cm [14]. In the field-cooled magnetisation measurement along the $[01\bar{1}]$ direction in fig. 7.16, such a shift is not visible and the Vervey transition is stable, likely because the maximum applied electric field of 4 kV/cm is less than the electric field in literature.

However, an effect on the magnetic hysteresis at room temperature is observable (fig. 7.17). The coercive field reduces by 15% (i.e. from 0.148±0.003 T to 0.126±0.004 T), while the saturation magnetisation and remanence approximately remain constant, from 3.11±0.01 $\mu_B$/f.u. to 3.08±0.01 $\mu_B$/f.u. and from 2.85±0.01 $\mu_B$/f.u. to 2.80±0.01 $\mu_B$/f.u., respectively.

At 126 K, i.e. at the Verwey transition, no change of the hysteresis is found ($H_C$=0.127±0.003 T). The electric coercive field of PMN-PT is at about 8 kV/cm, so a switching of the polarisation is not achieved within the electric field range applied here [113]. If in the future an electric field higher than the coercive field of PMN-PT can be applied in the SQUID setup, this could answer the question how the Verwey transition can be influenced by strain and electric field.

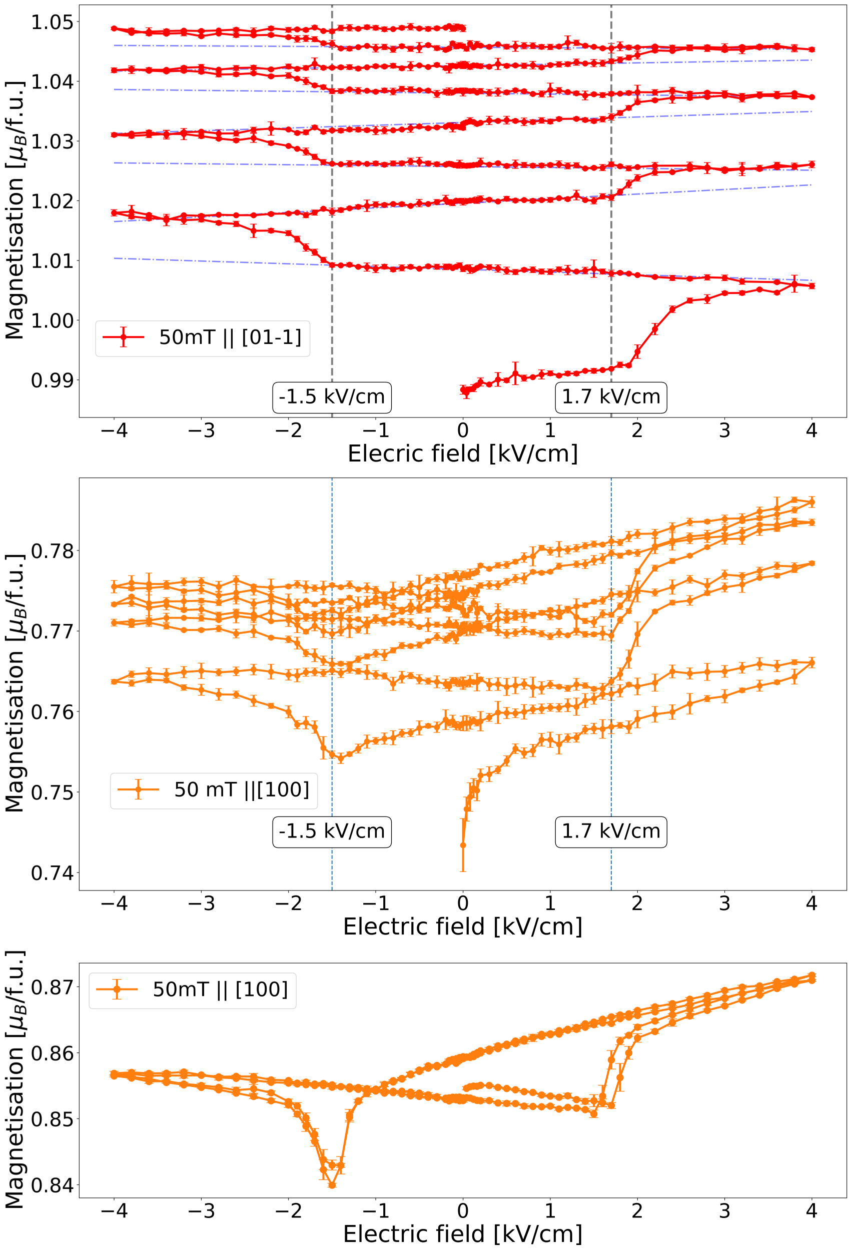

**Figure 7.13:** Magnetoelectric measurement for sample F3C Fe$_3$O$_4$/PMN-PT(011) showing multiple loops for +50 mT applied along [$01\bar{1}$] (**top**) and [100] (**middle**) at 300 K. The dashed blue lines in the top image indicate the change in magnetisation in the linear regime for each loop. On the **bottom**, the measurement along [100] in the non-remanent regime is shown for sample F5A Fe$_3$O$_4$/PMN-PT(011).

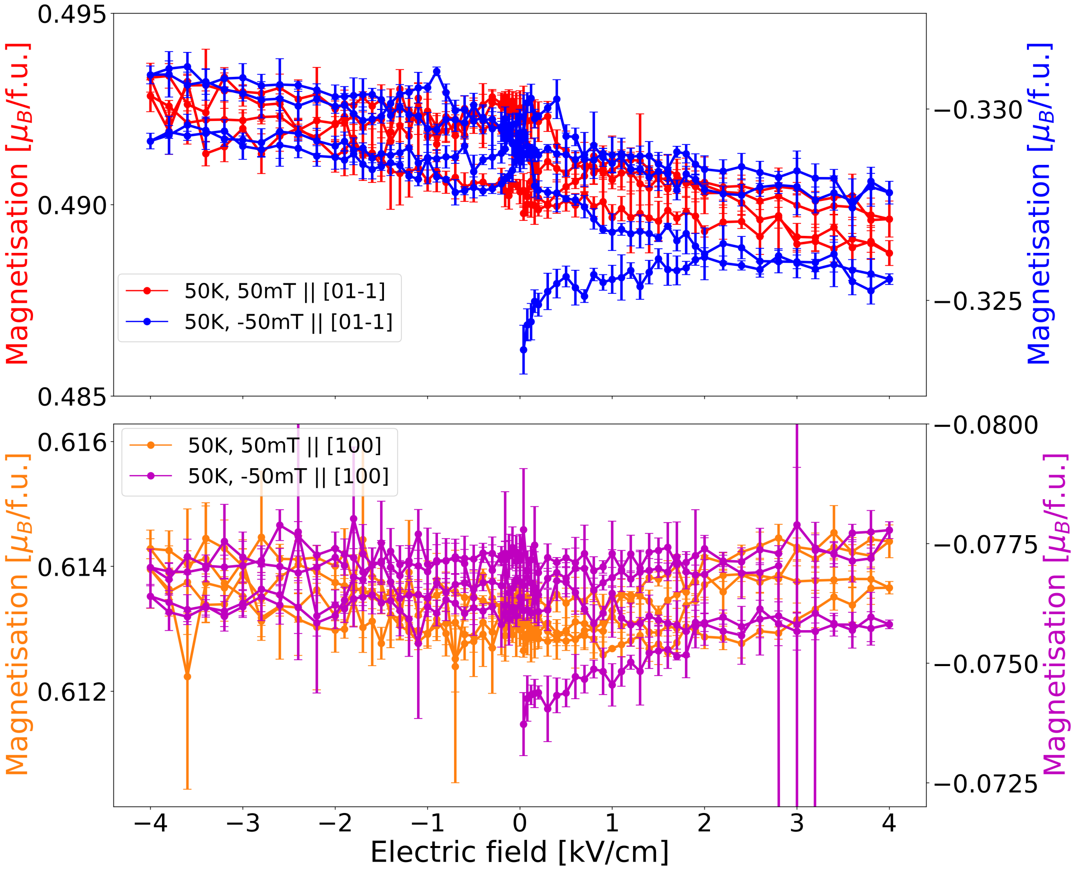

**Figure 7.14:** Magnetoelectric coupling measurement for sample F2 $Fe_3O_4$/PMN-PT(011) at 50 K with ±50 mT applied along the $[01\bar{1}]$ (**top**, sample F2D) [100] direction (**bottom**, sample F2B) and electric field between ±4 kV/cm. The 50 mT loops for both orientations are measured using different sample pieces and the -50 mT loops are taken directly after the +50 mT loop.

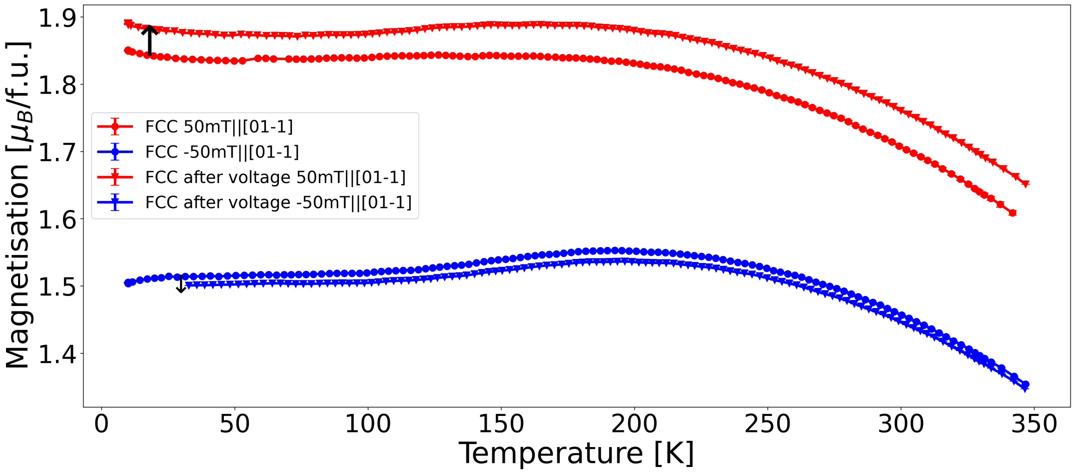

**Figure 7.15:** Field cooled magnetisation measurements of sample F5A $Fe_3O_4$/PMN-PT(011) along the $[01\bar{1}]$ direction. The first set was measured on the as prepared sample at ±50 mT and the second after two voltage cycle.

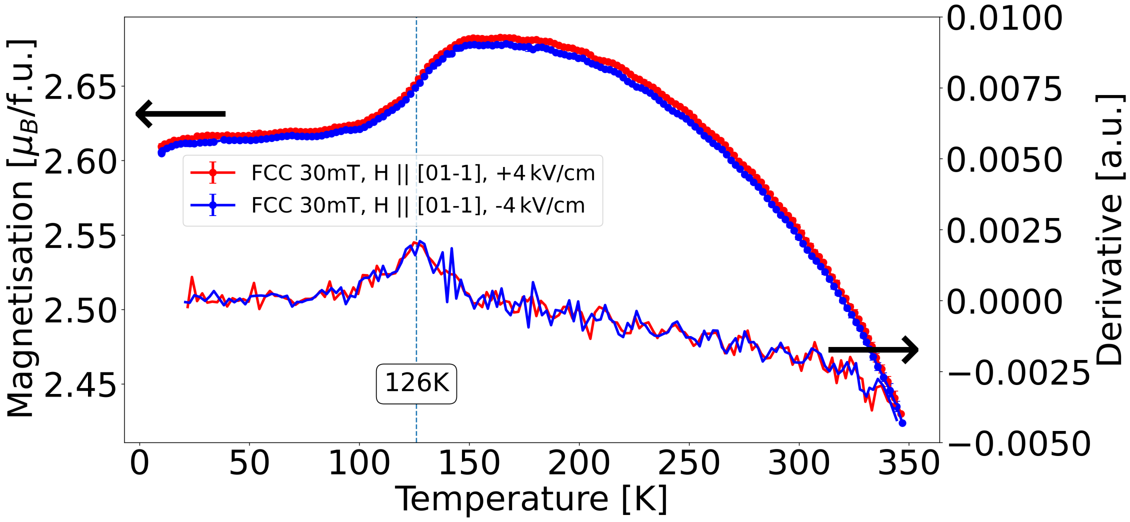

**Figure 7.16:** Field cooled magnetisation measurements of sample F2C1 $Fe_3O_4$/PMN-PT(011) at ±50 mT along the $[01\bar{1}]$ direction with an applied electric field of ±4 kV/cm.

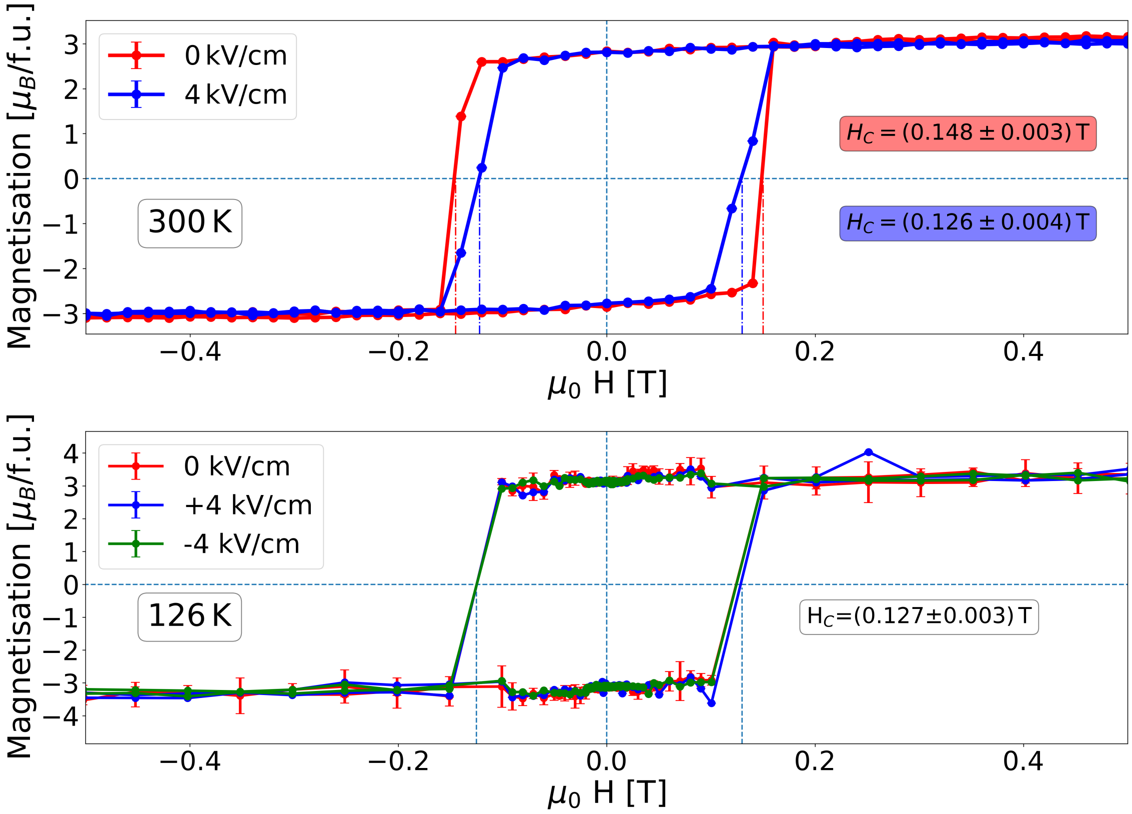

**Figure 7.17:** Hysteresis loops of sample F3C $Fe_3O_4$/PMN-PT(011) samples with the magnetic field along the $[01\bar{1}]$ direction with and without electric field. **Top:** at 300 K (sample F3); measurement performed by A. Sarkar. **Bottom:** at the Verwey transition temperature 126 K (sample F2C1)

## 7.2.3 Magnetoelectric coupling with PNR

Investigating the change of the magnetization with depth resolution may shed new insight into the switching behavior of magnetite films under strain by distinguishing switching due to interfacial strain and due to strain propagation throughout the layer. If the strain influence is mainly concentrated in the interface region, a large change of the magnetisation should be observed with little change in the rest of the film. Polarised neutron reflectometry (PNR) is the method of choice for such a problem, since it provides information about the magnitude and orientation of the magnetization with depth resolution.

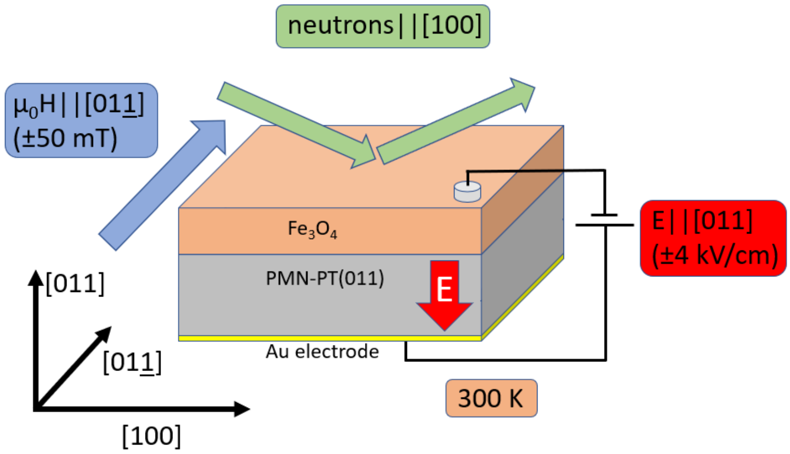

**Figure 7.18:** Sketch of the sample geometry for polarised neutron reflectometry.

PNR was performed with the polarized beam reflectometer (PBR) at the NIST Center for Neutron Research (NCNR). All measurements were performed at room temperature and in applied magnetic field of 50 mT along the [01$\bar{1}$] direction of the PMN-PT(011) substrate and thus a scattering direction along [100] (fig. 7.18). Similar to the SQUID measurements, the electric field is applied along the [011] out-of-plane direction.

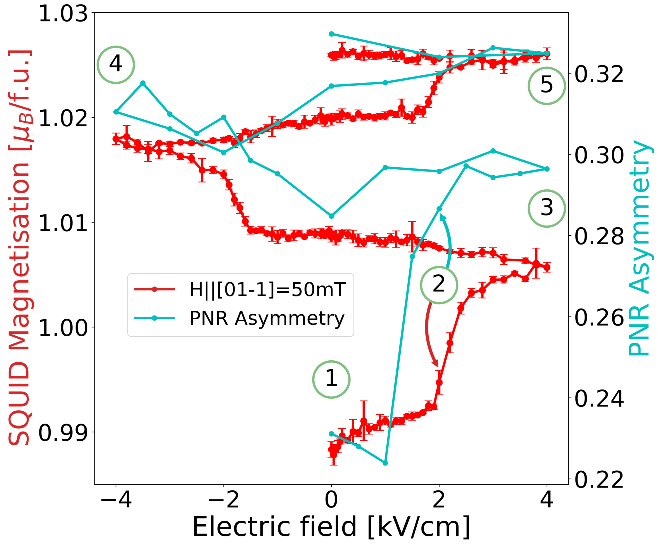

**Figure 7.19:** Comparison of the magnetoelectic coupling measurement of sample F3 Fe$_3$O$_4$/PMN-PT(011) with PNR asymmetry at Q=0.02 Å$^{-1}$.

As the PNR asymmetry, $(uu + dd)/(uu - dd)$, is a measure of magnetisation, the neutron results can be compared with the magnetoelectric SQUID measurements. The intensity of both non spin-flip channels was measured at Q=0.02 Å for 0.5 kV/cm steps while ramping the voltage. The Q-value was chosen, because the intensity is very high, and a clear difference between the up and down channels is visible. The asymmetry shows similar behaviour as the magnetisation in SQUID when sweeping the electric field between ±4 kV/cm (fig. 7.19), which confirms that the macroscopic magnetisation behaves similarly for both measurements.

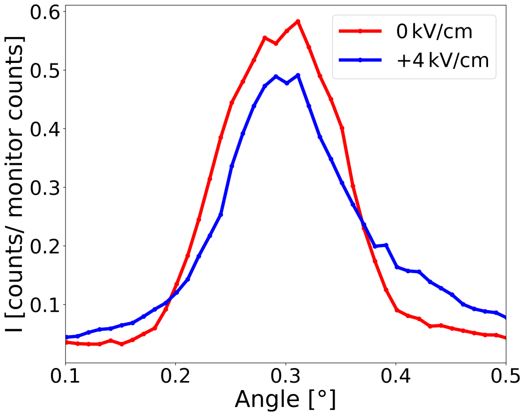

**Figure 7.20:** Rocking curves for the first and last PNR measurement: 0 kV/cm and +4 kV/cm of sample F3 $Fe_3O_4$/PMN-PT(011).

In contrast to the voltage XRR measurements, the rocking curve in PNR shows only slight broadening (fig. 7.20), the reason for this is still unclear.

At the indicated electric fields, 0 kV/cm, 2 kV/cm, 4 kV/cm, -4 kV/cm, and 4 kV/cm again, PNR curves for all four channels were measured. For a direct comparison to SQUID measurement, the sample was exposed only to a single continuous electric field loop. This means that after the initial measurement, the field was ramped to 2 kV/cm and kept there during the PNR measurement, after which, the electric field was ramped from 2 kV/cm to 4 kV/cm and the next PNR measurement taken. The measured reflectometry curves are reduced with Reductus, which includes correcting for diffuse scattering. Fits performed with Refl1D [114] (fig. 7.21). All five data sets were fit together, to maintain a consistent model of the sample.

**Table 7.3:** Fit of the PNR measurements of F3 $Fe_3O_4$/PMN-PT(011). The magnetisation angle is the angle between the magnetisation of the layer and the applied magnetic field (and thus the neutron polarisation). The thickness of the $Fe_3O_4$ layer remained independent for the first measurement and fixed for the later 4.

| Electric field [kV/cm] | Layer | Thickness [Å] | roughness [Å] | Nuclear SLD [$10^{-6}$Å$^{-2}$] | Magnetic SLD [$10^{-6}$Å$^{-2}$] | Magnetisation angle [°] |
|---|---|---|---|---|---|---|
| 0 | Top | $19.0^{+0.1}_{-0.1}$ | $5.94^{+0.06}_{-0.05}$ | $4.69^{+0.04}_{-0.04}$ | $0.49^{+0.01}_{-0.01}$ | $61^{+3}_{-2}$ |
| 0 | $Fe_3O_4$ | $434.2^{+1.0}_{-0.9}$ | $10.5^{+0.1}_{-0.1}$ | $6.30^{+0.01}_{-0.01}$ | $0.34^{+0.01}_{-0.01}$ | $32^{+2}_{-4}$ |
| 0 | Substrate | - | $23.6^{+0.2}_{-0.2}$ | $4.14^{+0.04}_{-0.02}$ | - | - |
| +2 | Top | $18.2^{+0.1}_{-0.1}$ | $8.0^{+0.1}_{-0.1}$ | $4.69^{+0.04}_{-0.04}$ | $0.49^{+0.01}_{-0.01}$ | $67^{+1}_{-1}$ |
| +2 | $Fe_3O_4$ | $447.0^{+1.2}_{-1.2}$ | $14.9^{+0.1}_{-0.1}$ | $6.30^{+0.01}_{-0.01}$ | $0.41^{+0.01}_{-0.01}$ | $21^{+1}_{-1}$ |
| +2 | Substrate | - | $22.6^{+0.2}_{-0.1}$ | $4.14^{+0.04}_{-0.02}$ | - | - |
| +4 | Top | $11.3^{+0.1}_{-0.1}$ | $8.9^{+0.1}_{-0.1}$ | $4.69^{+0.04}_{-0.04}$ | $0.20^{+0.01}_{-0.01}$ | $-88^{+1}_{-2}$ |
| +4 | $Fe_3O_4$ | $447.0^{+1.2}_{-1.2}$ | $8.3^{+0.1}_{-0.1}$ | $6.30^{+0.01}_{-0.01}$ | $0.45^{+0.01}_{-0.01}$ | $28^{+1}_{-1}$ |
| +4 | Substrate | - | $23.5^{+0.2}_{-0.3}$ | $4.14^{+0.04}_{-0.02}$ | - | - |
| -4 | Top | $8.8^{+0.1}_{-0.1}$ | $8.2^{+0.1}_{-0.1}$ | $4.69^{+0.04}_{-0.04}$ | $0.49^{+0.01}_{-0.02}$ | $126^{+1}_{-2}$ |
| -4 | $Fe_3O_4$ | $447.0^{+1.2}_{-1.2}$ | $13.3^{+0.1}_{-0.1}$ | $6.30^{+0.01}_{-0.01}$ | $0.47^{+0.02}_{-0.01}$ | $21^{+1}_{-2}$ |
| -4 | Substrate | - | $22.7^{+0.1}_{-0.2}$ | $4.14^{+0.04}_{-0.02}$ | - | - |
| +4 | Top | $10.1^{+0.1}_{-0.1}$ | $6.1^{+0.1}_{-0.1}$ | $4.69^{+0.04}_{-0.04}$ | $0.47^{+0.02}_{-0.01}$ | $-28^{+1}_{-3}$ |
| +4 | $Fe_3O_4$ | $447.0^{+1.2}_{-1.2}$ | $11.6^{+0.1}_{-0.1}$ | $6.30^{+0.01}_{-0.01}$ | $0.48^{+0.01}_{-0.01}$ | $25^{+2}_{-1}$ |
| +4 | Substrate | - | $21.0^{+0.2}_{-0.1}$ | $4.14^{+0.04}_{-0.02}$ | - | - |

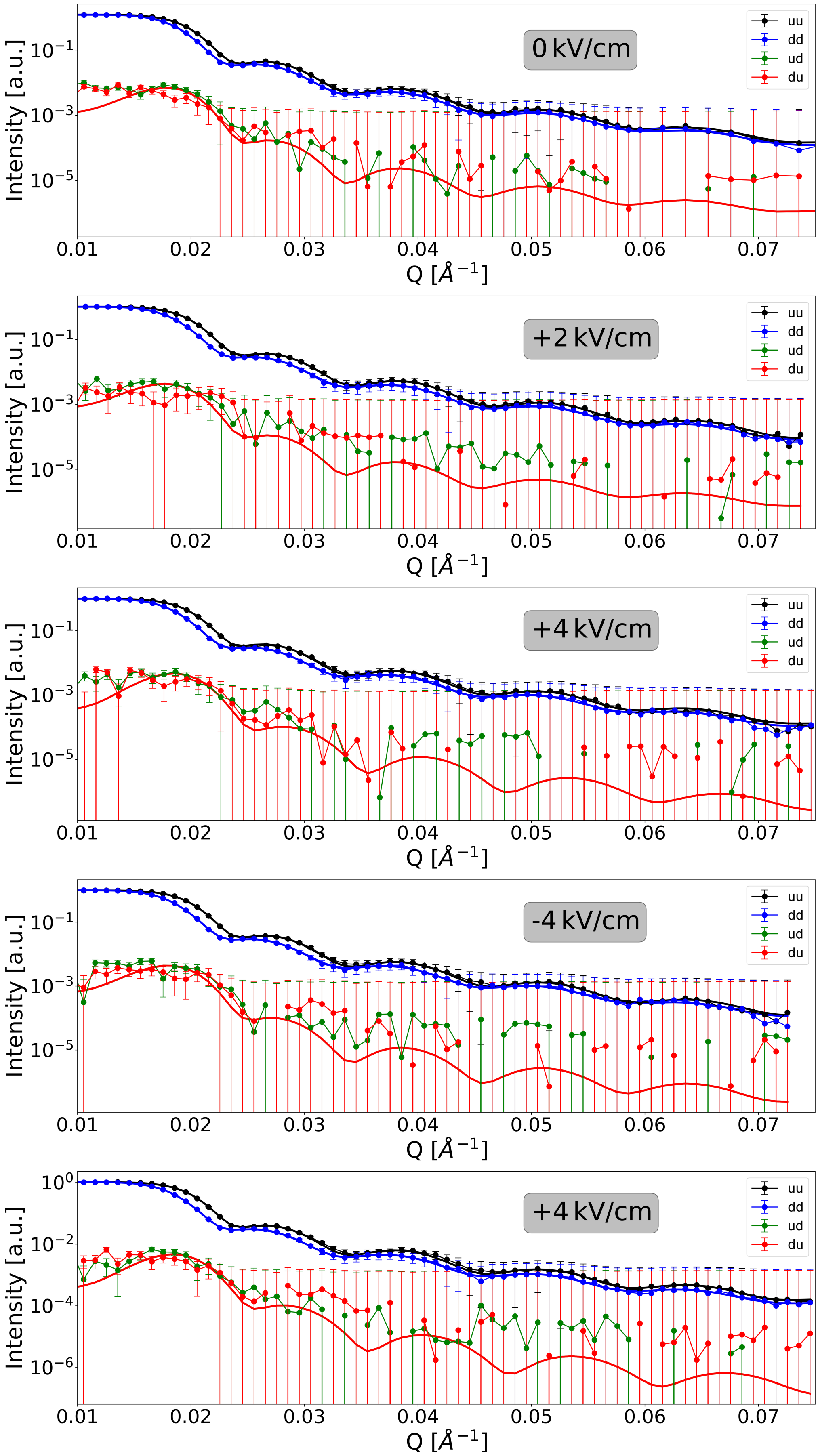

**Figure 7.21:** PNR measurements with fit of sample F3 $Fe_3O_4$/PMN-PT(011) with the application of voltage.

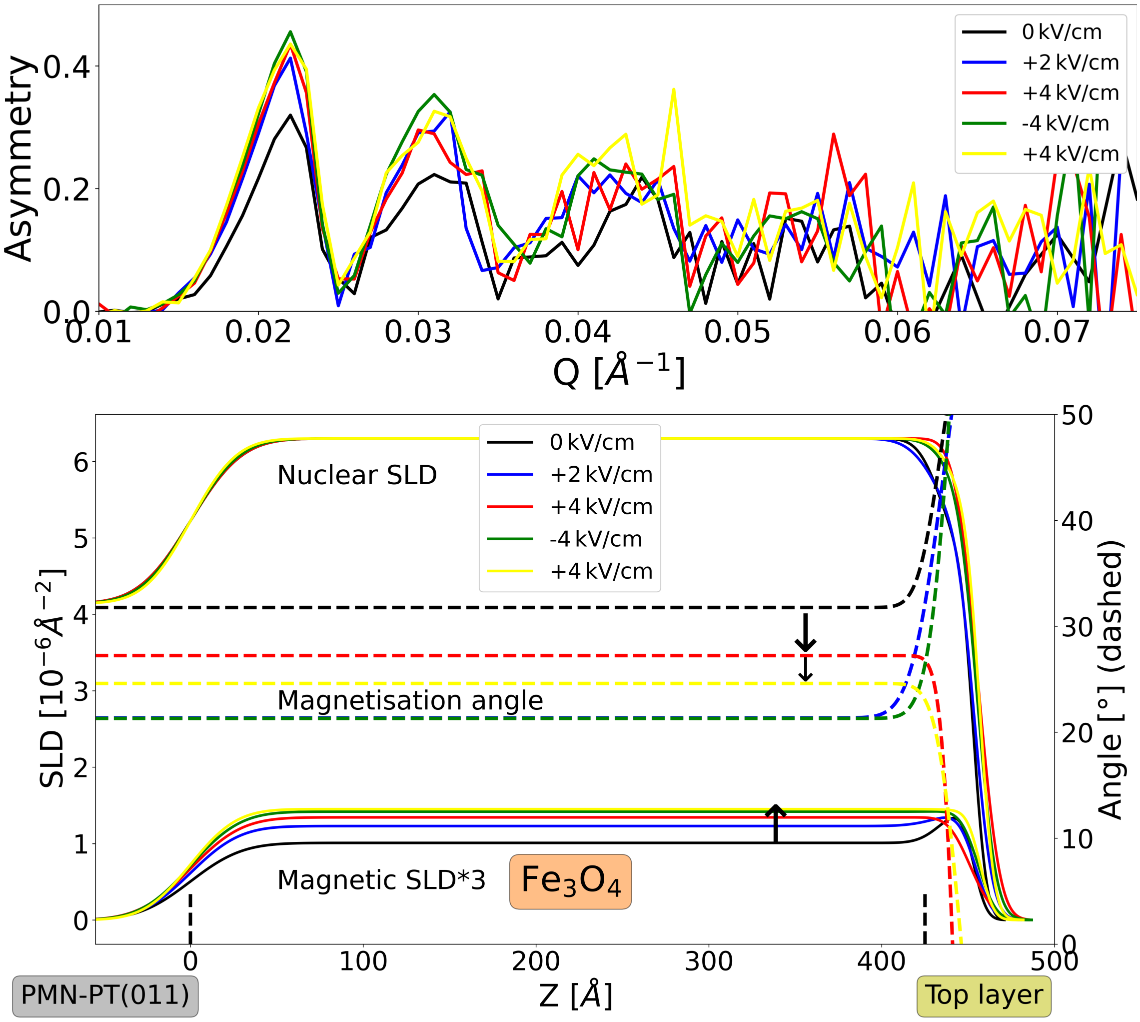

**Figure 7.22:** Asymmetry of the uu and dd channels of corresponding to the PNR curves in fig. 7.21 (**top**) and scattering length density profiles (**bottom**). The magnetic SLD is multiplied by a factor of 3 for better visibility.

The nuclear scattering length density (SLD) of all layers were fixed to the same value for all 5 measurements, while the thickness of the $Fe_3O_4$ layer remained independent for the first measurement and fixed for the later 4. The reason was to account for possible structural changes in the sample upon the first application of voltage. The magnetic SLD, the magnetisation angle of the $Fe_3O_4$ layer and the top layer parameters were allowed to vary independently. Fixing the top layer magnetisation angle to the same value as for the $Fe_3O_4$ layer resulted in a worse fit (see supplementary information S.2). The fit parameters are listed in table 7.3. Overall, the simulation agrees very well with the measurements for all electric fields.

The fits reveal a steady increase of the $Fe_3O_4$ magnetic scattering length density (MSLD) with electric field (although the change between the last three measurements is relatively small), as was expected from the increase in the asymmetry, while the top layer magnetisation remains nearly constant (fig. 7.22). This means that the interface between substrate and film behaves like the $Fe_3O_4$ layer and the strain is transferred to the whole layer. With increasing electric field, the angle

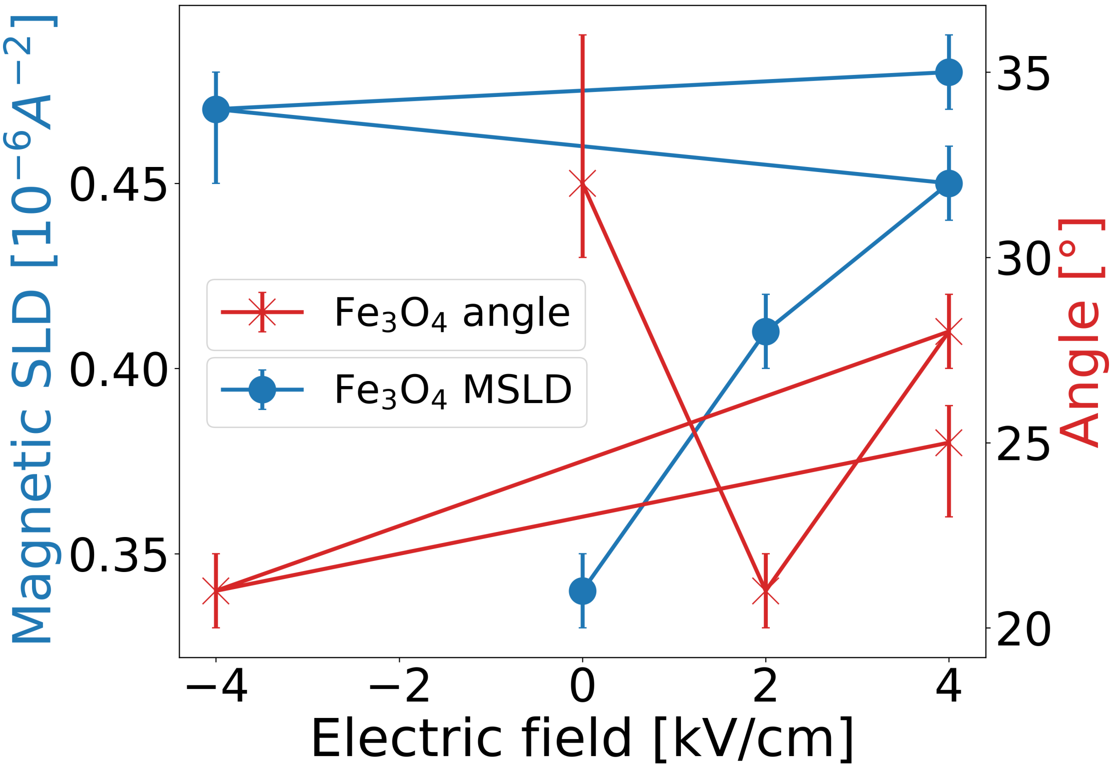

**Figure 7.23:** Change of magnetic SLD and magnetisation angle of the $Fe_3O_4$ layer with electric field.

of the $Fe_3O_4$ magnetisation to the magnetic field decreases, i.e. the magnetisation rotates towards the $[01\bar{1}]$ easy axis. There is no correlation between the change in MSLD and the angle of magnetisation with electric field (fig. 7.23).

The total change in magnetic SLD of 41% between the first and last measurement is significantly higher than the magnetisation change of 8% for the corresponding SQUID measurement. This could be due to the preceding exposure of the sample to voltage and magnetic field during the PNR measurement.

The listed errors are the calculated 90% confidence intervals of the parameter, as given by the Refl1D program. It has to be noted that the error for the magnetisation angle is probably underestimated, especially for the top layer, as the spin-flip signal reaches background levels at around 0.035 Å $^{-1}$. Since the magnetisation angle is determined by fitting the intensities of the spin-flip and non spin-flip channels, the diminished intensity of the spin-flip channel at higher Q introduces an uncertainty into the angle determination. Given that the roughness of the top layer is nearly as large as its thickness, a meaningful interpretation of the magnetisation angle is likely impossible.

The relation of the PNR measurement to the previous SQUID measurement will be discussed in the next section.

## 7.3 Interpretation of magnetoelectric coupling effects

To understand the effects involved in the magnetoelectric coupling discussed in the previous section, first the results for $Fe_3O_4$/PMN-PT(001) will be analysed. From the SQUID magnetisation measurements with varying electric field in figs. 7.10 and 7.11, it was found that the change in magnetisation for the first few electric field loops is different from later loops. Initially, there is a strong remanent increase in the magnetisation, with a pronounced jump around the electrical coercive field of the substrate (figs. 7.10 and 7.11 bottom).

In the remanent regime, the increase in magnetisation is likely caused by a realignment of the magnetisation along the [100] direction due to the effects of magnetostriction on the easy axis of the magnetite film. A sketch of the geometry is given in fig. 7.24. As the magnetostriction constant of magnetite along [100] is negative ($\lambda_{100} \sim$-$2{\cdot}10^{-5}$ [115]), the magnetisation should increase for increasing compressive strain. For PMN-PT(001), the in-plane strain between zero electric field and the coercive field is tensile, while for fields above ~2 kV/cm it becomes compressive (see fig. 5.1 top-right). As the applied magnetic field is constant, a change in strain towards the compressive regime shifts the magnetic easy axis towards [100], explaining the jump in magnetisation at the coercive electrical field. The reorientation also explains the much larger increase in magnetisation for the first loop at -50 mT compared to +50 mT in fig. 7.10, as the initial magnetisation state at -50 mT is less ordered.

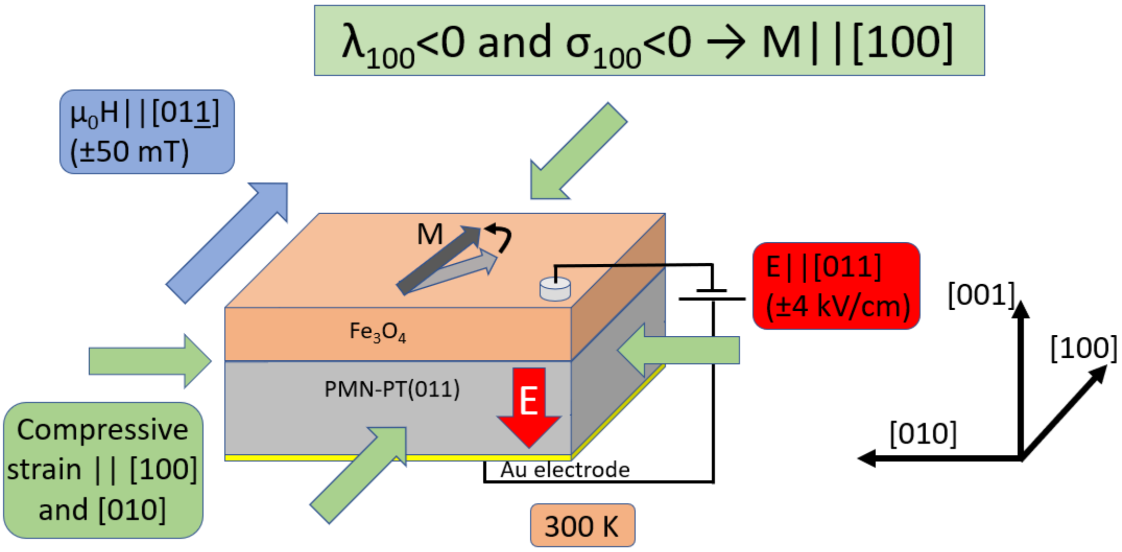

**Figure 7.24:** Sketch of the magnetisation reorientation in the remanent regime for $Fe_3O_4$/PMN-PT(001).

After 4-5 loops, there is little increase of the magnetisation per loop. Instead the magnetisation follows a butterfly shape (fig. 7.11 top) similar to the strain of PMN-PT(001). Hence this behaviour is called butterfly regime.

Because of magnetite's negative $\lambda_{100}$ magnetostriction constant, the magnetisation should decrease for increasing tensile strain, i.e. between 0 kV/cm and ∼ ±2 kV/cm. This matches exactly to the observed magnetisation behaviour (fig. 7.11 top). The magnetisation exhibits a butterfly loop with the lowest magnetisation for maximum tensile strain, i.e. at the coercive electric field of PMN-PT(001) (∼ ±1 kV/cm), and increasing magnetisation for higher compressive strain. A similar effect was observed in $La_{2/3}Sr_{1/3}MnO_3$/PMN-PT(001) heterostructures [100]. However pure strain mediation would result in a symmetric butterfly loop, which is not the case in the experiment for $Fe_3O_4$/PMN-PT(001), as the crossover point is shifted toward negative electric field. To understand this asymmetry, strain and polarisation experienced by $Fe_3O_4$ through the substrate under applied electric field are plotted qualitatively in fig. 7.25 top. This model is only qualitative, as the shape of the strain and polarisation curves are recreated based on the literature figures [47] and normalised to 1. The coercive field is taken to be 1.6 kV/cm, as in literature. If the magnetisation is influenced by the substrate polarisation, it should follow the shape of the polarisation hysteresis. Combining the inverted butterfly shape for strain coupling and a hysteretic behaviour for the polarisation coupling, results in an asymmetric butterfly loop, with the crossover point at negative electric field (fig. 7.25). The relative contribution of strain and polarisation to the magnetoelectric coupling is estimated in the following, by varying the magnitude of the coupling to match the measured magnetisation. As the model is based purely on the shape of the coupling given in literature and the electrical coercive field, it is only meant as a approximation. A quantitative model would require measurement of strain and polarisation for the specific substrates used, as even small deviations in the PMN to PT composition can have a large influence on the properties of the substrate, especially close to the $PMN_{0.7}$-$PT_{0.3}$ stoichiometry [116].

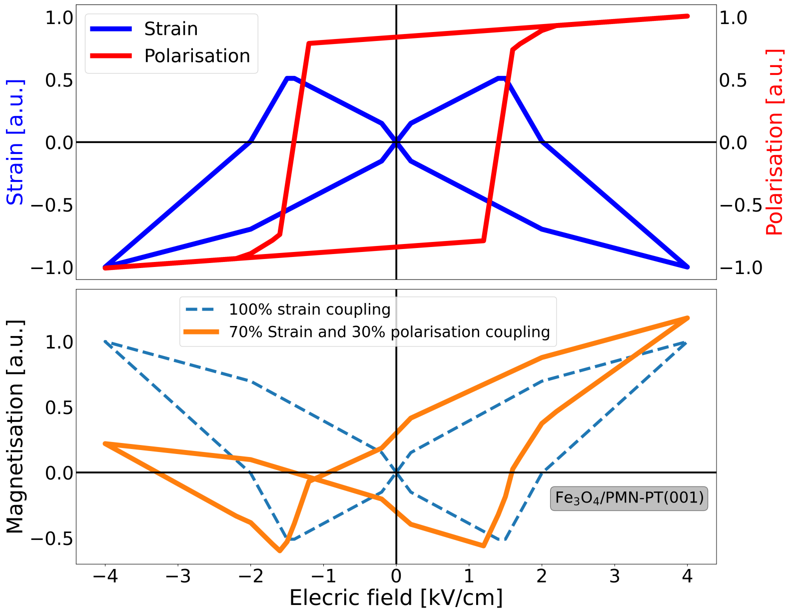

**Figure 7.25:** Strain and polarisation contributions to the magnetoelectric coupling for PMN-PT(001).

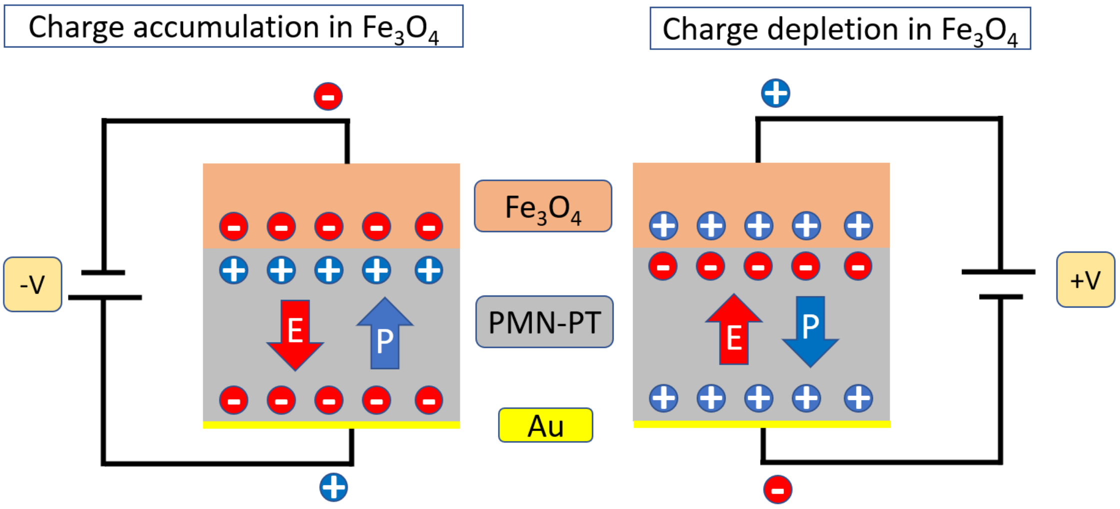

**Figure 7.26:** Polarisation and related charge accumulation or depletion.

The polarisation coupling could be due to charge accumulation and depletion of the $Fe_3O_4$ layer (fig. 7.26) [117]. In the neutral state, $Fe_3O_4$ has 16 electrons, 5 on each of the $Fe^{3+}$ ions, with the spins on one ion aligned antiparallel to the spins on the other $Fe^{3+}$ ions, and 6 electrons on the $Fe^{2+}$ ion (see chapter 2.3.2). As the 3d orbitals are more than half filled for $Fe^{2+}$, 5 electrons are aligned parallel and the last one antiparallel. Due to Hubbard splitting, the antiparallel electron has the highest energy and is the easiest to remove when a positive voltage is applied to the sample. A removal of the antiparallel electron increases the magnetisation. This fits to the observed behaviour, as a positive voltage increases the magnetisation and a negative voltage decreases it. This explanation can be supported by future studies of other transition metal oxide systems with a transition metal like Mn, which has a less than half filled 3d orbital. In that case, the voltage dependence of the linear component should be reversed, i.e. a decrease in magnetisation for increasing voltage. Combining strain and polarisation coupling, the asymmetric butterfly loop observed in the measurement can be recreated very well. The ratio of strain and polarisation contribution was varied to reproduce the overall shape of the measured butterfly loop, as well as the crossover point.

Comparing this model to the magnetisation loops of fig. 7.11 top, only the electrical coercive field of PMN-PT has to be reduced. Then the model fits very well to the measured data (fig. 7.27). The reduction in coercive field is likely due to structural effects, as for the first electric field loop, $E_C$ was close to the literature value. Thus the narrower butterfly loop is not attributed to magnetoelectric coupling, but sample deterioration. The main contribution to the magnetoelectric coupling is the strain with 80% of the total coupling and polarisation coupling accounting for the remaining 20%.

For $Fe_3O_4$/PMN-PT(011), the behaviour along the two in-plane directions is substantially different from each other (fig. 7.12). Along [100], the response of the magnetisation with electric field is similar to the case described above for PMN-PT(001), as the strain along [100] for both substrate orientations describes a butterfly loop

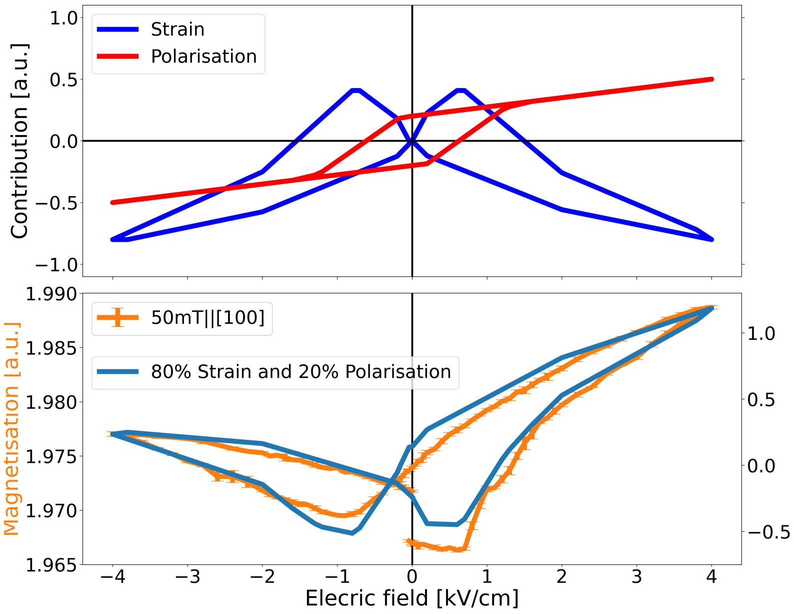

**Figure 7.27:** Qualitative model of the magnetoeelctric coupling in sample F1 $Fe_3O_4$/PMN-PT(001).

(fig. 7.12 bottom). For $Fe_3O_4$/PMN-PT(011) there is almost no remanent increase per electric field loop, as the easy axis is along [01$\bar{1}$]. Hence the remanent regime doesn't exist. Thus the behaviour along [100] is mainly an inverse magnetostriction and polarisation effect, without magnetisation reorientation. The butterfly shape has one important difference however, as there is an observable negative jump at the coercive field. There is a definite sample dependence for the measurements along [100], with some showing a symmetric loop (fig. 7.14 bottom) and others very asymmetric (fig. 7.13 bottom). Both loops can be modelled, however, by increasing the polarisation contribution for increasing asymmetry and introducing a contribution of the strain along [01$\bar{1}$] to account for the strain jump (fig. 7.28). The sharp decrease at the strain jump is likely due to the sudden anisotropy change favouring an alignment of the magnetisation along [01$\bar{1}$], as the strain jump towards the tensile regime coupled with the positive magnetostriction coefficient along that direction. This in turn reduces the magnetisation along [100]. As the strain along [01$\bar{1}$] quickly reverts to the remanent compressive regime, the magnetisation increases again. Both magnetisation loops mentioned above (fig. 7.14 bottom and 7.13 bottom), can be modelled well with the inclusion of the strain along [01$\bar{1}$] (fig. 7.29 and 7.30). The contribution to the magnetoelectric coupling from the strain along [100] is roughly twice as large as that along [01$\bar{1}$]. The polarisation coupling accounts for 20% in fig. 7.29 and is absent in fig. 7.30.

Along [01$\bar{1}$], the magnetisation behaviour at 300 K is entirely remanent (fig. 7.13). The magnetostriction constant along [011] for magnetite is $\lambda_{011} \sim 1\cdot 10^{-4}$ ($\lambda_{111} \sim 8\cdot 10^{-5}$) and, as seen in fig. 7.6 the magnetic easy axis lies along [01$\bar{1}$]. As $\lambda_{011}$ is positive, tensile strain increases the magnetisation. At 0 kV/cm, the strain along [01$\bar{1}$] is strongly compressive (negative) which, coupled with the positive magnetostriction coefficient suppresses the alignment of the magnetisation along [01$\bar{1}$]. When the

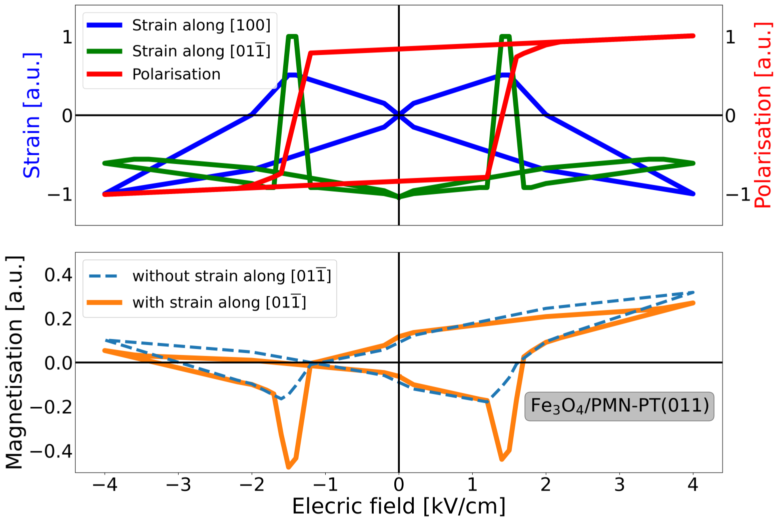

**Figure 7.28:** Strain and polarisation contributions to the magnetoelectric coupling for PMN-PT(011). For the blue dashed line the contributions are 70% strain along [100] and 30% polarisation coupling. For the orange line the contributions are 41% strain along [100], 41% along [01$\bar{1}$], and 18% polarisation coupling.

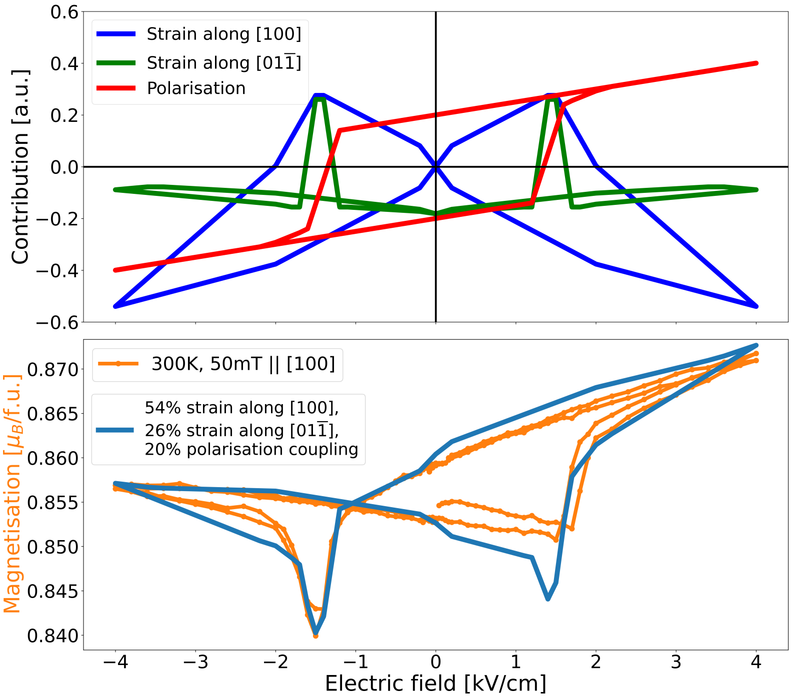

**Figure 7.29:** Strain and polarisation contributions to the magnetoelectric coupling for F5 Fe$_3$O$_4$/PMN-PT(011).

electric field is ramped up and reaches the coercive electric field of PMN-PT, the strain suddenly jumps from strongly compressive towards the tensile regime. This creates an anisotropy jump which favours the alignment of the magnetisation along [01$\bar{1}$]. Additionally, as the strain along [100] also reaches its maximum tensile (positive) value at the coercive electric field and $\lambda_{100}$ is negative, this effect is further enhanced. Since [01$\bar{1}$] is already the magnetic easy axis, the reorientation is rema-

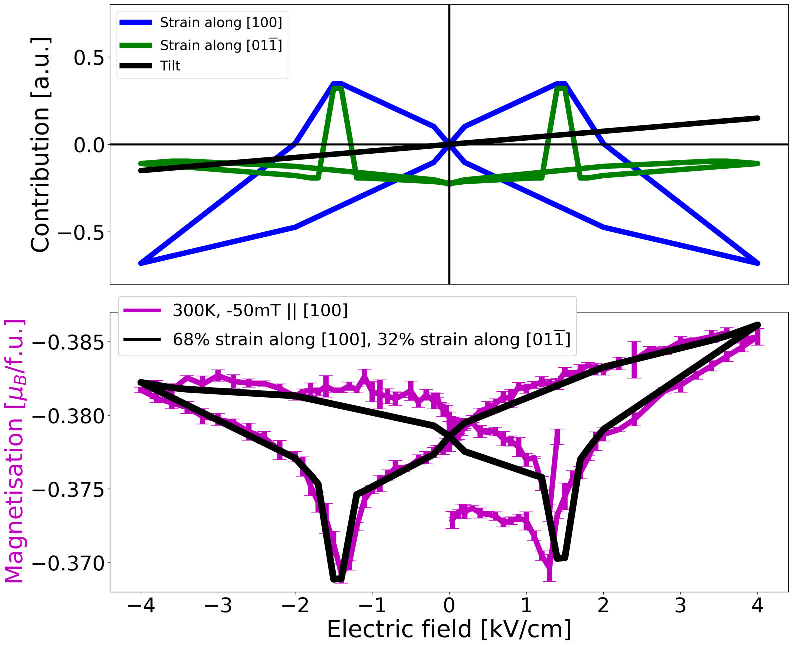

**Figure 7.30:** Strain and polarisation contributions to the magnetoelectric coupling for F2 $Fe_3O_4$/PMN-PT(011).

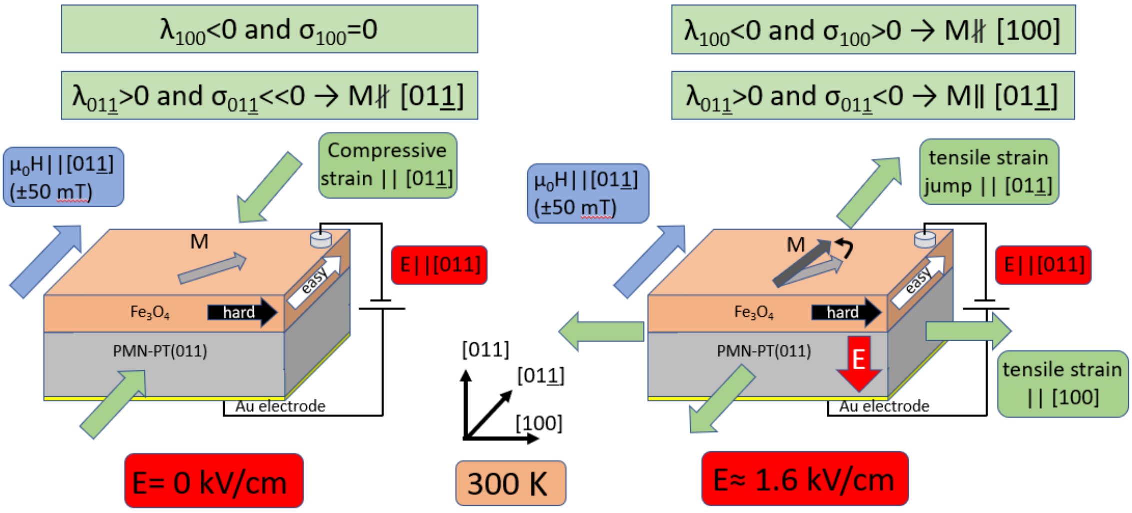

**Figure 7.31:** Sketch of the magnetisation reorientation in the remanent regime for $Fe_3O_4$/PMN-PT(011).

nent, explaining the plateaus in the SQUID measurements. The increase while the field is ramped from negative to positive tends to be larger than in the opposite direction, mirroring the asymmetry of the butterfly loops caused by polarisation coupling (fig. 7.32). This indicates that polarisation coupling also plays a role here.

PNR measurements were performed to determine if the remanent change is localised at the substrate-film interface region. However, there is no difference between the behaviour at the interface and in the film (fig. 7.22). This is somewhat surprising, given that the polarisation coupling should be locallised at the interface, but the

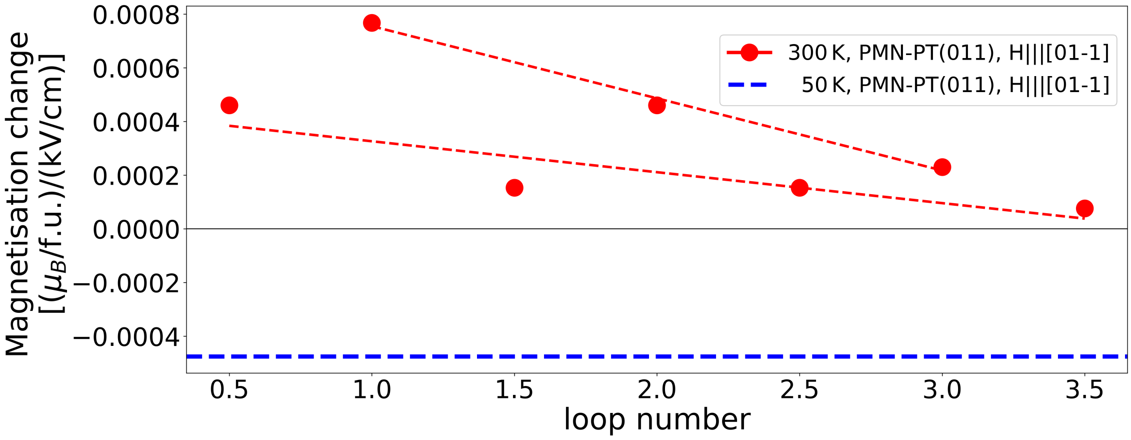

**Figure 7.32:** Relative change in magnetisation in the linear regime at 300 K (fig. 7.13 top) (red points, red dashed line shows a linear fit) and linear change at 50 K (fig. 7.14 top). The half-integer loop numbers denote a change of the electric field from positive to negative, while integer numbers relate to a sweep from negative to positive.

inclusion of an interlayer did not result in a better fit of the data. The top layer magnetisation is mostly unaffected by the electric field however. This could be either due to a decoupled (relaxed) strain state that is not affected by the piezostrain from the substrate, or a change in magnetisation is masked by the roughness, which in the fit is nearly as high as the toplayer thickness. In the film, the magnetic SLD increases for every measurement, in agreement with the SQUID data.

In the 50 K SQUID measurements, the strain coupling is severely reduced, as the polar nanoregions in PMN-PT get clamped and can no longer rotate [118]. An almost identical behaviour to the one measured along $[01\bar{1}]$ for $Fe_3O_4$/PMN-PT(011) was very recently described in $La_{2/3}Sr_{1/3}MnO_3$/PMN-PT(001) heterostructures [119]. The switching mechanism is attributed to a linear strain change, as the electrical coercive field of PMN-PT is higher than the applied field. Interestingly, the effect is not visible along [100], even though the strain in the linear regime is higher along [100] than $[01\bar{1}]$.

## 7.4 Conclusion

$Fe_3O_4$/PMN-PT(001) and $Fe_3O_4$/PMN-PT(011) samples were successfully prepared by PLD. The samples are crystalline, however have a high defect concentration, as seen in HRTEM measurements. XRR measurements show broad rocking curves on the plateau of total reflection, indicating a diffuse surface of the film. The $Fe_3O_4$ phase was confirmed by HAXPES, which showed a combination of $Fe^{2+}$ and $Fe^{3+}$ contribution to the Fe-$2p_{3/2}$ peak, as expected for the mixed valency of Fe in $Fe_3O_4$. Magnetometry measurements confirm the Verwey transition at 126 K for films on PMN-PT(011) and 106 K on PMN-PT(001). The saturation magnetisation is reduced compared to bulk because of structural defects. The $Fe_3O_4$/PMN-PT(011) samples have an in-plane anisotropy with the easy axis of magnetisation along $[01\bar{1}]$.

Magnetoelectric coupling measurements at 300 K were performed for $Fe_3O_4$/PMN-PT(001) in non-saturating magnetic field along [100] with the electric field along $[01\bar{1}]$ cycled between ±4 kV/cm. The change in magnetisation can be separated into two regimes: For the first few electric field loops, a remanent increase occurs, with large jumps at the coercive electric field of PMN-PT. This is attributed to a magnetisation reorientation due to a shift of the magnetic easy axis towards the magnetic field direction. After the initial remanent change, the magnetisation follows a butterfly shape, similar to the strain transferred to the film by the substrate. An additional contribution from the PMN-PT polarisation accounting for 20% of the coupling has to be considered, to describe the asymmetry of the butterfly loop.

For $Fe_3O_4$/PMN-PT(011), the magnetoelectric coupling along [100] is similar to the butterfly regime above, but there is no preceding remanent increase. For all measured samples, the polarisation coupling accounts for 20% or less of the overall coupling, and is absent for one sample. The strain contribution along [100] is twice as large as that along $[01\bar{1}]$. A cross-coupling of the strain along $[01\bar{1}]$ has to be taken into consideration to accurately model the magnetoelectric loops. Along $[01\bar{1}]$, the change is completely remanent, with strain jumps at the electrical coercive field. Polarised neutron reflectometry reveals that the behaviour of the interface region between substrate and film does not differ from the film, indicating that the strain is coherently transferred to the film.

# 8 Summary and Conclusion

In this thesis, the switching of magnetic properties of ferro- or ferrimagnetic thin films by a ferrelectric substrate was investigated. Two different sample structures were prepared, both on the ferroelectric PMN-PT substrate, with the aim of controlling the magnetisation of the layer via the strain imparted by the substrate upon the application of an electric field.

The first project focussed on $SrCoO_{3-\delta}$, which possesses different magnetic properties depending on the oxidation state. Due to the low oxygen pressure in the MBE chamber used to prepare the samples, the oxygen deficient brownmillerite $SrCoO_{2.5}$ phase forms during growth. The conditions for high quality growth of $SrCoO_{2.5}$ were determined, with a special focus on the Co to Sr stoichiometry. RHEED was used to provide a quick and precise way to evaluate the stoichiometry *in-situ* and adjust the growth parameter during a sample series. To transform the $SrCoO_{2.5}$ films into the ferromagnetic perovskite $SrCoO_3$ phase, samples were annealed in a tube furnace with oxygen flow. XRD measurements after annealing show that the films retain their excellent crystallinity. SQUID measurements reveal the presence of three distinct magnetic phases in the film, corresponding to different oxygen content. The oxygen vacancies are distributed randomly throughout the thickness of the layer, as determined by PNR. The presence of oxygen vacancies can be explained by the instability of $SrCoO_3$. The perovskite phase is fully stable in vacuum, however in air it transforms back to $SrCoO_{2.5}$ within 10 h.

$SrCoO_{2.5}$ was grown on PMN-PT(001) substrate, however, due to the large mismatch in lattice constants, $SrCoO_{2.5}$ does not grow well on PMN-PT. To mediate this problem an LSMO buffer layer was used as LSMO readily grows on PMN-PT in good quality and matches the $SrCoO_{2.5}$ lattice constant well. A $SrCoO_{2.5}$/LSMO/PMN-PT sample was measured with PNR in oxygen atmosphere to determine if the strain influences the magnetic properties, however several problems during the measurement made the fitting of the data impossible. Hence, this question can not yet be answered.

In the second project, the magnetoelectric coupling of PLD grown $Fe_3O_4$ films on PMN-PT(001) and PMN-PT(011) substrates was studied. The substrate strain and polarisation has a profound effect on the films, with different contributions depending on the cut of the substrate and the orientation of film in a non-saturating external magnetic field. For $Fe_3O_4$/PMN-PT(001) with the magnetic field in-plane along [100], the coupling can be divided into two regimes: a remanent increase and a butterfly shape. For the first few electric field cycles, always between ±4 kV/cm, the magnetisation increases at the electrical coercive field of PMN-PT, with the increase remaining at zero electric field, i.e. a remanent increase. For further cycles, the magnetisation increase per cycle decreases, until the magnetisation follows a reproducible butterfly shape. As the magnetostriction coefficient of $Fe_3O_4$ along [100] is negative, the magnetisation is reduced for compressive strain and increased for tensile strain. The strain in PMN-PT(001) follows a butterfly-like curve, with tensile strain for low electric fields and compressive strain for high fields. As a result, the magnetisation in $Fe_3O_4$ follows a butterfly shape that is inverted with respect to the strain butterfly curve in PMN-PT(001). The polarisation of the substrate also contributes to the coupling, however much less than the strain. For $Fe_3O_4$/PMN-PT(011), the behaviour along the two in-plane directions follows only one of the two behaviours discussed above. For a magnetic field applied along $[01\bar{1}]$ the magnetisation increases remanently, whereas for the field along [100], the magnetisation follows the butterfly loop. The strain along $[01\bar{1}]$ is compressive, but it exhibits a large jump towards tensile strain at the electric coercive field, which contributes to the strain coupling for the magnetic field along [100], causing a decrease in magnetisation at the electrical coercive field of PMN-PT.

As a conclusion of this thesis, two results are important. First, the $SrCoO_{2.5-3}$ project yielded important parameter for the growth of $SrCoO_{2.5}$ and the transformation to $SrCoO_3$. Using RHEED, the stoichiometry of $SrCoO_{2.5}$ can be evaluated *in-situ*, which enables easy reproducibility of high quality samples. The stability of $SrCoO_3$ in air needs to be improved to study the impact of magnetoelectric coupling in these films (see chapter 9). Second, the magnetoelectric coupling in $Fe_3O_4$/PMN-PT(001) and $Fe_3O_4$/PMN-PT(011) is found to be strongly dependent on the orientation of the sample in the magnetic field, as well as the substrate cut. The different contributions to the magnetoelectric coupling arising from these parameters and the influence of strain and polarisation of the substrate have been explained qualitatively.

# 9 Outlook

Reviewing the results for both investigated thin films, $SrCoO_{2.5-3}$ and $Fe_3O_4$, some opportunities for future studies become clear. As the magnetoelectric coupling in $Fe_3O_4$ was successful, in laboratory and PNR experiments, more experiments could help to differentiate the coupling mechanisms. Growing $Fe_3O_4$ on insulating substrates will allow the study of the pure charge coupling. Furthermore, growing different systems with less than half-filled 3d orbitals for comparison of the magnetisation increase or reduction for different electric field polarity could confirm or falsify the charge contribution. Also, strain and polarisation measurements on the substrates used here would allow for a quantitative model of the magnetoelectric coupling.

At the end of the $SrCoO_{2.5-3}$ investigation some open questions remain, but the present investigation provides a strong foundation for a continuation of this study. As $SrCoO_{2.5}$/LSMO/PMN-PT heterostructures were grown successfully, finding the correct annealing conditions for these films to switch to the perovskite structure is certainly possible and, as $SrCoO_{2.5}$/STO and $SrCoO_{2.5}$/LSAT films annealed to $SrCoO_3$ were proven to be stable in vacuum, the $SrCoO_3$/LSMO/PMN-PT heterostructures should be stable as well. Once $SrCoO_3$/LSMO/PMN-PT samples are produced, the influence of strain on the structure could be studied by XRD in the existing vacuum chamber used for the stability study. PNR experiments would be possible with moderate oxygen loss using the same cold-finger cryostat as for the experiment on $SrCoO_{2.5}$/STO and keeping the sample in vacuum between the annealing and mounting it on the experiment. Another interesting aspect to study is the change in Co valency when an electric field is applied to the sample, e.g. using X-ray magnetic circular dichroism instruments.

# Acknowledgements

Without the support of lots of people, this thesis would not have been possible, and I would like to thank them all for helping me in various ways.

**Prof. Dr. Thomas Brückel** for giving me the opportunity to work at the JCNS on very interesting research topics and for the support and discussions during my time here. I would especially like to thank him for allowing me to work in both Garching and Jülich and of course for reviewing my thesis.

**Prof. Dr. Joachim Mayer** for the second review of this thesis.

**Dr. Sabine Pütter** for the great guidance and support during this thesis that managed to find the balance between letting me work in my own way and noticing when I needed help. Working in the MBE lab together and learning from her expertise was invaluable in developing my own skills. I want to especially thank her for supporting me in my transfer to Jülich and the subsequent time.

**Tanvi Bhatnagar-Schöffmann** for scientific and emotional support throughout this thesis and in the future. I want to thank her for many, many discussions on all parts of this thesis and apologise for sometimes not being able to stop talking about work. Without her this thesis and my life would never have been the same.

**Dr. Anirban Sarkar** for trusting me to continue the $Fe_3O_4$ project, discussions and lots of fun times.

**Dr. Emmanuel Kentzinger** for lots of discussions on many topics and help and fun times during the PBR beamtime. I really appreciated his openness and advice.

**Annika Stellhorn** for support during this whole thesis, lots of fun even when I was stressed and her unbreakable joy.

**Dr. Markus Waschk** and **Dr. Paul Zakalek** for countless discussions on lots of topics and helping me during every stage of this thesis. Learning from both of you has helped me tremendously.

**Dr. Amir Syed Mohd** for the great time working together on the MBE in Garching and always talking with me when I got stuck.

**Dr. Mai Hussein Hamed** and **Prof. Dr. Martina Müller** for the preparation of the $Fe_3O_4$ films, the HAXPES measurement and discussions.

**Dr. Juri Barthel** for the TEM and EDX measurements and discussions.

**Dr. Jürgen Schubert** for the RBS measurements, help with the RBS analysis and discussions as well as **Willi Zander** and **Katja Palmen** for the RBS measurements.

**Dr. Brian J Kirby and Dr. Alexander J Grutter** for support during the PBR beamtime and data analysis and for making the beamtime a very positive experience. I acknowledge the support of the National Institute of Standards and Technology, U.S. Department of Commerce, in providing the neutron research facilities used in this work.

**Dr. Stefan Geprägs** for discussions of PMN-PT and voltage measurements in his X-ray reflectometer.

**Dr. Peter Link** and **Senay Öztürk** for lots of time on the X-ray reflectometer of the MLZ neutron optics group.

**Dr. Oleg Petracic** for help with the MPMS and discussions regarding magnetism.

**Dr. Ulrich Rücker** for help with the X-ray reflectometer and discussions.

**Dr. Kirill Zhernenkov** and **Dr. Stefan Mattauch** for help during the MARIA beamtimes.

**Dr. Alexander Weber** and **Daniel Vujevic** for help with difficult sample environments.

**Dr. Yixi Su**, **Xiao Wang**, **Jörg Perßon**, **Sabreen Hammouda**, and **Dr. Manuel Angst** for the use of the tube furnaces.

**Dr. Margret Giesen** for the use of her AFM/PFM.

**Dr. Gregor Mussler** and **Dr. Alexander Shkurmanov** for the RSM measurements.

**Alfred Richter**, **Frank Gossen**, **Berthold Schmitz**, **Simon Staringer**, **Marco Gödel**, **Daniel Vujevic**, **Bernhard Großmann**, **Harald Kusche** and **Vladimir Ossovyi** for the technical support.

**Franziska Michel**, **Monika Krug**, and **Barbara Daegener** for assistance in many forms.

**Xiao Wang**, **Nileena Nandakumaran**, **Joanna Michalska**, **Mohammed Ait Haddouch**, **Dr. Stefan Holler**, **Dr. Viviane Peçanha Antonio**, **Dr. Asmaa Qdemat**, **Venus Rai**, **Benjamin Krugmann**, **Tobias Köhler** for the great time working with you at the JCNS in Garching and Jülich and lots of fun outside work.

**My parents and brother** for all the help and support during this thesis my life, for being patient with me when I got frustrated and for tolerating my terrible handwriting thus far.

# List of publications

- **P. Schöffmann**, A. Sarkar, M. Hussein Hammed, T. Bhatnagar-Schöffmann, S. Pütter, B. Kirby, A. Grutter, E. Kentzinger, A. Stellhorn, J. Barthel, A. Gloskovski, M. Müller, and T. Brückel. Investigation of strain and charge contributions to the magnetoelectric coupling in $Fe_3O_4$/PMN-PT(001) and $Fe_3O_4$/PMN-PT(011) artificial multiferroic heterostructures. *in preparation* (2021).

- T. Bhatnagar-Schöffmann, E. Kentzinger, A. Sarkar, **P. Schöffmann**, L. Jin, Q. Lan, A. Kovács, B. Kirby, A. Grutter, R. Beerwerth, M. Waschk, A. Stellhorn, U. Rücker, R.E. Dunin-Borkowski, and Th. Brückel. Differentiation between strain and charge mediated magnetoelectric coupling in $La_{0.7}Sr_{0.3}MnO_3/Pb(Mg_{1/3}Nb_{2/3})_{0.7}Ti_{0.3}O_3(001)$. *New Journal of Physics* **23**, (2021).

- A. Steffen, T. Gutberlet, H. Ambaye, J. Schubert, S. Geprägs, J. Barthel, S. Mattauch, W. Zander, M. Kruth, **P. Schöffmann**, S. Pütter, and T. Brückel. Unexpected Precipitates in Conjunction with Layer-by-Layer Growth in Mn-Enriched LSMO Thin Films, submitted to *Thin Solid Films* (2021)

- **P. Schöffmann**, S. Pütter, J. Schubert, W. Zander, J. Barthel, P. Zakalek, M. Waschk, R. Heller, and T. Brückel. Tuning the Co/Sr stoichiometry of $SrCoO_{2.5}$ thin films by RHEED assisted MBE growth. *Mater. Res. Express* **7**, 116404 (2020).

- A. Stellhorn, A. Sarkar, E. Kentzinger, M. Waschk, **P. Schöffmann**, S. Schröder, G. Abuladze, Z. Fu, V. Pipich, and T. Brückel. Control of the stripe domain pattern in L10-ordered FePd thin films. *J. Magn. Magn. Mater* **476**, 483–486 (2019).

# Bibliography

[1] A. M. Turing. On Computable Numbers, with an Application to the Entscheidungsproblem. *Proceedings of the London Mathematical Society*, s2-42(1):230–265, 01 1937.

[2] Konrad Zuse. *Der Computer - mein Lebenswerk*.

[3] M. N. Baibich, J. M. Broto, A. Fert, F. N. Van Dau, F. Petroff, P. Etienne, G. Creuzet, A. Friederich, and J. Chazelas. Giant magnetoresistance of (001)Fe/(001)Cr magnetic superlattices. *Physical Review Letters*, 61(21), 1988.

[4] B. Grünberg, P. Grünberg, F. Saurenbach, and W. Zinn. Enhanced magnetoresistance in layered magnetic structures with antiferromagnetic interlayer exchange. *Physical review B*, 39(7):4828, 1989.

[5] https://www.nobelprize.org/prizes/physics/2007/press-release/.

[6] J. G. Bednorz and K. A. Müller. Possible high $T_c$ superconductivity in the Ba-La-Cu-O system. *Zeitschrift für Physik B Condensed Matter*, 64(2):189–193, 1986.

[7] M. Fiebig. Revival of the magnetoelectric effect. *Journal of Physics D: Applied Physics*, 38(8):R123–R152, 2005.

[8] E. J. W. Verwey. Electronic conduction of magnetite ($Fe_3O_4$) and its transition point at low temperatures. *Nature*, 144(3642):327–328, 1939.

[9] Hyoungjeen Jeen and Ho Nyung Lee. Structural evolution of epitaxial $SrCoO_x$ films near topotactic phase transition. *AIP Advances*, 5(12):127123, 2015.

[10] Bin Cui, Peter Werner, Tianping Ma, Xiaoyan Zhong, Zechao Wang, James Mark Taylor, Yuechen Zhuang, and Stuart S. P. Parkin. Direct imaging of structural changes induced by ionic liquid gating leading to engineered three-dimensional meso-structures. *Nature Communications*, 9(1):3055, 2018.

[11] Jonathan R. Petrie, Chandrima Mitra, Hyoungjeen Jeen, Woo Seok Choi, Tricia L. Meyer, Fernando A. Reboredo, John W. Freeland, Gyula Eres, and Ho Nyung Lee. Strain control of oxygen vacancies in epitaxial strontium cobaltite films. *Advanced Functional Materials*, 26(10):1564–1570, 2016.

[12] G. S. Parks and K. K Kelley. The heat capacities of some metallic oxides. *Journal of Physical Chemistry*, 30(47), 1926.

[13] Marin Alexe, Michael Ziese, Dietrich Hesse, Pablo Esquinazi, Kunihiko Yamauchi, Tetsuya Fukushima, Silvia Picozzi, and Ulrich Gösele. Ferroelectric switching in multiferroic magnetite ($Fe_3O_4$) thin films. *Advanced Materials*, 21(44):4452–4455, 2009.

[14] Ming Liu, Jason Hoffman, Jing Wang, Jinxing Zhang, Brittany Nelson-Cheeseman, and Anand Bhattacharya. Non-volatile ferroelastic switching of the verwey transition and resistivity of epitaxial $Fe_3O_4$/PMN-PT (011). *Scientific Reports*, 3(1), may 2013.

[15] Alexander Tkach, Mehrdad Baghaie Yazdi, Michael Foerster, Felix Büttner, Mehran Vafaee, Maximilian Fries, and Mathias Kläui. Magnetoelectric properties of epitaxial $Fe_3O_4$ thin films on (011) PMN-PT piezosubstrates. *Physical Review B*, 91(2):024405, 2015.

[16] Xue Zhao, Ming Feng, Mei Liu, Jie Hua, Jing Ma, Liang Wu, Hang Xu, Ao pei Wang, and Hai bo Li. Electric-field tuning of magnetic anisotropy in the artificial multiferroic $Fe_3O_4$ /PMN–PT heterostructure. *Materials Research Letters*, 6(10):592–597, aug 2018.

[17] Hendrik Bluhm, Thomas Brückel, Markus Morgenstern, Gero von Plessen, and Christopf Stampfer. *Electrons in solids*. De Gruyter, 2019.

[18] Rudolf Gross and Achim Marx. *Festkörperphysik*. De Gruyter, 3rd edition, 2018.

[19] Stephen Blundell. *Magnetism in Condensed Matter*. Oxford University Press, 2001.

[20] A. Munoz, C. de la Calle, J. A. Alonso, P. M. Botta, V. Pardo, D. Baldomir, and J. Rivas. Crystallographic and magnetic structure of SrCoO brownmillerite: Neutron study coupled with band-structure calculations. *Phys. Rev. B*, 78(5), August 2008.

[21] P. Bezdicka, A. Wattiaux, J. C. Grenier, M. Pouchard, and P. Hagenmuller. Preparation and characterization of fully stoichiometric $SrCoO_3$ by electrochemical oxidation. *Zeitschrift für anorganische und allgemeine Chemie*, 619(1):7–12, 1993.

[22] R. Kannan and Mohindar S. Seehra. Percolation effects and magnetic properties of the randomly diluted fcc system $Co_\rho Mg_{1-\rho}O$. *Phys. Rev. B*, 35:6847–6853, May 1987.

[23] AT Gorton, G Bitsianes, and TL Joseph. Thermal expansion coefficients for iron and its oxides from x-ray diffraction measurements at elevated temperatures. *Transactions of the Metallurgical Society of AIME*,

233(8):1519–1525, 1965.

[24] P. G. Radaelli, G. Iannone, M. Marezio, H. Y. Hwang, S-W. Cheong, J. D. Jorgensen, and D. N. Argyriou. Structural effects on the magnetic and transport properties of perovskite $A_{1-x}A'_xMnO_3$ ($x = 0.25, 0.30$). *Phys. Rev. B*, 56:8265–8276, Oct 1997.

[25] Darrell G. Schlom, Long-Qing Chen, Chang-Beom Eom, Karin M Rabe, Stephen K Streiffer, and Jean-Marc Triscone. Strain tuning of ferroelectric thin films. *Annu. Rev. Mater. Res.*, 37(1):589–626, July 2007.

[26] B. Noheda, D. E. Cox, G. Shirane, J. Gao, and Z.-G. Ye. Phase diagram of the ferroelectric relaxor (1-x)$PbMg_{1/3}Nb_{2/3}O_3$-x$PbTiO_3$. *Phys. Rev. B*, 66:054104, Aug 2002.

[27] Koichi Momma and Fujio Izumi. VESTA 3 for three-dimensional visualization of crystal, volumetric and morphology data. *Journal of Applied Crystallography*, 44(6):1272–1276, 2011.

[28] Victor Moritz Goldschmidt. Die Gesetze der Krystallochemie. *Naturwissenschaften*, 14(21):477–485, 1926.

[29] D.A. Mota, Y. Romaguera Barcelay, A.M.R. Senos, C.M. Fernandes, P.B. Tavares, I.T. Gomes, P. Sá, L. Fernandes, B.G. Almeida, F. Figueiras, et al. Unravelling the effect of $SrTiO_3$ antiferrodistortive phase transition on the magnetic properties of $La_{0.7}Sr_{0.3}MnO_3$ thin films. *Journal of Physics D: Applied Physics*, 47(43):435002, 2014.

[30] Hasan Albargi, Mohammed Alqahtani, Harry Blythe, A. Fox, N. Andreev, V. Chichkov, and Gillian Gehring. Magnetic and magneto-optical properties of films of multiferroic $GdMnO_3$ grown on LSAT $[(LaAlO_3)_{0.3}(Sr_2AlTaO_6)_{0.7}]$(100) and (111). *Thin Solid Films*, 645, 11 2017.

[31] P. W. Anderson. Antiferromagnetism. Theory of Superexchange Interaction. *Phys. Rev.*, 79:350–356, Jul 1950.

[32] John B. Goodenough. Theory of the role of covalence in the perovskite-type manganites [La,M(II)]$MnO_3$. *Phys. Rev.*, 100:564–573, Oct 1955.

[33] Junjiro Kanamori. Superexchange interaction and symmetry properties of electron orbitals. *Journal of Physics and Chemistry of Solids*, 10(2):87 – 98, 1959.

[34] Ming Liu, Ogheneyunume Obi, Zhuhua Cai, Jing Lou, Guomin Yang, Katherine S. Ziemer, and Nian X. Sun. Electrical tuning of magnetism in $Fe_3O_4$/PZN–PT multiferroic heterostructures derived by reactive magnetron sputtering. *Journal of Applied Physics*, 107(7):073916, 2010.

[35] K Siratori, K Kohn, and E Kita. Magnetoelectric effect in magnetic

materials. *Acta Physica Polonica A*, 81(4-5):431–466, 1992.

[36] E. Y. Tsymbal, E. R. A. Dagotto, C.-B. Eom, and R. Ramesh, editors. *Multifuctional Oxide Heterostructures.* Oxford, 2012.

[37] Youwen Long, Yoshio Kaneko, Shintaro Ishiwata, Yasujiro Taguchi, and Yoshinori Tokura. Synthesis of cubic $SrCoO_3$ single crystal and its anisotropic magnetic and transport properties. *Journal of Physics: Condensed Matter*, 23(24):245601, 2011.

[38] S. Balamurugan, K. Yamaura, A. B. Karki, D. P. Young, M. Arai, and E. Takayama-Muromachi. Specific-heat evidence of strong electron correlations and thermoelectric properties of the ferromagnetic perovskite $SrCoO_{3-\delta}$. *Phys. Rev. B*, 74:172406, Nov 2006.

[39] R. H. Potze, G. A. Sawatzky, and M. Abbate. Possibility for an intermediate-spin ground state in the charge-transfer material $SrCoO_3$. *Phys. Rev. B*, 51:11501–11506, May 1995.

[40] Youdi Gu, Cheng Song, Hongrui Zhang, Zechao Wang, Bin Cui, Fan Li, Jingjing Peng, Muhammad Shahrukh Saleem, Guangyue Wang, Xiaoyan Zhong, Fei Wang, Song Ma, Jirong Sun, Wei Liu, Feng Pan, and Zhidong Zhang. Controllable oxygen vacancies, orbital occupancy and magnetic ordering in $SrCoO_{3-\delta}$ films. *Journal of Magnetism and Magnetic Materials*, 454:228 – 236, 2018.

[41] Takayoshi Takeda, Yasuo Yamaguchi, and Hiroshi Watanabe. Magnetic structure of $SrCoO_{2.5}$. *Journal of the Physical Society of Japan*, 33(4):970–972, 1972.

[42] Hyoungjeen Jeen, Woo Seok Choi, Michael D. Biegalski, Chad M. Folkman, I-Cheng Tung, Dillon D. Fong, JohnW. Freeland, Dongwon Shin, Hiromichi Ohta, Matthew F. Chisholm, and Ho Nyung Lee. Reversible redox reactions in an epitaxially stabilized $SrCoO_x$ oxygen sponge. *Nature Materials*, 12, November 2013.

[43] Joaquín García and Gloria Subías. The Verwey transition—a new perspective. *Journal of Physics: Condensed Matter*, 16(7):R145–R178, feb 2004.

[44] Shujun Zhang, Nevin P. Sherlock, Richard J. Meyer, and Thomas R. Shrout. Crystallographic dependence of loss in domain engineered relaxor-PT single crystals. *Applied Physics Letters*, 94(16):162906, 2009.

[45] Gerald Burns and F. H. Dacol. Crystalline ferroelectrics with glassy polarization behavior. *Phys. Rev. B*, 28:2527–2530, Sep 1983.

[46] A. A. Bokov and Z.-G. Ye. Recent progress in relaxor ferroelectrics with perovskite structure. *Journal of Materials Science*, 41(1):31–52, 2006.

[47] Tao Wu, Ping Zhao, Mingqiang Bao, Alexandre Bur, Joshua L. Hockel, Kin Wong, Kotekar P. Mohanchandra, Christopher S. Lynch, and Gregory P. Carman. Domain engineered switchable strain states in ferroelectric (011) $[Pb(Mg_{1/3}\,Nb_{2/3})O_3]_{(1-x)}$-$[PbTiO_3]_x$ (PMN-PT, x≈0.32) single crystals. *Journal of Applied Physics*, 109(12):124101, 2011.

[48] Marian A. Herman, Wolfgang Richter, and Helmut Sitter. *Epitaxy - Physical Principles and Technical Implementation.* Springer, 2004.

[49] T. Brückel, D. Richter, G. Roth, A. Wischnewski, and R. Zorn. *Laboratory Course Neutron Scattering.* Forschungszentrum Jülich GmbH, 2017.

[50] G. L. Squires. *Introduction to the theory of thermal neutron scattering.* Cambridge University Press, 1978.

[51] R. P. Hermann. *Laboratory Course Neutron Scattering - Spin dependent and magnetic scattering*, chapter 7. Forschungszentrum Jülich GmbH, 2017.

[52] D. P. DiVincenso. *50th IFF Spring School 2019: Scattering! Soft, Functional and Quantum Materials - Interacions of X-rays, neutrons and electrons with matter*, chapter A3. Forschungszentrum Jülich GmbH, 2019.

[53] K. Oura, V. G. Lifshits, A. A. Saranin, A. V. Zotov, and M. Katayama. *Surface Science - an Introduction.* Springer, 2003.

[54] C Barry Carter and David B Williams. *Transmission electron microscopy.* Springer, 2nd edition, 2009.

[55] M Pl Seah and WA Dench. Quantitative electron spectroscopy of surfaces: A standard data base for electron inelastic mean free paths in solids. *Surface and interface analysis*, 1(1):2–11, 1979.

[56] Wei-Kan Chu, James W. Mayer, and Marc-A. Nicolet. *Backscattering Spectrometry.* Academic Press, 1978.

[57] Roger Pynn. 2008 NCNR/NSF Summer School: Surface Reflection - Lecture Notes.

[58] E. Kentzinger. *Laboratory Course Neutron Scattering - Neutron Reflectometry*, chapter 9. Forschungszentrum Jülich GmbH, 2017.

[59] G. Roth. *Laboratory Course Neutron Scattering - Diffraction*, chapter 4. Forschungszentrum Jülich GmbH, 2017.

[60] Ayahiko Ichimiya and Philip I. Cohen. *Reflection High-Energy Electron Diffraction.* Cambridge University Press, 2004.

[61] Jens Reichow. DCA MBE M600 technical system description, 2010.

[62] Paul Zakalek. *Magnetic Interface Effects in Thin Film Heterostructures.*

PhD thesis, RWTH Aachen, 2015.

[63] G. Sauerbrey. Verwendung von Schwingquarzen zur Wägung dünner Schichten und zur Mikrowägung. *Zeitschrift für Physik*, 155:206–222, 1959.

[64] Thomas Frey, Thomas Reisinger, Bernhard Folger, Marcus Kastner, and Wolfgang Gebhardt. Quantitative growth-investigation of zincblende ZnMgSe/GaAs(001) and ZnSe/GaAs(001) by means of RHEED, HRXRD and thickness monitoring. *Journal of Crystal Growth*, 184:31 – 36, 1998.

[65] Gernot Friedbacher and Henning Bubert. *Surface and Thin Film Analysis: A Compendium of Principles, Instrumentation, and Applications*. John Wiley & Sons, 2011.

[66] Franz J. Giessibl. Advances in atomic force microscopy. *Rev. Mod. Phys.*, 75:949–983, Jul 2003.

[67] David Nečas and Petr Klapetek. Gwyddion: an open-source software for SPM data analysis. *Central European Journal of Physics*, 10:181–188, 2012.

[68] Matts Björck and Gabriella Andersson. GenX: an extensible X-ray reflectivity refinement program utilizing differential evolution. *Journal of Applied Crystallography*, 40(6):1174–1178, Dec 2007.

[69] A. Glavic. Multiferroicity in oxide thin films and heterostructures. *PhD thesis, RWTH Aachen*, 2012.

[70] David Allan Bromley. *Treatise on Heavy-Ion Science: Volume 4 Extreme Nuclear States*. Springer Science & Business Media, 2012.

[71] Michael O. Thompson. RUMP: RBS analysis and plotting.

[72] *Magnetic Property Measurement System: MPMS XL, Hardware Reference Manual.*

[73] Mike McElfresh. *Fundamentals of Magnetism and Magnetic Measurements featuring Quantum Design's Magnetic Property Measurement System*, 1994.

[74] Matthias Schmelz and Ronny Stolz. *Superconducting Quantum Interference Device (SQUID) Magnetometers*, pages 279–311. Springer International Publishing, 2017.

[75] Philippe Mangin and Rémi Kahn. *Superconductivity*. Springer, 2017.

[76] Quantum Design. *Magnetic Property Measurement System: Reciprocating Sample Option User's Manual*, 2001.

[77] P. Borisov, A. Hochstrat, V. V. Shvartsman, and W. Kleemann. Superconducting quantum interference device setup for magnetoelectric measurements. *Review of Scientific Instruments*, 78(10):106105, 2007.

[78] Markus Schmitz. *Strain and electric field mediated manipulation of magnetism in* $La_{(1-x)}Sr_xMnO_3/BaTiO_3$ *heterostructures.* PhD thesis, RWTH Aachen, 2015.

[79] Li-Ming Wang. *Manipulation of magnetism in iron oxide nanoparticels /* $BaTiO_3$ *composites and low-dimentional iron oxide nanoparticle arrays.* PhD thesis, RWTH Aachen, 2018.

[80] Ernst Ruska-Centre for Microscopy and Spectroscopy with Electrons. FEI Tecnai G2 F20. *Journal of large-scale research facilities*, 2:A77, 2016.

[81] Ernst Ruska-Centre for Microscopy and Spectroscopy with Electrons. FEI Helios NanoLab 460F1FIB-SEM. *Journal of large-scale research facilities*, 2(A59), 2016.

[82] Stefan Mattauch, Alexandros Koutsioubas, and Sabine Pütter. MARIA: Magnetic reflectometer with high incident angle. *Journal of large-scale research facilities JLSRF*, 1:8, 2015.

[83] NIST Center for Neutron Research. Polarized Beam Reflectometer (PBR), https://www.nist.gov/ncnr/polarized-beam-reflectometer-pbr, accessed 08.07.2020, 2020.

[84] Patrick Schöffmann. Preparation and Characterisation of Thin $SrCoO_x$ Films. Master's thesis, TU Munich, 2017.

[85] Markus Waschk. *Interface Phenomena in* $La_{1/3}Sr_{2/3}FeO_3/La_{2/3}Sr_{1/3}MnO_3$ *heterostructures and a quest for p-electron magnetism.* PhD thesis, RWTH Aachen, 2017.

[86] H. Jeen, W. S. Choi, J. W. Freeland, H. Ohta, C. U. Jung, and H. N. Lee. Topotactic phase transformation of the brownmillerite $SrCoO_{2.5}$ to the perovskite $SrCoO_{3-\delta}$. *Advanced Materials*, 25:3651–3656, 2013.

[87] S. Hu, Z. Yue, J. S. Lim, S. J. Callori, J. Bertinshaw, A. Ikeda-Ohno, T. Ohkochi, C.-H. Yang, X. Wang, C. Ulrich, and J. Seidel. Growth and properties of fully strained $SrCoO_x$ ($x \approx 2.8$) thin films on $DyScO_3$. *Advanced Materials Interfaces*, 2(8):1500012–n/a, 2015. 1500012.

[88] Janghyun Jo, Venkata Raveendra Nallagatlla, Susant Kumar Acharya, Youngho Kang, Yoonkoo Kim, Sangmoon Yoon, Sangmin Lee, Hionsuck Baik, Seungwu Han, Miyoung Kim, and Chang Uk Jung. Effects of the heterointerface on the growth characteristics of a brownmillerite $SrFeO_{2.5}$ thin film grown on $SrRuO_3$ and $SrTiO_3$ perovskites. *Scientific reports*, 10(32123253):3807–3807, March 2020.

[89] D. G. Schlom J. Lettieri, J. H. Haeni. Critical issues in the heteroepitaxial growth of alkaline-earth oxides on silicon. *Journal of Vacuum Science & Technology A*, 20, 2002.

[90] Y. S. Kim, N. Bansal, C. Chaparro, H. Gross, and S. Oh. Sr flux stability against oxidation in oxide-molecular-beam-epitaxy environment: Flux, geometry, and pressure dependence. *Journal of Vacuum Science & Technology A*, 28(2):271–276, 2010.

[91] Christian Edelmann. *Vakuumphysik*. Spektrum Akad. Verl., 1998.

[92] P. Schöffmann, S. Pütter, J. Schubert, W. Zander, J. Barthel, P. Zakalek, M. Waschk, R. Heller, and T. Brückel. Tuning the Co/Sr stoichiometry of $SrCoO_{2.5}$ thin films by RHEED assisted MBE growth. *Materials Research Express*, 7(11):116404, 11 2020.

[93] William T. A. Harrison, Steven L. Hegwood, and Allan J. Jacobson. A powder neutron diffraction determination of the structure of $Sr_6Co_5O_{15}$, formerly described as the low-temperature hexagonal form of $SrCoO_3$. *J. Chem. Soc., Chem. Commun.*, pages 1953–1954, 1995.

[94] Songbai Hu, Yu Wang, Claudio Cazorla, and Jan Seidel. Strain-enhanced oxygen dynamics and redox reversibility in topotactic $SrCoO_{3-\delta}$. *Chem. Mater.*, 29(2):708–717, January 2017.

[95] C. K. Xie, Y. F. Nie, B. O. Wells, J. I. Budnick, W. A. Hines, and B. Dabrowski. Magnetic phase separation in $SrCoO_x$ ($2.5 \leq x \leq 3$). *Applied Physics Letters*, 99(5), 2011.

[96] S. J. Callori, S. Hu, J. Bertinshaw, Z. J. Yue, S. Danilkin, X. L. Wang, V. Nagarajan, F. Klose, J. Seidel, and C. Ulrich. Strain-induced magnetic phase transition in $SrCoO_{3-\delta}$ thin films. *Physical Review B*, 91, April 2015.

[97] C. Michel, S. D. Baranovskii, P. J. Klar, P. Thomas, and B. Goldlücke. Strong non-arrhenius temperature dependence of the resistivity in the regime of traditional band transport. *Applied Physics Letters*, 89(11):112116, 2006.

[98] Quantum Design. *MPMS Application Note 1014-210 - Oxygen Contamination.*

[99] Nianpeng Lu, Pengfei Zhang, Qinghua Zhang, Ruimin Qiao, Qing He, Hao-Bo Li, Yujia Wang, Jingwen Guo, Ding Zhang, Zheng Duan, Zhuolu Li, Meng Wang, Shuzhen Yang, Mingzhe Yan, Elke Arenholz, Shuyun Zhou, Wanli Yang, Lin Gu, Ce-Wen Nan, Jian Wu, Yoshinori Tokura, and Pu Yu. Electric-field control of tri-state phase transformation with a selective dual-ion switch. *Nature*, 546(7656):124–128, June 2017.

[100] K. Dörr, C. Thiele, J.-W. Kim, O. Bilani, K. Nenkov, and L. Schultz. Approaches towards ferroelectric control of thin film magnetism. *Philosophical Magazine Letters*, 87(3-4):269–278, 2007.

[101] Laihui Luo, Matthias Dietze, Claus-Henning Solterbeck, Haosu Luo, and Mohammed Es-Souni. Tuning the functional properties of PMN-PT single

crystals via doping and thermoelectrical treatments. *Journal of Applied Physics*, 114(22):224112, 2013.

[102] Boyuan Huang, Zhenghao Li, and Jiangyu Li. An artificial intelligence atomic force microscope enabled by machine learning. *Nanoscale*, 10(45):21320–21326, 2018.

[103] C. Thiele, K. Dörr, O. Bilani, J. Rödel, and L. Schultz. Influence of strain on the magnetization and magnetoelectric effect in $La_{0.7}A_{0.3}MnO_3$/PMN-PT(001) (A=Sr,Ca). *Phys. Rev. B*, 75:054408, Feb 2007.

[104] O. Bilani-Zeneli, A. D. Rata, A. Herklotz, O. Mieth, L. M. Eng, L. Schultz, M. D. Biegalski, H. M. Christen, and K. Dörr. $SrTiO_3$ on piezoelectric PMN-PT(001) for application of variable strain. *Journal of Applied Physics*, 104(5):054108, 2008.

[105] Juri Barthel, Markus Lentzen, and Andreas Thust. On the influence of the electron dose rate on the hrtem image contrast. *Ultramicroscopy*, 176:37 – 45, 2017.

[106] W Eerenstein, TTM Palstra, T Hibma, and S Celotto. Origin of the increased resistivity in epitaxial $Fe_3O_4$ films. *Physical Review B*, 66(20):201101, 2002.

[107] Amalio Fernandez-Pacheco. *Magnetotransport Properties of Epitaxial $Fe_3O_4$ Thin Films.* Springer Berlin Heidelberg, Berlin, Heidelberg, 2011.

[108] R Arras, B Warot-Fonrose, and L Calmels. Electronic structure near cationic defects in magnetite. *Journal of Physics: Condensed Matter*, 25(25):256002, may 2013.

[109] Tatsuo Fujii, FMF De Groot, GA Sawatzky, FC Voogt, T Hibma, and Kozo Okada. In situ XPS analysis of various iron oxide films grown by $NO_2$-assisted molecular-beam epitaxy. *Physical review B*, 59(4):3195, 1999.

[110] Susana Gota, Eric Guiot, Michèle Henriot, and Martine Gautier-Soyer. Atomic-oxygen-assisted mbe growth of $\alpha$-$Fe_2O_3$ on $\alpha$-$Al_2O_3$(0001): Metastable FeO(111)-like phase at subnanometer thicknesses. *Physical Review B*, 60(20):14387, 1999.

[111] JP Shepherd, JW Koenitzer, R Aragón, J Spal, JM Honig, et al. Heat capacity and entropy of nonstoichiometric magnetite $Fe_{3(1-\delta)}O_4$: The thermodynamic nature of the verwey transition. *Physical Review B*, 43(10):8461, 1991.

[112] Ricardo Aragón. Magnetization and exchange in nonstoichiometric magnetite. *Phys. Rev. B*, 46:5328–5333, Sep 1992.

[113] Yan Chen, Yang Zhang, Robert Keil, Michael Zopf, Fei Ding, and Oliver G Schmidt. Temperature-dependent coercive field measured by a quantum dot strain gauge. *Nano letters*, 17(12):7864–7868, 2017.

[114] P.A. Kienzle, B.B. Maranville, K.V. O'Donovan, J.F. Ankner, N.F. Berk, and C.F. Majkrzak. https://www.nist.gov/ncnr/reflectometry-software.

[115] L. R. Bickford, J. Pappis, and J. L. Stull. Magnetostriction and permeability of magnetite and cobalt-substituted magnetite. *Phys. Rev.*, 99:1210–1214, Aug 1955.

[116] Yiping Guo, Haosu Luo, Di Ling, Haiqing Xu, Tianhou He, and Zhiwen Yin. The phase transition sequence and the location of the morphotropic phase boundary region in (1- x)[Pb($Mg_{1/3}Nb_{2/3}$)$O_3$]–x$PbTiO_3$ single crystal. *Journal of Physics: Condensed Matter*, 15(2):L77, 2003.

[117] Y. L. Lu, A. Jain, N. Wang, F. L. Wang, Y. Li, Y. G. Wang, and F. M. Pan. Strain and charge modulated magnetization in a BTO/$Fe_3O_4$/Au/BTO multilayered heterostructure. *Applied Physics Letters*, 115(13):132405, 2019.

[118] Fei Li, Shujun Zhang, Zhuo Xu, Xiaoyong Wei, Jun Luo, and Thomas R. Shrout. Piezoelectric activity of relaxor-$PbTiO_3$ based single crystals and polycrystalline ceramics at cryogenic temperatures: Intrinsic and extrinsic contributions. *Applied Physics Letters*, 96(19):192903, 2010.

[119] T. Bhatnagar-Schöffmann, E. Kentzinger, A. Sarkar, P. Schöffmann, L. Jin, Q. Lan, A. Kovács, B. Kirby, A. Grutter, R. Beerwerth, M. Waschk, A. Stellhorn, U. Rücker, R.E. Dunin-Borkowski, and Th. Brückel. Differentiation between strain and charge mediated magnetoelectric coupling in $La_{0.7}Sr_{0.3}MnO_3$/Pb($Mg_{1/3}Nb_{2/3}$)$_{0.7}Ti_{0.3}O_3$(001). *in preparation*, 2021.

# Acronyms

**AES** Auger electron spectroscopy ........................................ 40, 44

**AFM** Atomic force microscopy ........................................ 44

**BM-SCO** $SrCoO_{2.5}$ ........................................ 17, 55, 91

**DESY** Deutsches Elektronen-Synchrotron ........................................ 47, 113, 172

**EDX** Energy-dispersive x-ray spectroscopy ........................................ 95

**$Fe_3O_4$** Magnetite ........................................ 17, 105

**FIB** Focussed ion beam ........................................ 51

**HAXPES** Hard X-ray photoemission spectroscopy ........................................ 47

**HRTEM** High resolution transmission electron microscopy ........................................ 111

**JCNS** Jülich Centre for Neutron Science ........................................ 46, 49

**LEED** Low-energy electron diffraction ........................................ 40, 43

**LSAT** $(La_{0.26}Sr_{0.76})(Al_{0.61}Ta_{0.37})O_3$ ........................................ 6

**LSMO** $La_{0.67}Sr_{0.33}MnO_3$ ........................................ 91, 92

**MARIA** Magnetic reflectometer with high incident angle ........................................ 53, 81, 100

**MBE** Molecular beam epitaxy ........................................ 20, 39, 55

**MBE-MLZ** Molecular beam epitaxy system in Garching ........................................ 39

**MLZ** Heinz-Meier Leibnitz Zentrum ........................................ 52, 100

**MPMS** Magnetic properties measurement system ........................................ 49, 75

**NCNR** NIST Center for Neutron Research ........................................ 52, 121

**OMBE** Molecular beam epitaxy system in Jülich ........................................ 39

**P-SCO** $SrCoO_3$ ........................................ 15, 55, 91

**PBR** Polarized beam reflectometer ........................................ 53, 121

| | | |
|---|---|---|
| **PFM** | Piezoresponse force microscopy | 46, 87 |
| **PLD** | Pulsed laser deposition | 40 |
| **PMN-PT** | $[Pb(Mg_{1/3}Nb_{2/3})O_3]_{0.7}$–$[PbTiO_3]_{0.3}$ | 18, 85, 91, 105 |
| **PNR** | Polarised neutron reflectometry | 32, 52, 81, 100, 121 |
| **PPMS** | Physical properties measurement system | 50 |
| **QCM** | Quartz crystal micro balance | 40, 55 |
| **RBS** | Rutherford backscattering spectroscopy | 47 |
| **RHEED** | Reflection high-energy electron diffraction | 40–42, 66 |
| **SCO** | $SrCoO_{3-\delta}$ | 15, 55, 91 |
| **SLD** | Scattering length density | 81, 125 |
| **SQUID** | Superconducting quantum interference device | 49, 75 |
| **STEM** | Scanning transmission electron microscopy | 51, 95 |
| **STO** | $SrTiO_3$ | 6 |
| **TEM** | Transmission electron microscopy | 51, 95 |
| **TMO** | Transition metal oxide | 1, 129 |
| **UHV** | Ultra high vacuum | 40 |
| **XRD** | X-ray diffraction | 33, 46 |
| **XRR** | X-ray reflectometry | 28, 46 |

# Supplementary information

## S.1 Combined PNR models for sample LP2 SrCoO$_{2.5}$/LSMO/PMN-PT

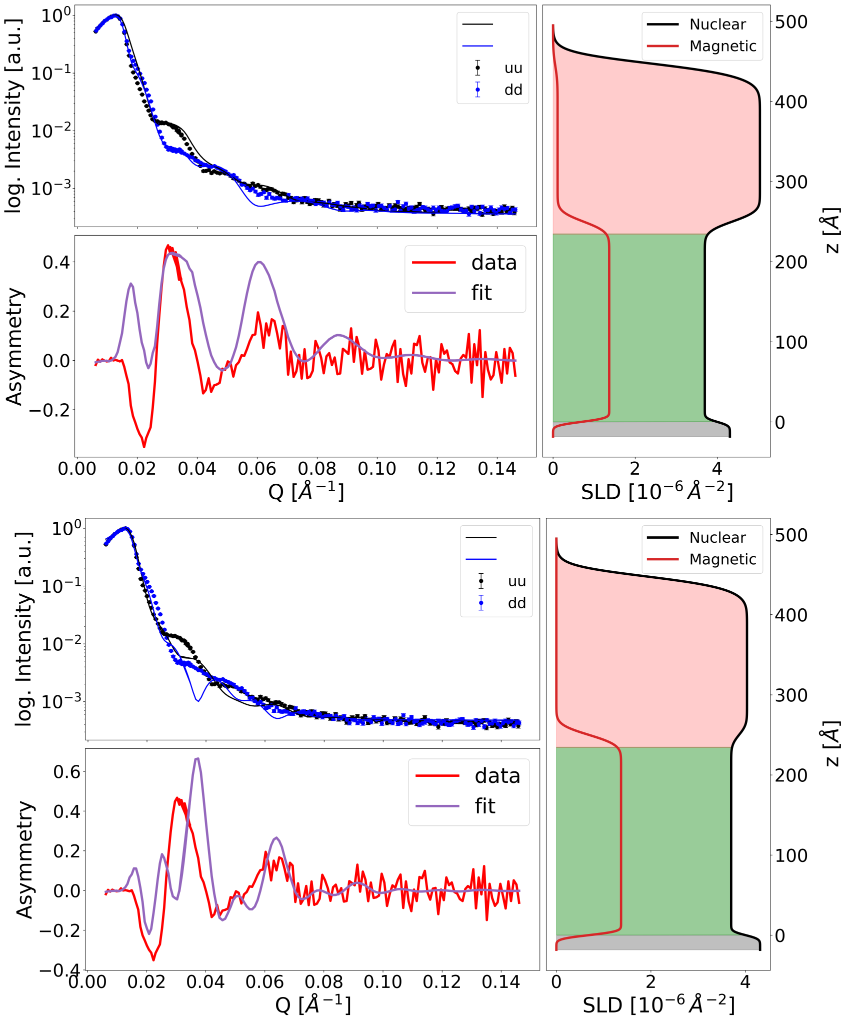

**Figure S1:** Attempt at fitting the PNR measurement of sample LP2 SCO/LSMO/PMN-PT at 300 K and 0 kV/cm by simulating the two parts, SrCoO$_{2.5}$/LSMO/PMN-PT and LSMO/PMN-PT separately and then combining them.

## S.2 PNR simulation for sample F3 $Fe_3O_4$/PMN-PT(011) with fixed top layer magnetisation angle

**Table S1:** Fit of the PNR measurements of F3 $Fe_3O_4$/PMN-PT(011) with fixed top layer magnetisation angle.

| Electric field [kV/cm] | Layer | Thickness [Å] | roughness [Å] | Nuclear SLD [$10^{-6}$Å$^{-2}$] | Magnetic SLD [$10^{-6}$Å$^{-2}$] | Magnetisation angle [°] |
|---|---|---|---|---|---|---|
| 0 | Top | $19.27^{+0.03}_{-0.04}$ | $9.97^{+0.03}_{-0.05}$ | $4.33^{+0.04}_{-0.03}$ | $0.48^{+0.02}_{-0.03}$ | $31.9^{+0.2}_{-0.1}$ |
| 0 | $Fe_3O_4$ | $429.5^{+0.3}_{-0.3}$ | $10.0^{+0.1}_{-0.1}$ | $6.28^{+0.02}_{-0.01}$ | $0.33^{+0.02}_{-0.02}$ | $31.9^{+0.2}_{-0.1}$ |
| 0 | Substrate | - | $10.56^{+0.04}_{-0.04}$ | $4.17^{+0.07}_{-0.03}$ | - | - |
| +2 | Top | $19.17^{+0.03}_{-0.03}$ | $9.98^{+0.01}_{-0.04}$ | $4.33^{+0.04}_{-0.03}$ | $0.48^{+0.01}_{-0.03}$ | $17.5^{+0.2}_{-0.1}$ |
| +2 | $Fe_3O_4$ | $431.6^{+0.4}_{-0.2}$ | $10.1^{+0.1}_{-0.1}$ | $6.28^{+0.02}_{-0.01}$ | $0.40^{+0.02}_{-0.02}$ | $17.5^{+0.2}_{-0.1}$ |
| +2 | Substrate | - | $10.5^{+0.1}_{-0.1}$ | $4.17^{+0.07}_{-0.03}$ | - | - |
| +4 | Top | $19.27^{+0.02}_{-0.03}$ | $9.97^{+0.03}_{-0.03}$ | $4.33^{+0.04}_{-0.03}$ | $0.48^{+0.02}_{-0.02}$ | $17.8^{+0.2}_{-0.2}$ |
| +4 | $Fe_3O_4$ | $431.6^{+0.4}_{-0.2}$ | $10.1^{+0.1}_{-0.1}$ | $6.28^{+0.02}_{-0.01}$ | $0.41^{+0.02}_{-0.01}$ | $17.8^{+0.2}_{-0.2}$ |
| +4 | Substrate | - | $11.1^{+0.1}_{-0.3}$ | $4.17^{+0.07}_{-0.03}$ | - | - |
| -4 | Top | $19.12^{+0.04}_{-0.03}$ | $10.0^{+0.1}_{-0.1}$ | $4.33^{+0.04}_{-0.03}$ | $0.48^{+0.02}_{-0.04}$ | $21^{+1}_{-2}$ |
| -4 | $Fe_3O_4$ | $431.6^{+0.4}_{-0.2}$ | $10.0^{+0.1}_{-0.1}$ | $6.28^{+0.02}_{-0.01}$ | $0.47^{+0.02}_{-0.02}$ | $21^{+1}_{-2}$ |
| -4 | Substrate | - | $10.5^{+0.1}_{-0.2}$ | $4.17^{+0.07}_{-0.03}$ | - | - |
| +4 | Top | $18.9^{+0.1}_{-0.1}$ | $10.0^{+0.1}_{-0.1}$ | $4.33^{+0.04}_{-0.03}$ | $0.48^{+0.02}_{-0.02}$ | $23^{+1}_{-1}$ |
| +4 | $Fe_3O_4$ | $431.6^{+0.4}_{-0.2}$ | $10.1^{+0.1}_{-0.1}$ | $6.28^{+0.02}_{-0.01}$ | $0.48^{+0.02}_{-0.03}$ | $23^{+1}_{-1}$ |
| +4 | Substrate | - | $10.7^{+0.1}_{-0.1}$ | $4.17^{+0.07}_{-0.03}$ | - | - |

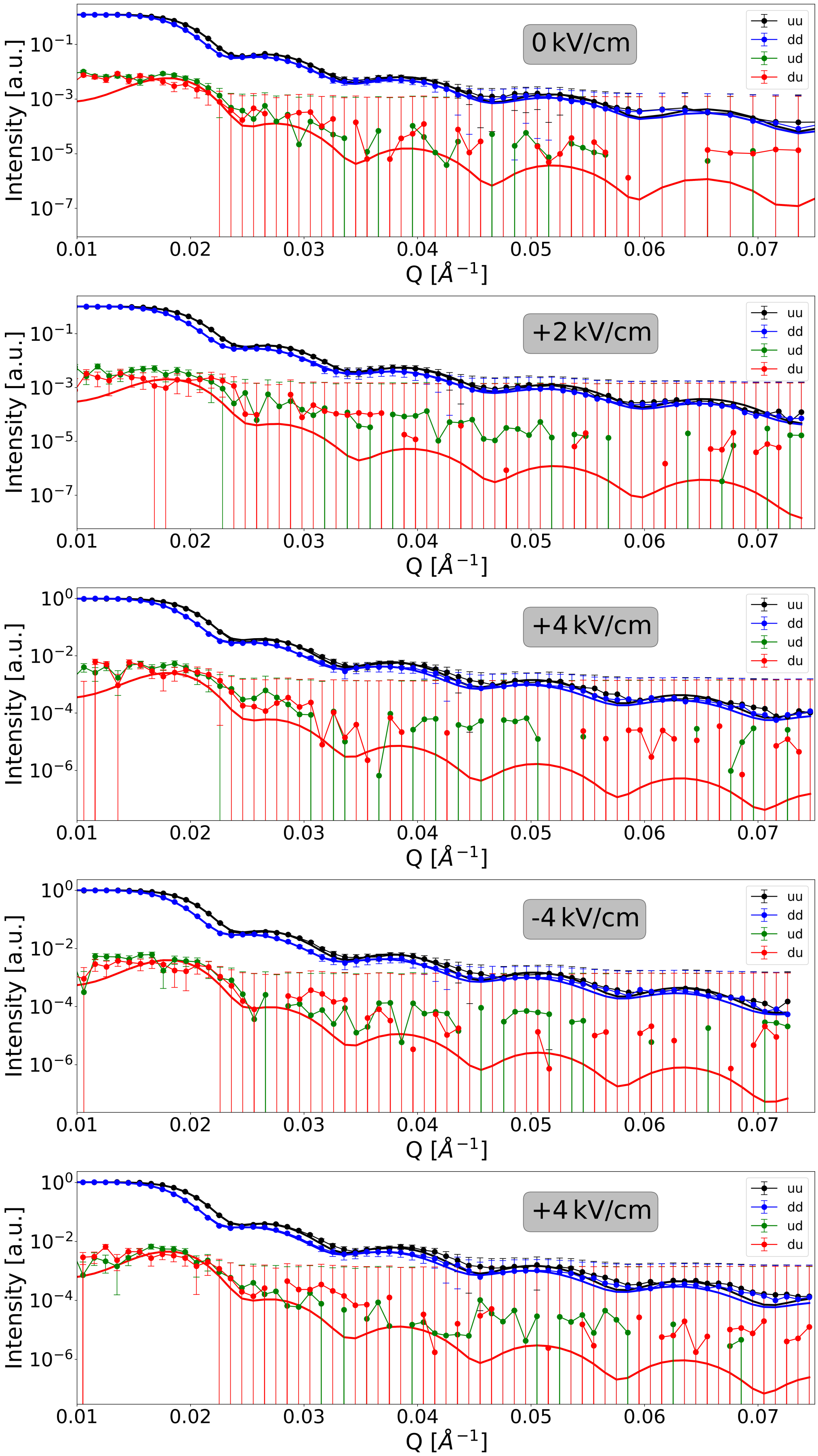

**Figure S2:** PNR measurements with fit of sample F3 $Fe_3O_4$/PMN-PT(011) with the application of voltage.

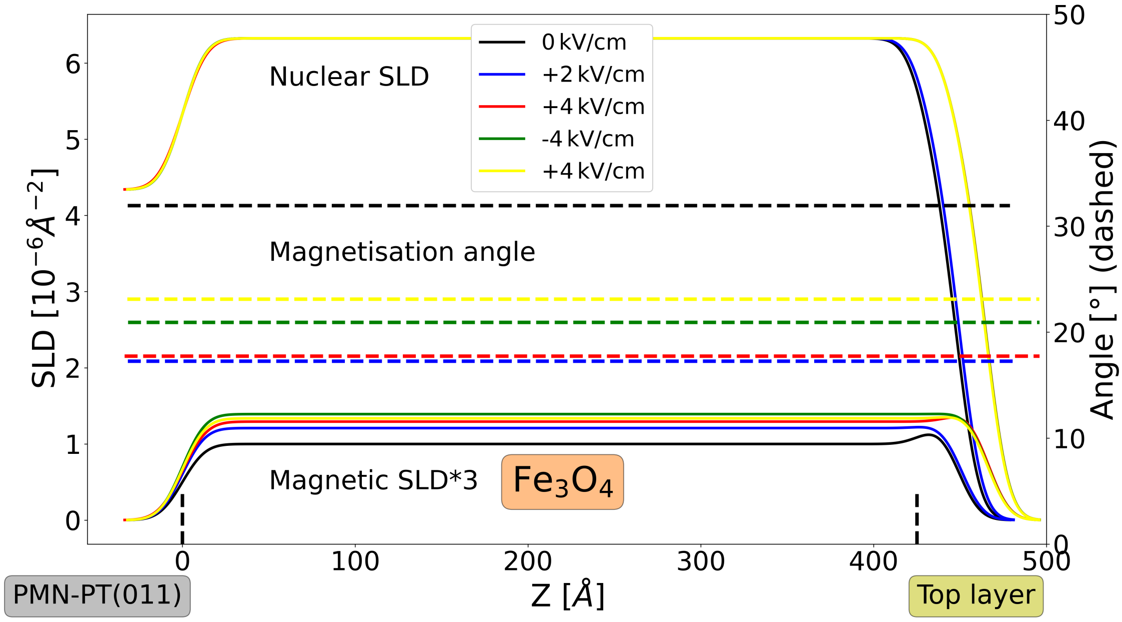

**Figure S3:** Scattering length density profiles based on the fit of the PNR measurement in fig. S2. The magnetic SLD is multiplied by a factor of 3 for better visibility.

# S.3 Samples and growth parameter

In the following tables, the growth parameter for all samples used in this thesis are given. The samples are identified by a sample ID consisting of a prefix depending on the film and substrate and a sequential number, based on the order of appearance in the thesis. The prefixes are:
"**S**" for $SrCoO_{2.5}/SrTiO_3(001)$,
"**L**" for $SrCoO_{2.5}$/LSAT(001),
"**P**" for $SrCoO_{2.5}$/PMN-PT(001),
"**LP**" $SrCoO_{2.5}/La_{2/3}Sr_{1/3}MnO_3$/PMN-PT(001) and
"**FM**" for $Fe_3O_4$/PMN-PT(011) grown by MBE
"**F**" for $Fe_3O_4$/PMN-PT(001) and $Fe_3O_4$/PMN-PT(011) grown by PLD

Alongside the ID, the number used for the sample in the lab is given, which can also be used to search for the sample information in the sample database[a]. Tables S2 and S3 list parameter used for all MBE and PLD samples. Tables S4 - S7 list the specific growth conditions and sample numbers.

**Table S2:** General MBE parameter

| System | Substrate annealing conditions | postannealing conditions | Oxygen flow [$cm^3$/min] | Oxygen plasma power [W] |
|---|---|---|---|---|
| SCO/STO and SCO/LSAT | 1000°C for 120 min in UHV | 730°C for 90 min and 200°C for 30 min in $O_2$ | 0.12 | 300 |
| SCO/PMN-PT and SCO/LSMO/PMN-PT | 730°C for 60 min in UHV | - | 0.12 | 300 |
| LSMO/PMN-PT | 730°C for 60 min in oxygen | - | 0.15 | 350 |
| $Fe_3O_4$/PMN-PT | 500°C for 60 min | 500°C for 10 min | 0.15 | 300 |

**Table S3:** General PLD parameter

| Oxygen pressure [mbar] | Substrate temperature [°C] | Laser frequency [Hz] | Laser fluence [J/$cm^2$] | Target |
|---|---|---|---|---|
| $2 \cdot 10^{-6}$ | 500 | 5 | 1.5 | $Fe_2O_3$ |

---

[a] https://iffsamples.fz-juelich.de/

**Table S4:** $SrCoO_{2.5}$ sample numbers and growth parameter

| ID | Number | Substrate temperature [°C] | cooling rate [$\frac{^\circ C}{\mathrm{min}}$] | Growth time [min] | Pressure [mbar] | Co frequency change [Hz/s] | Sr frequency change [Hz/s] |
|---|---|---|---|---|---|---|---|
| **S1** | 716 | 850 | 50 | 120 | $8.3\cdot10^{-6}$ | -0.061 | -0.148 |
| **S2** | 715 | 750 | 50 | 120 | $8.5\cdot10^{-6}$ | -0.061 | -0.147 |
| **S3** | 720 | 600 | 50 | 90 | $7.9\cdot10^{-6}$ | -0.061 | -0.148 |
| **S4** | 927 | 600 | 50 | 63 | $7.1\cdot10^{-6}$ | -0.061 | -0.147 |
| **S5** | 893 | 600 | 50 | 75 | $7.1\cdot10^{-6}$ | -0.062 | -0.175 |
| **S6** | 638 | 600 | 50 | 60 | $6.0\cdot10^{-6}$ | -0.061 | -0.189 |
| **S7** | 543 | 600 | 50 | 60 | $1.0\cdot10^{-5}$ | -0.061 | -0.130 |
| **S8** | 547A | 600 | 50 | 60 | $1.0\cdot10^{-5}$ | -0.061 | -0.204 |
| **S9** | 817 | 600 | 50 | 90 | $7.2\cdot10^{-6}$ | -0.061 | -0.154 |
| **S10** | 641 | 600 | 50 | 60 | $7.7\cdot10^{-6}$ | -0.061 | -0.214 |
| **S11** | 699 | 600 | 50 | 120 | $9.7\cdot10^{-6}$ | -0.061 | -0.149 |
| **S12** | 647 | 600 | 50 | 60 | $8.4\cdot10^{-6}$ | -0.060 | -0.225 |
| **S13** | 675 | 600 | 50 | 60 | $7.2\cdot10^{-6}$ | -0.061 | -0.134 |
| **S14** | 646 | 600 | 50 | 60 | $1.0\cdot10^{-5}$ | -0.060 | -0.267 |
| **S15** | 674 | 600 | 50 | 60 | $6.7\cdot10^{-6}$ | -0.061 | -0.134 |
| **S16** | 747B | 600 | 5 | 60 | $8.3\cdot10^{-6}$ | -0.061 | -0.147 |
| **S17** | 746 | 600 | 5 | 60 | $8.5\cdot10^{-6}$ | -0.061 | -0.148 |
| **S18** | 745 | 600 | 5 | 60 | $7.7\cdot10^{-6}$ | -0.061 | -0.147 |
| **L1** | 0651[a] | 600 | 50 | 90 | $4.1\cdot10^{-6}$ | -0.080[c] | -0.100[c] |
| **L2** | 0653[a,b] | 600 | 50 | 100 | $3.9\cdot10^{-6}$ | -0.080[c] | -0.100[c] |
| **L3** | 0652[a] | 600 | 50 | 90 | $4.0\cdot10^{-6}$ | -0.080[c] | -0.100[c] |
| **P1** | 939 | 600 | 50 | 43 | $6.8\cdot10^{-6}$ | -0.061 | -0.163 |
| **LP1**[d] | 894(0602) | 600 | 50 | 48 | $7.2\cdot10^{-6}$ | -0.062 | -0.177 |
| **LP2**[d] | 871(0588) | 600 | 50 | 111 | $7.6\cdot10^{-6}$ | -0.061 | -0.091 |

**Table S5:** $La_{2/3}Sr_{1/3}MnO_3$ layer growth parameter

| Number | Substrate temperature [°C] | cooling rate [$\frac{^\circ C}{\mathrm{min}}$] | Growth time [min] | Pressure [mbar] | La frequency change [Hz/s] | Sr frequency change [Hz/s] | Mn frequency change [Hz/s] |
|---|---|---|---|---|---|---|---|
| 0602[a] | 730 | 2 | 72 | $7.5\cdot10^{-6}$ | -0.110[c] | -0.038[c] | -0.091[c] |
| 0587[a,e] | 730 | 2 | 107.5 | $6.5\cdot10^{-6}$ | -0.110[c] | -0.038[c] | -0.091[c] |
| 0588[a,e] | 730 | 2 | 107 | $6.0\cdot10^{-6}$ | -0.110[c] | -0.038[c] | -0.091[c] |

**Table S6:** $Fe_3O_4$ layer growth parameter with MBE

| ID | Number | Substrate | Substrate temperature [° C] | cooling rate [$\frac{^\circ C}{\mathrm{min}}$] | Growth time [min] | Pressure [mbar] | Fe frequency change [Hz/s] |
|---|---|---|---|---|---|---|---|
| **FM1** | 0625[a,e] | PMN-PT(011) | 500 | 20 | 72 | $4.8\cdot10^{-6}$ | -0.51[b] |

[a] Samples grown in the OMBE system in Jülich.

[b] 4 samples grown simultaneously in special sample holder

[c] Frequency changes calibrated in oxygen.

[d] The sample number in brackets is for the LSMO layer.

[e] Sample deposited by A. Sarkar.

**Table S7:** $Fe_3O_4$ layer growth parameter with PLD; Samples deposited by M. Hussain Hamed

| ID | Number | Substrate | Substrate annealing conditions | Deposition time [min] |
|---|---|---|---|---|
| **F1** | PrT3 | PMN-PT(001) | 500°C for 90 min | 24 |
| **F2** | PrT1 | PMN-PT(011) | 500°C for 90 min | 24 |
| **F3** | An10 | PMN-PT(011) | 400°C for 90 min | 40 |
| **F4** | An3 | PMN-PT(011) | 500°C for 90 min | 40 |
| **F5** | PrT2 | PMN-PT(011) | 500°C for 90 min | 24 |

## S.4 Fit parameter for substrate roughness

In the following the fit results for a comparison of substrate roughnesses are listed, for representative samples on STO, LSAT, and PMN-PT substrates.

**Table S8:** Fit of the XRR measurement of sample 0587 LSMO/PMN-PT (fig. 5.3 bottom)

| layer | thickness [$\mathring{A}$] | roughness [$\mathring{A}$] |
|---|---|---|
| Top layer | $22\,^{+1}_{-2}$ | $6.8\,^{+0.5}_{-0.7}$ |
| LSMO | $319\,^{+4}_{-5}$ | $2\,^{+4}_{-0}$ |
| PMN-PT substrate | - | $12\,^{+1}_{-1}$ |

**Table S9:** Fit of the XRR measurement of S9 $SrCoO_{2.5}$/STO before annealing (fig. 4.22)

| layer | thickness [$\mathring{A}$] | roughness [$\mathring{A}$] |
|---|---|---|
| Top layer | $46\,^{+2}_{-3}$ | $12.8\,^{+0.3}_{-0.5}$ |
| $SrCoO_{2.5}$ | $241\,^{+3}_{-2}$ | $13\,^{+5}_{-2}$ |
| STO substrate | - | $6\,^{+2}_{-1}$ |

**Table S10:** Fit of the XRR measurement of L1 $SrCoO_{2.5/3}$/LSAT before annealing (fig. 4.16).

| layer | thickness [$\mathring{A}$] | roughness [$\mathring{A}$] |
|---|---|---|
| Top | $15^{+2}_{-1}$ | $3.8^{+0.2}_{-0.00002}$ |
| $SrCoO_{2.5}$ | $222^{+2}_{-4}$ | $3^{+2}_{-0.0002}$ |
| LSAT | - | $6^{+1}_{-2}$ |

# List of Figures

# List of Tables

Fakultät für
Mathematik, Informatik
und Naturwissenschaften

RWTH AACHEN UNIVERSITY

**Eidesstattliche Erklärung**

Ich, Patrick Schöffmann

erklärt hiermit, dass diese Dissertation und die darin dargelegten Inhalte die eigenen sind und selbstständig, als Ergebnis der eigenen originären Forschung, generiert wurden.

Hiermit erkläre ich an Eides statt

1. Diese Arbeit wurde vollständig oder größtenteils in der Phase als Doktorand dieser Fakultät und Universität angefertigt;

2. Sofern irgendein Bestandteil dieser Dissertation zuvor für einen akademischen Abschluss oder eine andere Qualifikation an dieser oder einer anderen Institution verwendet wurde, wurde dies klar angezeigt;

3. Wenn immer andere eigene- oder Veröffentlichungen Dritter herangezogen wurden, wurden diese klar benannt;

4. Wenn aus anderen eigenen- oder Veröffentlichungen Dritter zitiert wurde, wurde stets die Quelle hierfür angegeben. Diese Dissertation ist vollständig meine eigene Arbeit, mit der Ausnahme solcher Zitate;

5. Alle wesentlichen Quellen von Unterstützung wurden benannt;

6. Wenn immer ein Teil dieser Dissertation auf der Zusammenarbeit mit anderen basiert, wurde von mir klar gekennzeichnet, was von anderen und was von mir selbst erarbeitet wurde;

7. Ein Teil oder Teile dieser Arbeit wurden zuvor veröffentlicht und zwar in:

   P. Schöffmann, S. Pütter, J. Schubert, W. Zander, J. Barthel, P. Zakalek, M. Waschk, R. Heller, and T. Brückel. Tuning the Co/Sr stoichiometry of $SrCoO_{2.5}$ thin films by RHEED assisted MBEgrowth. *Mater. Res. Express,* **7**, 116404 (2020).

09.07.2021